



PHD

**Development of an advanced composite sandwich structure
(Alternative Format Thesis)**

Flora, Francesco

Award date:
2022

Awarding institution:
University of Bath

[Link to publication](#)

Alternative formats

If you require this document in an alternative format, please contact:
openaccess@bath.ac.uk

Copyright of this thesis rests with the author. Access is subject to the above licence, if given. If no licence is specified above, original content in this thesis is licensed under the terms of the Creative Commons Attribution-NonCommercial 4.0 International (CC BY-NC-ND 4.0) Licence (<https://creativecommons.org/licenses/by-nc-nd/4.0/>). Any third-party copyright material present remains the property of its respective owner(s) and is licensed under its existing terms.

Take down policy

If you consider content within Bath's Research Portal to be in breach of UK law, please contact: openaccess@bath.ac.uk with the details. Your claim will be investigated and, where appropriate, the item will be removed from public view as soon as possible.



PHD

**Development of an advanced composite sandwich structure
(Alternative Format Thesis)**

Flora, Francesco

Award date:
2022

Awarding institution:
University of Bath

[Link to publication](#)

Alternative formats

If you require this document in an alternative format, please contact:
openaccess@bath.ac.uk

Copyright of this thesis rests with the author. Access is subject to the above licence, if given. If no licence is specified above, original content in this thesis is licensed under the terms of the Creative Commons Attribution-NonCommercial 4.0 International (CC BY-NC-ND 4.0) Licence (<https://creativecommons.org/licenses/by-nc-nd/4.0/>). Any third-party copyright material present remains the property of its respective owner(s) and is licensed under its existing terms.

Take down policy

If you consider content within Bath's Research Portal to be in breach of UK law, please contact: openaccess@bath.ac.uk with the details. Your claim will be investigated and, where appropriate, the item will be removed from public view as soon as possible.

Development of an advanced composite sandwich structure



Francesco Flora

A thesis submitted for the degree of

Doctor of Philosophy

University of Bath

Department of Mechanical Engineering

January 2022

Copyright

Attention is drawn to the fact that copyright of this thesis/portfolio rests with the author and copyright of any previously published materials included may rest with third parties. A copy of this thesis/portfolio has been supplied on condition that anyone who consults it understands that they must not copy it or use material from it except as licenced, permitted by law or with the consent of the author or other copyright owners, as applicable.

Signature of Author



Francesco Flora

Acknowledgements

This thesis work represents the final step of my PhD course and life experience at the University of Bath, performed under the supervision of Professor Michele Meo and Dr Fulvio Pinto and financially supported by the EXTREME and NHYTE projects of the European Union's Horizon 2020 research and innovation programme, for which I am honoured and grateful.

I would like to extend my thanks to my supervisors for their excellent guidance throughout my PhD. Michele, I am incredibly grateful for your endless support. I am thankful for the suggestions and encouragements you were always ready to furnish me. I really appreciate the great working relationship we have enjoyed over the past years, and I hope to continue our collaboration in future. Thank you to Fulvio for all the support which helped make my time in Bath so productive and rewarding. With your passion and enthusiasm, you have been a fundamental guide during these years, especially in the most difficult times.

I would like to thank all the members of the research group who have supported me during my PhD experience. In particular, thanks to Marco for his great friendship, for always being on my side whenever I needed it. Thanks also to all my fellow PhD students, Postdoc researchers and visiting students, past and present, from the 2E 4.9 office. The list of people that has had a seat in the office, even if for just the time of a true Italian coffee, during these years is endless, but every one of you has somehow contributed to my path.

I would also like to thank all my friends back in Naples, especially my long-time friend Dario, a companion always by my side in all my experiences, even for part of my time in Bath. Your friendship is a cornerstone for me that I can always count on.

I am forever grateful to my wonderful family: my mum and dad Ivana and Achille, my brothers Emiliano and Luca, and my grandmother Raffaella. I owe it all to the endless love, inspiration and support you have provided me throughout my life.

Lastly, but not least, I would like to thank Giulia, my huge love, my strength. You totally changed my life, and your immense love has become my source of inspiration to face every challenge. You have revolutionized me, making me grow and more aware of myself. You have made me a better man, and I am infinitely grateful to you for that. Now it is time to get closer and start our life together.

Francesco

Abstract

The increasing interest of engineering sectors, such as aerospace and automotive, in research of lighter and stronger materials has stimulated the design of new typologies of composite materials and in the development of their manufacturing processes. In this context, composite sandwich structures represent the main solution when a high ratio of flexural stiffness to weight is required. Sandwich is a composite structure usually made of two thin and strong face sheets, usually laminated composites, bonded to a very light material core, such as lattice cores. The combination of these components makes such materials a complex structure, and their development is intrinsically linked with their manufacturing techniques. This thesis focusses on the improvements of their common weak points, providing solutions for the design, manufacturing and development of novel advanced composite sandwich structures and their components. The processes and structures studied are intended for high performance engineering applications, where sandwich materials composed of fiber reinforced polymers skins and cellular cores (such as aluminium or Nomex honeycomb) are widely used. In detail, the scope of the thesis was approached on different levels. From the manufacturing point of view, improvement of interlaminar properties of laminates was studied through analytical and experimental study of the influence of ultrasound consolidation in debulking of prepreg layers. In addition, a novel *real-time* non-destructive evaluation technique methodology based on an innovative undamaged baseline was developed, which is able to promptly detect defected parts in automatic composite manufacturing processes. From the design point of view, a novel high-performance carbon fibre reinforced sandwich core with thermal induced prestresses was developed. The core was analytically, numerically and experimentally characterised, proving high in-plane and out-of-plane mechanical properties and a remarkable compressive strength to density ratio. To conclude the work, a final novel 3D fibre reinforced sandwich structure, with skins and core constituted by the same material, without adhesive layers and with enhanced mechanical properties was designed, manufactured and characterised under low-velocity impact tests.

Each of these approaches represents a solution for the development of novel improved sandwich structures and can be applied in engineering sectors where low number of manufacturing defects and high performance materials and structures are required.

Table of Contents

ACKNOWLEDGEMENTS	III
ABSTRACT	V
LIST OF FIGURES	IX
LIST OF TABLES	XIV
1. INTRODUCTION	1
1.1. OVERVIEW	1
1.2. OBJECTIVES.....	2
1.3. OUTLINE OF THE THESIS	6
2. BACKGROUND OF COMPOSITE AND SANDWICH MATERIALS	8
2.1. COMPOSITE MATERIALS	8
2.1.1. <i>Introduction</i>	8
2.1.2. <i>Manufacturing of composite laminates in aerospace</i>	9
2.2. SANDWICH STRUCTURES	13
2.2.1. <i>Historical background</i>	13
2.2.2. <i>Sandwich Design</i>	15
2.2.3. <i>Failure mechanisms of sandwich structures</i>	20
2.3. CONCLUSIVE REMARKS	24
3. PAPER 1: ULTRASONIC CONSOLIDATION (UC) DEBULKING OF THERMOSETTING PREPREG 27	
4. PAPER 2: DEVELOPMENT OF AN ANALYTICAL MODEL FOR OPTIMISATION OF THE ULTRASONIC CONSOLIDATION OF COMPOSITE PREPREG	48
5. PAPER 3: REAL-TIME THERMOGRAPHY SYSTEM FOR COMPOSITE WELDING: UNDAMAGED BASELINE APPROACH	89
6. PAPER 4: MANUFACTURING AND CHARACTERISATION OF THERMAL PRE-STRESSED CARBON FIBRE REINFORCED LATTICE CORE	126
7. PAPER 5: EXPERIMENTAL AND NUMERICAL ANALYSIS OF AN IMPACT RESISTANT SANDWICH STRUCTURE WITH THERMAL PRE-STRESSED CARBON-FIBRE REINFORCED LATTICE CORE 181	
8. CONCLUSIONS	223

8.1. FUTURE WORKS	226
8.2. PHD ACTIVITIES.....	226
REFERENCES.....	229

List of Figures

<i>Figure 2.1 - Schematic representation of FRP composite lamina and laminate</i>	9
<i>Figure 2.2 - Air package entrapped between prepreg layers during hand lay-up</i>	11
<i>Figure 2.3 – Epoxy resin cure cycle, from [14]</i>	12
<i>Figure 2.4 - World's largest autoclave, from ASC Process Systems [15]</i>	12
<i>Figure 2.5 - Schematic representation of a symmetric sandwich beam subjected to a 3-point bending load</i>	16
<i>Figure 2.6 - Force, stresses and bending moments positive sign convention</i>	18
<i>Figure 2.7 – Stress and shear stress distribution in a sandwich beam (a), under assumption of constant shear stress through the core (b) and constant stress through the skins (c) thickness</i>	20
<i>Figure 3.1 – a) Dibble tool for air removal and b) vacuum bag set-up (figure from [14])</i>	34
<i>Figure 3.2 - Ultrasonic consolidation setup: 1 vacuum ultrasonic transducer; 2 waves generator; 3 amplifier; 4 transducer vacuum pump; 5 vacuum bag pump; 6 aluminium plate bottom part</i>	37
<i>Figure 3.3 – Ultrasonic consolidation schematic representation</i>	37
<i>Figure 3.4 - a) Laminates after autoclave cure and b) samples after diamond blade cut</i>	38
<i>Figure 3.5 - Compression-dedicated fixture used during experimental campaign tests</i>	40
<i>Figure 3.6– Sketch of ILSS test setup</i>	41
<i>Figure 3.7 - Plots of compression tests results for 3 UC configurations and reference: a) stress-strain curves, b) compressive strength, c) compressive modulus and d) relative statistical data and percentage variation in comparison with reference (PC)</i>	42
<i>Figure 3.8 - Plots ILSS results: a) stress-displacement curves, b) interlaminar strength graph with standard deviation bars and c) relative statistical data and percentage variation in comparison with reference (PC)</i>	43
<i>Figure 4.1 - Stress intensification due to the presence of void</i>	56
<i>Figure 4.2 – Deformation of cylindrical channel walls by ultrasonic waves generated from the source (S)</i>	61
<i>Figure 4.3 - Net flow rate Q [mm^3/s] versus the travelling wave velocity c [m/s]</i>	70
<i>Figure 4.4 – Net flow rate Q [mm^3/s] versus the average channel radius r_0 [mm] in the case of ultrasonic radiation only (green line), vacuum pressure only (red line) and ultrasonic radiation plus vacuum pressure (blue line)</i>	71
<i>Figure 4.5 - Net flow rate Q [mm^3/s] versus the wave a) frequency (kHz) and b) amplitude (m)</i> ..	72
<i>Figure 4.6 – Ultrasonic consolidation debulking setup</i>	73
<i>Figure 4.7 – Representative microscope images of sample a) PC, b) UC1, c) UC2, d) UC3. The voids are represented by the black spots</i>	75
<i>Figure 4.8 - Setup of three-points bending test</i>	77

<i>Figure 4.9 - Flexural results plots for 3 ultrasonic consolidation configurations and reference: a) stress-strain curves, b) flexural strength, c) flexural strain, d) flexural modulus graphs with standard deviation bars</i>	79
<i>Figure 4.10 - Charpy impact test apparatus: specimen (1), hammer (2) and scale (3)</i>	80
<i>Figure 4.11 - Charpy impact strength graph with standard deviation bars</i>	81
<i>Figure 5.1 - Induction heating process</i>	99
<i>Figure 5.2 - Infrared active thermography general setup</i>	102
<i>Figure 5.3 - Thermal images capturing process at the beginning (a), middle (b) and end (c) of the welding line.</i>	103
<i>Figure 5.4 - Summary of thermal image processing and building of TI 3D matrix and dTI image.</i>	104
<i>Figure 5.5 - Processing of thermal images using the frame stack (a), thermal intensity over the width (b) and the final aggregate thermal intensity (c)</i>	105
<i>Figure 5.6 - Welding system: induction heating coil (1); PA6-Ti sample (2); PTFE pressure roller (3); rear IR cameras (4); cooling fan (5) [30]</i>	107
<i>Figure 5.7 – Samples damage configuration [31]</i>	108
<i>Figure 5.8 - Thermal dTI images for undamaged baseline (a), undamaged sample (b), baseline subtraction dTIsub (c)</i>	110
<i>Figure 5.9 - wTI for UD1 (a), wTI for UD2 (b), aTI for UD1 (c), aTI for UD2 (d), aTIsub(e)</i>	111
<i>Figure 5.10 - Thermal dTI images for undamaged baseline (a), damaged sample D1 (b), baseline subtraction dTIsub (c)</i>	112
<i>Figure 5.11 - wTI undamaged baseline (a), wTI image for D1 (b), aTI undamaged baseline (c), aTI profile for D1 (d), aTIsub (e)</i>	113
<i>Figure 5.12 - Thermal dTI images for undamaged baseline (a), damaged sample D2 (b), baseline subtraction dTIsub (c)</i>	114
<i>Figure 5.13 - wTI undamaged baseline (a), wTI image for D2 (b), aTI undamaged baseline (c), aTI profile for D2 (d), aTIsub (e)</i>	115
<i>Figure 5.14 - Thermal dTI images for undamaged baseline (a), damaged sample D3 (b), baseline subtraction D3-UD (c)</i>	116
<i>Figure 5.15 - wTI undamaged baseline (a), wTI image for D3 (b), aTI undamaged baseline (c), aTI profile for D3 (d), aTIsub (e)</i>	117
<i>Figure 5.16 - dTIsub profiles for UD2 (a), D1 (b), D2 (c) and D3 (d) samples with samples illustration</i>	118
<i>Figure 6.1 - Circular cell honeycomb distribution. The red circle highlights the gap between adjacent cells.</i>	134

<i>Figure 6.2 - Circular cell honeycomb structure: a) detail of the intercellular spaces filled by the resin; b) comparison with hexagonal cell and detail of the avoided sharp corners.....</i>	<i>137</i>
<i>Figure 6.3 - CPCC unit cell.....</i>	<i>137</i>
<i>Figure 6.4 - Geometrical approximations of the unit cell under in-plane compressive loads.....</i>	<i>140</i>
<i>Figure 6.5 - Geometry of the composite laminate and axes orientations: a) cross section of flat configuration; b) first stable configuration with curvature along the y-direction; c) second stable configuration with curvature along the x-direction.....</i>	<i>142</i>
<i>Figure 6.6 - FEM model of the unit cell wall with fiber orientation [0 (red), 90 (blue)].....</i>	<i>145</i>
<i>Figure 6.7 - Thermal stress [GPa] t-direction component for a) [0,90] and b) [90,0] configurations.....</i>	<i>146</i>
<i>Figure 6.8 - Cell wall model boundary conditions. Blue nodes (bottom): all DOF constrained; red nodes (top): in-plane DOF constrained and out-of-plane prescribed motion; yellow nodes (sides) periodic conditions at all DOF.....</i>	<i>147</i>
<i>Figure 6.9 - a) Force-displacement curves from FEM analysis on prestressed and not prestressed unit cell wall model in [0,90]; b) details from FEM analysis results on pre-stressed [0,90] model.....</i>	<i>148</i>
<i>Figure 6.10 - Force-displacement curves from FEM analysis on prestressed and not prestressed unit cell wall model in [90,0].....</i>	<i>149</i>
<i>Figure 6.11 - FEM model of the unit cell in a) [0,90]s and b) [90,0]s configurations. In red the 0 and in blue the 90 fiber orientations.....</i>	<i>150</i>
<i>Figure 6.12 - Force-displacement curves from FEM analysis on prestressed and non-prestressed unit cell model in a) [0,90]s and b) [90,0]s configurations.....</i>	<i>151</i>
<i>Figure 6.13 - Bistable buckling failures of unit cells.....</i>	<i>152</i>
<i>Figure 6.14 - Thermal stress [GPa] t-direction component.....</i>	<i>153</i>
<i>Figure 6.15 - FEM analysis stress-strain curves of compression-out-of-plane simulated tests at various percentages of modified nodes.....</i>	<i>154</i>
<i>Figure 6.16 - CPCC manufacturing fixture.....</i>	<i>156</i>
<i>Figure 6.17 - CPCC lay-up steps: a) the first row of pins (blue) is placed in the base (grey) grooves; b) the first CFRP layer (purple) is placed on top of the pins; c) another row of pins is placed on the CFRP layer following the pattern of spaces left from pins of the first row; d) a second CFRP layer is positioned on the second row of pins.....</i>	<i>157</i>
<i>Figure 6.18 - Manufacturing of CPCC samples.....</i>	<i>158</i>
<i>Figure 6.19 - CPCC a) fibre orientation and b) final product.....</i>	<i>158</i>
<i>Figure 6.20 - CPCC mechanical tests: a) compression out-of-plane; b) compression in-plane (w direction); c) beam flexure.....</i>	<i>160</i>
<i>Figure 6.21 - Compression out-of-plane stress-strain curves of CPCC and honeycomb samples.....</i>	<i>162</i>

<i>Figure 6.22 - Compression out-of-plane stress-strain curves of CPCC samples: elastic part detail</i>	163
<i>Figure 6.23 - Compression in-plane stress-strain curves along a) L and b) W directions</i>	164
<i>Figure 6.24 - In-plane compressive failure of CPCC (a) (l-direction) and (b) (w-direction) and aluminium honeycomb (c) (l-direction) and (d) (w-direction)</i>	165
<i>Figure 6.25 - Beam flexure stress-flexural strain curves</i>	166
<i>Figure 6.26 - Detail of failure between the core and upper skin during the beam flexure test</i>	166
<i>Figure 6.27 - Modified Ashby's chart for compressive strength vs. density for low density materials. Original figure from [31]</i>	170
<i>Figure 6.28 - Compression out-of-plane stress-strain curves, comparison between numerical and experimental results</i>	172
<i>Figure 6.29 - Compression in-plane stress-strain curves in a) w and b) l directions, comparison between numerical and experimental results</i>	173
<i>Figure 7.1 - CPCC core manufacturing frame</i>	191
<i>Figure 7.2 - CPCC core manufactured sample</i>	192
<i>Figure 7.3 - CPCC Sandwich sample before (a) and after (b) skins cure</i>	195
<i>Figure 7.4 - Impactor testing machine: sample holder (1), impactor striker (2) and impactor head (3)</i>	196
<i>Figure 7.5 -Residual thermal Von Mises stress contour plot of the CPCC sandwich FE model.</i>	201
<i>Figure 7.6 - Time vs force and displacement vs force curves obtained from 20J impact tests on CP, C and H representative sandwich samples</i>	202
<i>Figure 7.7 - Time vs force and displacement vs force curves obtained from 45J impact tests on CP, C and H representative sandwich samples</i>	202
<i>Figure 7.8 - Representative 20J (left) and 45J (right) CP (a and b), C (c and d), H (e and f) tested samples and a detail of the side view (g) of 45J H tested sample</i>	204
<i>Figure 7.9 - TOF C-scan and Amplitude C-Scan imaging - 20 J a) C sample; b) CP sample</i>	209
<i>Figure 7.10 - TOF C-scan and Amplitude C-Scan imaging - 45 J a) C sample; b) CP sample</i>	210
<i>Figure 7.11 – CT scan quarter sections from representative CP (left) and C (right) samples impacted at 20J (top) and 45J (bottom)</i>	211
<i>Figure 7.12 - Comparison between numerical (orange) and experimental (blue) results for 20J (top) and 45J (bottom) LVI tests</i>	212
<i>Figure 7.13 – Comparison of impacted structure and residual core thickness between CT scan (left) and FE model (right) of 20J (top) and 45 (bottom) impacted CPCC samples</i>	214
<i>Figure 7.14 – Von Mises stress distribution in GPa in CP (left) and C (right) core along central section for [0] (top) and [90] (bottom) orientation before impact event (T0)</i>	215
<i>Figure 7.15 - Von Mises stress distribution in GPa in CP (left) and C (right) core along central section for [0] (top) and [90] (bottom) orientation during the impact event (T1)</i>	215

Figure 7.16 - Von Mises stress distribution in GPa in CP (left) and C (right) core along central section for [0] (top) and [90] (bottom) orientation during impact event at the crush failure of the core (T2)..... 216

List of Tables

<i>Table 3.1 - Manufacturing debulking times and thicknesses of samples</i>	38
<i>Table 3.2 - Tests sample dimensions</i>	38
<i>Table 4.1 – Samples voids projected area: average and standard deviation</i>	75
<i>Table 4.2 – Flexural results, statistical data and percentage variation in comparison with reference (PC)</i>	80
<i>Table 4.3 - Charpy impacts results, statistical data and percentage variation in comparison with reference (PC)</i>	82
<i>Table 4.4 - Summary of percentage variation from reference of UC configurations</i>	84
<i>Table 5.1 - Samples nomenclature and damage dimensions</i>	108
<i>Table 6.1 - Material properties (subscripts 11 refer to fiber direction, 22 to in-plane direction perpendicular to the fibers and 33 through the thickness): ρ density; E modulus of elasticity; ν Poisson's ratio; G shear modulus; X_C and X_T longitudinal compressive and tension strengths; Y_C and Y_T transverse compressive and tension strength; SC shear strength.</i>	144
<i>Table 6.2 - Tie-break contact properties: F_S and F_D static and dynamic coefficients of friction; $NFLS$ normal failure stress; $SFLS$ shear failure stress.</i>	144
<i>Table 6.3 - Cores specifications</i>	161
<i>Table 6.4 - Mechanical tests results mean values, standard deviation in brackets: compression out-of-plane and compression in-plane L</i>	167
<i>Table 6.5 - Mechanical tests results mean values, standard deviation in brackets: compression in-plane W and beam flexure</i>	168
<i>Table 6.6 - Specific Mechanical tests results mean values: compression out-of-plane and compression in-plane L</i>	168
<i>Table 6.7 – Specific mechanical tests results mean values: compression in-plane W and beam flexure</i>	169
<i>Table 6.8 - Specific mechanical properties percentage variation between aluminium honeycomb and CPCC</i>	169
<i>Table 6.9 - Unit-cell elastic moduli: analytical and FEM evaluations</i>	171
<i>Table 7.1 - Material properties used in the model for MAT 054, MAT 059 and MAT 001 (subscripts 11 refer to fibre direction, 22 to in-plane direction perpendicular to the fibres and 33 through the thickness): ρ density; E modulus of elasticity; ν Poisson's ratio; G shear modulus; X_C and X_T longitudinal compressive and tension strengths; Y_C and Y_T transverse compressive and tension strength; Z_C and Z_T (only for solid elements) normal compressive and tension strength; SC shear strength; subscriptions steel and mass refer to bottom and top part of the striker; F_S and F_D contact static and dynamic coefficients of friction; $NFLS$ contact normal failure stress; $SFLS$ contact shear failure stress.</i>	200

<i>Table 7.2 – 20J LVI experimental results mean values, standard deviation in brackets, and percentage variations</i>	<i>205</i>
<i>Table 7.3 - 45J LVI experimental results mean values, standard deviation in brackets, and percentage variations</i>	<i>205</i>
<i>Table 7.4 - LVI experimental specific results mean values and percentage variations. Specific properties (divided by the density) are denoted by *</i>	<i>207</i>
<i>Table 7.5 – Damage area and residual thickness values resulting from NDE analysis of CP and C samples with percentage variation</i>	<i>211</i>
<i>Table 7.6 – Average experimental results and numerical results for 20J and 45J impact tests ...</i>	<i>213</i>

1. Introduction

1.1. Overview

During the last decades, weight reduction of materials and structures has been a driving force of engineering research in many sectors such as aerospace, automotive and energy. In this context, composite materials play an important role, substituting traditional materials, such as aluminium, in many applications. Nowadays, at least the 50% in weight of the external parts and 70% of the internal parts of the aircraft is made of composite materials [1]. Among the different kinds of composite materials, the most important in engineering sectors are the Fibre Reinforced Polymers (FRPs), consisting of a fiber reinforcement (typically carbon, glass or Kevlar) embedded in a polymeric (thermoset or thermoplastic) matrix. The reason of the relative recent large diffusion of this typology of materials in engineering sectors is to be searched in their unique combination of low weight and high mechanical properties, in addition to a high tailorability and versatility. Advanced FRPs typically are in a laminated configuration, where the laminate consists of layers of different fibre orientations. The design of fiber reinforcement orientation along the layers allows high tailorability of the mechanical properties of the final part.

When a high ratio of flexural stiffness to weight is required, composite sandwich structures are the best solution. Sandwich is a composite structure usually made of two thin and strong face sheets bonded to a very light material core. From a theoretical point of view, if the core is not very flexible, sandwiches can be seen as composite laminates in which one of the layers, typically the middle one, is the core. The advantage in adding the core layer, thus creating the sandwich structure, is related to a very simple mechanical principle. If a structure is loaded under bending, the bending stress is related to the moment of inertia of the part: increasing the thickness, the moment of inertia, and therefore the bending stiffness, of the structure is enhanced. To increase the thickness of a composite laminate without compromising the weight of the structure, lightweight materials are used as core.

In a sandwich composite, generally, each component is relatively weak if stressed along certain directions (in-plane for the core, out-of-plane for the skins) but when combined, the result is an extremely stiff and lightweight structure. Despite this, as for all the composite laminates, sandwich structures present some limitations. Usually, skins are bonded to the core using adhesives, creating interfaces that represent weak points in the structures. Indeed, the first major failure mode for sandwiches under impact loadings is the delamination, either between layers of the skins or at the interface between skins and core [2]. Moreover, the core is usually designed to reach low levels of density to the detriment of mechanical properties along the in-plane directions. These are usually considered negligible for sandwich core because all the in-plane stresses are carried out by face sheets under bending conditions. Nevertheless, in-plane properties of the core play an important role when talking about manufacturing [3] and lateral and impact loadings [4].

The research and development of novel mechanically improved sandwich structures require solutions to overcome these limitations, exploring new manufacturing techniques for core, skins and their bonding.

1.2. Objectives

This thesis focusses on solutions for the design, manufacturing and development of novel advanced composite sandwich structures and their components, for high performance applications, such as the aerospace and automotive sectors, where sandwich materials composed of fiber reinforced polymers skins and cellular cores (such as aluminium or Nomex honeycomb) are widely used. As it will be shown in the following chapter, the main weak points of sandwich structures are the mechanical properties of the core and the interlaminar strength of laminated skins and at the interface between core and skins, particularly if loaded under in-plane and impact stresses.

The scope of this thesis is to develop novel techniques for the manufacturing of core, skins and bonding between the two in order to enhance the mechanical

properties of the final structure and overtake the sandwich weaknesses. The approach to obtain this aim is based on the following points:

- The use of ultrasound consolidation procedure on prepreg layers to obtain improvements in terms of interlaminar properties of the laminates;
- Development of a novel NDE technique methodology based on an innovative undamaged baseline able to promptly detect defected parts in an automatic composite manufacturing process;
- The design and manufacturing of a novel high-performance CFRP core with thermal induced prestresses with improved in-plane and out-of-plane mechanical properties;
- The design, manufacturing and impact characterisation of a novel high-performance all-composite sandwich structure.

This thesis starts with a literature study on composite and sandwich materials, particularly focusing on the manufacturing techniques, the theory behind sandwich design and their principal failure mechanisms. Starting from this analysis, the thesis illustrates the works performed during the PhD program with the aim to act against the known weak points of such materials and realise an improved sandwich structure.

The first work is on the study of the ultrasound consolidation (UC) technique and its application during the hand lay-up manufacturing of prepreg laminates in order to minimise the air entrapped between the layers and minimise the porosity of the final product. The influence of the technique on the mechanical properties of the laminates is experimentally studied in comparison with samples manufacturing with traditional method. The results show large improvements, particularly in terms of manufacturing time and Interlaminar Shear Strength (ILSS). In order to give a more detailed study of the influence of UC on the debulking of the prepreg material, the study continues with the development of an analytical model. The model simulates the propagation of the ultrasonic waves through the material as a peristaltic pump, which transports the air bubbles along the interface between the

layers thanks to the deformations of the walls. The ultrasonic waves are combined with the pressure gradient given by a vacuum pump, and the results demonstrate that the phenomenon is particularly efficient in the removal of air bubbles with small dimensions. Moreover, the analytical model provides important information and guidelines about the optimisation of the process parameters. Some additional experimental studies are also described, whose results show the low levels of voids content through microscope analysis and the increment of the compressive modulus of final parts.

The following section illustrates the development of an innovative real-time manufacturing NDE technique. Composite materials are strongly sensible to the presence of defects in the part, which can drastically decrease the mechanical performances and lead to premature fail of the component. Given the high demand of automated manufacturing processes for composite materials, such as automatic fibre placement (AFP), automatic tape placement (ATP) and automatic induction welding, the need of efficient NDE techniques is in large increment. An innovative NDE technique for automatic manufacturing processes was developed, focused on the improving of traditional NDE thermography by means of building an undamaged baseline. In this way, a damaged part can be easily detected, even in a strong heterogeneous heat field, such as in the case of manufacturing processes based on induction heating. The technique was experimentally tested on an automatic induction welding machine, improving the detection and characterisation of several kinds of defects. This NDE technique can improve automatic processes, reduce the defects in the parts and reduce manufacturing costs, therefore facilitating the implementation of new composite structures in many applications.

The successive section describes the development of a novel sandwich core, whose design is focused on three concepts:

- The use of CFRP material to obtain high mechanical properties along the loaded directions, maintaining a low density;
- The use of a circular cell *close-packing* 2D structure design;

- The application of residual thermal stresses in order to enhance the compressive and energy absorption properties.

Based on these, the novel core was named Circular Prestressed Carbon Core (CPCC). The design of the core started with the analytical study of the properties of the unit cell. A numerical study of the improvements on the mechanical properties of the core unit-cell given by the applied thermal stresses and an analysis of contribution of the fiber orientation is described. The FEM model was used to predict the compressive properties of the core along the out-of-plane and in-plane directions and the influence of the structure defects on the final properties. The CPCC core was manufactured applying the UC technique to improve the ILSS of the CFRP strips and using an *ad hoc* mould to generate the 2D circular cell pattern. The residual stresses were generated with a sudden cooling down cycle after the oven cure. The core was experimentally characterised, and results compared with a traditional aluminium honeycomb core. The results showed large improvements when compared to traditional cores, especially in terms of in-plane properties and out-of-plane compressive strength to density ratio.

Finally, a novel sandwich structure is realised using the CPCC core and CFRP skins, both manufactured using the same prepreg material. UC technique was applied during the manufacturing of the skins, core and the bonding of them. The mechanical properties of the final structure were experimentally and numerically studied under impact loadings and the results compared with the same structure realised without core thermal residual stresses. Furthermore, a comparative campaign was conducted with sandwich panels made with aerospace grade aluminium honeycomb core in order to evaluate the competitiveness of the CPCC core in the field. Damage extension in skins and core was evaluated through NDE analysis of the impacted samples, and the results showed the significant improvements in damage reduction carried by the novel core and the residual thermal stresses.

In conclusion, the aim of the thesis to improve manufacturing processes to obtain high-performance composite structures was achieved using UC technique during

the manufacturing of composite skins and sandwich structures to reduce the number of voids in the parts, developing a new *real-time* NDE technique for automatic composing manufacturing processes to reduce the number of defects in CFRP laminates, and designing a novel composite core and sandwich structure with enhanced mechanical properties.

1.3. Outline of the Thesis

This thesis follows the alternative format, meaning that some of the papers realised during the PhD programme are presented as chapters.

Chapter 2 provides the background and a literature review on research works focused on the manufacturing of composite materials, sandwich structures, sandwich theory and their main failure mechanisms.

In chapters 3, 4, 5, 6 and 7 five papers are reported, which describe the aforementioned four main approaches followed to accomplish the aim of this work. Each article is preceded by an introduction, where aim, methodology and results of the paper are summarised.

In chapter 3, the first paper describes the experimental study aimed to analyse the benefits provided by the use of ultrasonic consolidation during the debulking of CFRP prepregs. The technique provided large reductions in terms of manufacturing time and voids content, while experimental results showed significant improvements of ILSS of the final laminates.

In chapter 4, a publication that continuous the work described in the previous paper is reported. In this second paper, an analytical model is developed, which describes the influence of the ultrasonic waves on the air flux through the prepreg layers and gives some guidelines on process optimisation. Additionally, some experimental studies are illustrated, which consist in the microscope analysis of the sample section for voids content evaluation and compressive and impact tests.

In chapter 5, a paper describing the development of the NDE technique for *real-time* damage detection during automatic manufacturing processes is presented. The

methodology, focused on the building of an undamaged baseline, is experimentally tested during automatic induction welding of thermoplastic composites, detecting different kinds of defects, and showing clear improvements in comparison with classic thermography.

Chapter 6 illustrates the work published about the design and development of the CPCC core. The paper starts with some analytical considerations about the unit cell geometry, material properties and composite bistability. The manufacturing process used to produce core samples and the mechanical tests are described. The experimental results, which show excellent compressive and shear properties and a unique specific compressive strength of the core, were used to validate the FEM model.

Chapter 7 concerns the description of the final experimental part of the project. A final sandwich structure is manufactured using the UC technique and the CPCC core. Experimental tests were performed in order to evaluate the impact properties of the structure and the influence of the residual thermal stresses on the damage extension in the impacted parts, and compared with samples manufactured with aluminium core in order to evaluate its competitiveness in the field, demonstrating large improvements.

The conclusions of the thesis and some possible future developments are reported in chapter 8.

2. Background of composite and sandwich materials

This chapter aims to provide a preface of the research, giving an overview of composite materials and sandwich structures. The first section constitutes a general introduction on composite laminates and their principal manufacturing techniques, showing the development reached in the last decades in the production of this kind of materials. The second section focuses on sandwich structures, main subject of this thesis, describing the mechanical principle behind their design and the principal failure mechanisms.

2.1. Composite materials

2.1.1. Introduction

The term composite means that two or more materials or phases combine on a macroscopic scale to constitute a third material [5]. The difference with other kinds of materials that are a combination of two or more elements, such as alloys, is that composites are heterogeneous at macroscopic level and each phase maintain its characteristics, which combine to create a material with improved properties. This concept of combined properties gives to composite materials their main advantage among traditional materials, which is their high tailorability. Indeed, combining materials with different properties, shapes or even orientations, it is possible to design the parts to obtain characteristics and properties specific for the application.

An important example of highly tailorable composites are the fiber-reinforced polymers (FRPs), which are constituted by a fibrous phase (glass, carbon and Kevlar the most commons) that generally gives high mechanical properties along certain directions, and a polymeric matrix (thermoplastic or thermoset), which mainly plays the role of transfer the load between fibres. The fiber reinforcement can be distributed and oriented through the matrix in such a way that the highest mechanical properties are along the directions of the predicted loads, while the polymeric matrix keeps the fibers in position while maintaining a relative low density, making FRP a valid lighter alternative to traditional structural materials,

such as metals. The most important role for high properties applications of FRPs is played by composite laminates, which are layered structures where each lamina is typically characterised by a fiber orientation, unidirectional or interwoven, as schematically represented in Figure 2.1.

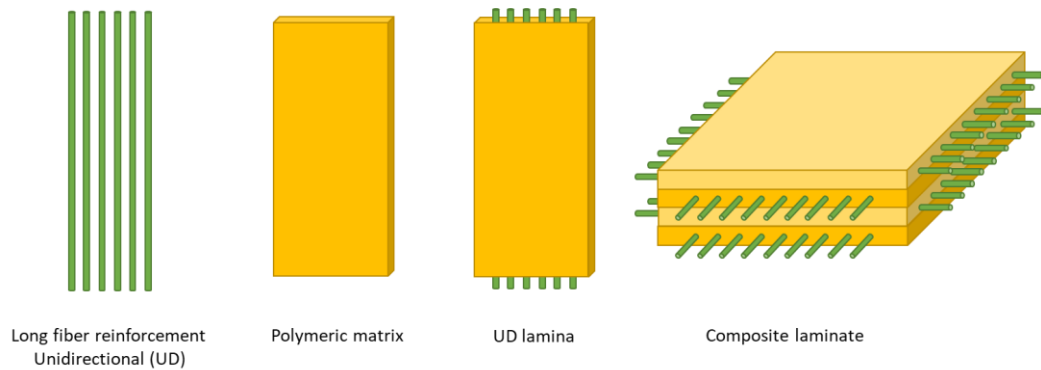


Figure 2.1 - Schematic representation of FRP composite lamina and laminate

FRPs play a crucial role in modern material engineering, being extensively used and developed in several sectors, such as aerospace, automotive and naval industries. Laminated FRP composites gained large diffusion in the aerospace sector, where they replaced traditional materials in both primary and secondary structures. An example of this is the modern Airbus A350 XWB aircraft, which is composed by 52% in weight by composites, and a similar percentage can also be found in the new Boeing 787 Dreamline, characterised by its unique all-composite fuselage [6].

2.1.2. Manufacturing of composite laminates in aerospace

The high versatility and tailorability of composite materials required manufacturing techniques highly specific for each application, with a strong correlation between the manufacturing of the composite material and the fabrication process of the final structure [7]. Therefore, due to the numerous techniques developed during the last decades for the several applications, it is not possible nor in the aim of this work to provide a complete description of the manufacturing processes of this kind of materials. The scope of this section is to provide an overview of the manufacturing techniques generally utilised in advanced applications, such as for the aerospace sector, the R&D and the production of laminated composites.

Some of the most diffused manufacturing techniques for composite materials are compression moulding, resin transfer moulding (RTM), vacuum-assisted resin transfer moulding (VARTM), filament winding, hand and automatic lay-up and autoclave curing. For the aerospace sector, in primary structures, the largest portion of components (more than 70% [8]) are manufactured starting by layers of unidirectional or woven fibers preimpregnated in a resin matrix. Thin sheets of preimpregnated material, commonly named prepreg, are generally cut to the desired shape and stacked layer by layer following the required fiber orientation to produce the final laminate. The extensive use of prepreg layers is due to their ideal fiber volume content, uniformity and adaptability to different shapes and dimensions, allowing to achieve optimum mechanical properties and quality of final products. The prepreg layers are generally laid-up on a mold and enclosed in a sealed bag in order to be subsequently processed at resin cure temperature and pressure to obtain the final laminate.

This manufacturing process of laminated FRPs have seen many variables in the years. During the last 20 years, cut and lay-up of prepreg layers, originally done manually by the operators, has been increasingly automatized by using automatic tape layers (ATLs) machines. Despite the extensive research and applications in industrial sectors, particularly aerospace, of these large and expensive machines, hand lay-up of prepreg laminates remains a process widely applied [9] thanks to several advantages: low initial costs, flexibility in design and shape of the part, high quality of the final products. Based on this, hand lay-up is extensively used for the manufacturing of smaller components, prototypes and generally for research and development of composite laminates. On the other side, this process has numerous limitations, such as low replicability of the parts and very low production rate, which make it not suitable for large scale productivity.

One of the most important steps during the prepreg lay-up for the quality of the ultimate products is the debulking step, which consist in apply pressure to the stacked prepreg layers in order to remove the air entrapped between the plies. Figure 2.2 shows an example of a large air package entrapped between two prepreg layers.

For the automatic system, this step is generally done by a pressure roll that follows the placement of the prepreg layers. During the hand lay-up, the debulking is ensured by the operator which applies pressure by means of a tool during the layer placement, operates vacuum cycles during the stacking and applies pressure during the cure process. This is one of the reasons why the hand lay-up produces better-quality laminates at the cost of a more time-consuming process.



Figure 2.2 - Air package entrapped between prepreg layers during hand lay-up

Automatic lay-up processes are highly customisable production mechanisms for composite materials that can be associated to Additive Manufacturing (AM) processes [10] and are typically distinguished in Automatic Tape laying (ATL) [11] and Automated Fibre Placement (AFP) [12], which mainly differentiate in the dimensions of the feeding material. AFP is designed to lay-up prepreg layers within the range of 6.35-25.4 mm in width, while for the ATP process they can be up to 1000 mm [13].

Both manual and automatic laid-up thermoset prepreg laminates are commonly cured in autoclave at an optimal temperature-pressure cycle to obtain the maximum mechanical properties from the matrix. Figure 2.3 shows a typical curing cycle of an epoxy resin prepreg. The autoclaves can be of various dimensions, with the largest ones arriving up to almost 10 meters of internal diameter and several tens of meters in length (Figure 2.4). The gas generally used in the autoclave to reach the desired temperature and pressure is Nitrogen, and the laminates are commonly enclosed in a vacuum bag film with several layers of materials to provide a correct flow of the air remained between the layers and of the excess resin. The mould is

coated with a release agent in order to facilitate the removal of the part after the curing. The enclosure of the laminate in the bag is typically a manual process.

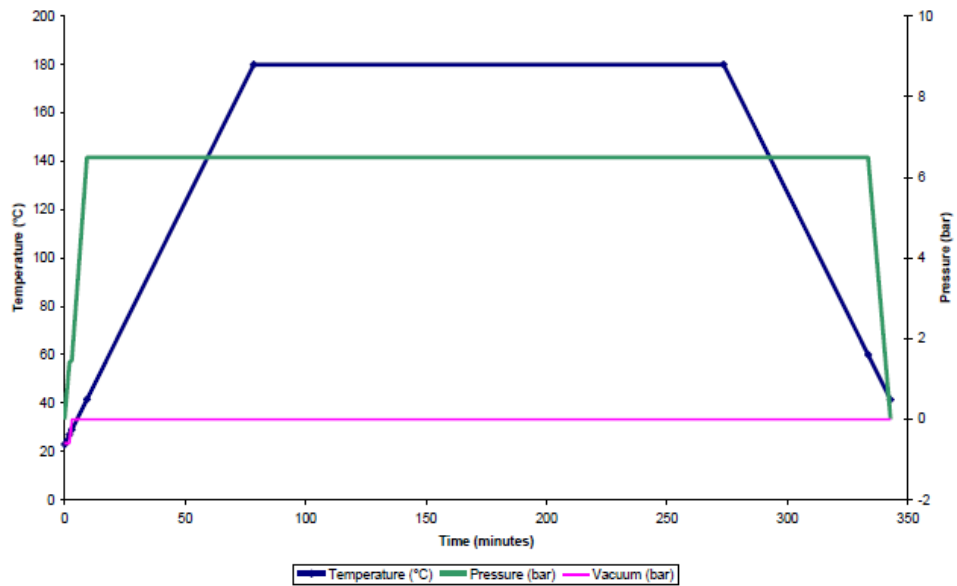


Figure 2.3 – Epoxy resin cure cycle, from [14]



Figure 2.4 - World's largest autoclave, from ASC Process Systems [15]

The high control of the environment temperature and pressure inside the autoclave allows to reach optimal compaction and curing of the laminates. On the downside, these machines are considerably expensive, in particular if of large dimensions, require high maintenance and the curing process is laborious and include the use of

several consumables. Despite this, autoclave curing remains the most used process for the manufacturing of airframe composite components [16], but the research of out-of-autoclave manufacturing processes is expanding in favour of less cost-consuming processes.

While the ATL and AFP processes were originally limited to the use of thermoset resin prepreg, the development of technologies and the increasing need of lower cost and more environmentally friendly materials have pushed the diffusion of thermoplastic composites (TPCs) materials. If traditional prepreg layers can take advantage of the stickiness of the uncured resin to be consolidated during the lay-up, thermoplastic matrix layers need to be heated-up locally over the melting point in order to create the laminate, providing some limitations in the consolidation and manufacturing processes. On the other side, TPCs do not require cost-consuming curing processes, do not need time-limited low-temperature storage such as in the case of thermoset resins, are characterised by a combination of high damage tolerance and fracture toughness, and provide high recyclability [17]. These are the main reasons that are pushing the large diffusion of research and application around TPCs for the manufacturing of aircraft components.

2.2. Sandwich structures

2.2.1. Historical background

Sandwich structures are a special class of composite materials, which are typically composed of two thin face sheets or skins made of high-performance material separated by a very light material core in order to increase the second moment of inertia and therefore enhance bending stiffness. This principle is the same that delivers the design of the I beam structure, therefore the born of the sandwich concept is to be found back in the history.

The discovery of the advantage in terms of stiffness given by distancing two faces using a lightweight material is attributed to Duleau [18] in circa 1820. In this first

work about the concept, Duleau tested some spaced bolted bars and found a correlation between the stiffness of the structure and the space between the bolts. Noor et al. [19] traced the concept of sandwich back to the 1849, in the work Fairbairn [20] about projects of tubular bridges, but the wide diffusion of these structures began with World War II thanks to the invention and expansion of structural adhesives in the 1930's, when British air force used constructions made of plywood skins with balsa wood, cork or synthetic materials core for aircraft applications. In particular, due to a shortage of traditional materials, the building of the British Mosquito night bomber aircraft have seen wide application of sandwich laminates made of veneer facings and balsa core [21]. Furthermore, Feichtinger [22] claims that United States also began to study sandwich materials made of fiberglass-reinforced polyester facings and glass-fabric honeycomb and balsa wood core for the Vultee BT-15 aircraft fuselage in 1943.

In the decades after the World War II, the use of sandwich structures had a wide diffusion, developing a large variety of theoretical studies. Given their diffusion, ASTM recognised the need for test methods for this relative new structure, and commissioned in 1957 a symposium [23] to collect all the works published about the field. In this book, a significant portion of the cited papers are from works carried out by the U.S. Forest Products Laboratory between the 1944 and 1949. The papers, both theoretically and experimentally, studied various cases and applications of sandwich structures, e.g. shear fatigue [24] or buckling [25] tests. A milestone on the subject of sandwich structure is the theory elaborated by Reissner between 1944 and 1947 [26–28], where a system of differential equations describing stress and displacement conditions of thin plates under bending loads is given. Numerous successive theories based on the Reissner theory were published, focused on various boundary conditions [29–32]. Other important early theories about sandwich constructions are those elaborated by Libove and Batdorf [33], based on small-deflection of orthotropic flat plates, and Mindlin [34], who studied the influence of shear deflections and rotary inertia on the motion of isotropic plates. In 1969 Allen [35] published an important book on the principal aspects of sandwich construction theory, summarising the important theories present in the

literature at the time and proving a complete guide on the subject. These theories are still valid and used for analytical calculations of sandwich structures. Further developments in solutions were given by the introduction and progression of FEM models, which allowed for even more accurate results than the analytical models that often need approximations and assumptions to be solved.

Parallel to the theoretical progresses, numerous innovations were developed from a manufacturing and experimental point of view, particularly for the cores, as it will be better discussed in chapter 6 and 7. During the 1940's and 1950's, the aerospace industry introduced the concept of honeycomb cores. This kind of cellular core is still the most used one in high-performance applications thanks to its great combination of shear strength, stiffness, and weight. In the 1948, a group of engineers from the University of California founded the Hexcel Corporation, which became a leader company in the field of honeycomb cores, sandwich structures and composites. Nowadays Hexcel is the main manufacturer of honeycomb materials for aerospace applications, with more than 700 varieties of materials and cell configurations.

During the decades following the wars, many attempts were made to obtain the best properties from the honeycomb cores, combining different materials and geometrical parameters, such as the cell geometry. However, their diffusion to the medium and low performance applications is limited by their relative high cost.

On the other side, medium and low-cost core materials, such as foams and polymers cellular cores, have seen their commercial expansion from the middle 1950's [21] with the development of new plastic materials such as PVC and PUR. During the last decades, the development of 3D printed plastic cores has gained interest, thanks to the versatility of the design, the low costs and the possibility of producing complex geometry cell cores.

2.2.2. Sandwich Design

In this section, in order to provide the basic concepts behind the design of sandwich structures and their components, the solutions given by the elastic analysis of

sandwich beams are described. The theory is an extension of the Euler–Bernoulli beam theory, in which shear deformations and rotational bending effects are also included. This theory, known as Timoshenko beam theory, describes the behaviour of sandwich beams when subjected to bending, and is used as basic theory for the stress analysis of sandwich structures. Allen [35] provided a detailed description of the theory and derived the solutions for various scenarios; in this section, the resulting equations are reported.

Consider a symmetric sandwich beam, which is when the two facings have same dimensions and material, with unit width and skins perfectly bonded to the core, subjected to a 3-point bending, as illustrated in Figure 2.5.

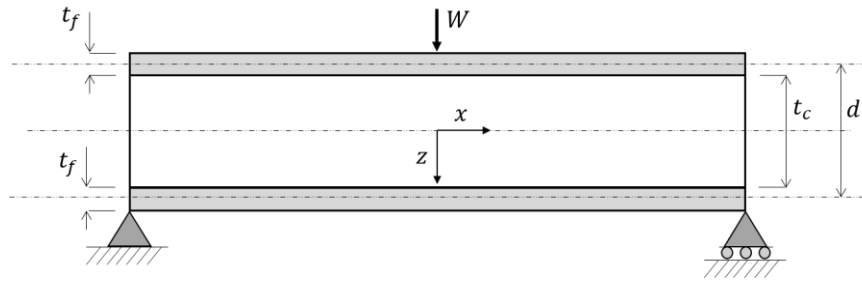


Figure 2.5 - Schematic representation of a symmetric sandwich beam subjected to a 3-point bending load

If we assume that the cross-sections in the yz plane remain plane and perpendicular to the beam longitudinal axis during the bending, the flexural rigidity, or bending stiffness, D of the structure can be written as the sum of the flexural rigidity of its components about their centroidal axis (D_c and D_f) and the flexural rigidity of the faces about the beam middle axis (D_{f0}):

$$D = \int E z^2 dz = D_c + 2D_f + D_{f0} = \frac{E_c t_c^3}{12} + \frac{E_f t_f^3}{6} + \frac{E_f t_f d^2}{2} \quad (1)$$

where the subscripts c and f refer to the core and faces, respectively, E is the material in-plane young moduli, and d is the distance between the faces centroidal axis, that is equal to $t_c + t_f$ for the symmetric sandwich case.

Equation (1) and all the following equations in this section are written per unit width. Of the three terms in Equation (1), the flexural rigidity of the faces about the beam middle axis is the dominant one. Therefore, under the assumptions of thin faces ($t_f \ll t_c$) and weak core ($E_c \ll E_f$), it is possible to approximate the total bending stiffness to:

$$D = \frac{E_f t_f d^2}{2} \quad (2)$$

The assumptions of thin faces and weak core are valid under the following two conditions, respectively ($2D_f$ and D_c contribute with less than 1%):

$$\frac{d}{t_f} > 5.77 \quad (3)$$

$$\frac{E_f t_f d^2}{E_f t_f^3} > 16.7 \quad (4)$$

While the first condition is usually satisfied for sandwich beams with metal or FRP skins, where the ratio of thicknesses is around 1:10 or lower, the second is less obvious and depends on the core properties.

The strain and stresses in the faces and core at the coordinate z are given by:

$$\varepsilon_f = \frac{Mz}{D}, \quad \sigma_f = \frac{Mz}{D}E_f \quad (5)$$

$$\varepsilon_c = \frac{Mz}{D}, \quad \sigma_c = \frac{Mz}{D}E_c \quad (6)$$

where M is the bending moment. The positive sign convention for forces, stresses and bending moments used in this work is illustrated in Figure 2.6.

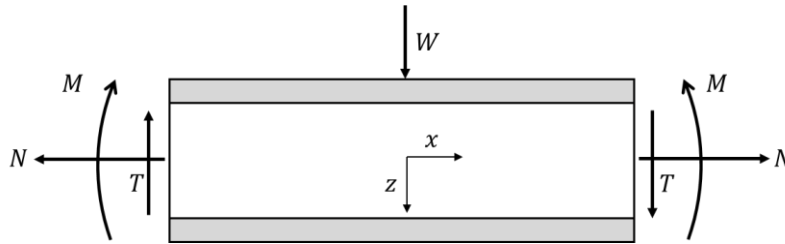


Figure 2.6 - Force, stresses and bending moments positive sign convention

Therefore, given a positive bending moment, the stress is negative (compression) for the upper face and positive (tension) for the lower face. The stress increases linearly along each component of the sandwich, with maximum values at $z = \pm t_c/2$ for the core and $z = \pm t_f/2$ for the faces.

The shear stress, τ , of a beam composed of elements with different material properties, such as the sandwich, at a depth z is given by:

$$\tau = \frac{T}{D} \sum SE \quad (7)$$

where T is the shear force and S the first moment of area. The summation is to be calculated for each section of the sandwich. For the core and the faces, Equation (7) becomes:

$$\tau_c(z) = \frac{T}{D} \left[\frac{E_f t_f d}{2} + \frac{E_c}{2} \left(\frac{t_c^2}{4} - z^2 \right) \right] \quad (8)$$

$$\tau_f(z) = \frac{T}{(D_0 + 2D_f)} \frac{E_f}{2} \left(\frac{t_c^2}{4} + t_f t_c + t_f^2 - z^2 \right) \quad (9)$$

The core shear stress $\tau_c(z)$ has its maximum at the neutral axis and minimum at the core-faces interface:

$$\tau_{c,max}(z = 0) = \frac{T}{D} \left(\frac{E_f t_f d}{2} + \frac{E_c t_c^2}{8} \right), \quad \tau_{c,min} \left(z = \frac{t_c}{2} \right) = \frac{T}{D} \frac{E_f t_f d}{2} \quad (10)$$

The ratio of the maximum to minimum shear stress tends to zero for $E_c \ll E_f$, which means that under this condition the shear stress is constant over the thickness of the core, reducing Equation (8) to its minimum value.

The stress and shear stress distributions for the different grades of approximations are graphically illustrated in Figure 2.7. As mentioned above, under the assumptions of thin faces and weak core, the faces carry the in-plane and bending stresses, while the core transfer the shear stresses of the sandwich structure.

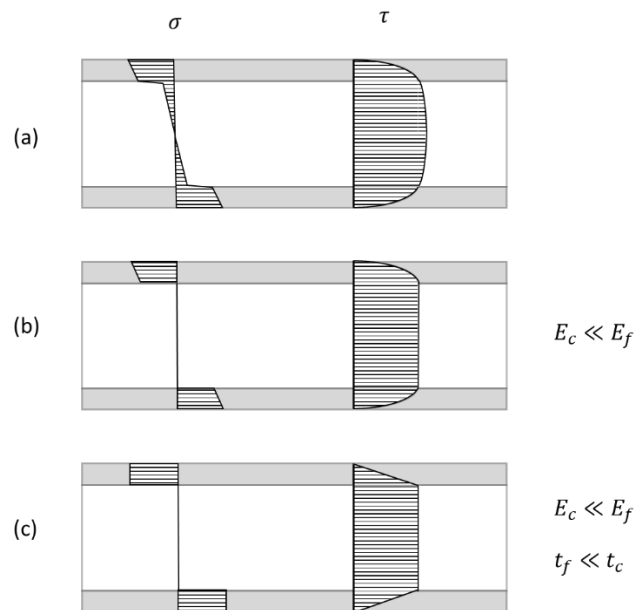


Figure 2.7 – Stress and shear stress distribution in a sandwich beam (a), under assumption of constant shear stress through the core (b) and constant stress through the skins (c) thickness

These equations provide the reasons behind the design of each component of the sandwich structures. Based on these, it is evident the reason why the material selected for the faces is generally strong in compression and tension along the in-plane directions, while the core is selected to have high shear modulus and strength. Nevertheless, when the loading and boundary conditions do not respect the assumptions behind these equations, the design of the structure fails under several mechanisms.

2.2.3. Failure mechanisms of sandwich structures

As illustrated in the previous section, the mechanical performances of the sandwich structure depend on the geometry, the material properties of each component (skins, core and adhesive) and their interaction. Given that a sandwich panel is a complex

structure generally composed by various constituent materials, the number of possible failure modes is large and two or more of them can combine during the same event. An extensive literature research can be found on the failure mechanisms of the various typologies of sandwich panels [36–39].

The prediction of the failure mode of a sandwich panel is hard to be achieved due to the inelastic behaviour of the materials of which it is generally constituted and their complex interaction. In order to analyse the failure mechanisms, Gdoutos et al. performed an extensive experimental work to test the sandwich beams under various typologies of load [37–46]. Based on the numerous experimental works that can be found in literature, sandwich failure mechanisms can be divided in the following three main categories.

Skin failure

When the sandwich beam is subjected to bending or out-of-plane shear, the facings can fail under tension or compression stress if the core is sufficiently stiff, such as in the case of aluminium honeycomb core [47,48]. The type of failure depends on the facing material properties, and in the case of FRP skins, the compression failure is the most likely [35,38,49]. Daniel et al. [38] also demonstrated that the compressive strength of the top skin of a sandwich beam subjected to four-point bending test reached higher stress than the values of strength obtained from the skin material subjected to direct compression. The authors attributed this behaviour to the contribution of the core in suppressing the buckling of the skin.

Under the assumption of thin facings and core with a stiffness considerably lower than the skin material, and thus of negligible core contribution, the bending moment needed to provoke compressive skin failure in sandwich beams can be predicted by the moment equilibrium:

$$M \cong \sigma_{fc} t_f (t_f + t_c) \quad (11)$$

Where M is the bending moment at failure and σ_{fc} is the facing compressive strength.

When subjected to in-plane compression load, which can result from bending moment or pure compression, face skins may fail by wrinkling. Failure of the compressed skin of sandwich structures can be seen as buckling of a plate supported by an elastic continuum [50,51]. This kind of event is strongly dependent from the core modulus, thus it is a failure mode that typically involves sandwich structures with foam cores rather than honeycomb ones [42].

Skin to core adhesion failure

The skin to core debonding is a type of failure that can be generated during external events, such as impacts, or during the fabrication of the sandwich panel. Indeed, especially for lattice cores such as the honeycomb ones, the contact area between the core and the skin is very small, making the interface between the two components a weak point of the structure. Moreover, the core and the facings are generally made of different materials, and thus require special adhesives to create a strong bonding.

Mansourinik et al. [52] proved that the initiation of artificial debonding areas created during the manufacturing of sandwich beams made of closed cell PVC foam and glass fibre reinforced skins reduced the ultimate flexural loads up to the 56%. The study of Vadakke et al. [53] was the first about the compression failure of sandwich panels with initiated debonding of face to core interface, showing that the buckling of the skin at the point of debonding area was the main cause of failure, causing successively the propagation of the debonding.

Yan et al. [54] studied the influence of debonding area size on the mechanical performances of edge-closed honeycomb sandwich structure by experimental and numerical tests, showing a decrease of uniaxial compressive strength up to 22%.

In a not defective sandwich sample, skin to core debonding is not a common failure mechanism during both quasi-static and dynamic tests, as proved by the experimental study conducted by Gdoutos et al. [37–46]. Anyway, as proved by the literature, the presence of debonding area initiated during the manufacturing phase can strongly decrease the mechanical performances of the sandwich structure.

Core failure

The core carries principally the shear and out-of-plane compressive loads of the sandwich beams. Core shear failure is a common failure mode for sandwich beams subjected to short-beam tests, while, with the increase of the span length, the through thickness compressive stresses contribute in a combined failure mode. In the first case, the failure stress can be easily predicted as the core shear strength [38]. For prediction of biaxial stress failures, such as for long beam three-point bending, more complex criteria are needed. Generally, the plastic deformation of the core, which can be due to compression, shear or a combination of the two, creates a lack in the supporting role of the core, commonly provoking the failure of the loaded skin.

Indentation is a type of sandwich failure that consists of localised core yielding and resulting facing collapse. It is the typical sandwich failure mode under highly concentrated load, such as in the case of impact or localised load at joints.

Soden et al. [55,56] analysed the indentation of sandwich structures as linear elastic bending of the top facing placed on the core, modelled as a rigid-perfectly plastic foundation, while in the theory developed by Olsson et al. [57] it is modelled as an elastic-perfectly plastic core. Both models are simply and valid for sandwich beams rigidly supported on the bottom side, but loose validity in the case of simply

supported and clamped structures, where the bending load need to be encountered in the prediction.

In order to predict core indentation failure load in honeycomb core sandwich beams under three-point bending, Petras et al. [58] combined the elastic high-order sandwich beam theory (HOSBT), formulated by Frosting et al. [59] and Reddy [60], with empirical failure criterion obtained from biaxial tests. The HOSBT treats the sandwich beam as elastic until the core failure and predicts the shear and out-of-plane compression stresses in the core, while the experimental biaxial tests were used to derive a linear failure criterion that combines both compression and shear components.

Generally, the most important properties of the sandwich cores are the out-of-plane compression and shear properties, which play the main role in all the prediction theories of core failures.

2.3. Conclusive remarks

As it was possible to see from the analysis of the sandwich structures illustrated in this chapter, their failure modes can be attributed to the failure of the three main components: skins, core and their interface. Analysing the possible developments that can lead to an improvement in the factors that influence the principal failure modes, skins failure strongly depends on the in-plane compressive properties of the constituent material. In the case of CFRP skins, which is the common material used for aerospace skins, voids and defects generated during the manufacturing process have large influence, leading to a premature compressive failure of the part. On the core side, the out-of-plane compressive and shear properties plays a fundamental role in the failure mechanisms, which are mainly related to constituent material and cell geometry in the case of lattice cores. Finally, the presence of the adhesive layers between these two components represents itself a weak point, because creates

interfaces and is a point where manufacturing defects, such as debonded areas, are not visible from the external of the sandwich structures.

The following chapters illustrate the works accomplished during the PhD course aimed to enhance these components and reduce their possibility of a premature failure. The first works are focused on the reduction of defects in the composite laminates by acting on the manufacturing techniques. The voids content in CFRP laminates produced by hand lay-up is reduced by means of ultrasonic waves coupled with a vacuum bag. The Ultrasonic Consolidation procedure allowed a sensible reduction of voids in the final parts, considerably increasing the mechanical properties of the components and thus reducing the possibility of skin failure. On the automatic manufacturing of composite laminates, the detection of defected parts has been improved thanks to the development of a real-time thermography system that can be implemented in heat-based manufacturing machines. The system is based on an undamaged baseline that improves the detection of defects in non-homogeneous heat fields, with the aim of reducing the production of defected parts that can lead to premature failure of the structure.

The following works conducted during the PhD course are instead concentrated on the design of a novel sandwich core and structure. First, the design of a CFRP 2D lattice core has been analytically and numerically studied to optimise its properties along both in-plane and out-of-plane directions, also involving the structural contribution of residual thermal stresses. Then, the core has been manufactured and experimentally and numerically characterised, demonstrating its unique specific properties. The PhD work concludes with the realisation of a novel advanced CFRP sandwich structure, based on the CPCC core connected to CFRP skins made of the same material, in absence of a third adhesive material, and manufactured through the UC procedure.

As it has been illustrated in the previous section, an extensive literature work [36-40] has been conducted on the failure mechanisms of sandwich structures. The literature study has demonstrated the numerous possible ways a complex structure as sandwich materials can fail. Generally, these failures are linked to the single

components (skins, core or adhesive layers) and their interaction. It is then clear that, to obtain a general improvement of a final sandwich structure, working on the improvement of a single property or a single component it is not sufficient, but a more multilevel approach is necessary. This thesis summarises the principles investigated during the PhD to improve the failure mechanisms of sandwich structures by means of the design a high performance all-composite sandwich that demonstrated outstanding mechanical properties and failure resistance.

3. Paper 1: Ultrasonic consolidation (UC) debulking of thermosetting prepreg

The principal aim of the publication illustrated in this chapter is to enhance the mechanical properties of CFRP laminates produced by lay-up of pre-impregnated layers by means of reducing the interlaminar air content.

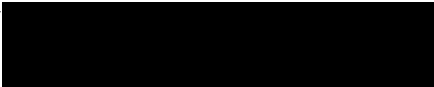
The quality and performances of the composite laminates is strongly influenced by the level of porosity in the parts. Particularly, interlaminar shear strength (ILSS) and compressive strength of the laminate strongly reduce with the increment of void content of the part [61]. These defects derive from the manufacturing process, where air packages remain entrapped in the matrix after the crystallisation of the resin.

The most common manufacturing technique for the production of composite components for aerospace applications is the lay-up of prepreg layers [8], thanks to the capacity of such technique to produce top quality components. To facilitate the removal of the air between the layers, numerous debulking steps are commonly performed, especially in manual lay-up of prepregs, resulting in a time-consuming and often low-efficient process. The use of ultrasound waves may help in this procedure [62–64], facilitating the movement of air through the prepreg layers.

In this work, the developed Ultrasonic Consolidation debulking method is aimed to provide a valid tool for the reduction of manufacturing time and voids content of autoclave cured prepreg laminates. An ultrasonic vacuum bag system was applied on several samples for different time of exposure, in order to study the influence of the technique on the mechanical properties of the final part. Experimental results showed an increment of more than 20% of ILSS of the samples in comparison with reference, with a reduction of the manufacturing time of more than 85%. This work can contribute to the aim of the thesis by providing a valid method to improve the interlaminar failure resistance of sandwich skins and of every part composed of laminated composites, in addition to reduce the manufacturing costs.

The Statement of Authorship Form and the paper can be found next.

This declaration concerns the article entitled:	
Ultrasonic consolidation (UC) debulking of thermosetting prepreg for autoclave curing of composite laminates	
Publication status (tick one)	
Draft manuscript	
Submitted	
In review	
Accepted	
Published	✓
Publication details (reference)	
Flora, F., Rizzo, F., Pinto, F., & Meo, M. (2021). Ultrasonic consolidation (UC) debulking of thermosetting prepreg for autoclave curing of composite laminates. <i>Materials Today: Proceedings</i> , 34, 106-112.	
Copyright status (tick the appropriate statement)	
I hold the copyright for this material	✓
Copyright is retained by the publisher, but I have been given permission to replicate the material here	
Candidate's contribution to the paper (detailed, and also given as a percentage)	
The candidate contributed to/ considerably contributed to/predominantly executed the...	

Formulation of ideas:	85%	My supervisor proposed the idea to use the ultrasonic waves for the manufacturing of the CFRP laminates. I suggested to maintain the room temperature of the prepreg layers during the debulking step, to combine ultrasonic waves with vacuum bagging and how to test the material to prove the efficiency of the technique in the voids removal.	
Design of methodology:	80%	I manufactured all the samples used in the experimental campaign and designed all the experimental tests carried out in the work. My fellow Francesco Rizzo helped me in this procedure.	
Experimental work:	90%	I carried out all the experimental tests, collected all the data, and analysed all the outputs. My fellow Francesco Rizzo helped me in the performing of some experimental tests.	
Presentation of data in journal format:	90%	I designed the manuscript structure, wrote all the drafts and realised all. My colleague Francesco Rizzo and my supervisors provided feedback on the draft and help for the paper review and submission.	
Statement from Candidate			
This paper reports on original research I conducted during the period of my Higher Degree by Research candidature.			
Signed			Date 29/01/2022

Ultrasonic consolidation (UC) debulking of thermosetting prepreg for autoclave curing of composite laminates

Francesco Flora^{1,*}, Francesco Rizzo¹, Fulvio Pinto¹, Michele Meo¹

¹ *Department of Mechanical Engineering, University of Bath, Bath, Ba2 7AY, UK*

* Corresponding author: f.flora@bath.ac.uk

Keywords: *ultrasound; ultrasonic consolidation; prepreg debulking; thermosetting prepreg curing; CFRP.*

Abstract

Debulking of prepreg (pre-impregnated resin system) layers during hand lay-up manufacturing of carbon fibre reinforced polymers (CFRP) is a key-step to reduce air content and maximise the mechanical properties of the final product. Debulking is usually performed using vacuum-bag cycles of 10-15 minutes applied after the lay-up of every three or five prepreg layers, leading to a considerable time-consuming process. In this work, the use of ultrasonic stimulation during vacuum is studied to improve the efficiency of the debulking process and reduce the number of operations in order to decrease the overall manufacturing time. Three CFRP laminates were laid-up using the proposed ultrasonic consolidation (UC) with three different exposition times (5, 10 and 15 minutes) and cured in autoclave. The UC debulking process consists in a vacuum cycle with ultrasonic waves sent to the uncured material through an ultrasonic transducer. In order to evaluate the efficiency of this process interlaminar shear strength (ILSS) and in-plane compressive properties were tested. Experimental results show for 15 minutes UC samples compressive properties comparable with the ones obtained from reference samples manufactured using the traditional debulking technique, and high improvements in terms of ILSS (>20%). Therefore, UC debulking process can be used during hand lay-up of prepreg in order to improve the interlaminar properties of the final part and reduce the debulking time by over 85%.

1. Introduction

The use of composite materials for both primary and secondary structures is increased in the last decades, particularly for high-performance applications such as aerospace, racing automotive and wind blades due to its high mechanical properties (such as strength, elastic modulus and fatigue strength) and low weight. An example of advanced composite materials commonly used is Carbon Fibre Reinforced Polymer (CFRP), a polymeric matrix (thermosetting or thermoplastic) reinforced with carbon fibres. Several manufacturing processes are available for CFRPs. Breuer published [1] a detailed state of the art of composite materials manufacturing technologies, reporting that the majority of airframe composite components are manufactured by lay-up of pre-impregnated layers known as 'prepreg'. Prepreg material is a layer of carbon fibres arranged in a Unique Direction (UD) or woven together to form a texture impregnated with a thermosetting resin and stored at low temperatures (i.e. -18°C) in order to delay the cure of the matrix. The influence of the fibre orientation of each prepreg ply along the stacking sequence over the mechanical properties of the final part is well known [2–5], providing high flexibility in the design of the final properties of the part.

Despite the increasing interest of industry in automated processes of advanced composite manufacturing, such as Automated Tape Laying (ATL) [6] and Automated Fibre Placement (AFP) [7], hand layup of prepreg layers remains the main manufacturing method in many cases, especially for research and development of new components and several high performance manufacturing facilities due to its flexibility and adaptability [8]. The process consists in cutting prepreg layers to the desired dimensions and shapes, and manually laminating each one to a mould or to the previous layer. Very high-quality and flexible structures can be designed and produced by hand lay-up with a low start-up cost.

In order to guarantee the maximum quality and mechanical properties of the laminate, the removal of the air entrapped between the layers (consolidation) is a key step in the prepreg lay-up. Porosity directly affects the mechanical properties of the laminate, especially interlaminar shear strength (ILSS) and compressive

strength [9–13]. Indeed, Jeong [9] presented an experimental study on laminated composites with a wide range of void contents, showing that the mechanical properties (in particular the ILSS) are strongly dependent not only on void content but also on voids geometry. A statistical approach on a similar study was also published by Yoshida et al. [11] while Hancox [13] carried out a theoretical study on the influence of the contents and geometry flaws and voids in shear properties of CFRP rods and tubes.

In order to remove air and reduce (final) void content, different procedures are used during the hand lay-up process. Firstly, pressure is manually applied during the lamination step of every ply using a specific tool ('Dibber' tool) to remove big air packages (Figure 3.1.a) [8]. Then, as suggested by Hexcel® in the HexPly® Prepreg Technology guidelines [14], prepreg sheets need to be consolidated using a vacuum bag assisted procedure (Figure 3.1.b) for 10-15 minutes every 3 or 5 layers, depending on the geometry and shape of the part. After the stacking has been completed, the consolidation is ensured by vacuum and pressure applied during the autoclave cure. Given that the autoclave pressure is applied during the resin cure, it has no influence on the total duration of the manufacturing, while the hand pressure and the numerous vacuum cycles during the lamination are the main time consuming steps for prepreg hand lay-up process, particularly for components with large thickness.

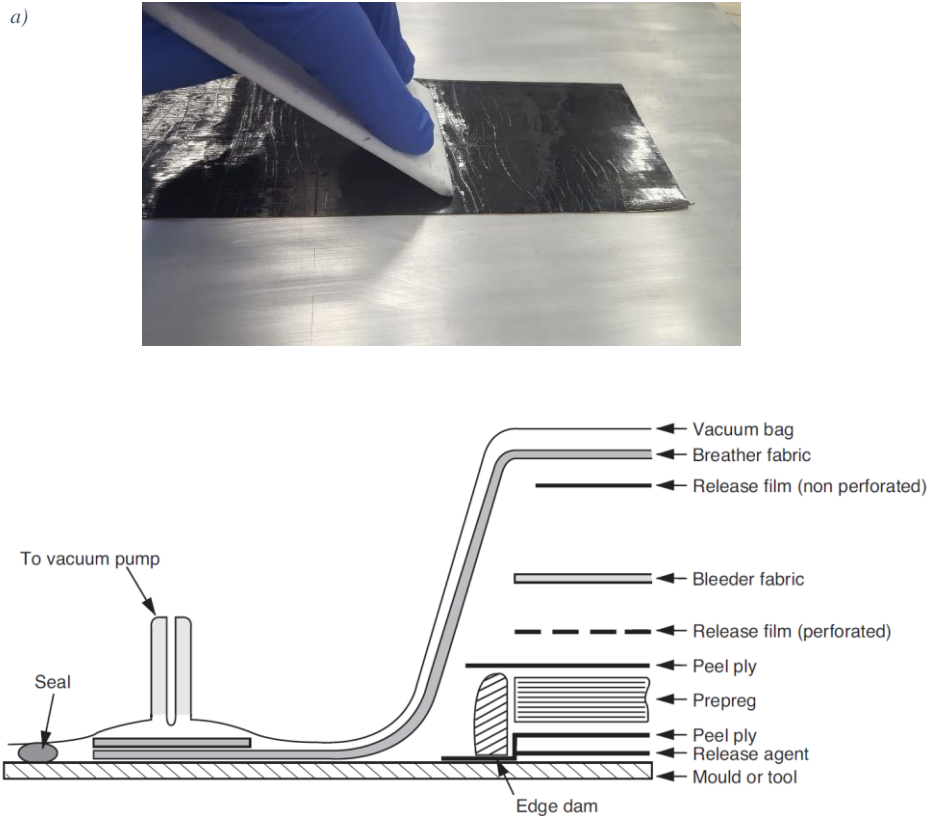


Figure 3.1 – a) Dibber tool for air removal and b) vacuum bag set-up (figure from [14])

Based on these premises, in order to reduce the process time and ensure high level of consolidation, the use of ultrasound waves is considered. This technique, called ultrasonic consolidation (UC), takes advantage of vibrations generated by the waves in to the material in order to facilitate the removal of the air trapped between layers. The benefits in the use of UC are well known for automated lay-up of both thermosetting and thermoplastic composites [15–18], where ultrasound waves are used for both matrix debulking and curing (heat generation), with a frequency generally in the range of 20-120 kHz [15]. Lionetto et al. [16] presented both experimental and numerical analyses of an automated lay-up process that uses ultrasonic propagation in order to provide pressure and heat during filament winding of thermoplastic matrix composite, reporting a void content within the typical range for composites processed by filament winding and other traditional methods. Rizzolo et al. [17] experimentally studied the UC process during AFP of PET/carbon composite samples resulting in significantly higher mechanical properties in comparison with those obtained by hot-press manufacturing process.

In their work, Chu et al. [18] analysed the influence of ultrasonic AFP (UAFP) on the mechanical properties and microstructure crystallization of thermoplastic composites showing a good match with properties of the same specimens produced by hot-press.

However, there are cases in which debulking and heating are undesired to take place at the same moment. When UC is applied to a thermosetting prepreg, the transmission of high levels of energy to the material through ultrasonic waves may activate chemical reactions, generating cross-links between polymer's molecules via frictional heat and consequently cure the matrix. This is particularly undesirable when maximum mechanical properties in the part can be reached only with autoclave cure, or when it is necessary to maintain the stickiness of the material. Foster-Miller company, now part of QinetiQ, patented several manufacturing methods and devices based on the use of ultrasound waves for prepreg compaction: they designed a method for the manufacturing composites, called ultrasonic tape lamination, where an ultrasonic horn induces shear waves with a small angle and low frequency [19] to the surface of thermosetting prepreg plies for consolidation [20]; the same process was also applied on thermoplastics [21]. The device was proved to generate enough energy to remove the air between the plies without activating the matrix cure and allowing the stuck of the following layer.

In this work, the UC is proposed as debulking procedure of manual lay-up before the autoclave cure for CFRP prepreps in order to decrease the time of the manufacturing process. Also, the process is used to reduce the porosity and therefore improve the interlaminar properties of the material. Using a low level of frequency (and thus of generated heat) and constantly monitoring the material temperature, the layers were consolidated without generating the amount of heat required to activate the cure. A manufacturing set-up is then presented and used to fabricate three different sample using different UC exposition times. In order to prove the efficiency of the process, the mechanical properties (compressive and interlaminar) of the samples were experimentally evaluated and compared with reference samples, obtained using a standard consolidation technique.

2. Samples manufacturing

In this section, the manufacturing of three different samples using ultrasonic consolidation (UC) method is illustrated. Three different laminates of dimensions 400x100 mm were manufactured via manual stratification of prepreg layers with a very limited pressure applied manually with a Dibber tool and without any vacuum-bag assisted process during the lay-up. The chosen lamination sequence was $[(-45/0/45/90)_2/-45/0/45/(90)]_S$ and the used material is a unidirectional carbon fibre prepreg with 977-2 epoxy resin system and Tenax® - E IMS65 fibres produced by Cycom®. Each laminate was attached to an aluminium plate (previously covered with release agent to facilitate the removing) and enclosed in a vacuum bag. Afterwards, the UC process was carried out: an ultrasonic transducer was connected to the centre of the opposite side of the aluminium plate through a vacuum pump, as shown in Figure 3.2, in order to transmit the ultrasonic waves to the plate and thus to the material. Simultaneously, a second pump attached to the bag applied the vacuum over the uncured laminated to apply pressure over the prepreg. In order to limit the frictional heat generated inside the material and avoid the matrix to start the cure, the used signal was a sine wave with a frequency of 28.0 kHz (central frequency of the transducer) and the material temperature constantly monitored using thermocouples. Figure 3.3 shows a schematic representation of a section of the consolidation plate. The ultrasonic consolidation procedure was applied for 5, 10 and 15 minutes respectively to each of the three uncured laminates (UC1, UC2, and UC3).

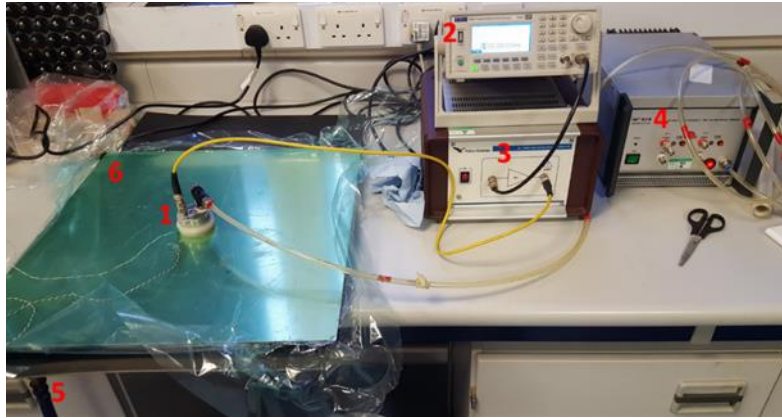


Figure 3.2 - Ultrasonic consolidation setup: 1 vacuum ultrasonic transducer; 2 waves generator; 3 amplifier; 4 transducer vacuum pump; 5 vacuum bag pump; 6 aluminium plate bottom part.

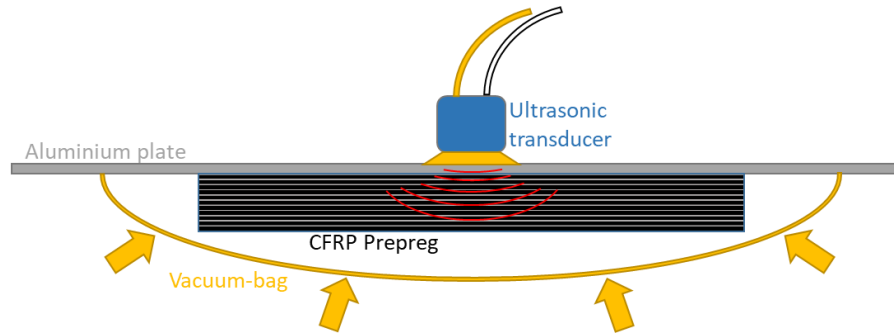


Figure 3.3 – Ultrasonic consolidation schematic representation

In order to evaluate the effective advantages and possible limitations of the UC process for the manual stratification, a reference laminate sample was manufactured in similar conditions following the standard debulking process: a vacuum cycle of 15 minutes every 3 plies, for a total of 120 minutes. Afterwards, the three UC samples and the reference sample (PC) were cured via autoclave at 180°C and a pressure of 100 psi for 3 hours (Figure 3.4.a). A heating and cooling rate of 2°C/min was used. Table 3.1 summarises the debulking techniques, times and average thicknesses of the four cured laminates. In the calculus of process times, side procedures were not considered, such as the time to prepare the vacuum bag and enclose the laminate in it, because strongly depending on the operator ability. Anyway, these side procedures are significantly less in the UC debulking process (only one vacuum bag) in comparison with traditional one (one vacuum bag for every three layers). After the cure, the laminates were cut using a diamond blade

obtaining the appropriate specimen dimensions (Table 3.2) for the experimental campaign (Figure 3.4.b).

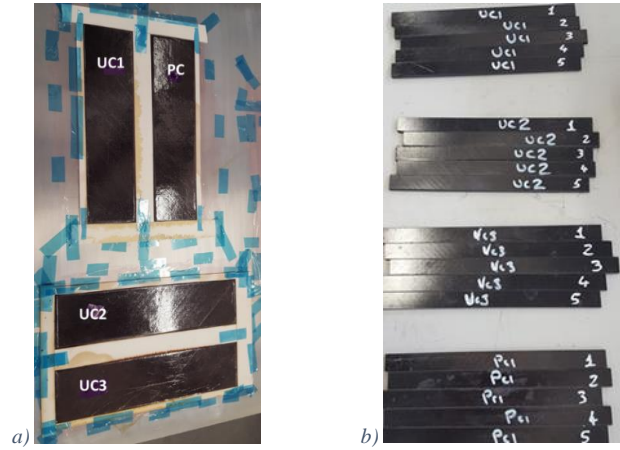


Figure 3.4 - a) Laminates after autoclave cure and b) samples after diamond blade cut

Table 3.1 - Manufacturing debulking times and thicknesses of samples

	UC1	UC2	UC3	PC
Debulking method	Ultrasonic Consolidation	Ultrasonic Consolidation	Ultrasonic Consolidation	Classic
Debulking time (min)	5	10	15	120
Thickness (mm)	3.78	3.74	3.76	3.77

Table 3.2 - Tests sample dimensions

Test	L (mm)	W (mm)	Number of specimens
ILSS	38	19	5
Compression	110	10	5

Based on the number of layers used in this experimental study (23), the reductions in terms of debulking process time are 95.8%, 91.7% and 87.5% (UC1, UC2 and UC3 respectively). The total debulking time of the classic procedure can be illustrated with equation Equation 1:

$$T = t * \left(\frac{n}{3}\right) \quad \text{Equation 1}$$

where t is the debulking time of each cycle and n is the number of layers. Considering the manufacturing conditions of this work, the equation of UC debulking time is:

$$T_{UC} = t_{UC} * \left(\frac{n}{23}\right) \quad \text{Equation 2}$$

where t_{UC} is the optimal exposure time (5, 10 or 15 minutes) of the process to consolidate 23 plies, that will be identified via experimental campaign. It is possible to calculate the time reduction as follow:

$$T_{UC} = \frac{t_{UC}}{t} * \left(\frac{3}{23}\right) * T \quad \text{Equation 3}$$

3. Experimental Setup

In order to investigate the mechanical properties of the different samples and evaluate the influence of inner porosity on mechanical properties in function of the UC time of process, two experimental tests were performed.

3.1. Compression

In order to evaluate in-plane compressive properties, compression tests were carried out according to the standard BS-EN-ISO-14126:1999. The samples were placed into a dedicated fixture (Figure 3.5) in order to avoid bending and buckling and guarantee a uniform uniaxial compressive load. The sample was inserted into the fixture and symmetrically clamped on both edges using two steel blocks and eight bolts (four for each edge) to guarantee a good grip during the test. Two axial rods, parallel to the sample axis, were used as guiderail to ensure the correct positioning of the blocks. Afterwards, the assembly was placed on a Universal testing machine Instron 5585 and tested with a cross-head speed of 1mm/min.



Figure 3.5 - Compression-dedicated fixture used during experimental campaign tests

The compressive strength σ_c was then obtained using the formula:

$$\sigma_c = \frac{F_c}{A} \quad \text{Equation 4}$$

where F_c is the maximum compressive load (N) applied during the test and A is the cross-section of the sample (mm^2).

3.2. Interlaminar shear strength (ILSS)

In order to evaluate the interlaminar mechanical properties of CFRP parts obtained with different time of exposition to UC, ILSS tests were carried out using a Universal testing machine Instron 3369, according to BS EN ISO 14130:1998. Two steel rollers (4 mm in diameter) were used as supports for the CFRP samples with a span of 19mm (span-to-ratio 5:1) and a steel roller of 10mm was used as loading nose to apply the transverse load. A sketch of the test setup is reported in Figure 3.6.

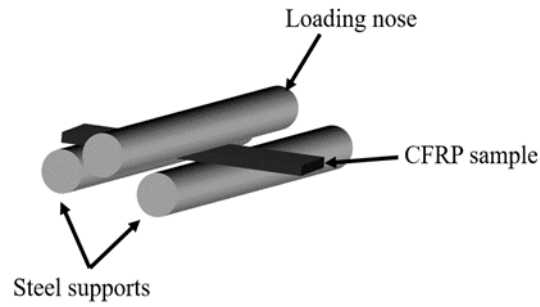


Figure 3.6– Sketch of ILSS test setup

In order to calculate the interlaminar shear stress τ (MPa) for ILSS test, the following equation is used:

$$\tau = 0.75 \frac{F}{bh} \quad \text{Equation 5}$$

Where b is the width (mm) of the sample, h is the thickness (mm) and F is the applied load (N). To obtain the interlaminar shear strength τ_s (MPa), the maximum force value recorded during the test is used.

4. Results and discussion

Results of compression tests are reported in Figure 3.7 where stress-strain curves are reported with relative mean and standard deviation on compressive strength and compressive modulus.

Analysing the experimental data from Figure 3.7, it is possible to notice that the UC samples presented a variation of -9%, -10% and -3% for the compressive modulus and -3%, +9% and +4% for compressive strength (UC1, UC2 and UC3, respectively) in comparison with the reference samples.

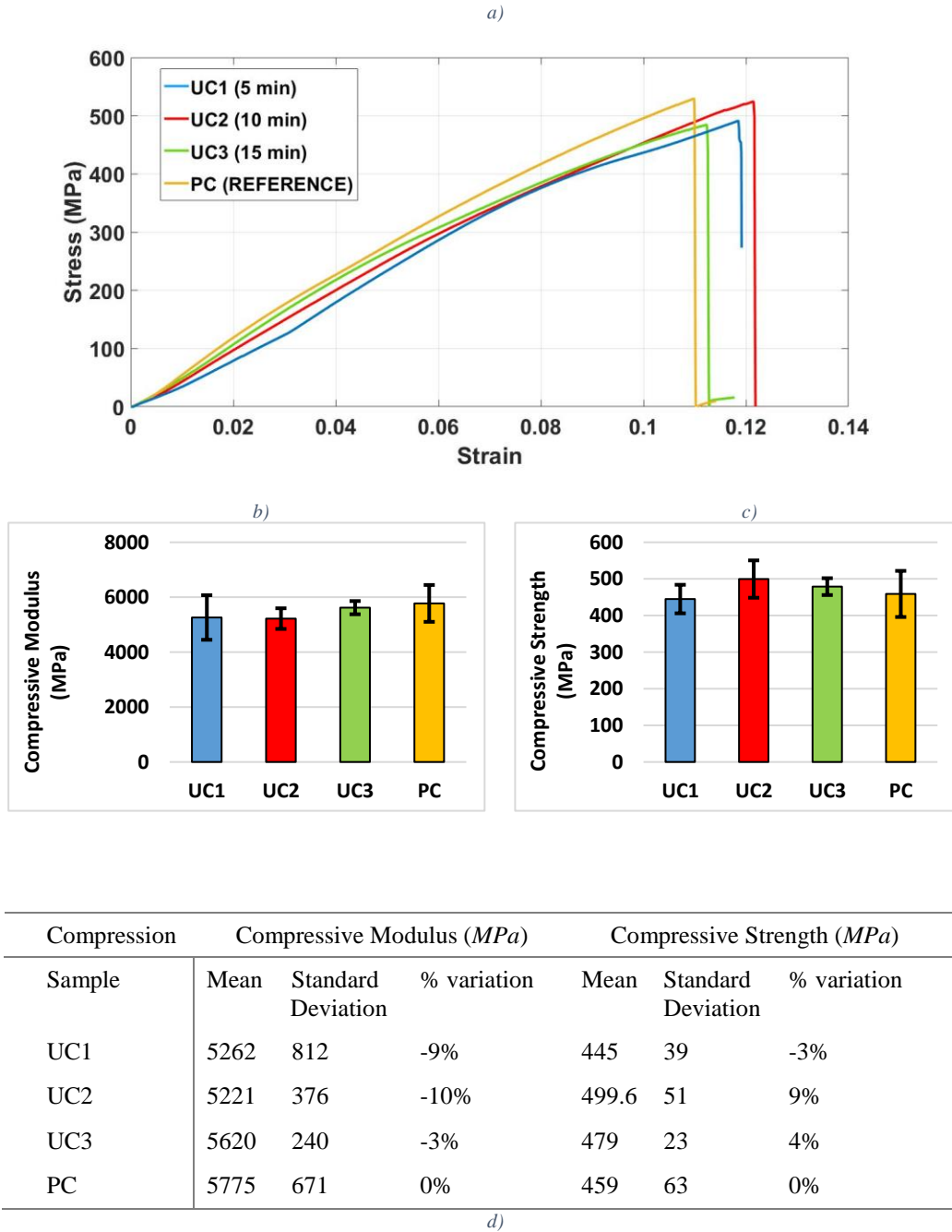
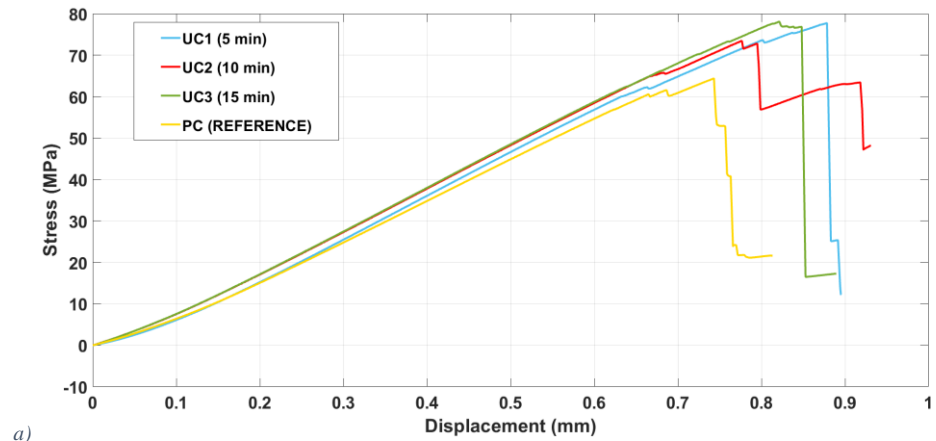
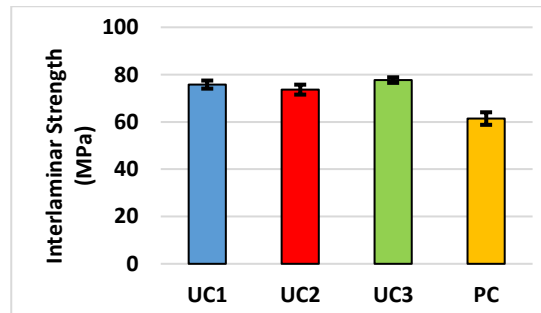


Figure 3.7 - Plots of compression tests results for 3 UC configurations and reference: a) stress-strain curves, b) compressive strength, c) compressive modulus and d) relative statistical data and percentage variation in comparison with reference (PC)

Results on ILSS are reported in Figure 3.8 where stress-displacement curves are displayed reporting mean and standard deviation of interlaminar strength in bar plot.



a)



b)

ILSS	Interlaminar strength (MPa)		
	Mean	Standard deviation	% variation
Sample			
UC1	75.78	1.71	23%
UC2	73.65	2.1	20%
UC3	77.69	1.18	26%
PC	61.42	2.65	0%

c)

Figure 3.8 - Plots ILSS results: a) stress-displacement curves, b) interlaminar strength graph with standard deviation bars and c) relative statistical data and percentage variation in comparison with reference (PC).

The results from the ILSS tests showed excellent interlaminar properties for all the UC samples, with an increase of 23%, 20% and 26% (UC1, UC2 and UC3 respectively) in ILSS in comparison with the reference and small values of standard deviation.

Considering all the experimental results, it is possible to analyse the effect of UC on the mechanical properties of the samples obtained with the three different

exposition times. UC3 showed similar compressive properties when compared to reference ones with a very low percentage variation (under 5%). Similarly, UC1 and UC2 showed good results, but with higher percentage variations (up to 10%). Anyway, analysing the standard deviation and error bar plot of these results, it is possible to state that these variations fall in the statistical errors. On the other hand, the increment in terms of ILSS of all the UC samples compared to reference ones is clear (above the 20%), confirming the effective reduction of voids between layers due to the UC process [9]–[13]. It is important to highlight that this test presented relative low values of standard deviation. This is probably due to the strong dependency of the ILSS properties from laminate matrix characteristics and inner porosity. On the other hand the compressive test have a higher dependency on different experimental variables, including position of the laminates during the autoclave cure, position of the sample cut along the laminate, samples thickness, and others. Although this dependency leads to higher standard deviation values, the UC3 results showed a very good match with reference ones, with both positive and negative variations under 5%. Based on this, it is possible to consider 15 minutes (UC3) as enough UC process time to reach a considerable increment in terms of ILSS and thus of consolidation without affecting the compressive properties. The reduction in terms of debulking time can be estimated using equation Equation 3 substituting $t_{UC} = 15$ min and $t = 15$ min:

$$T_{UC} = 0.13 * T \quad \text{Equation 6}$$

5. Conclusions

In this work, ultrasonic consolidation was studied and used to improve the debulking step for hand lay-up of autoclave cure prepregs and decrease the manufacturing process time. Debulking is a considerable time-consuming process usually performed using vacuum-bag cycles of 15 minutes applied after the lay-up of every three prepreg layers. An ultrasonic vacuum bag system was used on three uncured CFRP laminates, laid without the traditional vacuum debulking steps. UC was applied for three different times for the three laminates: 5, 10 and 15 minutes

(UC1, UC2 and UC3 samples respectively). The resonant frequency of the ultrasonic transducer was set to low levels (in the range of the common UC frequencies) in order to avoid the generation of high levels of frictional heat between the polymer molecules, and thus the cure of the matrix. The procedure led to a consolidation time reduction from the 120 minutes of the traditional process down to 5 minutes for the laminate analysed.

In order to evaluate the reliability of the debulking process, the mechanical properties of the samples were experimentally studied and compared with a reference laminate, manufactured with traditional debulking steps. The ILSS property is particularly effective for the study of voids content between layers in composite laminates. The results from this experimental test showed an increment of ILSS for all the three UC samples of at least 20% in comparison with the reference ones. Moreover, compressive properties were experimentally studied. Results showed a very good match with reference for UC3 sample, with percentage variations under $\pm 5\%$.

In conclusion, the results confirmed the reliability of the proposed process for the consolidation and debulking of prepregs, with a substantial reduction in terms of time of hand lay-up manufacturing process (over 85%) and large improvements in terms of interlaminar properties.

Acknowledgement

The authors acknowledge the “EXTREME” project, which has received funding from the European Union’s Horizon 2020 research and innovation program under grant agreement no.636549.

References

- [1] U. P. Breuer, "Manufacturing Technology," in *Commercial Aircraft Composite Technology*, Springer, 2016, pp. 73–132.
- [2] P. Naghipour, M. Bartsch, L. Chernova, J. Hausmann, and H. Voggenreiter, "Effect of fiber angle orientation and stacking sequence on mixed mode fracture toughness of carbon fiber reinforced plastics: Numerical and experimental investigations," *Mater. Sci. Eng. A*, 2009.
- [3] D. H. A. Lukaszewicz, K. D. Potter, and J. Eales, "Composites : Part B A concept for the in situ consolidation of thermoset matrix prepreg during automated lay-up," *Compos. Part B*, vol. 45, no. 1, pp. 538–543, 2013.
- [4] F. C. Campbell Jr, *Manufacturing processes for advanced composites*. elsevier, 2003.
- [5] B. T. Astrom, *Manufacturing of polymer composites*. CRC press, 1997.
- [6] A. C. Wilson, M. A. Us, H. Zhang, and S. B. Glazer, "COMPOSITE TAPE LAYING APPARATUS AND METHOD," vol. 2, no. 12, 2016.
- [7] K. C. C. G.G. Liversidge J.F. Bishop, D.A. Czekai, "FIBER PLACEMENT MACHINE," vol. 96, no. 19, pp. 62–66, 1980.
- [8] M. Elkington et al., "Hand layup : understanding the manual process Hand layup : understanding the manual process," *Adv. Manuf. Polym. Compos. Sci.*, vol. 1, no. 3, pp. 138–151, 2015.
- [9] H. Jeong, "Effects of Voids on the Mechanical Strength and Ultrasonic Attenuation of Laminated Composites," *J. Compos. Mater.*, vol. 31, no. 3, pp. 276–292, 1997.
- [10] N. C. W. Judd and W. W. Wright, "Voids and their effects on the mechanical properties of composites- an appraisal," *Sampe J.*, vol. 14, pp. 10–14, 1978.
- [11] H. Yoshida, T. Ogasa, and R. Hayashi, "Statistical approach to the relationship between ILSS and void content of CFRP," *Compos. Sci. Technol.*, vol. 25, no. 1, pp. 3–18, Jan. 1986.

- [12]K. J. Bowles and S. Frimpong, “Void Effects on the Interlaminar Shear Strength of Unidirectional Graphite-Fiber-Reinforced Composites,” *J. Compos. Mater.*, vol. 26, no. 10, pp. 1487–1509, Oct. 1992.
- [13]N. L. Hancox, “The effects of flaws and voids on the shear properties of CFRP,” *J. Mater. Sci.*, vol. 12, no. 5, pp. 884–892, May 1977.
- [14]H. P. P. Tech, “HexPly Prepreg,” FGU 017c, January, 2013.
- [15]B. Harras, K. C. Cole, and T. Vu-Khanh, “Optimization of the Ultrasonic Welding of PEEK-Carbon Composites,” *J. Reinf. Plast. Compos.*, vol. 15, no. 2, pp. 174–182, 1996.
- [16]F. Lionetto, R. D. Anna, F. Montagna, and A. Maffezzoli, “Modeling of continuous ultrasonic impregnation and consolidation of thermoplastic matrix composites,” *Compos. PART A*, vol. 82, pp. 119–129, 2016.
- [17]R. H. Rizzolo and D. F. Walczyk, “Ultrasonic consolidation of thermoplastic composite prepreg for automated fiber placement,” 2016.
- [18]Q. Chu, Y. Li, J. Xiao, and D. Huan, “Processing and characterization of the thermoplastic composites manufactured by ultrasonic vibration – assisted automated fiber placement,” no. 29, 2018.
- [19]M. A. Us and D. T. Thomson, “Device for ultrasonically consolidating fiber reinforced composite structures,” vol. 2, no. 12, 2003.
- [20]N. Attleboro et al., “Ultrasonic method of fabricating a thermosetting matrix fiber-reinforced composite structure and the product thereof,” 2002.
- [21]J. S. Boyce, “Method of fabricating a polymer-matrix fiber-reinforced composite and the product thereof,” vol. 2, no. 12, 2003.

4. Paper 2: Development of an analytical model for optimisation of the ultrasonic consolidation of composite prepreg

The work illustrated in Chapter 4 aims to provide a continuous of the study of the Ultrasonic Consolidation debulking during hand lay-up of prepregs. The detailed work illustrated here has the object of understand the phenomena and provide additional validations of its efficiency and reliability.

With this aim, the article illustrated in this chapter propose an analytical model of the phenomena of ultrasonic waves propagating through the prepreg stack under vacuum. Ultrasonic waves are used to promote the removal of air entrapped during the compaction of prepreg layers in different automatic techniques, for both thermoplastic and thermoset matrices. In order to optimise the process parameters to be used for the application of UC during hand lay-up, it is necessary to understand how these parameters influence the phenomena. The analytical model proposed here is based on the peristaltic transport mechanism of the air bubbles caused by the propagation of ultrasonic waves along two layers of prepregs, coupled with the pressure gradient given by the vacuum pump.

The model is based on some assumptions, aimed to simplify the analytical study of the complex structure made of uncured reinforced polymer and the elaborate propagation of the waves in such system. Due to the high viscosity of uncured polymeric matrix, the gas diffusion (Fick's first law of diffusion [65]) of air through the matrix has been considered negligible in comparison to the air momentum transport (Darcy flow [66]). The second assumption is that the air transportation is considered as a laminar gas flow, which is admissible for the value of Reynolds number of these conditions [65]. The third and last assumption is that, at the room temperature, due to the high viscosity of the resin, the predominant flow is along the interface between prepreg layers, neglecting the flow through the thickness of

the uncured laminate. These assumptions lead to the formulation of net axial velocity and net flow of the gas through the media.

The final equations obtained from the analytical model have been included in a code for the numerical calculations, studying the influence of the process parameters over the net air flow. Based on this study, it was possible to define some guidelines aimed to the optimisation of the UC procedure in order to maximise the air removal, such as the transducer position, frequency and amplitude range.

Sample manufacturing and microscope images analysis of the material sections have validated the efficiency of the technique, showing a significant reduction of voids content in the part manufactured applying the UC procedure for longer time. With the aim of provide additional experimental validation to the manufacturing technique, and to study eventual side effect of the propagation of ultrasonic waves on the mechanical properties of the material, flexural and Charpy impact tests were performed. The mechanical properties obtained showed similar results with reference, also illustrating an increment in terms of flexural modulus.

The work described in Chapter 3 and Chapter 4 provide a reliable method to effectively reduce the voids content in composite laminates, reducing the manufacturing time (and thus costs) and considerably improving some mechanical properties of the part.

The Statement of Authorship Form and the paper can be found next.

This declaration concerns the article entitled:	
Development of an analytical model for optimisation of the ultrasonic consolidation of composite prepreg	
Publication status (tick one)	
Draft manuscript	
Submitted	
In review	✓
Accepted	
Published	
Publication details (reference)	
Flora, F., Rizzo, F., Pinto, F., & Meo, M. (2022). Development of an analytical model for optimisation of the ultrasonic consolidation of composite prepreg. Submitted (under review) at <i>Composites Part B</i> .	
Copyright status (tick the appropriate statement)	
I hold the copyright for this material	✓
Copyright is retained by the publisher, but I have been given permission to replicate the material here	
Candidate's contribution to the paper (detailed, and also given as a percentage)	
The candidate contributed to/ considerably contributed to/predominantly executed the...	

Formulation of ideas:	100%	I provided the entire idea, the hypothesis, the methodology and the experimental tests.	
Design of methodology:	80%	I manufactured all the samples used in the experimental campaign and designed all the experimental tests carried out in the work. My fellow Francesco Rizzo helped me in this procedure.	
Experimental work:	90%	I carried out all the experimental tests, collected all the data, and analysed all the outputs. My fellow Francesco Rizzo helped me in the performing of some experimental tests.	
Presentation of data in journal format:	90%	I designed the manuscript structure, wrote all the drafts and realised all. My supervisors provided feedback on the draft and help for the paper submission, review and submission.	
Statement from Candidate			
This paper reports on original research I conducted during the period of my Higher Degree by Research candidature.			
Signed		Date	29/01/2022

Development of an analytical model for optimisation of the ultrasonic consolidation of composite prepreg

Francesco Flora¹, Francesco Rizzo¹, Fulvio Pinto¹, Michele Meo^{1,*}

¹ *Department of Mechanical Engineering, University of Bath, Bath, Ba2 7AY, UK*

* Corresponding author: m.meo@bath.ac.uk

Keywords: *Ultrasonic Consolidation; Debulking; analytical model; porosity; voids; CFRP.*

Abstract

Mechanical properties of composite laminates are directly affected by the level of porosity of the part. Therefore, it is important to ensure that an adequate air debulking is provided during the manufacturing in order to obtain high quality products. The use of ultrasonic waves during the hand lay-up of prepreg layers can enhance this step. In a previous work we have demonstrated that this technique, named ultrasonic consolidation (UC), can lead to a large reduction in terms of manufacturing time and improvements of the Interlaminar Shear Strength (ILSS) of the final part. In this work, a model is proposed to analytically describe the influence of the ultrasonic stimulation on the air flux through the material and optimise the procedure, showing how the use of ultrasonic waves significantly increases the net air flow rate, particularly for small radius voids. The study provided some guidelines for the optimisation of the process parameters such as the frequency and location of the transducers. The efficiency of the method was experimentally validated by manufacturing several samples using UC debulking procedure with three exposition times (5-10-15 minutes). Microscope images showed a large decrement (up to 96%) of the voids projected area in samples section in comparison with reference. Flexural and Charpy impact properties were evaluated through mechanical tests, showing properties comparable to the reference samples, with improvements in terms of flexural modulus (up to 9%). Results from the analytical study and experimental tests indicate that the UC process is a reliable debulking procedure for the hand lay-up of prepreg that largely reduces manufacturing time and voids content, leading to improvements of the mechanical properties of the final part.

1. Introduction

Composite materials have seen a large expansion in use as both primary and secondary structures during the last two decades. In many sectors this kind of materials has replaced the traditional ones, particularly in automotive, aerospace and sport applications due to their high specific mechanical properties. The most common type of composite material in these sectors consists of two phases: a matrix (commonly a thermoplastic or thermosetting polymer) and a reinforcement (glass, Kevlar or carbon fibers). Particularly in aerospace section, carbon fiber reinforced polymers (CFRPs) are increasingly replacing traditional metals for primary and secondary structures, up to more than the 50% in mass of an aircraft [1], due to the good combination between lightness and mechanical properties. The large use of composite materials has pushed the research to study many manufacturing techniques in order to achieve higher mechanical properties, large scale productions and reduce the costs. In aerospace, most of the CFRP structures (more than 70%) are manufactured using layers of pre-impregnated material (prepreg) due to their ideal fiber volume content, uniformity and adaptability to automated processes, as stated in the extensive state of the art of manufacturing technologies for composite materials published by Breuer [2]. Prepreg layers are laid-up and cured at high temperature and pressure in order to obtain a final laminate part, whose anisotropic mechanical properties can be predicted and designed through the stacking sequence of layers with different fiber orientations. In order to enhance the productivity and repeatability of composite materials, automatic manufacturing techniques, such as Automated Tape Laying (ATL) [3] and Automated Fibre Placement (AFP) [4], have seen large diffusion in industrial sectors, particularly aerospace and automotive. Despite this, manual manufacturing process of prepreg laminates, known as “hand lay-up”, remains one of the main manufacturing techniques of composite laminates [5]. This manual technique provides many advantages, such as high tailorability in design and materials, low initial costs and the high quality of the final parts, when compared to the automatic processes. However, the manual stratification of the prepreg layers and its side procedures, such as air debulking,

are relative very slow processes, even for the manufacturing of simple parts. Therefore, hand lay-up is not suitable for large scale production due to its very low production rate, low replicability and high cost per part. Elkington et al. [5] gave a detailed study about prepreg hand lay-up and its features, particularly focusing on the methods used to manipulate the layers into shapes by the operators. In their work, it is reported how hand lay-up remains a key step in many applications, especially for small complex geometries, for both research and industry, and therefore a deeper knowledge of its characteristics and influence of its process parameters on the properties of the final part is needed.

Very few attempts can be found in literature about studies and improvements of hand lay-up technique in order to partially overcome its limitations. Hancock et al. [6] provided a kinematic model capable of predict the deformations of woven prepreg layers and how the results may be used to enhance material manipulation during hand lay-up of complex shapes. Kikuchi et al. [7] published a study on the influence of the operator skills and experience, concluding that there is a clear difference on the mechanical properties of laminates manufactured by expert and unskilled operators. Indeed, one of the most common defects generated by the hand lay-up of prepreg material is the creation of air bubbles between the layers, especially for unskilled operators [7], generating high levels of porosity in the final part. Many studies were conducted on the relation between the level of porosity and the mechanical properties of the final part [8–12], whose results showed that particularly the Interlaminar Shear Strength (ILSS) and compressive strength can be strongly affected by the porosity. Indeed, the presence of voids can be seen as an area of significant discontinuity of mechanical properties, thus causing intensification of stress locally, as stated by Anderson [13] and illustrated in Figure 4.8. In resin matrix composites, these points of stress intensification lead to crack generation and propagation, thus reducing the mechanical properties of the part, as experimentally proved by Goodwin et al. [14]. This is particularly true for unidirectional (UD) prepreg, as demonstrated by Jeong [8], that performed a comparison study on mechanical properties for different levels of porosity showing a ILSS degree of void sensitivity for UD materials around 80% higher than the one

for the fabrics. This work confirmed the fact that fabric laminates are less sensitive to resin dishomogeneities such as voids due to the resistance of woven construction to crack propagation along the resin phase. Based on this, it is possible to say that the removal of the air entrapped between the prepreg layers is a key-step to obtain high quality laminates, particularly for UD materials.

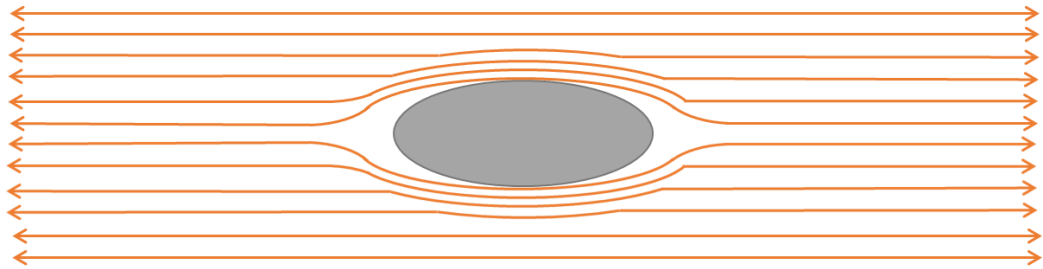


Figure 4.1 - Stress intensification due to the presence of void

Based on this premise, it is not surprising that the traditional hand lay-up includes various steps to ensure the removal of the air: pressure is manually applied during the stacking of every layer using a specific tool, known as Dibber tool [5]; consolidation cycles of 10-15 mins are applied using vacuum pressure, typically between the lamination of every 3-5 layers depending on the dimensions and complexity of the part [15] and followed by a final long-time consolidation cycle at the end of the lamination process; finally, high pressure is applied during autoclave curing. These steps, and particularly the numerous vacuum cycles, are the most time-consuming factors in the manufacturing of prepreg laminates, especially when large thickness, and thus high number of layers, is required.

Ultrasonic vibration is widely used for improvement of densification processes, such as in powder compaction [16–18], obtaining values of density considerably higher and better arranged structures in comparison to traditional processes [19]. Moreover, ultrasonic vibrations are generally used in melted metals and polymers prior to casting manufacturing processes, where it has been shown that ultrasonic waves induce a cavitation effect facilitating the degassing of the melts [20]. Ning et al. [19] provided an extensive state of the art of the ultrasonic vibration-assisted processes, explaining how the ultrasonic vibration properties are used in several ways, from intermittent contact to particle resonance, from material softening to

shear scrubbing, always obtain substantial improvements in the quality of the manufactured part.

In order to improve the debulking of the prepreg layers, and thus the quality of the final part, ultrasonic waves are widely used in automatic systems in a technique known as ultrasonic consolidation (UC). The ultrasonic waves are propagated through the layered material, generating small vibrations at the layers interfaces that promote the removing of the air. The UC used for manufacturing of polymer-based materials is not to be confused with metal UC, which is an additive manufacturing technique that combines ultrasonic welding and CNC machines to fabricate complex metal structure starting from metal foils [21]. The UC technique can be found in numerous composite manufacturing applications, particularly for automated placement of both thermoset and thermoplastic prepregs ([22–24]), where the ultrasonic waves are also used to generate heat in the material, mainly through friction events.

A different approach has been followed in the works patented from Forst-Miller ([25–27]), where a low frequency UC system is designed for debulking during automated placement of both thermoset and thermoplastic layers, without generating enough heat to activate the cure mechanism of the matrix.

In a previous work from the same authors [28], the UC process was applied as the only debulking step during the hand lay-up of thermoset prepreg. The technique has been proved to reduce the debulking time of hand lay-up by more than 85%. In addition, the mechanical properties of the samples were tested and compared with traditional hand lay-up manufactured samples showing a considerable improvement (>20%) in terms of interlaminar shear strength (ILSS).

The aim of this work is to analytically investigate the benefits of this technique over the traditional manufacturing of CFRP prepreg laminates, by studying the interaction of the prepreg layers and interlaminar voids with the ultrasonic waves in order to evaluate the influence of the different process parameters on the air flux. In the proposed analytical model, a study on the effect of ultrasonic waves on the air flow along the layers interfaces and how it is coupled with the pressure gradient

given by the vacuum pump was carried out. The phenomenon was modelled as a peristaltic transport mechanism under a pressure gradient.

The model was then experimentally validated by testing samples manufactured following the guidelines pointed out from the analytical results. In order to analyse the efficiency of the process in reducing the porosity of the part, microscope image analysis of the samples sections was performed. Samples mechanical properties were experimentally studied through flexural and Charpy impact tests and compared with traditional samples in order to verify the absence of unwanted secondary detriments.

2. Analytical model

2.1 Methodology

The aim of this paragraph is to analytically study the effects of ultrasonic radiation and pressure gradient on the air flow rate within a laminated prepreg material. The complexity of the wave generated by the ultrasonic shaker and the elaborate internal structure of the uncured prepreg system make the development of a complete analytical model a problematic goal. Based on this consideration, some approximations were applied in this study to simplify the analysis, without compromising the validity of the analysis of the ultrasound/pressure gradient air flow phenomena and the relative effect on the laminate's voids content.

The process parameters that drive the phenomena of void formation, evolution and removal in composite materials are commonly analysed with two transport mechanisms: gas momentum transport (Darcy flow through porous medium [29]) or gas diffusion (Fick's first law of diffusion [30]). In this work, the system considered is a laminate made of uncured prepreg at room temperature. Between each couple of layers, there is an interface with numerous air packages entrapped in the material during the lay-up. In this kind of system, where the polymeric matrix is a high viscosity fluid, the first phenomena (momentum transport) is prevalent over the second one (diffusion), and so only the gas momentum transport has been considered. This hypothesis is confirmed by Farhang in his work [65], where it is

stated that the uncured prepreg debulking time for the diffusion phenomena is over six orders of magnitude higher than the gas momentum transport for a long room temperature debulk process. The voids momentum transport in this kind of system can be expressed by Darcy's law:

$$Q = -\frac{KA \Delta P}{\mu \Delta x} \quad \text{Equation 1}$$

where K is the gas permeability, μ the gas dynamic viscosity, P the gas pressure, A the cross-sectional area and Δx the distance that the voids have to cover to be removed. This law is based on the hypothesis that the gas flow is laminar, which is admissible for the current conditions, as proved by the Reynolds number calculations provided by Farhang [30] for a similar prepreg system.

The Darcy flow can be used to estimate the gas transport in both directions: along the interface between two prepreg layers and through the thickness. At room temperature, the polymeric matrix is a high viscosity fluid and the value of permeability through thickness is three orders of magnitude lower than the in-plane one [30]. As a consequence, the flow will have a predominant direction along the interface between the prepreg layers in the direction of the closest edge, hence only this flow will be considered in this study. This is due to the relative low adhesion between the prepreg layers at room temperature that creates a facilitated way out for the trapped gas.

Equation 1 is not sufficient to completely describe the airflow through the prepreg layers under the ultrasonic radiation, thus a more accurate analysis is needed. In order to describe the system, the way out of the entrapped air packages from the laminate can be seen as a channel between the prepreg layers. In the UC procedure, ultrasonic waves are sent through the material and deform the walls of the channel following the shape of a travelling wave. Ganiev et al. [31] explained how the flow of a liquid through a porous medium is facilitated by ultrasonic waves due to the

generation of travelling transversal waves along the pores. Their results showed that the effect of the ultrasonic waves on the movement of a fluid in a channel can be analysed as a peristaltic transport mechanism, where a travelling transversal wave propels the liquid along a tube. In Aarts et al. work [32] the flow of a compressible viscous liquid through a porous media under an ultrasonic radiation is studied. Unlike other studies, they took into account both viscosity and compressibility of the fluid, relating the amplitude of the wave with the net flow through the porous media and observed that the liquid compressibility has a considerable influence on the final net flow, and thus it is important to consider it into the calculations.

The aim of this section is to analytically describe the contribution of the ultrasonic waves in the air flow and analyse how this is coupled with the flow generated by the pressure difference (caused by the vacuum pump). The approach is similar to the one proposed by Aarts et al [32], with the difference that in this case a difference in pressure between the two extremes of the channel is taken into account. A similar approach was adapted by Yin et al. [33], who analysed the peristaltic pumping of a viscous incompressible liquid in a circular cylindrical tube. However, in this case, even if an initial pressure gradient was considered, the calculations were carried out for a gradient equal to zero.

2.2 Model

Giving the small dimensions of the pores radius in comparison with the length of the path travelled by the air to reach the edge of the laminate, the channel has been assumed as an axisymmetric cylindrical tube with a varying radius in order to substantially facilitate the calculations. The channel is represented in Figure 4.2.

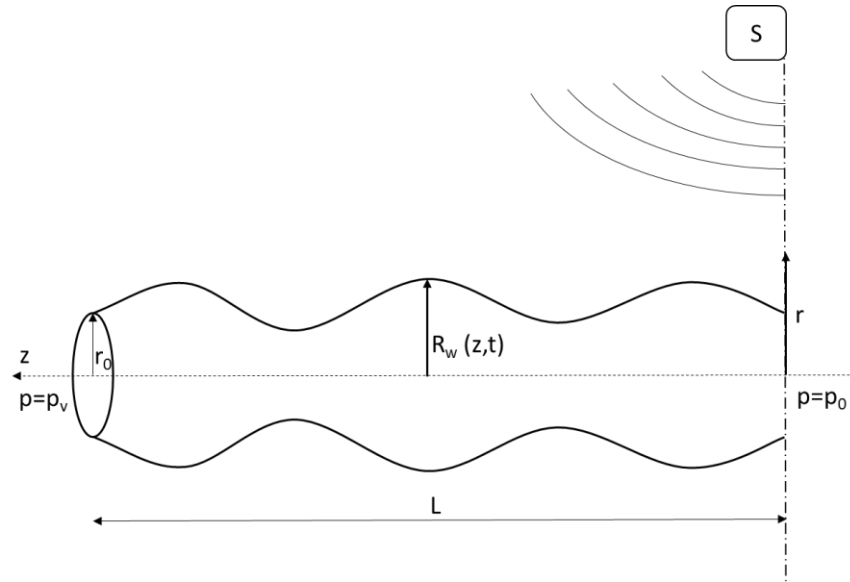


Figure 4.2 – Deformation of cylindrical channel walls by ultrasonic waves generated from the source (S)

The generated wave is travelling from the source through the prepreg layers and for every interface, it is divided, reflected and transmitted in numerous complex ways. Nevertheless, a component of the generated waves propagates along the interface plane in a radial direction from the transducer, with its own wave amplitude, length and speed (A , λ and c). The wall of the channel is deformed by this travelling wave in the direction perpendicular to the axis of the channel, varying the wall radius (R_w) according to the equation below:

$$R_w(z, t) = r_0 + A \cos\left[\frac{2\pi}{\lambda}(z - ct)\right] \quad \text{Equation 2}$$

In equation 2, r_0 is the initial average of the channel radius, while t represents the time. The air inside the pores has a pressure equal to the atmospheric pressure p_0 , whereas there is a lower pressure applied on the external edges of the part by the vacuum pump p_v . The velocity of the fluid travelling through the channel can be expressed in cylindrical coordinates (r, θ, z) :

$$\bar{\mathbf{u}} = u_r(r, z, t)\bar{\mathbf{e}}_r + u_z(r, z, t)\bar{\mathbf{e}}_z \quad \text{Equation 3}$$

where $\bar{\mathbf{e}}_r$ and $\bar{\mathbf{e}}_z$ are versors in r and z direction, respectively. The flow rate through the channel is given by:

$$Q(z, t) = 2\pi \int_0^{R_w(z,t)} u_z(r, z, t)r \, dr \quad \text{Equation 4}$$

Considering equations 3 and 4, it is necessary to find the components of the velocity \mathbf{u} to calculate the flow rate. To do this, we need several equations to describe the flow, therefore it is possible to write the Navier-Stokes equations as:

$$\begin{aligned}
& -\frac{\partial p}{\partial r} + \frac{1}{Re} \left(\frac{\partial^2 u_r}{\partial r^2} + \frac{1}{r} \frac{\partial u_r}{\partial r} - \frac{u_r}{r^2} + \frac{\partial^2 u_r}{\partial z^2} \right) \\
& \quad + \frac{1}{3Re} \frac{\partial}{\partial r} \left(\frac{\partial u_r}{\partial r} + \frac{u_r}{r} + \frac{\partial u_z}{\partial z} \right) \\
& = \rho \left[\frac{\partial u_r}{\partial t} + u_r \frac{\partial u_r}{\partial r} + u_z \frac{\partial u_z}{\partial z} \right]
\end{aligned}$$

Equation 5

$$\begin{aligned}
& -\frac{\partial p}{\partial z} + \frac{1}{Re} \left(\frac{\partial^2 u_z}{\partial r^2} + \frac{1}{r} \frac{\partial u_z}{\partial r} + \frac{\partial^2 u_z}{\partial z^2} \right) \\
& \quad + \frac{1}{3Re} \frac{\partial}{\partial z} \left(\frac{\partial u_r}{\partial r} + \frac{u_r}{r} + \frac{\partial u_z}{\partial z} \right) \\
& = \rho \left[\frac{\partial u_z}{\partial t} + u_r \frac{\partial u_z}{\partial r} + u_z \frac{\partial u_z}{\partial z} \right]
\end{aligned}$$

And the balance of mass:

$$\frac{\partial \rho}{\partial t} + u_r \frac{\partial \rho}{\partial r} + u_z \frac{\partial \rho}{\partial z} + \rho \left(\frac{\partial u_r}{\partial r} + \frac{u_r}{r} + \frac{\partial u_z}{\partial z} \right) = 0$$

Equation 6

where p is the pressure, ρ is the density and μ the viscosity of the fluid. We are considering a compressible fluid, where the compressibility is defined by:

$$k = \frac{1}{\rho} \frac{d\rho}{dp}$$

Equation 7

The value of density in function of pressure can be find solving equation 7, where the solution is given by the following:

$$\rho = \exp[k(p - p_0)]$$

Equation 8

It is important to underline that the equations above are in the dimensionless form (tildes were omitted), therefore the following dimensionless terms were used:

$$\begin{aligned} \tilde{v}_r = \frac{v_r}{c}; \quad \tilde{v}_z = \frac{v_z}{c}; \quad \tilde{Q} = \frac{Q}{cr_0^2}; \quad \tilde{R}_w = \frac{R_w}{r_0}; \\ \tilde{t} = \frac{ct}{r_0}; \quad \tilde{\rho} = \frac{\rho}{\rho_0}; \quad \tilde{p} = \frac{p}{\rho_0 c^2}. \end{aligned}$$

Equation 9

In addition, we introduce the following dimensionless parameters:

$$\varepsilon = \frac{A}{r_0}; \quad \alpha = \frac{2\pi r_0}{\lambda}; \quad Re = \frac{\rho_0 c r_0}{\mu}; \quad \chi = k\rho_0 c^2.$$

Equation 10

The term ε is called amplitude ratio, α is the wave number and Re is the Reynolds number.

In order to proceed with the analysis, and introduce the boundary conditions, we assume no-slip conditions, or in other words that the motion of the fluid is coupled with the wall when in contact ($r = R_w$):

$$u_r(R_w, z, t) = \frac{\partial R_w}{\partial t}; \quad u_z(R_w, z, t) = 0$$

Equation 11

The term R_w in the dimensionless form is equal to:

$$R_w(z, t) = 1 + \eta(z, t); \quad \eta(z, t) = \varepsilon \cos \alpha(z - t). \quad \text{Equation 12}$$

Equations 5, 6 and 8, together with boundary conditions described by 11, constitute a system of equations that needs to be solved in order to find the components of \mathbf{u} .

To find the solution of equations 5,6 and 8, we assume that they are in the form:

$$\begin{aligned} p &= p_0(z) + \varepsilon p_1(r, z, t) + \varepsilon^2 p_2(r, z, t) + \dots, \\ u_r &= \varepsilon u_{r1}(r, z, t) + \varepsilon^2 u_{r2}(r, z, t) + \dots, \\ u_z &= u_{z0}(r) + \varepsilon u_{z1}(r, z, t) + \varepsilon^2 u_{z2}(r, z, t) + \dots, \\ \rho &= \rho_0(z) + \varepsilon \rho_1(r, z, t) + \varepsilon^2 \rho_2(r, z, t) + \dots, \end{aligned} \quad \text{Equation 13}$$

The zero-order components of equation 13 refer to the condition of $\varepsilon = 0$ (absence of ultrasonic radiation), where we assume to have a constant pressure gradient that generates a fluid velocity (in the dimensionless form) equal to:

$$V_0 = \bar{u}_{z0} = \frac{r_0^2}{8\mu c} \left(-\frac{dp_0}{dz} \right) \quad \text{Equation 14}$$

where $u_{z0}(r)$ is the fluid velocity in absence of the ultrasonic wave, calculated with the classical Poiseuille flow [34], and \bar{u}_{z0} is its average over r .

To simplify the calculations, we have used the average value of the velocity \bar{u}_{z0} in order to eliminate the dependence on r , and its relative dimensionless flow rate:

$$Q_0 = V_0\pi = \frac{r_0^2\pi}{8\mu c} \left(-\frac{dp_0}{dz}\right) \quad \text{Equation 15}$$

The first order approximation terms of equation 13 can be expressed in the form:

$$\begin{aligned} p_1 &= P_1(r)e^{i\alpha(z-t)} + \bar{P}_1(r)e^{-i\alpha(z-t)}, \\ u_{r1} &= U_{r1}(r)e^{i\alpha(z-t)} + \bar{U}_{r1}(r)e^{-i\alpha(z-t)}, \\ u_{z1} &= U_{z1}(r)e^{i\alpha(z-t)} + \bar{U}_{z1}(r)e^{-i\alpha(z-t)}, \\ \rho_1 &= \chi P_1(r)e^{i\alpha(z-t)} + \chi \bar{P}_1(r)e^{-i\alpha(z-t)}; \end{aligned} \quad \text{Equation 16}$$

where the overbar $\bar{}$ indicates the complex conjugate.

The values of P_1 , U_{r1} and U_{z1} can be found by substituting the first order approximation solutions in the set of equations 5, 6, 8 and 11 resulting in:

$$\begin{aligned} P_1(r) &= C_1 \frac{v^2 - \beta^2}{v\gamma} I_0(vr), \\ U_{r1}(r) &= C_1 I_1(vr) + C_2 I_1(\beta r), \\ U_{z1}(r) &= \frac{i\alpha}{v} C_1 I_0(vr) + \frac{i\beta}{\alpha} C_2 I_0(\beta r). \end{aligned} \quad \text{Equation 17}$$

where:

$$\begin{aligned} \gamma &= Re - \frac{1}{3}i\alpha\chi(1 + V_0), \quad \beta^2 = \alpha^2 - i\alpha Re(1 + V_0), \quad B \\ &= 1 - \frac{i\alpha\chi(1 + V_0)}{\gamma}, \end{aligned} \quad \text{Equation 18}$$

$$v^2 = \beta^2 - \frac{\beta^2 - \alpha^2}{B},$$

$$C_1 = \frac{\alpha\beta v i I_0(\beta)}{2[\alpha^2 I_0(v) I_1(\beta) - v\beta I_0(\beta) I_1(v)]},$$

$$C_2 = \frac{-\alpha^3 i I_0(v)}{2[\alpha^2 I_0(v) I_1(\beta) - v\beta I_0(\beta) I_1(v)]}.$$

The second order approximation terms of equation 13 can be expressed as:

$$\begin{aligned}
p_2 &= P_{20}(r) + P_2(r)e^{2i\alpha(z-t)} + \bar{P}_2(r)e^{-2i\alpha(z-t)}, \\
u_{r2} &= U_{r20}(r) + U_{r2}(r)e^{2i\alpha(z-t)} + \bar{U}_{r2}(r)e^{-2i\alpha(z-t)}, \\
u_{z2} &= U_{z20}(r) + U_{z2}(r)e^{2i\alpha(z-t)} + \bar{U}_{z2}(r)e^{-2i\alpha(z-t)}, \\
\rho_2 &= D_{20}(r) + D_2(r)e^{2i\alpha(z-t)} + \bar{D}_2(r)e^{-2i\alpha(z-t)},
\end{aligned}$$

Equation 19

Following the same approach used for first order approximation, the value of P_{20} , U_{r20} , U_{z20} and D_{20} can be find by substituting equation 19 in the set of equations 5, 6, 8 and 11. The results are the following:

$$\begin{aligned}
P_{20}(r) &= D_3 - \frac{4\chi}{3Re} H(r) - \int_0^r F(y) dy, \\
U_{r20}(r) &= -\chi(P_1(r)\bar{U}_{r1}(r) + \bar{P}_1(r)U_{r1}(r)), \\
U_{z20}(r) &= D_2 \\
&\quad - Re \int_r^1 \left[\frac{1}{(1+V_0)} \int \left(U'_{r1}(y)\bar{U}_{z1}(y) \right. \right. \\
&\quad \left. \left. + \frac{1}{y}U_{r1}(y)\bar{U}_{z1}(y) + \frac{1}{y}\bar{U}_{r1}(y)U_{z1}(y) \right) dy \right. \\
&\quad \left. + \int (U_{r1}(y)\bar{U}'_{z1}(y) \right. \\
&\quad \left. + U_{r1}(y)U'_{z1}(y)) dy \right] dy.
\end{aligned} \tag{Equation 20}$$

where:

$$\begin{aligned}
D_2 &= \frac{i\alpha}{2} \bar{C}_1 I_1(\bar{v}) + \frac{i\bar{\beta}^2}{2\alpha} \bar{C}_2 I_1(\bar{\beta}) - \frac{i\alpha}{2} C_1 I_1(v) - \frac{i\beta^2}{2\alpha} C_2 I_1(\beta), \\
D_3 &= P_{20}(0) + \frac{4\chi}{3Re} H(0), \\
F &= i\alpha\chi(P_1\bar{U}_{r1} - \bar{P}_1U_{r1}) + U_{r1}\bar{U}'_{r1} + \bar{U}_{r1}U'_{r1} \\
&\quad + i\alpha(\bar{U}_{z1}U_{r1} - U_{z1}\bar{U}_{r1}), \\
H &= \frac{1}{r} \frac{d}{dr} [r(P_1\bar{U}_{r1} - \bar{P}_1U_{r1})].
\end{aligned} \tag{Equation 21}$$

As demonstrated by Aarts et al. [32], if we consider only the net flow, the functions U_{r2} , U_{z2} , P_2 and D_2 in equation 19 do not contribute to the final solutions, therefore, they were not considered in the calculations.

Finally, the value of u_z can be find by substituting the value of u_{z1} and u_{z2} in equation 13, resulting in the following solutions, written neglecting the $O(\varepsilon^3)$ terms, following the same approach of Aarts et al [32]:

$$\hat{u}_z = \frac{\alpha}{2\pi} \int_0^{\frac{2\pi}{\alpha}} u_z(r, t) dt = V_0 + \varepsilon^2 U_{z20}(r). \quad \text{Equation 22}$$

$$\hat{Q} = \frac{\alpha}{2\pi} \int_0^{\frac{2\pi}{\alpha}} Q(z, t) dt = \pi V_0 + 2\pi \varepsilon^2 \int_0^1 U_{z20}(r) r dr, \quad \text{Equation 23}$$

The term \tilde{u}_z in equation 22 represents the net axial velocity (averaged over one period of time), while \tilde{Q} is the dimensionless net flow. Analysing the equations above it is possible to observe that in case of absence of ultrasonic radiation ($\varepsilon = 0$) both flow and axial velocity reduce to the classic Poiseuille law, and therefore they will depend only on the pressure gradient. As for the ultrasonic-term of the net flow, it is possible to see that it strongly depends on the wave amplitude/pore radius ratio (ε^2) and on the zero order velocity (equation 20).

To confirm the reliability of the results, the net flow rate was evaluated assuming $\varepsilon = 0.15$, $Re = 100$, $\alpha = 0.2$, $\chi = 0$ and considering the absence of initial pressure gradient. The result matches what previously reported in literature obtaining a value of \hat{Q} equal to 0.2708, which is the same value obtained by Aarts et al [32].

2.3 Numerical results

To analyse the results, numerical analyses were carried out using Matlab software. The aim of these simulations is to study the value of the flow rate in function of the ultrasonic wave parameters, such as wave amplitude, frequency and transducer position. The values of the net axial velocity and net flow rate were made dimensional again by using equation 9 and the following parameters were used:

$$\rho_0 = 1.3 [kg/m^3], k = 0.7 \cdot 10^{-5} [m^2/N], \mu = 1.81 \cdot 10^{-5} [kg/m \cdot s],$$

$$A = 5 \cdot 10^{-6} [m], f = 50 \cdot 10^3 [Hz], c = 125 [m/s],$$

$$r_0 = 10^{-5}[m], p_0 = 101325 [Pa], p_v = 0[Pa], L = 0.2 [m].$$

The wave amplitude was chosen to be half of the radius, in order to completely close the channel and simulate the unconnected pores travelling along the interlaminar interface.

Firstly, the calculations were computed varying the value of the travelling wave speed c , which is function of numerous parameters depending on the way the source waves are divided and reflected by the material and the numerous interfaces. As a consequence, it is very complicated to predict or measure this parameter, however, as it is possible to see from Figure 4.3, a value of around 125 m/s represents the optimal value to maximise the flow rate and therefore it was used for the numerical calculations. It is important to underline that, even if the chosen value of c obviously influences the numerical results, the general discussions at the end of this paragraph are valid for any value of the travelling wave speed.

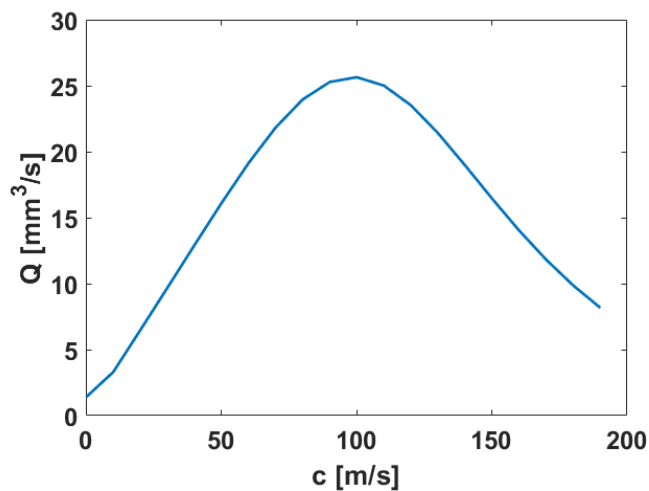


Figure 4.3 - Net flow rate Q [mm³/s] versus the travelling wave velocity c [m/s]

The flow rate was calculated in function of r_0 and plotted in Figure 4.4. As it is possible to observe from the curves, the UC debulking procedure is significantly

more efficient than the traditional procedure in removing small interlaminar air bubbles entrapped in closed channels ($r_0 < 0.052$ mm), showing a flow rate of over $50 \text{ mm}^2/\text{s}$ for air bubbles radius around 0.02 mm, while the flow rate for traditional procedure is below $2 \text{ mm}^2/\text{s}$.

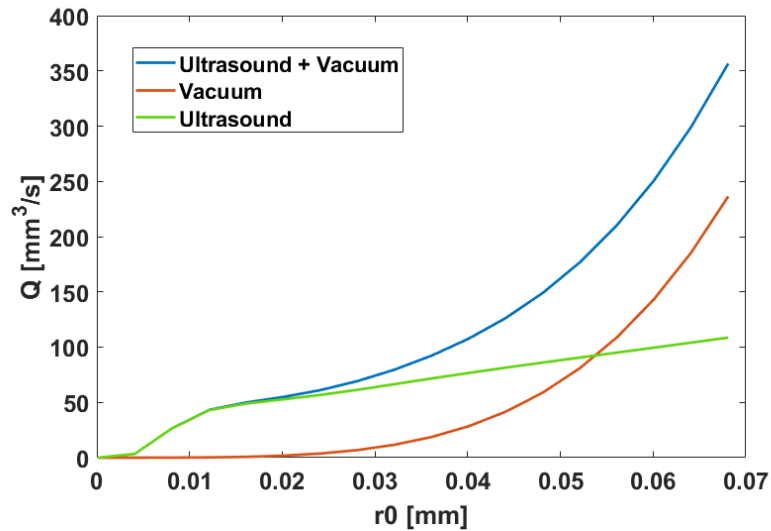


Figure 4.4 – Net flow rate Q [mm^3/s] versus the average channel radius r_0 [mm] in the case of ultrasonic radiation only (green line), vacuum pressure only (red line) and ultrasonic radiation plus vacuum pressure (blue line).

In Figure 4.5 the net flow rate is plotted versus the wave frequency and amplitude, and it increases with both. As it can be seen from the first plot, the flow reaches a plateau for frequencies above the 80-90 kHz. High frequencies may cause increment in temperature of the material, which is undesirable in this case, as declared in the introduction of this work. In addition, higher values of frequency would cause a faster decrement of the energy of the wave while travelling through the material. Based on these considerations, a frequency in the range between 20 and 60 kHz is optimal.

As shown in the second plot of Figure 4.5, the flow rate increases with the wave amplitude in a parabolic form, therefore high levels of amplitude would maximise the procedure. The wave amplitude is decreased by the distance from the source

and the number of interfaces through the material, meaning that the procedure efficiency decreases with the increment of the number of layers.

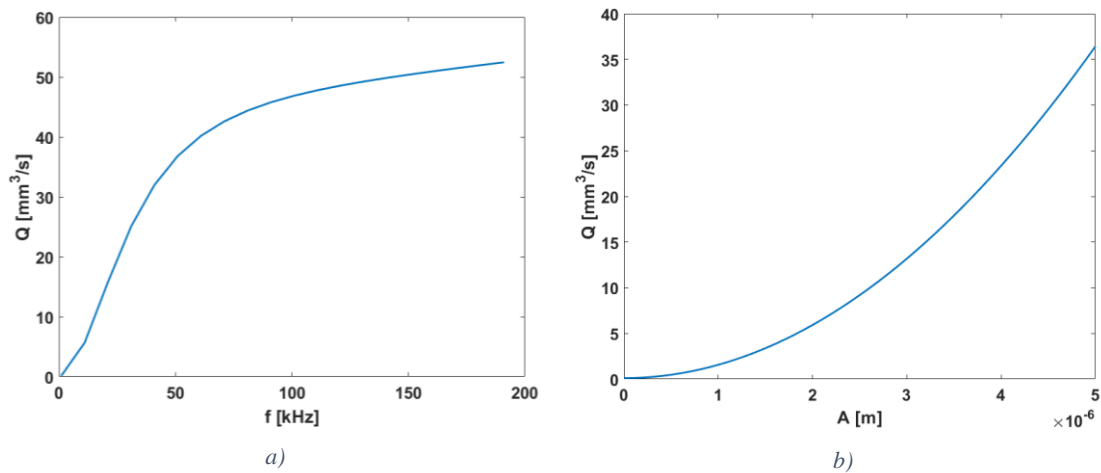


Figure 4.5 - Net flow rate Q [mm^3/s] versus the wave a) frequency (kHz) and b) amplitude (m)

Based on this study, it is possible to write some guidelines for the optimization of the UC procedure:

- The ultrasonic transducer needs to be positioned in correspondence of the centre of the laminated part in order to have a uniform distribution of the waves through the material.
- The value of frequency of the source waves needs to be in a range between 20 and 60 kHz to be efficient.
- The value of amplitude of the source waves needs to be as high as possible without reaching the curing temperature of the resin (thermocouples or similar are suggested to check the material temperature).

- For thick parts, the use of multiple transducers on both sides of the part is suggested in order to obtain high levels of amplitude through the thickness.
- For large parts, the use of two or more transducers in a symmetrical disposition around the centre is suggested in order to decrease the distance between voids and wave sources.

3. Samples manufacturing

In order to further investigate how the UC debulking process effects the voids content and mechanical properties of a composite laminate, three different sets of samples were manufactured. The material used was a UD prepreg produced by Cycom[®] that consists in Tenax[®] - E IMS65 carbon fibres preimpregnated in a 977-2 epoxy resin matrix and laminated in the sequence $[(-45/0/45/90)_2/-45/0/45/\overline{90}]_s$. After the manual stratification, performed without any debulking step, UC was applied following the procedure illustrated in Figure 4.6 and following the guidelines given in the previous section.

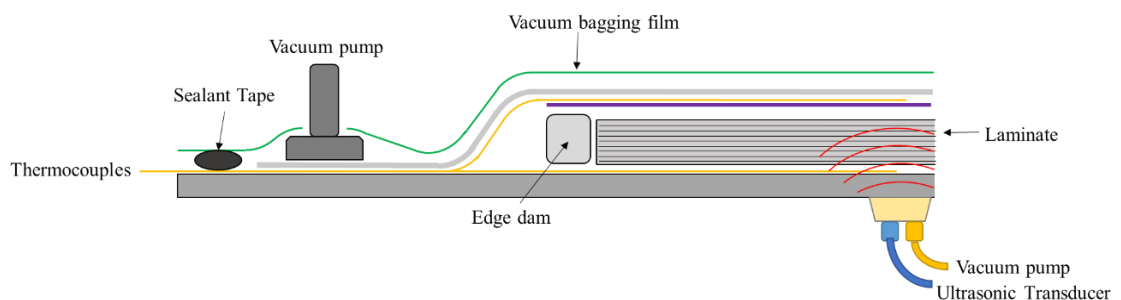


Figure 4.6 – Ultrasonic consolidation debulking setup

The laminated material was placed under vacuum pressure and attached to a piezoelectric transducer (Piezoshaker PS-X03-06/1000, ISI-SYS), through a

suction cup and coupled with ultrasonic gel, from the mould side at the position corresponding to the centre of the part. A sine form with a frequency of 28 kHz was chosen for the ultrasonic waves, as this value is the central frequency of the transducer, which allows the maximum amplitude of the wave (300 V), and it is in the range of optimal frequencies suggested by the analytical model. The temperature was monitored with two thermocouples during the procedure, one at the ultrasonic transducer and one at laminate edge, in order to ensure that the curing reaction does not take place, reaching a maximum value of 45°C at the transducer. The three configurations of samples differentiate from each other for the time of exposure to the UC debulking procedure: 5 (UC1), 10 (UC2) and 15 (UC3) minutes. Control samples (labelled PC samples) with the same stacking sequence were manufactured using traditional hand lay-up technique and debulking steps of 15 minutes vacuum cycles every 3 stratified layers. The four sets of samples were then cured in autoclave at of 180°C and 100 psi for 3 hours, following the manufacturer's instructions.

The UC procedure has sensibly reduced the manufacturing time of the CFRP samples in comparison with traditional procedure. In particular, the traditional debulking time of 15 minutes of vacuum bag every 3 plies, for a total of 120 minutes, has been reduced by 96% for UC1 (5 min), 92% for UC2 (10 min) and 87% for UC3 (15 min). This calculation has been conducted without considering the time spent for bagging and the bagging of the laminate for each vacuum cycle and is therefore underestimated.

4. Microscope images analysis

Microscope images were acquired from the same portions of each laminate in three points from the centre to the edge, after the autoclave curing cycle. Images were captured using a stereo microscope Leica M205 C and elaborated in order to highlight the different colour given by the voids in the section. The projected area occupied by the interlaminar voids was calculated in each sample in order to study the validity of the UC debulking procedure. Representative elaborated images are showed in Figure 4.7 while Table 4.1 summarises the average and standard

deviation of the percentage of section area occupied by the voids for each sample (black spots in figures).

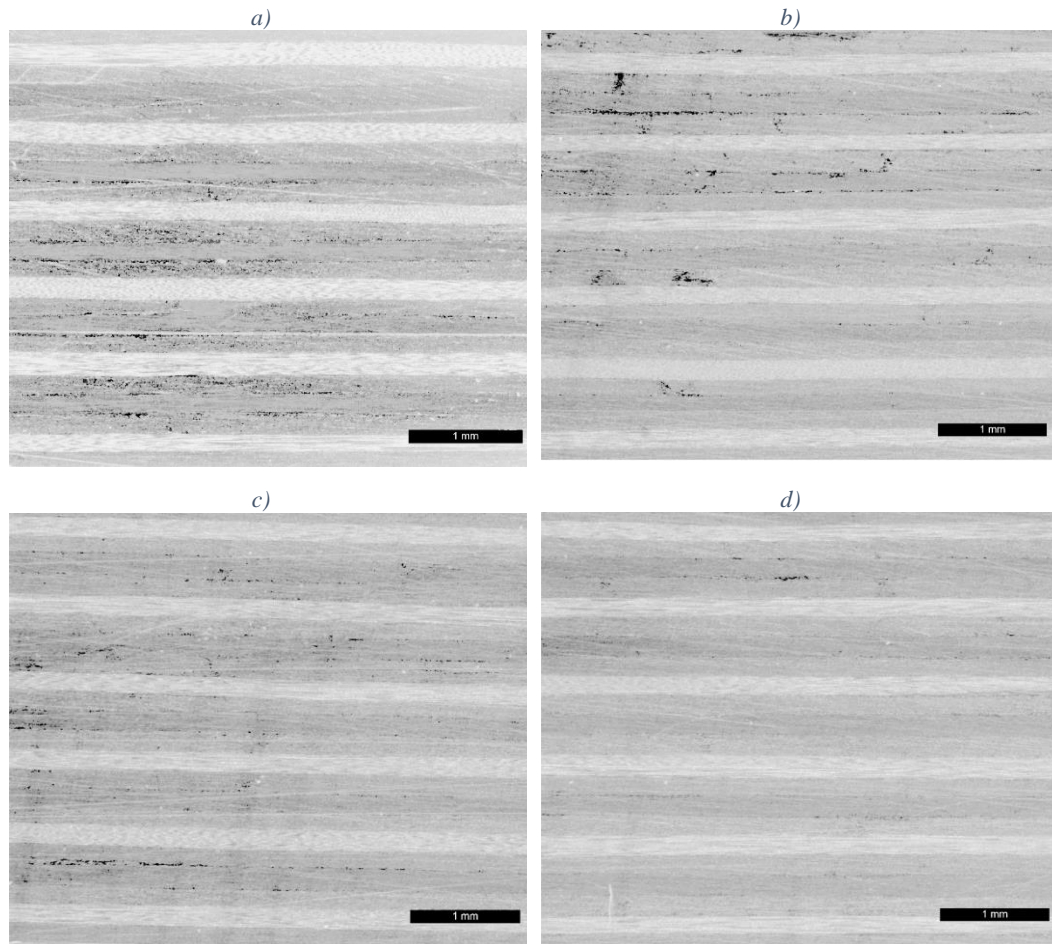


Figure 4.7 – Representative microscope images of sample a) PC, b) UC1, c) UC2, d) UC3. The voids are represented by the black spots

Table 4.1 – Samples voids projected area: average and standard deviation

	PC	UC1	UC2	UC3
Voids projected area (average)	0.52%	0.31%	0.24%	0.02%
Standard deviation	1.47E-03	6.53E-03	4.08E-04	8.16E-06

As it is clearly shown in the images, all three UC samples presented a reduction in terms of voids content, especially for the UC3 sample, where the voids content is 96% lower than the reference. It is important to highlight that these results may be influenced by the shape of the voids, given that the images are related to a two-dimensional projection of the voids. Indeed, a void distributed along the interface area, with a reduced dimension through the thickness of the laminate, will result in a reduced projected area. Despite this, the large difference between the UC3 sample and the reference still suggests a strong reduction of voids and confirms the hypothesis of diffusion of them along the prepreg interfaces. Moreover, as it is possible to state from the standard deviation value, the uniformity of voids along the samples (from the center position to the edge) increases with the increment of UC time. These results suggest that the conclusions obtained from the analytical model are correct, confirming the reliability of the UC procedure in the removal of the air bubbles.

5. Experimental campaign

Alterations in the traditional manufacturing methodology, such as the introduction of the UC debulking step, could result in unwanted side effects, such as the local heating up of some regions of the laminate due to the accumulation of ultrasonic waves, that leads to dishomogeneities during the curing reaction. These side effects may decrease the ultimate mechanical properties of the final part. The analytical model provided some guidelines to optimise the air removal during the UC but does not consider its influence on the curing of the resin. Therefore, in order to prove the absence of unwanted detriments, mechanical tests were performed on the cured samples and compared with a reference laminate manufactured following traditional debulking procedure.

The use of the UC debulking step during the manufacturing of CFRP laminates has already been proven to provide large improvements in terms of ILSS (+26%) in the final part [28]. The aim of this section is to illustrate the experimental campaign conducted to test other mechanical properties. In particular, three-point bending and Charpy impact tests were performed on the manufactured laminates; five samples

for each configuration were tested, leading to a total of twenty samples for each test.

5.1 Three-Point Bending Tests

In order to evaluate the influence of the UC procedure on flexural properties of the laminates, three-point bending tests were performed using a universal testing machine Instron 3369 and following the BS EN ISO 14125:1998 standard. The supports and loading nose used to apply the load were steel rods of 5 mm in radius with a span-to-length ratio of 40:1. The test setup is illustrated in Figure 4.8.

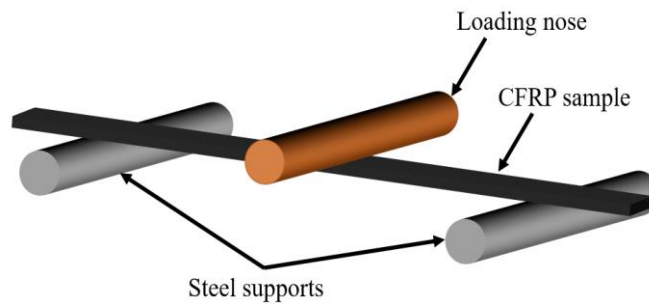


Figure 4.8 - Setup of three-points bending test

The flexural stress σ_f (MPa) for three-point bending was calculated using the formula:

$$\sigma_f = \frac{3FL}{2bh^2}$$

Equation 24

where F is the load (N), L is the span length, b the width and h the thickness of the sample (mm). The maximum flexural strength (σ_{fs}) for each sample was calculated using the equation 24 considering the maximum force applied during the test. Flexural strain ϵ_f was calculated using the formula:

$$\varepsilon_f = \frac{6sh}{L^2}$$

Equation 25

where s is the sample deflection (mm) recorded during the test. The flexural modulus E_f (MPa) was calculated using the formula:

$$E_f = \frac{L^3}{4bh^3} \left(\frac{\Delta F}{\Delta s} \right)$$

Equation 26

where ΔF is the difference in force for deflection s' and s'' at flexural strain of 0.0005 and 0.001 and Δs is their difference.

Experimental results for three-point bending are reported in Figure 4.9 and Table 4.2 where stress-strain plots and properties for all the configurations are compared. In Figure 4.9.a one representative stress-strain curve has been plotted for each sample. Mean and standard deviation for flexural strength, flexural strain and flexural modulus are reported.

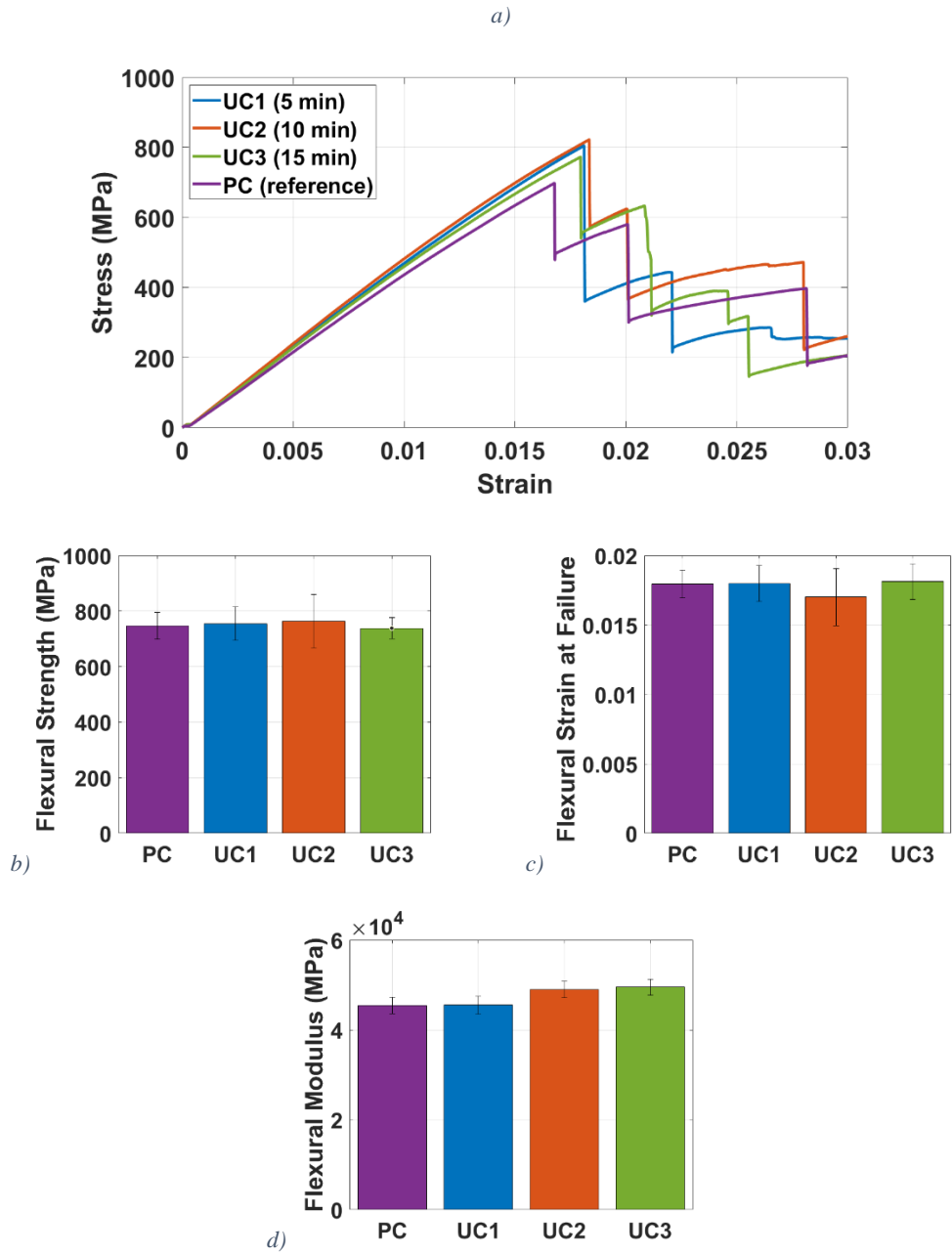


Figure 4.9 - Flexural results plots for 3 ultrasonic consolidation configurations and reference: a) stress-strain curves, b) flexural strength, c) flexural strain, d) flexural modulus graphs with standard deviation bars

Table 4.2 – Flexural results, statistical data and percentage variation in comparison with reference (PC)

3PB	Flexural Modulus (MPa)			Flexural Strength (MPa)			Flexural Strain At Failure		
	Mean	Standard Deviation	% variation	Mean	Standard Deviation	% variation	Mean	Standard Deviation	% variation
UC1	45489	3080	0%	754.8	60.6	+1%	0.018	0.001063	+1%
UC2	48979	797	+8%	763.3	96.8	+2%	0.017	0.001445	-5%
UC3	49489	5817	+9%	738.4	38.5	-1%	0.0181	0.0014	+1%
PC	45434	5370	0%	747.2	48.6	0%	0.0179	0.0014	0%

Based on the experimental results for UC samples, no effect is evaluated in terms of flexural strength and strain at failure in comparison with the traditional CFRP. Different are the results in terms of flexural modulus, where good increments are reported for UC2 and UC3 (+8% and +9%, respectively) in comparison with PC.

5.2 Charpy Impact Tests

Charpy impact strength was determined via unnotched tests that were carried out using a Charpy pendulum (Figure 4.10) and following the standard BS EN ISO 179-1:2010. Unnotched samples were placed in the support location with a span of 62mm, and afterwards the hammer was located in its starting position and released using the dedicated system, impacting the samples in their centre.

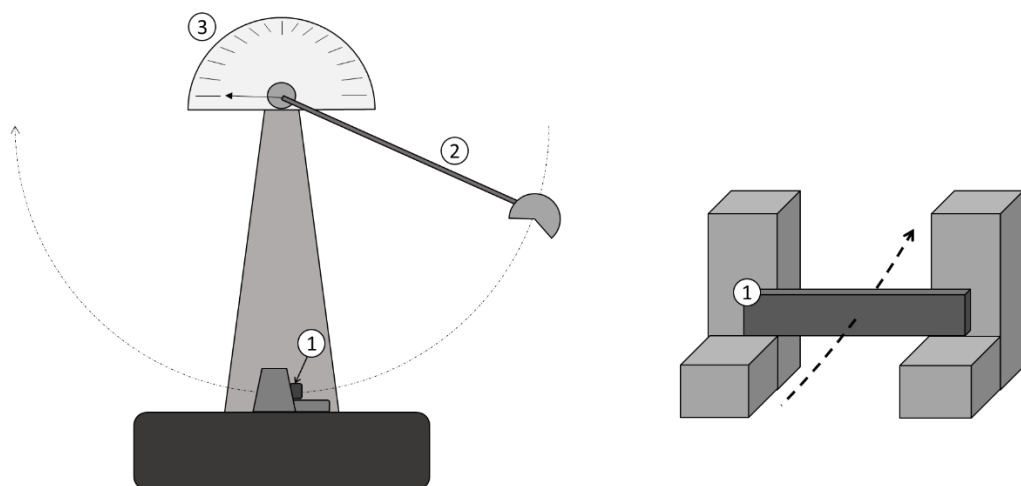


Figure 4.10 - Charpy impact test apparatus: specimen (1), hammer (2) and scale (3)

The absorbed energy was recorded by the machine while the impact strength a_{cN} (kJ/m^2) was calculated using the formula:

$$a_{cN} = \frac{E_c}{hb} \cdot 10^3$$

Equation 27

where E_c is the energy (J) absorbed by breaking the sample, b is the width (mm) of the sample and h is its thickness (mm).

Results from the Charpy impact analysis are reported in Figure 4.11, where the impact strength is reported in the bar plot, and Table 4.3, where statistical data and percentage variations are summarised.

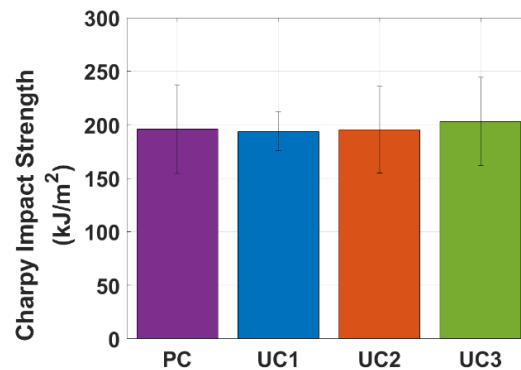


Figure 4.11 - Charpy impact strength graph with standard deviation bars

Table 4.3 - Charpy impacts results, statistical data and percentage variation in comparison with reference (PC)

CHARPY	Charpy Impact Strength (kJ/m ²)		
	Mean	Standard Deviation	% variation
UC1	188.5	20.34	-3%
UC2	195.2	40.44	0%
UC3	203.1	41.21	+4%
PC	195	41	0%

Analysing the results from Table 4.3 it is possible to conclude that the UC samples showed variations in terms of Charpy impact strength that fall in the statistical error (under 5%) when compared to ones obtained from reference samples. Therefore, the UC process does not affect the impact properties of the final part.

6. Discussion

Evaluating the analytical model, the microscope image analysis and the experimental tests results, some discussions can be done on the advantages of the UC procedure over the properties of the CFRP laminates. The debulking procedure is a key step to reduce the porosity of the final part during the manufacturing of prepreg laminates. A low level of porosity is required when talking about composite materials, due to its strong relationship with the mechanical properties of the laminate. Indeed, a higher number of voids leads to the formation of discontinuity areas causing an intensification of the notch sensitivity and stress [13], that can in turn lead to the initiation of matrix crack and delamination in the voids locations [14].

Some numerical results were obtained from the proposed analytical model, from which it is possible to draw the following considerations. Firstly, it was shown that the flow rate of the interlaminar air generated by the ultrasonic waves is particularly efficient for air bubbles with small radius when compared to the one generated only by the vacuum pressure gradient. The analytical model also suggests that high levels of amplitude are required to obtain the maximum effect of the debulking procedure, while the optimal values of frequency are in the range of 20-60kHz. For high values

of frequency, there are no significant increments in terms of flow rate, while there would be an undesired increment of temperature in the material due to friction heat. In addition, some guidelines on the positioning of the ultrasonic transducer were provided.

Considering this concept and comparing the microscope image analysis results, it is possible to confirm the effective reduction of voids between layers hypothesized by the analytical model. Indeed, there is a substantial reduction in terms of voids projected area of the samples that increases with the UC exposure time from 0.52% of the reference sample down to 0.02% of the UC3 sample, leading to an improvement of 96%. These results suggests both a considerable reduction of voids content and a diffusion through the layers interfaces, confirming the hypothesis and results of the analytical model.

Experimental tests showed that the decrement in porosity leads to an increment of flexural modulus, with a value of +9% of the UC3 sample in comparison with the reference. It was also shown that the use of UC during the manufacturing process allows to preserve other mechanical properties of the material. Indeed, UC samples show similar values of flexural strength, strain at failure and Charpy impact strength when compared to the reference with percentage variations falling in the statistical error (see Table 4.4).

Based on these results, it is possible to consider 15 minutes (UC3 sample) as an optimal UC process time to obtain high mechanical properties in the final part during hand lay-up of prepreg material. These results, in conjunction with the ones obtained in the previous work [28], were it was proven a substantial increment in terms of ILSS (+26%) and a reduction of manufacturing time (over 85%) of the UC samples, prove the important advantages in the use of the UC debulking during the hand lay-up of prepreg materials.

Table 4.4 - Summary of percentage variation from reference of UC configurations

Reference % variation	Voids Content	Flexural modulus	Flexural strength	Flexural strain at failure	Charpy impact strength
UC1	-40%	0%	1%	1%	-3%
UC2	-54%	8%	2%	-5%	0%
UC3	-96%	9%	-1%	1%	4%

7. Conclusions

In this work, the ultrasonic consolidation debulking process and its advantages in voids removal during hand lay-up of prepreg materials were analysed. This study provided a deeper understanding of the procedure illustrated in the previous work [28], by developing an analytical model based on the study of the air flow between the prepreg layers, given by ultrasonic waves and vacuum pressure gradient, that allows for the optimisation of the process parameters.

The air flow between the prepreg layers was simulated as a peristaltic pump, where a flow is generated inside a pipe by the movement of the walls caused by the travelling wave. The pressure gradient given by the vacuum pump was also considered in the calculations. The model proved the efficiency of the UC in air removal and provided some practical guidelines to optimise the debulking procedure and how it is influenced by the procedure parameters such as frequency and amplitude. Numerical results showed that the use of ultrasonic waves not only increases the general air flow rate, but it is also particularly efficient in the removal of small radius air bubbles that cannot be removed by means of only vacuum pressure, leading to a significant reduction of the porosity in the final part in comparison with traditional debulking procedure.

Voids content was estimated via microscope images of sample sections, showing a significant decrement, up to 96% of projected area reduction in the UC3 sample. The results from the experimental tests showed an increment of flexural modulus of 8% for UC2 and 9% for UC3 samples and the absence of decrements in impact

properties in comparison with the reference. The manufacturing of the samples for the experimental campaign demonstrated the large reduction of debulking time (87% for UC3) that, together with the improvement of voids removal and mechanical properties of the part, constitute a fundamental improvement of the hand lay-up procedure for both research and industry sectors.

In conclusion, the study provided a deep understanding of the UC debulking phenomenon and investigated the effect of several process parameters (e.g., frequency and location of the transducer) on the porosity of the final part. The experimental results confirmed the reliability of the proposed process for the consolidation and debulking of prepregs, with a significant decrement in voids content and manufacturing time and increment in terms of mechanical properties.

References

- [1] Soutis C. Aerospace engineering requirements in building with composites. *Polym. Compos. Aerosp. Ind.*, Elsevier; 2020, p. 3–22. <https://doi.org/10.1016/b978-0-08-102679-3.00001-0>.
- [2] Breuer UP. *Manufacturing Technology. Commer. Aircr. Compos. Technol.*, Springer; 2016, p. 73–132.
- [3] Wilson AC, Us MA, Zhang H, Glazer SB. COMPOSITE TAPE LAYING APPARATUS AND METHOD 2016;2.
- [4] G.G. Liversidge J.F. Bishop, D.A. Czekai KCC. FIBER PLACEMENT MACHINE 1980;96:62–6. <https://doi.org/US005485919A>.
- [5] Elkington M, Bloom D, Ward C, Chatzimichali A, Potter K, Bloom D, et al. Hand layup : understanding the manual process Hand layup : understanding the manual process. *Adv Manuf Polym Compos Sci* 2015;1:138–51. <https://doi.org/10.1080/20550340.2015.1114801>.
- [6] Hancock SG, Potter KD. The use of kinematic drape modelling to inform the hand lay-up of complex composite components using woven reinforcements. *Compos Part A Appl Sci Manuf* 2006;37:413–22. <https://doi.org/10.1016/j.compositesa.2005.05.044>.
- [7] Kikuchi T, Hamada H, Nakai A, Ohtani A, Goto A, Takai Y, et al. Relationships between degree of skill, dimension stability and mechanical properties of composite structure in hand lay-up method. *ICCM Int. Conf. Compos. Mater.*, vol. 2013- July, Southampton, UK: CRC Press; 2013, p. 8034–42.
- [8] Jeong H. Effects of Voids on the Mechanical Strength and Ultrasonic Attenuation of Laminated Composites. *J Compos Mater* 1997;31:276–92. <https://doi.org/10.1177/002199839703100303>.
- [9] Judd NCW, Wright WW. Voids and their effects on the mechanical properties of composites- an appraisal. *Sampe J* 1978;14:10–4.
- [10] Yoshida H, Ogasa T, Hayashi R. Statistical approach to the relationship between ILSS and void content of CFRP. *Compos Sci Technol* 1986;25:3–18. [https://doi.org/10.1016/0266-3538\(86\)90018-7](https://doi.org/10.1016/0266-3538(86)90018-7).
- [11] Bowles KJ, Frimpong S. Void Effects on the Interlaminar Shear Strength of Unidirectional Graphite-Fiber-Reinforced Composites. *J Compos Mater* 1992;26:1487–509. <https://doi.org/10.1177/002199839202601006>.
- [12] Hancox NL. The effects of flaws and voids on the shear properties of CFRP. *J Mater Sci* 1977;12:884–92. <https://doi.org/10.1007/BF00540969>.
- [13] Anderson TL. *Fracture mechanics: fundamentals and applications*. 3rd Editio. CRC press; 2017.
- [14] Goodwin AA, Howe CA, Paton RJ. The role of voids in reducing the

interlaminar shear strength in RTM laminates. Proc. 11th Int. Conf. Compos. Mater. Compos. Process. Microstruct., vol. 4, 1997, p. 11.

- [15] Hex Ply Prepreg Tech. HexPly Prepreg. 2013.
- [16] Cha HR, Nakamura K. 3P-33 Analysis of Densification Mechanism under Ultrasonic Compaction Using Force Balance model. Proc. Symp. Ultrason. Electron., vol. 31, Institute for Ultrasonic Electronics; 2010, p. 521–2.
- [17] Khasanov OL, Dvilis ES. Net shaping nanopowders with powerful ultrasonic action and methods of density distribution control. Adv Appl Ceram 2008;107:135–41.
- [18] Tsujino J, Ueoka T, Suzuki H, Shinuchi S, Hashimoto K. Ultrasonic vibration press of metal and ceramic powders using complex vibration and vacuum condition. IEEE 1991 Ultrason. Symp., IEEE; 1991, p. 973–8.
- [19] Ning F, Cong W. Ultrasonic vibration-assisted (UV-A) manufacturing processes: State of the art and future perspectives. J Manuf Process 2020;51:174–90. <https://doi.org/10.1016/j.jmapro.2020.01.028>.
- [20] Eskin G, Eskin DG. Production of natural and synthesized aluminum-based composite materials with the aid of ultrasonic (cavitation) treatment of the melt. Ultrason Sonochem 2003;10:297–301.
- [21] Yang Y, Ram GDJ, Stucker BE. An analytical energy model for metal foil deposition in ultrasonic consolidation. Rapid Prototyp J 2010.
- [22] Rizzolo RH, Walczyk DF. Ultrasonic consolidation of thermoplastic composite prepreg for automated fiber placement 2016. <https://doi.org/10.1177/0892705714565705>.
- [23] Harras B, Cole KCC, Vu-Khanh T. Optimization of the Ultrasonic Welding of PEEK-Carbon Composites. J Reinf Plast Compos 1996;15:174–82. <https://doi.org/10.1177/073168449601500203>.
- [24] Lionetto F, Anna RD, Montagna F, Maffezzoli A. Modeling of continuous ultrasonic impregnation and consolidation of thermoplastic matrix composites. Compos PART A 2016;82:119–29. <https://doi.org/10.1016/j.compositesa.2015.12.004>.
- [25] Us MA, Thomson DT. Device for ultrasonically consolidating fiber reinforced composite structures 2003;2.
- [26] Attleboro N, Margaret E, Newton W, Woods JA, Us WA, Boyce JS, et al. Ultrasonic method of fabricating a thermosetting matrix fiber-reinforced composite structure and the product thereof, 2002.
- [27] Boyce JS. Method of fabricating a polymer-matrix fiber-reinforced composite and the product thereof 2003;2.
- [28] Flora F, Rizzo F, Pinto F, Meo M. Ultrasonic consolidation (UC) debulking of thermosetting prepreg for autoclave curing of composite laminates. Mater Today Proc 2021;34:106–12. <https://doi.org/10.1016/j.matpr.2020.01.376>.

- [29] Arafath ARA, Fernlund G, Poursartip A. Gas transport in preregs: model and permeability experiments. Proc 17th Int Conf Compos Mater 2009:1–9.
- [30] Farhang L. Void evolution during processing of out-of-autoclave prepreg laminates 2014:222.
- [31] Ganiev RF, Ukrainskii LE, Frolov K V. Wave mechanism for the acceleration of a liquid flowing in capillaries and porous media. Sov. Phys. Dokl., vol. 34, 1989, p. 519.
- [32] Aarts ACT, Ooms G. Net flow of compressible viscous liquids induced by travelling waves in porous media. J Eng Math 1998;34:435–50. <https://doi.org/10.1023/A:1004314014329>.
- [33] Yin F, Fung YC. Peristaltic Waves in Circular Cylindrical Tubes. J Appl Mech 2011;36:579. <https://doi.org/10.1115/1.3564720>.
- [34] Tuchinsky PM. Poiseuille's law. Modul. Appl. Math. - Vol. 68, 1976.
- [35] Hsiao K. Gas Transport And Water Vapourization in Out-of-Autoclave Prepreg Laminates 2012.

5. Paper 3: Real-time thermography system for composite welding: undamaged baseline approach

As highlighted in chapter 2, CFRP materials are particularly sensitive to manufacturing defects. The presence of discontinuities in the material, such as voids or other unwanted inclusions, can decrease the failure resistance of the component, creating points of stress densification and crack initiation. This is true for any component made of CFRP material, such as sandwich skins and core. If from one side it is important to provide novelties in manufacturing techniques able to reduce the amount of defects, such as the one proposed in chapter 3 and 4, it remains impossible to totally avoid them. Based on this, the need of non-destructive evaluation (NDE) techniques able to detect damages in the parts during the manufacturing of the same is increasing, particularly for highly automated systems.

In this contest, the work described in the publication of this chapter provide a technique able to improve the damage detection during automatic CFRP manufacturing systems based on heat sources, such as automatic welding, automatic tape placement and automatic fiber placement.

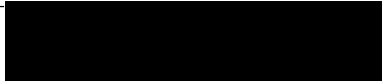
The NDE technique described here take advantage of the heat source to provide information about anomalies in the heat field during the automatic process, providing *real-time* feedback to the manufacturing process. The system relies on infrared active thermography inspections based on an undamaged baseline methodology to detect the damages. The undamaged baseline is built on the numerous data that can be recorded during automatic systems, therefore improving time by time the sensibility of the apparatus to the presence of anomalies in the process. The system has been experimentally realised and tested on an automatic induction welding system. The experiments were conducted on thermoplastics matrix composites with several typologies and dimensions of inducted process

defects, showing the efficiency of the methodology in identify the shape and location of the damages.

Given the flexibility of the technique to be applied to any kind of heat source-based manufacturing process, this work provide an important contribute to the word of automatic production of composite panels, cores and sandwich structures, allowing the reduction of costs and premature failures of parts due to manufacturing defects.

The Statement of Authorship Form and the paper can be found next.

This declaration concerns the article entitled:	
Real-time thermography system for composite welding: undamaged baseline approach	
Publication status (tick one)	
Draft manuscript	
Submitted	
In review	
Accepted	
Published	✓
Publication details (reference)	
Flora, F., Boccaccio, M., Fierro, G. P. M., & Meo, M. (2021). Real-time thermography system for composite welding: Undamaged baseline approach. <i>Composites Part B: Engineering</i> , 215, 108740.	
Copyright status (tick the appropriate statement)	
I hold the copyright for this material	✓
Copyright is retained by the publisher, but I have been given permission to replicate the material here	
Candidate's contribution to the paper (detailed, and also given as a percentage)	
The candidate contributed to/ considerably contributed to/predominantly executed the...	

Formulation of ideas:	80%	I provided most of the idea, the hypothesis, the methodology and the experimental tests, in collaboration with my fellow Fierro.	
Design of methodology:	90%	I realised the experimental machine for automatic induction welding and <i>real-time</i> NDE, in collaboration with my fellow Boccaccio. I manufactured all the samples used in the experimental campaign. My fellow Fierro contributed in the realisation of the code for the <i>real-time</i> data processing.	
Experimental work:	100%	I carried out all the experimental tests and collected all the data.	
Presentation of data in journal format:	80%	I designed the manuscript structure, wrote the drafts and realised all in collaboration with fellows Boccaccio and Fierro. My supervisors provided feedback on the draft and help for the paper review and submission.	
Statement from Candidate			
This paper reports on original research I conducted during the period of my Higher Degree by Research candidature.			
Signed			Date 29/01/2022

Real-time thermography system for composite welding: undamaged baseline approach

Francesco Flora¹, Marco Boccaccio¹, Gian Piero Malfense Fierro¹, Michele Meo*¹

¹ *Department of Mechanical Engineering, University of Bath, Bath, Ba2 7AY, UK*

* Corresponding author: m.meo@bath.ac.uk

Keywords: *Welding; Thermography; Thermoplastic.*

Abstract

The aerospace industry's current focus on recyclable materials and low-cost processes has accelerated research and implementation of thermoplastics matrix composites (TPC). In the last decades, researchers have researched weldability of these materials as a valid alternative to conventional mechanical fastening and adhesives, for improving the strength of the joint. Automatic induction welding of carbon fiber TPCs is one of the most promising techniques due to its numerous benefits, such as elevated energy efficiency and highly localised heat. As for all the manufacturing techniques, the importance of efficiently detecting the presence of defects during TPCs welding has pushed the need for automated *real-time* non-destructive evaluation (NDE) systems. This paper focuses on the development of an efficient NDE technique able to detect the presence of alterations and defects in *real-time* during the welding process. This technique relies on Infrared (IR) active thermography inspections performed using the induction welding heat as the source and an undamaged baseline methodology to detect differences in the heat field. The procedure was experimentally analysed by means of an apparatus capable of automatic welding of samples, performing the *real-time* NDE during the process. Results show the efficiency of the method to localise the damaged area and characterise the defects during the welding. The undamaged baseline methodology was proven to better clarify shape and location of defects, allowing for an efficient detection of damaged samples and areas where more detailed inspections can be performed after the welding process by means of the same IR apparatus.

1. Introduction

Recent interest of industries (such as aerospace and automotive) in new materials like carbon fiber reinforced polymers (CFRPs) has led to the development of advanced automated manufacturing systems. Some examples are automated fiber placement (AFP), automated tape placement (ATP) and automated welding systems [1].

The welding process, also known as fusion bonding, is one of the main advantages in the use of thermoplastic composites (TPCs) materials, where the material temperature is increased above the matrix melting point and joined to other parts. Automated welding processes produce high strength joints, without altering the structural integrity of the parts, as in the case of mechanical fastenings. Da Costa et al. [2] published a review on the welding techniques available for TPCs, differentiated by the heat source: ultrasonic, induction, microwave, resistance, hot plate, IR and laser welding are some of the most common. Particular interest is growing in research regarding induction welding, which involves the generation of heat by means of eddy currents generated at the welding interface using a high-frequency magnetic field, efficiently producing high quality joints between the composite and other thermoplastic [3,4] or metallic [5,6] materials. However, welded components need to be checked, particularly in critical application where weld failure can be fatal, such as nuclear field, power plants, pressure vessels and load-bearing structural component [7–9]. Indeed, the presence of a damage in the welded area may lead to a strong reduction of the joint strength, and thus a catastrophic premature failure of the final part. Thus, the importance of efficiently detecting the presence of defects during TPCs welding has pushed the need of automated non-destructive evaluation (NDE) systems.

Non-destructive testing (NDT) techniques have been developed over the years in many engineering processes as a powerful tool to reveal presence of damage in materials without affecting the structural and chemical properties of the inspected component. Conventional NDT methods used in industry for damage detection generally include liquid penetrant, magnetic particle, and phased-array ultrasonic

testing [10–12]. However, these techniques are based on contact inspections, thus representing a limitation where material contamination with coupling medium or contact sensor is prohibited. Nonlinear air-coupled ultrasound [13], radiography [14], and eddy current testing [15] provide non-contact inspections where coupling liquid are inappropriate, e.g. in such engineering processes where contact technique or immersion may not be practical, or, where water can affect the property of the material being inspected, such as reinforced plastics, electronic-packaging materials, wood, or stainless steel [8,16–19]. However, the above-mentioned technique generally requires voluminous equipment and time-consuming data processing and cannot be implemented in the welding apparatus to have a real-time evaluation of the inspected part. Therefore, there is need of an automatic NDE technique capable of performing damage evaluation of the joint during the welding procedure. Active infrared (IR) thermography techniques are widely used for surface and internal damages in many engineering contexts, in both military and civil engineering [20–22]. An IR-camera is employed to detect any non-uniform heat distribution along the surface of the sample, subjected to heat source or ultrasonic excitation [23,24]. In the case of induction welding of TPCs, *real-time* thermography NDE of the welding line is a possible solution for detection of damages in the part, but it is limited by the heterogeneity and intensity of the heat field. In addition, most of the defects, such as delamination at welding interface, are parallel to the eddy current field, thus not creating a significant interference in the heat generation [25,26]. Indeed, induction heating of CFRPs is based on the flow of an electric current through closed carbon fiber loops. Given that the density of closed loops of carbon fibers may substantially vary through the thickness of the part, CFRP is a highly inhomogeneous conductive material when compared with metals [27].

Many studies about eddy current testing (ECT) can be found in literature, which is a damage localisation technique based on detecting alterations in eddy currents induced in the part. De Goeje *et al.* [26] studied the influence of fiber orientations and process parameters on the ECT in creating C-scan images, highlighting its limitations and differences between unidirectional and weave reinforcements.

Koyama et al. [27] illustrated some of the problems relating to the use of ECT for CFRPs, proposing some inspecting probes able to efficiently detect the damages in the part. A strong limitation of these probes relies on the optimisation needed to be designed in function of part and material. He et al. [28] investigated the use of eddy current pulsed thermography for NDE of impacted CFRP using probes in reflection and transmission modes, obtaining the best results with the last. Heuer et al. [29] provided a detailed study on the efficiency of high frequency ECT system in detection of different material properties and defects, with the possibility of integrating the NDT system into some manufacturing processes for thermoset composites. Another example of integrated ECT system is the one proposed by Fierro et al. [30], where a thermography induction NDT system was used during automated fibre placement (AFP) process while principal component analysis (PCA) of the raw thermal images was conducted, obtaining clear images of typical damages. In a previous work, Flora et al. [31] provided an experimental study about a *real-time* thermography system during induction welding, which was able to detect damage in samples, but required further NDE analysis for the complete characterisation of the defects due to the inhomogeneities in the heat field.

Generally, the system and its parameters used for ECT NDE thermography of composite materials need to be customised for the specific part in order to overcome the natural inhomogeneities in the heat field and detect the real defects. This optimisation becomes more complicated when NDE is needed *in-situ* and *real-time* during automated induction processes, such as induction welding. Indeed, the parameters used for the welding process, such as frequency, movement speed, coil shape and position, may be far from the ones optimised for the NDE.

This work is focused on the development of a technique aimed to solve these limitations, easing the implementation of NDE thermography system to a general automated induction process. The technique is based on the building of an undamaged baseline that, coupled with the repeatability of the automated process and parameters, allows for the building of a thermographic image of the part and efficiently detect large and small variations in the heat field. Indeed, automated

induction welding machines designed for large-scale productions can weld with a rate up to 150 parts per minute [32]. Based on this it is possible to timely identify damaged parts and alterations in the system components, allowing for a prompt adjustment of the manufacturing line and reduction of the rejected parts, leading to large cost saving. The proposed system is able to detect discrepancies in the process automatically, highlight the defected part and perform a local *post-welding* thermography scan in an automatic manner, without the intervention of the manual operator. In order to experimentally prove the efficiency of the technique, the NDE thermography system is combined with an automated induction welding process composed of an induction coil and a pressure roller connected to a gantry system. Samples were welded using Titanium and TPCs parts, and some of the typical defects for this kind of process were simulated between the parts. Thermal data was recorded during the process using IR cameras and an algorithm was used to automatically allocate them in time and space, leading to a 3D thermal data matrix. Thermal images were obtained by characterising the thermal intensities (T_I) in three different features (depth, width, aggregate integrations) and subtracting the undamaged baseline, which was built scanning three undamaged samples. Results show the improvements provided using the undamaged baseline in the defect localisation, sizing and clarity when compared to traditional thermography-based analysis.

2. Induction heating

Induction heating is a well-established method for generation of heat in magnetically susceptible and electrically conductive material. Applying an alternate current to a coil made of a conductive material (induction coil), a time variable magnetic field with the same frequency is generated in the area around it. When the conductive part is placed into this primary magnetic field, eddy currents are generated through the material, which themselves generate heat, mainly due to Joule losses, and a secondary magnetic field. This phenomenon, illustrated in Figure 5.1, can be used for NDE of the parts by means of thermographic image

analysis or using probes, usually a secondary coil, able to detect the properties of the secondary magnetic field, and thus identifying eventual alterations. In addition, the generated heat can be used to melt the part and weld it to other materials, such as in the case of induction welding of TCPs.

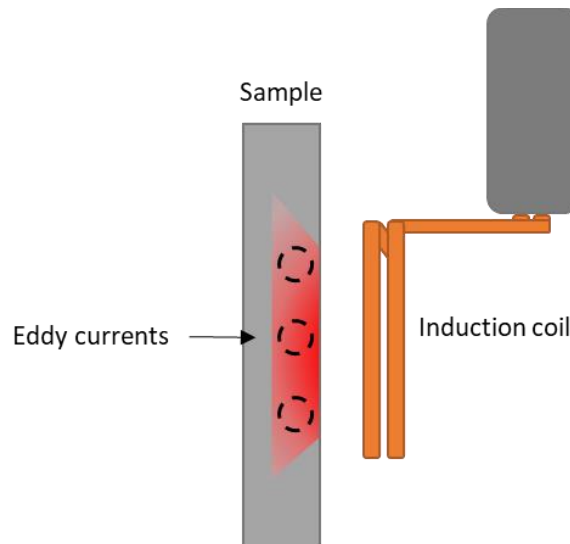


Figure 5.1 - Induction heating process

Eddy currents need closed-loop of conductive material in order to be generated. This is easy for a homogeneous conductive material, such as metals, where every section of the part is itself a closed-loop. Indeed, induction heating and welding was originally widely used for metals [33]. Only in the last decades this technique was extended to other materials such as CFRPs, with thermosetting or thermoplastic matrix, where the carbon fiber reinforcement plays the role of the magnetically susceptible and electrically conductive component. Given the heterogeneity of composite materials, the presence of carbon fiber closed-loops is not always guaranteed. An example is the unidirectional laminate, where all the reinforcement is aligned in one direction, thus not creating enough contacts to generate a significant quantity of eddy currents [34]. For induction welding, in the cases where the parts themselves cannot be heated by generation of eddy currents, heating elements sensible to the magnetic field are inserted at the welding interfaces in order to generate the heat [35].

When the part is immersed in the magnetic field generated by the coil, the eddy currents tend to flow along the surface rather than through the depth and dissipates quickly. This so-called “skin effect” is usually measured with the standard depth of penetration δ , that is the point in depth where eddy current field is decreased by the quantity $1/e$ (approximately 37%) [36]. This quantity is a function of the current frequency f and the electrical conductivity σ , and magnetic permeability μ of the material as given by the following equation.

$$\delta = \sqrt{\frac{1}{\pi\sigma\mu f}} \quad (1)$$

The frequency of the eddy currents is the same as the alternating current induced in the induction coil. Therefore, the eddy current field increases with the frequency following the Faraday’s law of induction states [29]. For materials with low electrical conductivity, such as CFRPs, high frequencies are needed to generate a significant amount of eddy currents and, thus, of heat. Despite the high values of frequency (f), the value of δ is maintained relatively high enough thanks to the low electrical conductivity (σ) of the material, generating eddy currents in depth.

The heated sample acts as an ohmic resistor, therefore the induced current, and thus the heat, is proportional to the generated power, defined by the following formula [34]:

$$P = \frac{(2\pi f\mu HA)^2}{R} \quad (2)$$

where H the magnetic field intensity, A the sectional area and R the resistance of the conductive material. From equations (1) and (2), the intensity and depth of the heat, for both welding or NDE purposes, is a function of several factors: frequency of the magnetic field, coil geometry and distance, sample dimensions and material properties. The optimisation and design of the induction system is complicated due to the non-linear relation between these parameters and is therefore unique for each application, making the combination of manufacturing and NDE processes a challenge.

3. Thermal data analysis

Infrared (IR) active thermography is a NDE technique widely used for damage detection in structures and materials in many sectors, such as aerospace, civil engineering and military [20,22,24,37]. IR techniques generally require an external energy source to induce a gradient of temperature within damaged and undamaged areas in the inspected component. As regards induction heating, damage detection relies on the change in the distribution of locally induced eddy currents due to damage region, thus leading to a higher heat generation near the cracks [38,39].

In this context, heat diffusion through a solid represents a three-dimensional problem which can be modelled by Fourier's heat equation [40]:

$$\nabla^2 T = \frac{1}{\alpha} \frac{\partial T}{\partial t} \quad (3)$$

Where T and t denote the temperature and time variables, respectively, $\alpha = k/\rho c_p$ is the thermal diffusivity of the inspected material, k is the thermal conductivity, ρ and c_p represent the density and the specific heat at constant pressure, respectively. A one-dimensional solution of equation (3) in a semi-infinite isotropic and homogeneous solid can be evaluated for the propagation of a Dirac heat pulse, which represents an ideal waveform defined as an instantaneous and intense unit-area pulse. The solution is given by:

$$T_i(z, t) = T_i(z, t = 0) + \frac{Q}{\sqrt{kc_p \rho \pi t}} e\left(-\frac{z^2}{4\alpha t}\right) \quad (4)$$

Where Q is the energy absorbed by the surface and z is the space variable through the sample thickness. A Dirac heat consists of periodic wave containing all the frequencies and amplitudes, and such a waveform cannot be reproduced. In practice, a heat pulse generated by a photographic flash or an induction coil has approximately a square shape. With this regard, the signal is a periodic wave with several frequency harmonic components, depending on the pulse duration. Indeed,

the shorter the pulse, the broader the frequency range. At the surface (i.e. $z = 0$), equation (4) can be written as follows:

$$T_i(z = 0, t) = T_i(z, t = 0) + \frac{Q}{\sqrt{kc_p\rho\pi t}} \quad (5)$$

Although equation (5) only represents an approximated solution of the complex 3-D Fourier's law in equation (3), several pulsed thermography-based processing techniques rely on this simplification to perform quantitative and qualitative analysis [41–43]. The second term of equation (5) quantifies in-time thermal distribution across the sample, which can be used to conduct NDE thermography investigations.

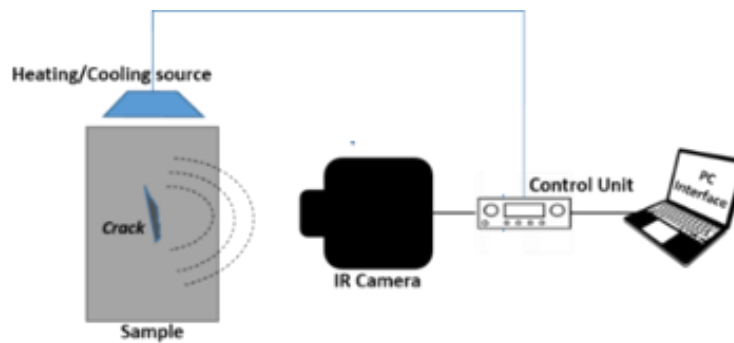


Figure 5.2 - Infrared active thermography general setup

Data acquisition and experimental setup of a general NDE thermography procedure are shown in Figure 5.2. The sample is subjected to a heat source, which in this work is Joule losses due to the eddy current generated by the induction coil. The heat field reflects the shape of the induction coil, which is of hair pin type, and is also influenced by the conductive properties of the material. As time elapses, the thermal front travels within the sample, and the superficial temperature will decrease nearly uniformly. Contrarily, subsurface inhomogeneities behave as a resistance to heat flow which produces anomalous temperature distributions at the surface.

In this work, during the process, IR cameras move with the welding system, recording images (frames) of a part of the heated sample, each of them representing the thermal status of a specific area and time. Thermal data were analysed in a

similar manner highlighted in previous works [30,31]. Knowing the position along the welding line and recorded time of each frame, it was possible to build the structure of the thermal data in space and time.

Indeed, given that a frame is a $M \times N$ matrix of pixels, and thus thermal data, of the sample, it is possible to overlap the images aligning the pixels relative to the same point in space at different times. The image relative to the part of the sample that was not recorded by the cameras at each time were filled with zeros, obtaining $M \times N'$ matrixes of thermal data of the sample. Figure 5.3 illustrates the recording of the thermal images during the welding process at three different points in time.

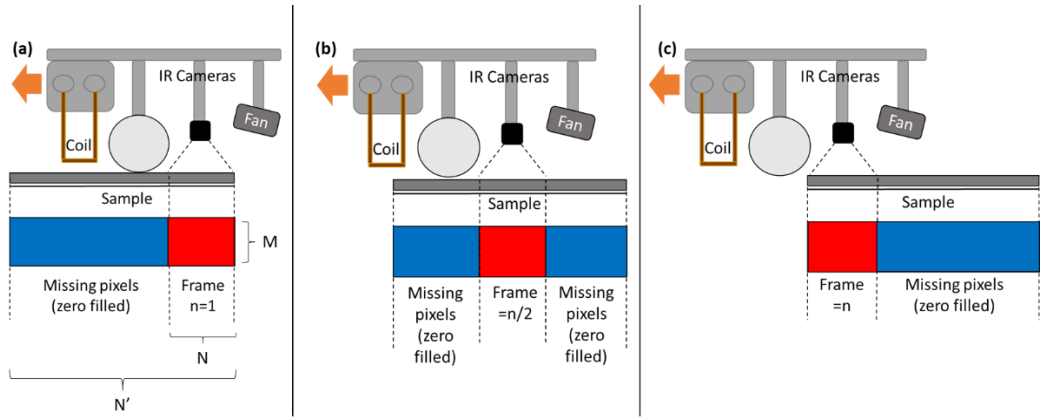


Figure 5.3 - Thermal images capturing process at the beginning (a), middle (b) and end (c) of the welding line.

$$dT_I(x, y) = \sum_{t=1}^n T_I(x, y, t) \quad (6)$$

Stacking all the frames, which total number n depends on the moving velocity of the system and the frame rate of the cameras, a 3D matrix of thermal data is obtained, where the third dimension represents the number of frames, and thus the time t . The other two dimensions of the thermal intensity T_I 3D matrix represents the two directions of each frame, labelled here as x and y , and can vary from 0 to N' and M , respectively. Summing the values in the T_I 3D matrix along the time, one obtains a final thermal image (dT_I 2D matrix) of the sample, as described by

equation (6). The building of the thermal data matrix and final image is illustrated in Figure 5.4.

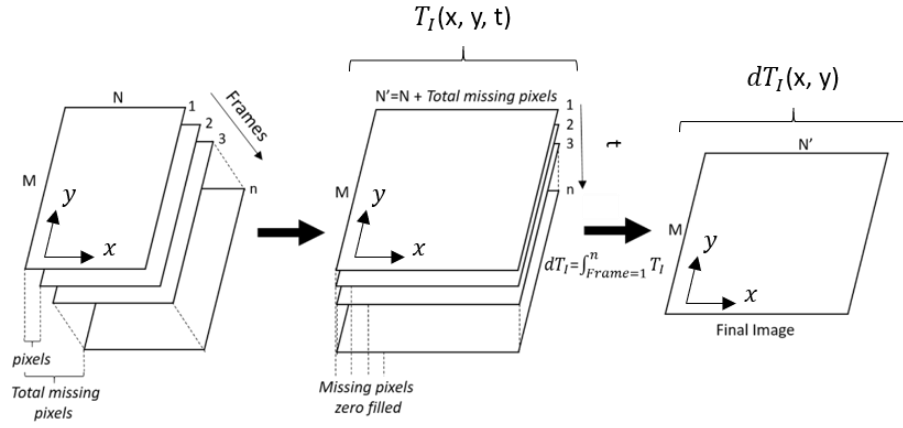


Figure 5.4 - Summary of thermal image processing and building of T_I 3D matrix and dT_I image.

$$wT_I(x, t) = \sum_{y=1}^M T_I(x, y, t) \quad (7)$$

$$aT_I(x) = \sum_{t=1}^n wT_I(x, t) \quad (8)$$

The high repeatability of the welding process allows for further simplification of the process used for analysis of the thermal images illustrated in Figure 5.4. Figure 5.5 illustrates the calculation process applied to obtain width [wT_I , (b)] and aggregate T_I [aT_I , (c)] images. The term wT_I was calculated by summing over the width y of the frame stack, as described in equation (7), providing a final image of the T_I through the depth t and length x of the sample. The aT_I provides a single line plot of the aggregate intensity values by integrating over the number of frames t of wT_I , as described in equation (8).

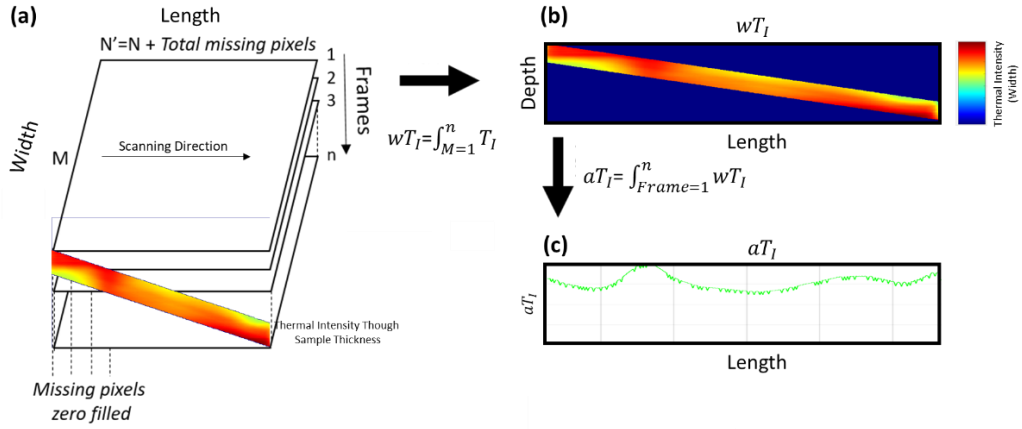


Figure 5.5 - Processing of thermal images using the frame stack (a), thermal intensity over the width (b) and the final aggregate thermal intensity (c)

Induction welding of TPCs is characterised by high repeatability for a given set of samples. The technique proposed in this work relies on the process repeatability, aiming to detect any kind of alteration in the heating field. With this regard, the baseline was built by welding and testing a set of undamaged samples. The undamaged results in terms of dT_I , wT_I and aT_I values were subtracted from the ones obtained from tested samples, thus highlighting any variation in the heat field during the welding, as illustrated by the following equations:

$$dT_{I_{sub}} = dT_I - dT_{I_{undamaged}} \quad (9)$$

$$wT_{I_{sub}} = wT_I - wT_{I_{undamaged}} \quad (10)$$

$$aT_{I_{sub}} = aT_I - aT_{I_{undamaged}} \quad (11)$$

4. Experimental setup

In order to simulate the automatic induction welding process, the same system showed in [31] and illustrated in Figure 5.6 was used. The system, consisting of an induction coil, compression roller, IR cameras and a cooling fan attached to a gantry

system, is able to pass over the samples and in order heat up, compress and cool down the two welding parts. The velocity used for the system and all its components is 6 mm/min. The induction heating system consists in an Ambrell® EasyHeat Induction Heating System 0224, with a maximum power of 2.4 kW and frequency in the range of 150-400kHz. The induction coil is made of a copper tube with 8 mm outside diameter and is of pin type shape, with a length of 150 mm and an internal distance of 10 mm (see number 1 in Figure 5.6). The pressure was applied using 50 mm diameter PTFE roller attached to two steel springs of a known elastic spring constant. The applied force was controlled during the process by measuring springs displacement and adjusting the pre-compression nuts. To record the thermal data during the process, two IR cameras (FLIR Lepton 3.12 μm , array format 160x120 pixels, frame rate 8.7 Hz, thermal sensitivity <50 mK) were used for the *real-time* scanning of the samples after the compression, for a total of 280 frames recorder for each sample. A fan was attached pointed towards the area after the compression in order to provide a fast cooling down of the samples, that gives benefits for both the welding process and the NDE analysis. Indeed, after the compression and welding of the part, the thermoplastic matrix needs to return below the crystallization temperature to avoid decompaction and delamination. On the other side, according to equation (3), the introduction of a cooling step after heating/welding increases the instantaneous temperature gradient (i.e. $\partial T/\partial t$), thus enhancing thermal imaging resolution [44].

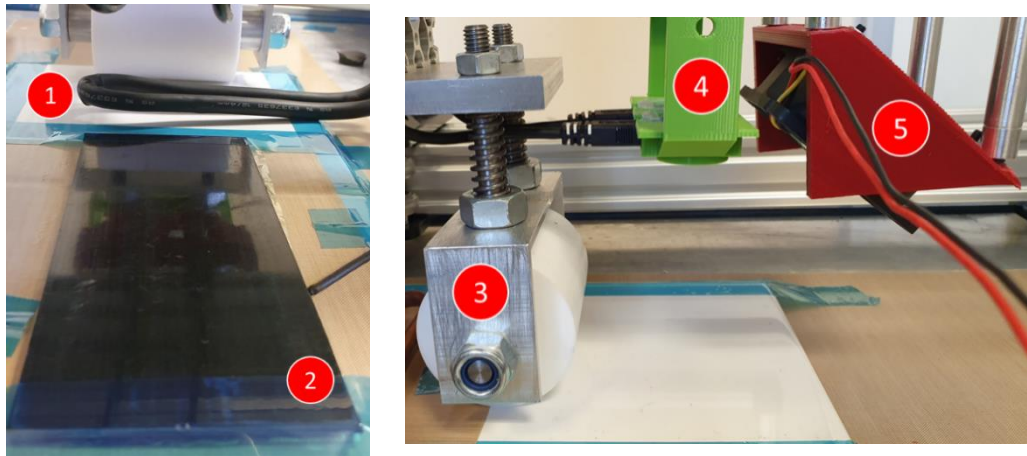


Figure 5.6 - Welding system: induction heating coil (1); PA6-Ti sample (2); PTFE pressure roller (3); rear IR cameras (4); cooling fan (5) [30]

The welding tests were performed between TPCs and Titanium samples. In order to have a comparison with similar tests performed without the undamaged baseline, samples with the same layout as the ones used in a previous work [31] were used: 150x65 mm samples manufactured using SGL Carbon[®] UD carbon fiber-reinforced PA6 laminates (2 mm thickness) and Ti 15-3-3-3 foils (0.1 mm thickness). The induction field was generated using a current of 151.2 A and a frequency of 290 kHz, while a force of 60 N was applied to the samples. The welding parameters were selected during a preliminary experimental campaign in order to provide the right temperature and pressure at the interface between the titanium foil and the TPC sample, without overheating and damage the material. In order to prove the reliability of the system for damage detection, four samples were tested, outlined in Table 6.5 and Figure 5.7. The first sample is an undamaged sample; therefore, the results are expected to show the absence of defects. The other three sample present different kind of defects: foam and titanium inserts with different dimensions, a hole and a wrinkle in the titanium foil. In the last sample, different damages were added in sequence to make the characterisation more complicated. Indeed, every damage creates alteration in the eddy currents that could lead in a strongly deformed heat field, hiding the presence of more than one defect.

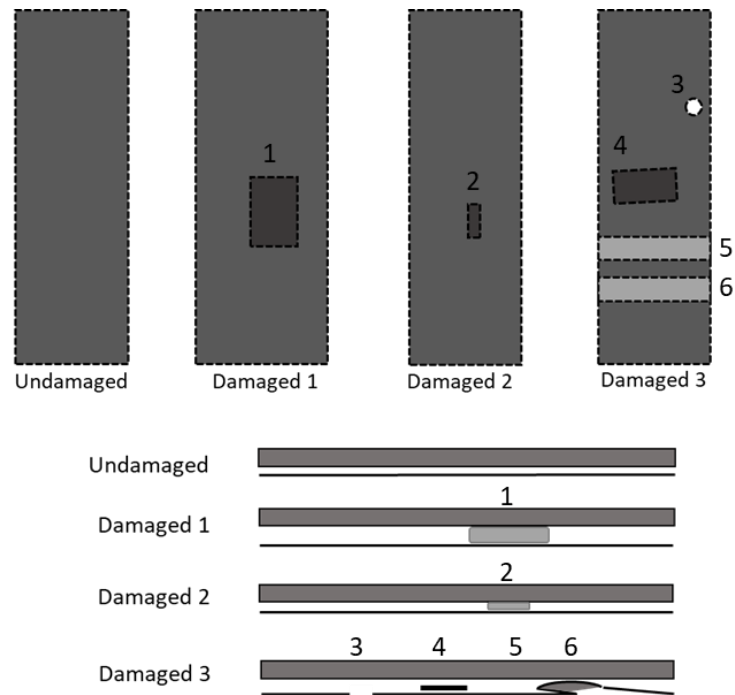


Figure 5.7 – Samples damage configuration [31]

Table 5.1 - Samples nomenclature and damage dimensions

<i>Sample</i>	<i>Damage</i>	<i>Dimensions</i>	<i>Label</i>	
<i>Undamaged (UD2)</i>	Undamaged	-		
<i>Damaged 1 (D1)</i>	Foam patch	10x20x10 mm	1	
<i>Damaged 2 (D2)</i>	Foam patch	10x10x3 mm	2	
<i>Damaged 3 (D3)</i>	Hole	5 mm diameter	3	
	Ti patch	20x30x0.1 mm	4	
	Wrinkle	Air gap	10x65 mm	5
		Overlap	10x65 mm	6

During the tests, the system recorded and analysed the thermal data in *real-time* using the algorithm previously described. If an alteration is detected, the sample can be recognised as damaged by the system analysing the difference from the

undamaged results and flagging values over a defined threshold, in particular for the aT_I profiles. In function of the dimensions of the sample, and therefore the amount of data to be analysed, and the computational capabilities of the computer, the analysis can take from just a few seconds up to some minutes. In the case of the samples and system used in this work, the analysis took around 45 seconds for each sample.

5. Results and discussion

The first tests were performed on three undamaged samples in order to build the undamaged baseline (UD). The integrity of the samples was double checked by using ultrasonic C-Scan, in order to verify the absence of unexpected defects such as delamination. In order to prove that the subtraction method recognised the absence of defects, an additional undamaged sample (UD2) was inspected. Thermal images were recorded and evaluated during the process.

Figure 5.8a and Figure 5.8b show dT_I images for the baseline and the undamaged samples respectively. As shown in Figure 5.8, the heating field is not uniform in both cases, especially between the central area and the edges, but the heating hotspots and patterns between the two images clearly match. After subtraction, variability between the values of dT_I was very low, as expected. The subtracted values of dT_I allows the building of a final thermal image (Figure 5.8c) that clearly shows the absence of alterations in the heat field.

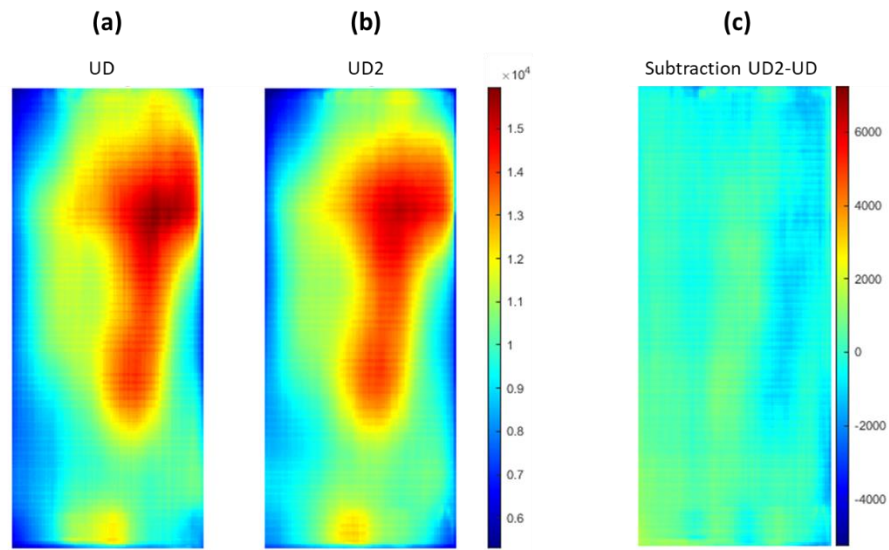


Figure 5.8 - Thermal dT_I images for undamaged baseline (a), undamaged sample (b), baseline subtraction $dT_{I_{sub}}$ (c).

Figure 5.9 shows the wT_I (a-b) and aT_I (c-d) responses for the baseline and the undamaged sample, with the direct comparison highlighted in (e). The abscissa in the graphs corresponds to the sequential number of the recorded frame, and therefore the position along the sample length. There are marginal differences between the two undamaged cases (UD and UD2), and the subtracted aT_I line plot results in an almost flat response. This indicates that there is no significant difference between the welding and material integrity of these two samples. The propagation of thermal waves across discontinuities (defects) results in varied heat field of inspected samples in that region. This variation should be clear when compared with a baseline (defect-free) measurement, with the results highlighted in the following sections.

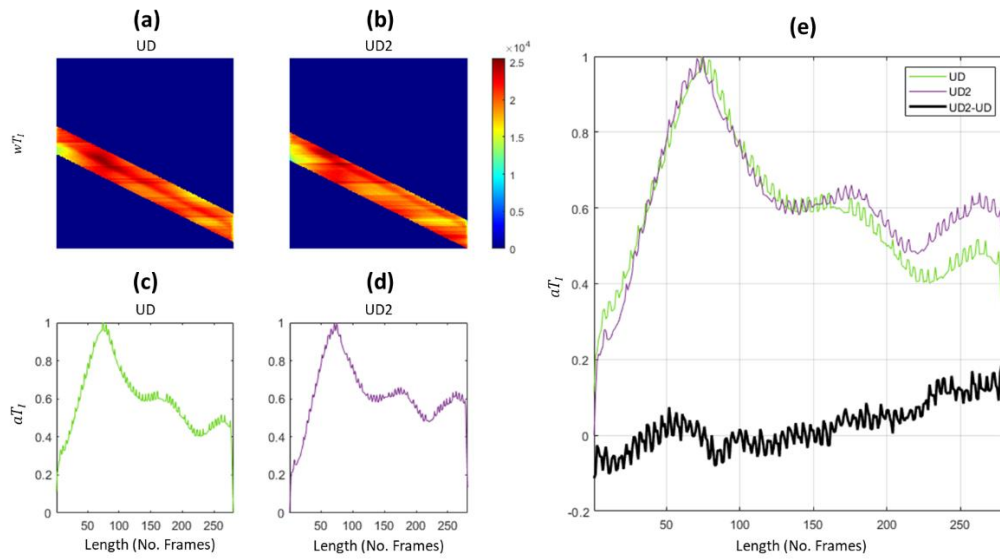


Figure 5.9 - wT_I for UD1 (a), wT_I for UD2 (b), aT_I for UD1 (c), aT_I for UD2 (d), $aT_{I_{sub}}$ (e).

Following the same procedure and parameters used for the undamaged samples, D1 damaged sample was welded, *real-time* recording thermal data from the welding line. The resulting thermal dT_I image of the sample D1 is shown in Figure 5.10b, where an irregularity in the heat distribution is already visible. Defect location and shape become clearer when the subtraction of the undamaged baseline (a) is applied, obtaining the image in Figure 5.10c.

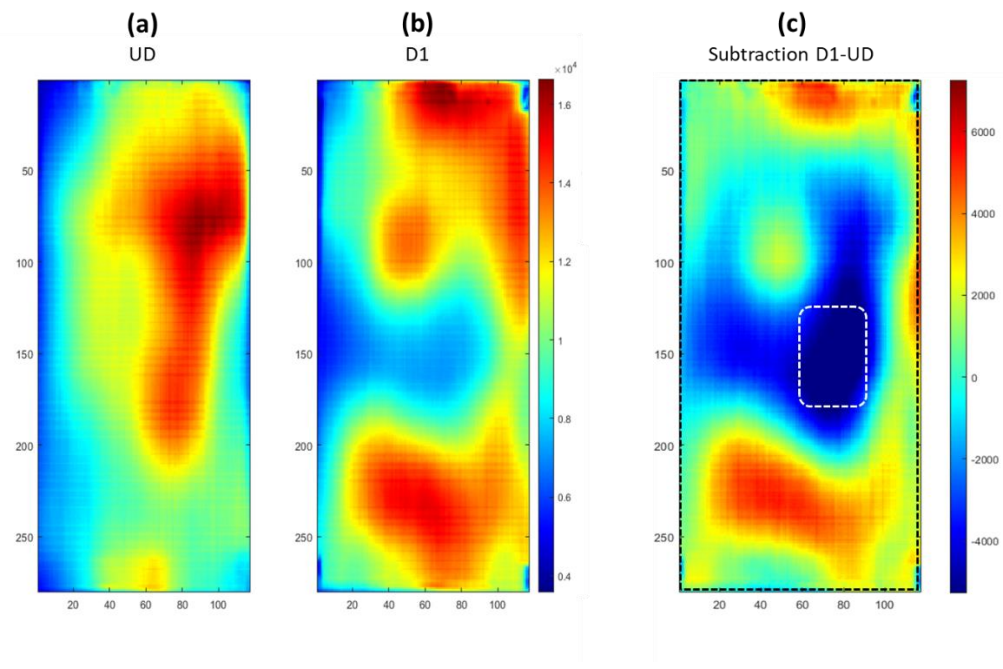


Figure 5.10 - Thermal dT_I images for undamaged baseline (a), damaged sample D1 (b), baseline subtraction $dT_{I_{sub}}$ (c).

Figure 5.11 shows the wT_I (a-b) and aT_I (c-d) calculations for the baseline and damaged samples. The comparison and subtraction of the two aT_I line plots (e) identify the location of the damage along the sample, highlighted in the plot. A visual representation of the sample and damage was added at the bottom part of the plot to show the accuracy of the technique. The results in both Figure 5.10 and Figure 5.11 show an accumulation of heat towards the top and bottom of the D1 sample. This is probably due to the fact that the heat generated in the titanium foil is shielded by the large foam, accumulating in the area before and after the damage.

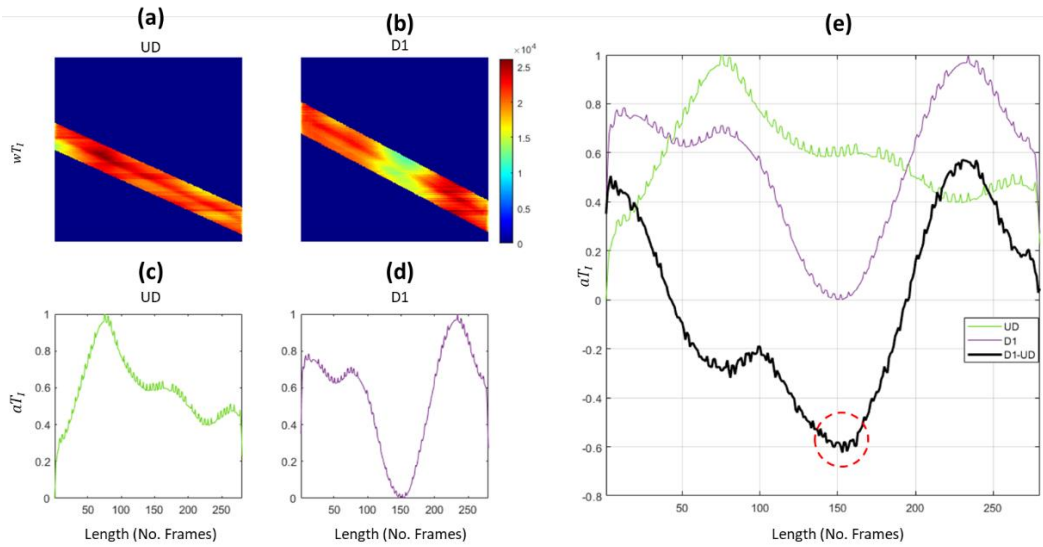


Figure 5.11 - wT_1 undamaged baseline (a), wT_1 image for D1 (b), aT_1 undamaged baseline (c), aT_1 profile for D1 (d), aT_1_{sub} (e).

Figure 5.12 shows thermal images from the welding of sample D2, which present the same kind of defect of the D1 sample but of a considerably smaller size. As shown in dT_1 image of the D2 sample (b), damage affects heat profile at different points. In Figure 5.12c related to the subtraction image, damage creates a colder area in the centre of the sample, dissipating the heat and thus creating hot spots in the area around it.

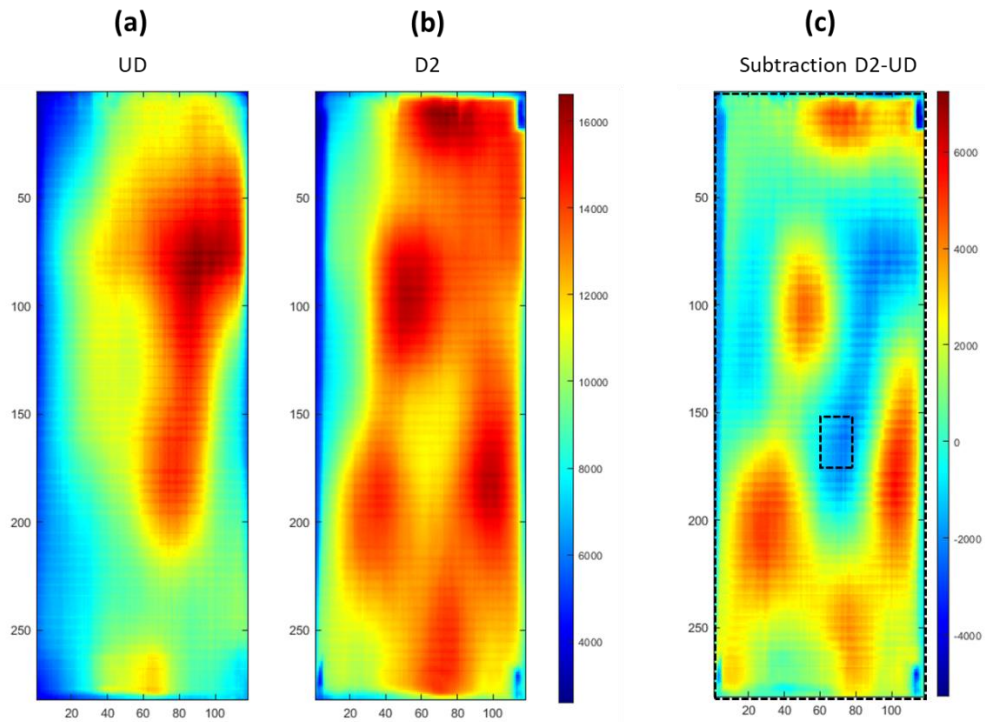


Figure 5.12 - Thermal dT_I images for undamaged baseline (a), damaged sample D2 (b), baseline subtraction $dT_{I_{sub}}$ (c).

Figure 5.13 shows the wT_I (a-b) and aT_I (c-d) responses for both UD baseline and D2 sample. The difference between the two aT_I curves, highlighted in the plot (e), is far from being flat, thus indicating presence of defects. The damage location corresponds to the non-zero values highlighted (1) in the curve. In addition, a second peak (2) was detected, thus suggesting the presence of a second damaged area. This area was successively linked to an unwelded part of the sample by visual inspection of the welded area. In this second sample, the damage is difficult to be distinguished, due to the smaller size of the defect and the generation of numerous secondary alterations in the heat field and the second unexpected defect (unwelded zone). However, from the analysis of the difference with the UD results, it is possible to determine the presence of defects in the sample, thus flagging it as damaged, which is the main aim of the technique.

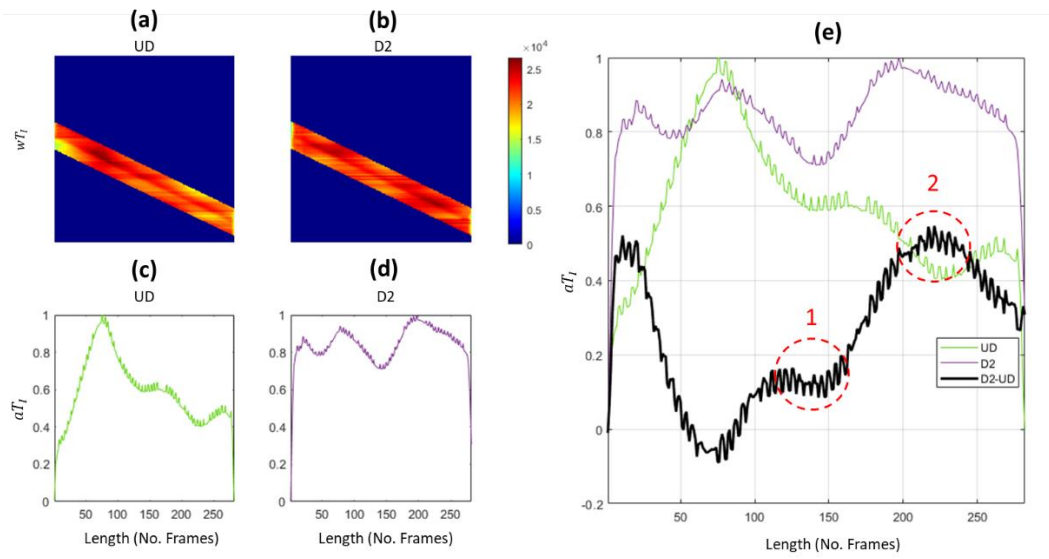


Figure 5.13 - wT_I undamaged baseline (a), wT_I image for D2 (b), aT_I undamaged baseline (c), aT_I profile for D2 (d), $aT_{I_{sub}}$ (e).

As described in the previous section, sample D3 presents three defects: a hole in the top part of the Ti foil, a titanium patch and a foil wrinkle. The scope of inspecting multiple defects in the sample is to test the efficiency of the undamaged baseline technique in the detection of more complex and overlapping discontinuities in the heat field. Figure 5.14 shows the dT_I images of the undamaged baseline (a), D3 sample (b) and the dT_I subtraction image (c). As shown in the subtraction image, the heat profile of the sample presents many alterations in correspondence with the defects. In central part, the presence of the titanium insert is clearly located by the hot spot (1). In the bottom part of the samples, two horizontal alterations are detected: a cold area (2) which correspond to an air gap before the wrinkle, followed by a hotter area (3) due to the higher amount of metal material at the wrinkle. Finally, in the top part of the welding area, a cold spot is clearly detected in correspondence with the hole (4).

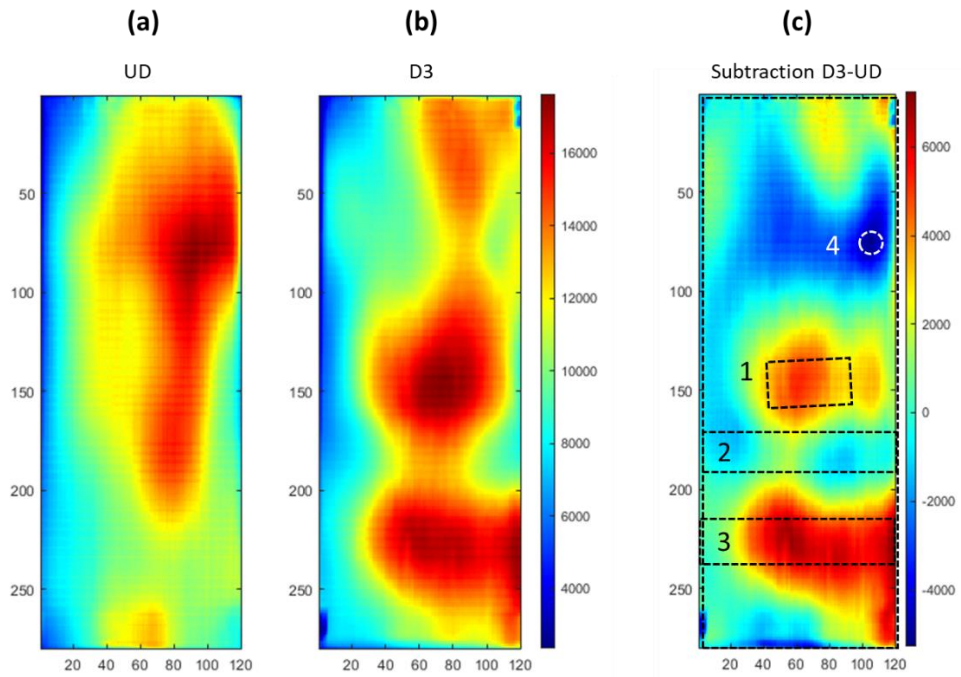


Figure 5.14 - Thermal dT_1 images for undamaged baseline (a), damaged sample D3 (b), baseline subtraction D3-UD (c).

Figure 5.15 shows the wT_1 (a-b) and aT_1 (c-d) for both undamaged and damaged samples. A good estimation of defects location can be identified by plotting the difference between the two total temperature profiles (e). As highlighted in the plot, each peak of the subtracted curve corresponds to the position of a defect. In the case of the wrinkle, there are a positive and negative peak arises, as expected.

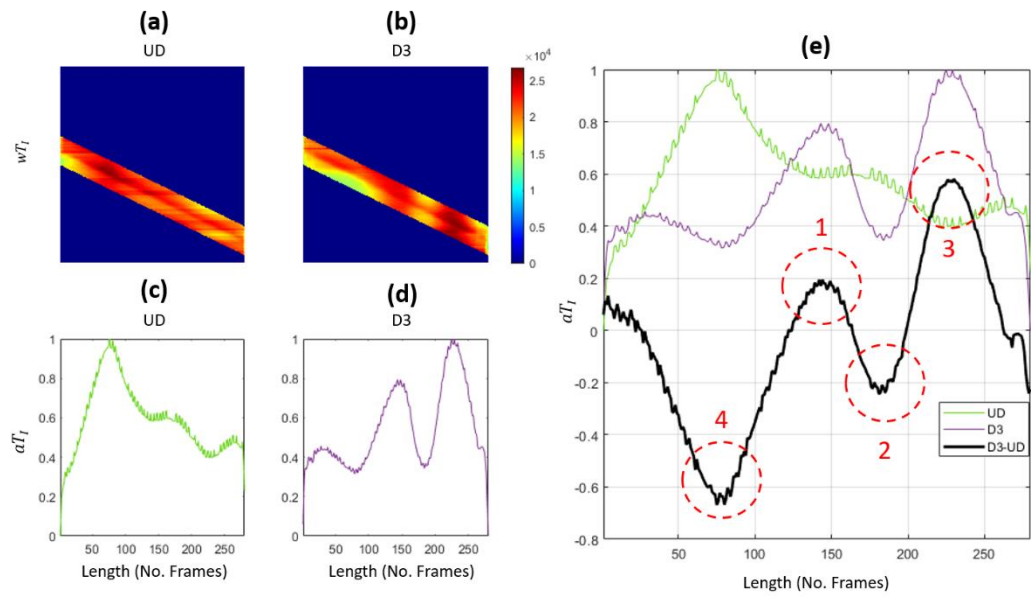


Figure 5.15 - wT_I undamaged baseline (a), wT_I image for D3 (b), aT_I undamaged baseline (c), aT_I profile for D3 (d), aT_I (e).

In Figure 5.16 the aT_I and $aT_{I_{sub}}$ profiles are summarised for all the tested samples with illustrations of the samples and defects. As it is possible to see, every defected sample showed a non-flat subtraction curve. The aT_I result with undamaged baseline subtraction is a valid method for detection of damaged samples. The process can be easily automated for detecting the eventual presence of peaks during the welding process, highlighting the damaged samples. In order to do this, a damage threshold needs to be defined, thus flagging as damaged every sample that shows values over the limit.

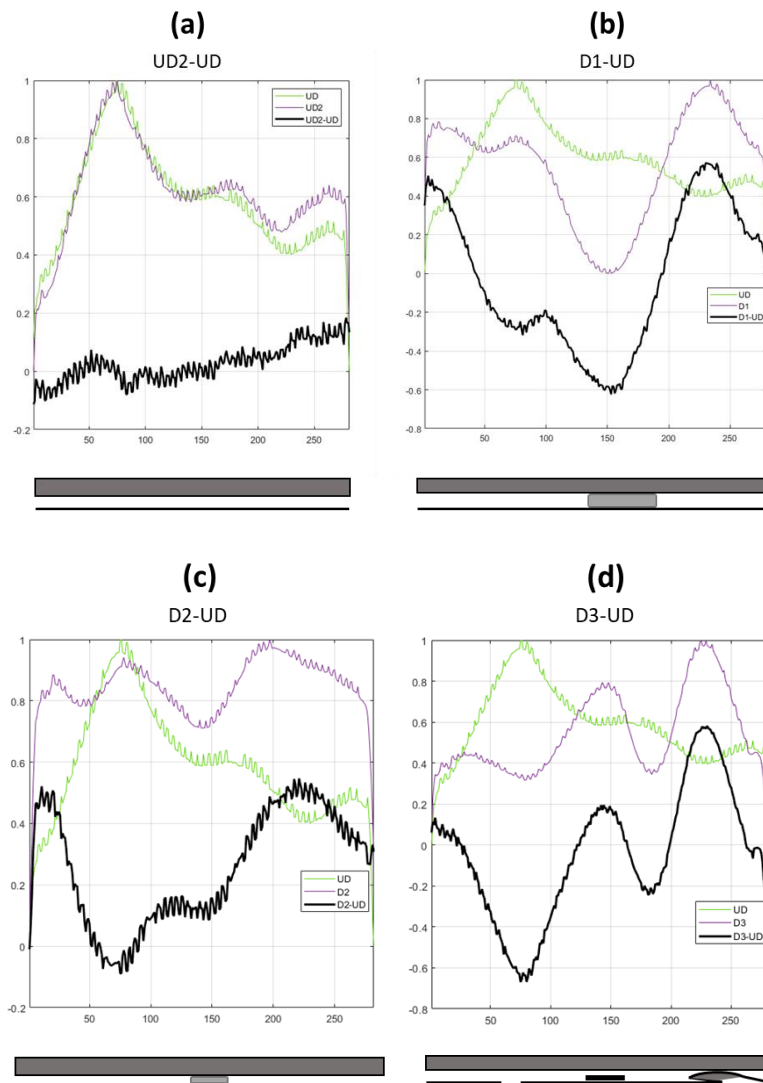


Figure 5.16 - $dT_{I_{sub}}$ profiles for UD2 (a), D1 (b), D2 (c) and D3 (d) samples with samples illustration

6. Conclusions

A thermography-based technique for *real-time* non-destructive evaluation of defects during automated manufacturing processes was developed. The technique was tested during electromagnetic induction welding of TPCs to evaluate and characterise various defects. The automated welding process was simulated attaching an induction coil, a pressure roller and IR cameras to a gantry system. Given the high repeatability of the process, thermal images were processed by

means of an undamaged baseline methodology. The integral of the thermal response dT_I was calculated for each point of the samples and subtracted from the undamaged baseline in order to highlight the alteration in heat field due to the presence of the defects. In addition, the width (wT_I) and aggregate T_I , (aT_I) were calculated for each sample. Applying the undamaged baseline subtraction to the aT_I line of the damaged samples, the resulting single line plot peaks were proved to highlight the position of strong alterations, and thus possible defects, in the heat field. Results show the efficiency of the method in *real-time* non-destructive localisation and characterisation of defects during induction welding of TPCs.

Generally, the undamaged baseline technique is able to highlight the heat variation due to the defects although the heat source itself is not homogeneous along the sample. Therefore, the proposed NDE technique can also be applied to other kinds of heat-based manufacturing process with high repeatability.

Acknowledgments

The present work is performed within NHYTE project (NHYTE, 2017–2020). The NHYTE project has received funding from the European Union’s Horizon 2020 research and innovation programme under grant agreement No. 723309.

References

- [1] Breuer UP. Manufacturing Technology. Commer. Aircr. Compos. Technol., Springer; 2016, p. 73–132.
- [2] da Costa AP, Botelho EC, Costa ML, Narita NE, Tarpani JR. A review of welding technologies for thermoplastic composites in aerospace applications. *J Aerosp Technol Manag* 2012;4:255–65. <https://doi.org/10.5028/jatm.2012.04033912>.
- [3] Pappadà S, Salomi A, Montanaro J, Passaro A, Caruso A, Maffezzoli A. Fabrication of a thermoplastic matrix composite stiffened panel by induction welding. *Aerosp Sci Technol* 2015;43:314–20. <https://doi.org/10.1016/j.ast.2015.03.013>.
- [4] Stokes VK. Experiments on the Induction Welding of Thermoplastics. *Polym Eng Sci* 2003;43:1523–41. <https://doi.org/10.1002/pen.10129>.
- [5] Reyes G, Kang H. Mechanical behavior of lightweight thermoplastic fiber-metal laminates. *J Mater Process Technol* 2007;186:284–90. <https://doi.org/10.1016/j.jmatprotec.2006.12.050>.
- [6] Antico FC, Zavattieri PD, Hector LG, Mance A, Rodgers WR, Okonski DA. Adhesion of nickeltitanium shape memory alloy wires to thermoplastic materials: Theory and experiments. *Smart Mater Struct* 2012;21:035022. <https://doi.org/10.1088/0964-1726/21/3/035022>.
- [7] Degrieck J, De Waele W, Verleysen P. Monitoring of fibre reinforced composites with embedded optical fibre Bragg sensors, with application to filament wound pressure vessels. *NDT E Int* 2001;34:289–96. [https://doi.org/10.1016/S0963-8695\(00\)00069-4](https://doi.org/10.1016/S0963-8695(00)00069-4).
- [8] Boccaccio M, Malfense Fierro GP, Meo M, Bolton G. Development and focusing enhancement of nonlinear air-coupled acoustic technique for damage

- characterization in materials. *Mater Today Proc* 2020. <https://doi.org/10.1016/j.matpr.2020.03.335>.
- [9] Sheiretov Y, Grundy D, Zilberstein V, Goldfine N, Maley S. MWM-Array Sensors for In Situ Monitoring of High-Temperature Components in Power Plants. *IEEE Sens J* 2009;9:1527–36. <https://doi.org/10.1109/JSEN.2009.2019335>.
- [10] Zolfaghari A, Kolahan F. Reliability and sensitivity of visible liquid penetrant NDT for inspection of welded components. *Mater Test* 2017;59:290–4. <https://doi.org/10.3139/120.111000>.
- [11] Pendry J, Smith D, Schurig D. Electromagnetic cloaking method 2017.
- [12] Habermehl J, Lamarre A. Ultrasonic Phased Array tools for composite inspection during maintenance and manufacturing. 2008.
- [13] Boccaccio M, Malfense Fierro GP, Meo M, Bolton G. Design of passive acoustic hyperbolic-shaped filter for nonlinear ultrasonic inspection method optimization. In: Gath K, Meyendorf NG, editors. *Smart Struct. NDE Ind.* 4.0, *Smart Cities, Energy Syst.*, vol. 11382, SPIE-Intl Soc Optical Eng; 2020, p. 5. <https://doi.org/10.1117/12.2558528>.
- [14] Shevchik S, Le-Quang T, Meylan B, Vakili Farahani F, Olbinado MP, Rack A, et al. Supervised deep learning for real-time quality monitoring of laser welding with X-ray radiographic guidance. *Sci Rep* 2020;10. <https://doi.org/10.1038/s41598-020-60294-x>.
- [15] Sophian A, Tian GY, Taylor D, Rudlin J. Electromagnetic and eddy current NDT: a review. *Insight* 2001;43:302–6.
- [16] Hillger W, Ilse D, the LB-P of, 2012 undefined. Practical applications of air-coupled ultrasonic technique. PdfsSemanticscholarOrg n.d.
- [17] Gan TH, Hutchins DA, Billson DR, Schindel DW. The use of broadband acoustic transducers and pulse-compression techniques for air-coupled

ultrasonic imaging. *Ultrasonics* 2001;39:181–94.
[https://doi.org/10.1016/S0041-624X\(00\)00059-7](https://doi.org/10.1016/S0041-624X(00)00059-7).

- [18] Wright WMD, Hutchins DA. Air-coupled ultrasonic testing of metals using broadband pulses in through-transmission. *Ultrasonics* 1999;37:19–22.
[https://doi.org/10.1016/S0041-624X\(98\)00034-1](https://doi.org/10.1016/S0041-624X(98)00034-1).
- [19] Blomme E, Bulcaen D, Cool T, Declercq F, Lust P. Air-coupled ultrasonic assessment of wood veneer. *Ultrasonics* 2010;50:180–7.
<https://doi.org/10.1016/j.ultras.2009.08.004>.
- [20] Maldague XPV. Introduction to NDT by active infrared thermography. *Mater Eval* 2002;60:1060–73.
- [21] Dionysopoulos D, Fierro GPM, Meo M, Ciampa F. Imaging of barely visible impact damage on a composite panel using nonlinear wave modulation thermography. *NDT E Int* 2018;95:9–16.
<https://doi.org/10.1016/j.ndteint.2018.01.005>.
- [22] Hung YY, Chen YS, Ng SP, Liu L, Huang YH, Luk BL, et al. Review and comparison of shearography and active thermography for nondestructive evaluation. *Mater Sci Eng R Reports* 2009;64:73–112.
<https://doi.org/10.1016/j.mser.2008.11.001>.
- [23] Fierro GPM, Calla D, Ginzburg D, Ciampa F, Meo M. Nonlinear ultrasonic stimulated thermography for damage assessment in isotropic fatigued structures. *J Sound Vib* 2017;404:102–15.
<https://doi.org/10.1016/j.jsv.2017.05.041>.
- [24] Madruga FJ, González DA, Mirapeix JM, López Higuera JM. Application of infrared thermography to the fabrication process of nuclear fuel containers. *NDT E Int* 2005;38:397–401. <https://doi.org/10.1016/j.ndteint.2004.11.002>.
- [25] Mook G, Lange R, Koeser O. Non-destructive characterisation of carbon-fibre-reinforced plastics by means of eddy-currents. *Compos Sci Technol* 2001;61:865–73. [https://doi.org/10.1016/S0266-3538\(00\)00164-0](https://doi.org/10.1016/S0266-3538(00)00164-0).

- [26]De Goeje MP, Wapenaar KED. Non-destructive inspection of carbon fibre-reinforced plastics using eddy current methods. *Composites* 1992;23:147–57. [https://doi.org/10.1016/0010-4361\(92\)90435-W](https://doi.org/10.1016/0010-4361(92)90435-W).
- [27]Koyama K, Hoshikawa H, Kojima G. Eddy current nondestructive testing for carbon fiber-reinforced composites. *J Press Vessel Technol Trans ASME* 2013;135:1–2. <https://doi.org/10.1115/1.4023253>.
- [28]He Y, Tian G, Pan M, Chen D. Impact evaluation in carbon fiber reinforced plastic (CFRP) laminates using eddy current pulsed thermography. *Compos Struct* 2014;109:1–7. <https://doi.org/10.1016/j.compstruct.2013.10.049>.
- [29]Heuer H, Schulze M, Pooch M, Gäbler S, Nocke A, Bardl G, et al. Review on quality assurance along the CFRP value chain - Non-destructive testing of fabrics, preforms and CFRP by HF radio wave techniques. *Compos Part B Eng* 2015;77:494–501. <https://doi.org/10.1016/j.compositesb.2015.03.022>.
- [30]Fierro GPM, Flora F, Meo M. Thermal wave imaging for defect determination during automated fibre placement. *Struct. Heal. Monit.* 2019 Enabling Intell. Life-Cycle Heal. Manag. Ind. Internet Things - Proc. 12th Int. Work. Struct. Heal. Monit., vol. 2, DEStech Publications Inc.; 2019, p. 2294–301. <https://doi.org/10.12783/shm2019/32369>.
- [31]Flora F, Boccaccio M, Malfense Fierro GP, Meo M. Non-destructive thermography-based system for damage localisation and characterisation during induction welding of thermoplastic composites. *Thermosense Therm. Infrared Appl.* XLII, 2020, p. 19. <https://doi.org/10.1117/12.2564925>.
- [32]Induction Welding. *Handb. Plast. Join.*, Elsevier; 2009, p. 113–20. <https://doi.org/10.1016/b978-0-8155-1581-4.50013-5>.
- [33]Ahmed TJ, Stavrov D, Bersee HEN, Beukers A. Induction welding of thermoplastic composites-an overview. *Compos Part A Appl Sci Manuf* 2006;37:1638–51. <https://doi.org/10.1016/j.compositesa.2005.10.009>.

- [34] Rudolf R, Mitschang P, Neitzel M. Induction heating of continuous carbon-fibre-reinforced thermoplastics. *Compos Part A Appl Sci Manuf* 2000;31:1191–202. [https://doi.org/10.1016/S1359-835X\(00\)00094-4](https://doi.org/10.1016/S1359-835X(00)00094-4).
- [35] Farahani RD, Dub M. Novel Heating Elements for Induction Welding of Carbon Fiber / Polyphenylene Sulfide Thermoplastic Composites 2017;1700294:1–10. <https://doi.org/10.1002/adem.201700294>.
- [36] Rudnev V, Loveless D, Cook raymond L. *Handbook of Induction Heating*. 2002. <https://doi.org/10.1201/9781420028904>.
- [37] He Y, Chen S, Zhou D, Huang S, Wang P. Shared excitation based nonlinear ultrasound and vibrothermography testing for CFRP barely visible impact damage inspection. *IEEE Trans Ind Informatics* 2018;14:5575–84. <https://doi.org/10.1109/TII.2018.2820816>.
- [38] Netzelmann U, Walle G. *Induction Thermography as a Tool for Reliable Detection of Surface Defects in Forged Components*. n.d.
- [39] Ibarra-Castanedo C, Piau J-M, Guilbert S, Avdelidis NP, Genest M, Bendada A, et al. Comparative Study of Active Thermography Techniques for the Nondestructive Evaluation of Honeycomb Structures. *Res Nondestruct Eval* 2009;20:1–31. <https://doi.org/10.1080/09349840802366617>.
- [40] Carslaw H, Jaeger J. *Conduction of heat in solids* 1992.
- [41] Zheng K, Chang YS, Wang KH, Yao Y. Improved non-destructive testing of carbon fiber reinforced polymer (CFRP) composites using pulsed thermograph. *Polym Test* 2015;46:26–32. <https://doi.org/10.1016/j.polymertesting.2015.06.016>.
- [42] Wang Z, Tian GY, Meo M, Ciampa F. Image processing based quantitative damage evaluation in composites with long pulse thermography. *NDT E Int* 2018;99:93–104. <https://doi.org/10.1016/j.ndteint.2018.07.004>.
- [43] Benítez H, Maldague X, Ibarra-Castanedo C, Loaiza H, Bendada A, Caicedo E. Modified differential absolute contrast using thermal quadrupoles for the

nondestructive testing of finite thickness specimens by infrared thermography. Can. Conf. Electr. Comput. Eng., Institute of Electrical and Electronics Engineers Inc.; 2006, p. 1039–42. <https://doi.org/10.1109/CCECE.2006.277741>.

- [44] Arndt RW. Square pulse thermography in frequency domain as adaptation of pulsed phase thermography for qualitative and quantitative applications in cultural heritage and civil engineering. *Infrared Phys Technol* 2010;53:246–53. <https://doi.org/10.1016/j.infrared.2010.03.002>.

6. Paper 4: Manufacturing and characterisation of thermal pre-stressed carbon fibre reinforced lattice core

Among the several types of sandwich cores available, the cellular cores are the most common ones that can be found in engineering sectors, such as automotive, aerospace and naval, thanks to their high mechanical properties combined with low values of density. The most performant cellular cores in terms of specific properties are the 2-D periodic prismatic cellular cores, such as the honeycombs, made of thin walls oriented along the thickness of the sandwich. Extensive research can be found on methods to design and improve novel cores, aimed to reach the highest values of strength at the lowest density. In this field, the expanding use of CFRPs has inspired some research works to design honeycomb cores made with such composite material.

In the article presented in this chapter, a novel CFRP lattice core, named CPCC, is developed, manufactured, and characterised. The design has been developed basing on three concepts: CFRP material, circular cell honeycomb geometry and use of thermal pre-stresses for energy absorption. The purpose of this work is to obtain a core with high specific stiffness and strength, along both in-plane and out-of-plane directions, that can be used in high performance engineering applications. The core is manufactured connecting UD CFRP strips manually laid-up in an asymmetrical orientation in order to generate residual thermal stresses along the unit-cell walls.

The study of the core design starts with some analytical considerations and calculations about the circular honeycomb cells, then the residual stress distribution and the fiber orientation contribution is studied through FEM analysis.

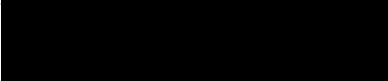
The numerical model of the core is used to predict its mechanical properties and study the possible effect of the manufacturing defects. For the validation and characterisation of the CPCC core, samples were manufactured and tested under bending, out-of-plane and in-plane compression tests. In order to compare the

properties of the material with a core used in sandwich structures for high-performance engineering applications, commercial aluminium honeycomb has been used as reference for experimental tests.

The work is aimed to provide a solution for the improvement of sandwich core failures, during both manufacturing phase and in-operation, and the compatibility with adhesives and skins. The results confirm the obtainment of the goal, showing mechanical performances that largely overcome the aluminium honeycomb ones. Of particular interest is the value of compressive strength to density ratio resulted from the tests, which is unique when compared to other typologies of low density cores in literature [67].

The Statement of Authorship Form and the paper can be found next.

This declaration concerns the article entitled:	
Manufacturing and characterisation of thermal pre-stressed carbon fibre reinforced lattice core	
Publication status (tick one)	
Draft manuscript	
Submitted	
In review	
Accepted	✓
Published	
Publication details (reference)	
Flora, F., Pinto, F., & Meo, M. (2021). Manufacturing and characterisation of a new thermal pre-stressed carbon fibre-reinforced lattice core for sandwich panels. Accepted for publication at <i>Journal of Composite Materials</i>	
Copyright status (tick the appropriate statement)	
I hold the copyright for this material	✓
Copyright is retained by the publisher, but I have been given permission to replicate the material here	
Candidate's contribution to the paper (detailed, and also given as a percentage)	
The candidate contributed to/ considerably contributed to/predominantly executed the...	

Formulation of ideas:	90%	I provided most of the idea, the hypothesis, the methodology and the experimental tests. My supervisor and I elaborated the idea of using bistability for energy absorption of the core.	
Design of methodology:	100%	I manufactured all the samples used in the experimental campaign and designed all the experimental tests carried out in the work. I realised the FEM of the core and conducted all the numerical analysis.	
Experimental work:	100%	I carried out all the experimental tests, collected all the data, and analysed all the outputs.	
Presentation of data in journal format:	90%	I designed the manuscript structure, wrote all the drafts, and realised all. My supervisors provided feedback on the draft and help for the paper review and submission.	
Statement from Candidate			
This paper reports on original research I conducted during the period of my Higher Degree by Research candidature.			
Signed			Date 29/01/2022

Manufacturing and characterisation of a new thermal pre-stressed carbon fibre reinforced lattice core for sandwich panels

Francesco Flora¹, Fulvio Pinto¹, Michele Meo^{1*}

¹ *Department of Mechanical Engineering, University of Bath, Bath, Ba2 7AY, UK*

* Corresponding author: m.meo@bath.ac.uk

Keywords: *Core; specific properties; compressions, pre-stress.*

Abstract

Development of high-performance sandwich structures is particularly attractive for aerospace applications, where novel lighter materials and structures are object of extensive research. This work is focused on the design of a new high-performance Carbon FRP core as alternative to traditional periodic prismatic ones. The innovative core is designed as a 2D close-packing pattern of circular cells and manufactured by connecting pre-preg corrugated laminates in specific locations. The corrugated laminates are layered following an asymmetric sequence in order to generate residual thermal stresses within the core to enhance energy absorption and compressive properties. The distribution of the residual thermal stress within the core was numerically studied with a finite element model of the unit cell, in order to prove the positive contribution of the asymmetric layup on the mechanical properties and study the failure mechanisms of the unit-cell. Composite core samples were manufactured, and their mechanical properties were experimentally evaluated through compression, both out-of-plane and in-plane, and beam flexure tests. Results were compared in terms of specific properties with traditional aluminium honeycomb core, showing large increments of specific compressive strength (+84.6%), in-plane compressive modulus (over +500%), Specific Energy Absorption (+145%) and shear (>20%). The FEM model was validated against experimental compressive results, showing an error below 10%. The results show that the core is suitable for applications in novel high-performance sandwich structures, leading to numerous advantages in comparison to traditional cores, such as higher specific properties, manufacturability of complex sandwich structures and higher adhesion and compatibility with CFRP skins.

1. Introduction

Composite sandwich materials are largely diffused in several engineering sectors, such as automotive, aerospace and naval, and can be found in many applications as both primary and secondary structures. In these sectors, panels made of thin fibre reinforced polymers skins and cellular cores [1] are commonly used to achieve high mechanical properties with a reduced structural weight. Given their diffusion, research on new cores is in rapid development in order to design advanced sandwich structures. Traditional cellular cores are honeycomb (2D periodic prismatic cores) [2–4], foam [5–8] and truss materials [9–12]. Despite the variety of research on truss cores thanks to the numerous possible combinations of 3D geometries and materials, 2D periodic prismatic cores, such as honeycomb cores, remain the preferred solution due to their relative high strength and stiffness, combined with a very low weight. Based on this, numerous researches are focused on the development of new kind of 2D periodic prismatic cores.

For instance, Bitzer [13] compared some of the common sandwich structures, showing that the honeycomb core has higher specific mechanical properties if compared to foam cores. An overview on the materials used to produce honeycomb cores (i.e. aluminium, Nomex, Kraft paper and fibreglass) and their manufacturing techniques is given in his work, and carbon fibre reinforced materials are mentioned as the first non-metallic core with shear moduli comparable to the aluminium honeycomb. Xiong et al. [14] provided a modified Ashby's chart [15] that shows mechanical properties (density versus strength) of the most common sandwich cores, showing a gap between the maximum strength for existing materials and the maximum theoretical strength, which is going to be filled by the developing of lattice cores, including pyramidal composites and carbon fibre honeycombs. Russell et al. [16] asserted that fiber reinforced cores are the natural development for sandwich structures to increase the specific strength and stiffness. In their work, they studied the out-of-plane properties of a square honeycomb core made of carbon fiber reinforced polymer (CFRP) layers connected by mechanical and adhesive joints, providing results in terms of specific compressive strength that reside in the

gap in the modified Ashby's chart. Their work shows the importance of the development of new fiber reinforced lattice cores, thanks to their high specific properties, but highlighting the complexity in the prediction of their mechanical response and their sensibility to manufacturing defects.

With the aim of manufacturing high strength and low-density sandwich cores, many attempts to use fibre reinforced materials can be found in literature. Petrone et al. [17–19] studied the vibrational performance and mechanical properties of honeycomb cores with different kinds of reinforcement, in particular flax fibres. They concluded that the use of long fiber reinforcement improves the mechanical performances, in particular compressive and shear modulus and strength (over +100%) but reduces damping (-40%) when compared to a polymer-only core. Integrated woven lattice cores, characterised by having skins and core woven together by the same fibre yarns, were designed, manufactured and experimentally characterised by Fan et al. [20–23] and Brandt et al. [24]. This kind of reinforcement leads to sandwich structures with a high skin-core debonding resistance, but the manufacturing process requires complex techniques and machines, limiting the design variability. Carbon fibres were also used as reinforcement for the manufacturing of Kagome [25,26], square [16,27,28], egg and pyramidal [29–31] and other lattice [32,33] cores, demonstrating excellent structural characteristics.

Difficulties in manufacturing continuous carbon fibres reinforce lattice core has limited the study of this kind of structures. Alia et al. [34] manufactured and tested a CFRP honeycomb core using the vacuum-assisted resin transfer molding method (VARTM), studying the compression and specific energy absorption properties. Different directions and typologies (unidirectional and fabric) of fibres were analysed, and results showed compression strengths of up to 35 MPa and specific energy absorption values of 47 kJ/kg.

One of the advantages in the use of CFRP materials for the manufacturing of the core is the increment of the in-plane properties, that are one of the main complications with the use of the traditional honeycombs [35]. Those properties become important during the manufacturing, where significant in-plane loads may

occur, for example during autoclave curing processes of sandwich structures, leading to costly part rejects and limitations in the design of complex geometries, as studied by Hsiao et al. [35]. The in-plane mechanical properties of 2D periodic prismatic cores are also strongly dependent on the cell geometry and distribution, as shown by Oruganti et al [36]. In their work, results of finite element method (FEM) analysis are used to study and compare creep deformation of different cell geometries, concluding that close-packing circular cell honeycombs (Figure 1) have higher mechanical properties than the hexagonal ones, due to internal constraints of the cells. The reason of the larger diffusion of hexagonal cell honeycomb cores is to be found in manufacturing limits: unlike hexagonal cells, a compact distribution in the space of circular cells would leave gaps, highlighted in red in Figure 6.1, that would be difficult to fill if metals are used as material. In addition, hexagonal honeycombs can be easily manufactured by folding and gluing thin strips of materials.

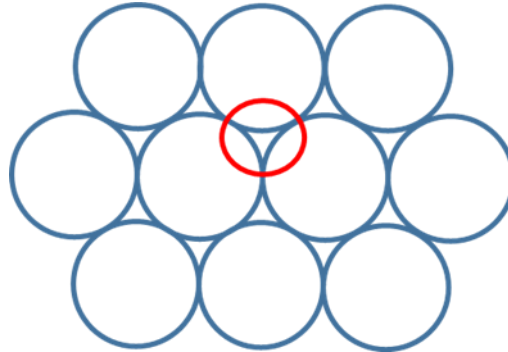


Figure 6.1 - Circular cell honeycomb distribution. The red circle highlights the gap between adjacent cells.

Despite the numerous benefits of fiber reinforced polymers, an issue associated with the use of carbon fibres parts is that CFRPs show low energy absorption due to their complex failure modes (fibre fracture, interlaminar debonding and matrix cracking) [37–39]. To increase the impact strength of CFRPs, many approaches have been investigated: reinforcement of carbon fibres–matrix interface [40,41]; stitches insertion along the laminate’s thickness [42–44]; hybridisation of composites mixing reinforcement materials [45–47]; insertion of metal wires within

laminates stacking sequence [48,49]. In this context, the use of residual stresses in the structure to increase energy absorption has attracted the attention of several researchers over the last decades. Indeed, the generation of residual stresses in thin structures can lead to the existence of two stable configurations, as explained by Scarselli et al [50], and the transition between the two requires energy, that can be absorbed from an external load. The residual stresses can be designed to act in the same direction of the predicted external load but with an opposite sign, as it happens with prestressed concrete [51]. Winkelmann et al. [52] analysed the concept of composite bistability and showed its advantages as energy absorption mechanism for tensile loading, basing on previous works by Whitman et al. on metal structures [53] and woven composites [54]. Keadze et al. [55] investigated the mechanics of the bistability induced by plastic bending of cylindrical shells and provided an analytical model able to predict the deformed shape. Recently, thermally-induced bistable composite structures have been used in aerospace structures as morphing components [50,56,57] for the aerodynamic control of the aircraft.

Hyer [58] was the first to study the circular cylinder bistable shape of composites, observing how this phenomenon happens only for thin asymmetric laminates, while thick laminates follow Classical Lamination Theory [59] that predicts a saddle shape. Later on, Dano and Hyer [60] provided a full analytical model to predict the curved shape of thin asymmetric laminates, such as [0/90]T. Daynes et al. [61] extended Heyer studies to symmetric laminates.

The literature shows that the interest in bistability and thermal prestresses in composite laminates is growing and many studies are emerging in the field of morphing structures, however the use of thermal prestress as an additional mechanism to improve energy absorption is a promising unexplored field.

Based on these premises, the aim of this work is to develop, manufacture and characterize a new lattice core characterised by high mechanical properties and based on three features:

- use of CFRP material

- circular cell honeycomb design
- application of thermal pre-stresses

The new core, herein referred to as circular prestressed carbon core (CPCC), is designed to obtain high specific stiffness and strength, along both in-plane and out-of-plane directions, to be employed for sandwich structures in high performance applications. To obtain this, asymmetric CFRP prepreg strips are corrugated and connected in order to obtain the circular honeycomb cells. Both analytical and FEM analyses are presented to study the residual thermal stress distribution in the structural unit-cell of the core. The numerical model of the unit-cell is successively expanded to the whole sample to simulate mechanical compressive tests and study the influence of manufacturing defects on the mechanical responses. In order to characterise the structure, the designed core is manufactured and experimentally studied through out-of-plane and in-plane compression and three-point bending tests. The results are compared with the one obtained from the same experimental tests performed on a traditional aluminium honeycomb core in order to have a comparison with a core widely used for manufacturing of sandwich structures.

2. Core design

The structure of the CPCC core consists of corrugated strips of material connected in precise points to create a pattern geometry. Two layers of prepreg are used to create the corrugate strips, in a $[0, 90]$ fiber configuration. An advantage in the use of resin impregnated material is in the filling of the previously mentioned empty spaces between the adjacent cells and thus the increase of the contact area between the strips, as schematically represented in Figure 6.2a. The main geometrical difference with the traditional honeycomb structure is in the cell: a circular cell is used instead of the hexagonal one during the manufacturing of the CFRP core. Using a circular cell it is possible to avoid sharp edges that may be points of stress concentration, especially for fibre reinforced materials [62], as highlighted in Figure 6.2b.

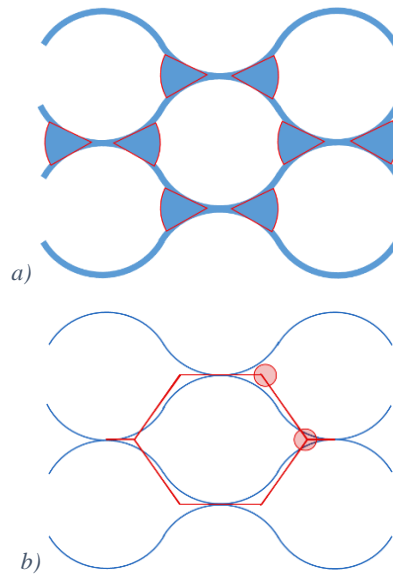


Figure 6.2 - Circular cell honeycomb structure: a) detail of the intercellular spaces filled by the resin; b) comparison with hexagonal cell and detail of the avoided sharp corners

The unit-cell design parameters and directions used in this work are illustrated in Figure 6.3. The value of s derives from the nominal value of the cured prepreg thickness (0.211 mm), while d is the radius of the steel cylinders used to give the shape of the cell and the b is a geometrical parameter (half of the distance between two adjacent cells) deriving from the close-packing pattern.

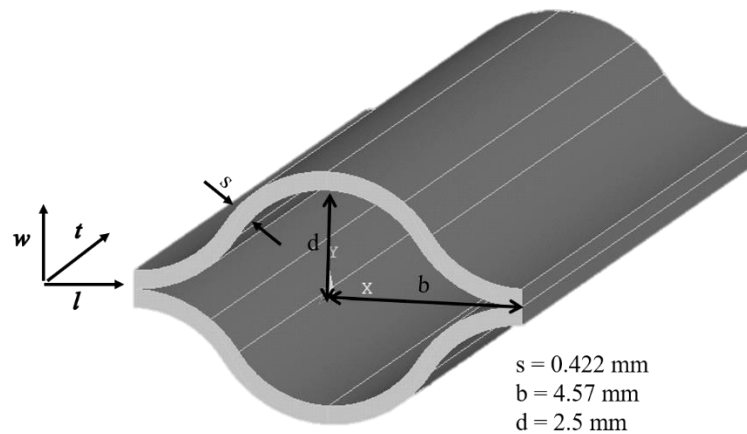


Figure 6.3 - CPCC unit cell

Analysing a quarter of the unit cell, it is possible to approximate the geometry to an area composed of two parallel curves vertically shifted by s . Based on this, it is possible to calculate the area, and thus the core density, of the quarter of unit cell with the following equations:

$$A^* = b \cdot s \quad (1)$$

$$A^s = b \cdot (d + s) \quad (2)$$

$$\frac{\rho^*}{\rho^s} = \frac{A^*}{A^s} = \frac{s}{d + s} \quad (3)$$

where ρ is the density, A is the sectional area and the superscripts $*$ and s refer respectively to the core and relative solid, which is a solid of the same material that occupies the volume of a unit cell without empty spaces. This formula is similar to the one obtained by Gibson et al. [1] for honeycomb structures, where the resulting ratio between the densities is approximated to the ratio of the thickness of the cell wall to the length of the cell side. In a similar way, it is possible to estimate the ratio between the Young's moduli of the core and the relative solid in compression along the out-of-plane direction:

$$\frac{E_t^*}{E_t^s} = \frac{s}{d + s} \quad (4)$$

Using the design values showed in Figure 6.3 and the nominal values of ρ and E of the cured prepreg in $[0, 90]$ configuration loaded along the fiber directions, the previous formulas give the following values for the predicted density and out-of-plane compressive elastic modulus of the core:

$$\rho^* = 0.228 \frac{g}{cm^3} \quad (5)$$

$$E_t^* = 10.53 \text{ GPa} \quad (6)$$

The estimated value of elastic modulus in (6) is to be considered as an upper reachable limit for the designed core, as it is calculated using the nominal material properties and fiber percentage provided by the prepreg manufacturer for optimal conditions of curing and on the assumption of the perfect alignment of the fibers

along both 0 and 90 directions. The analytical evaluation of the elastic shear moduli is more complicated, due to the geometrical complexity and non-uniformity of deformations of the cell walls, and can only be evaluated numerically [1].

Chung et al. [63] provided some analytical estimations of the in-plane elastic properties of elliptical cell honeycombs. Their calculations were made under the approximation of small ε (slight ellipticity), thus close to the case of circular cells. Based on their work, the elastic moduli for compression along the two principal directions can be estimated using the following equations:

$$\frac{E_l^*}{E^s} = \frac{C_{11}(\varepsilon)}{(1 - \nu^2)} \left(\frac{\rho^*}{\rho^s} \right)^3 \quad (7)$$

$$\frac{E_w^*}{E^s} = \frac{C_{21}(\varepsilon)}{(1 - \nu^2)} \left(\frac{\rho^*}{\rho^s} \right)^3 \quad (8)$$

Where $C_{11}(\varepsilon) = 1.396 + 2.345\varepsilon - 1.401\varepsilon^2 + O(\varepsilon^3)$; $C_{21}(\varepsilon) = 1.396 - 2.835\varepsilon + 2.260\varepsilon^2 + O(\varepsilon^3)$; $\varepsilon = (a_1/a_2) - 1$. a_1 and a_2 are respectively the major and minor semi-axis of the elliptical cell and ν is the material Poisson's ratio. The values of $C_{11}(\varepsilon)$ and $C_{21}(\varepsilon)$ derive from calculations made on the geometrical deformation of the elliptical cells, as described in [63].

Gibson et al. [1] provided the equations for the in-plane elastic moduli for hexagonal honeycomb structures as follow:

$$\frac{E_l^*}{E^s} = \frac{\cos \theta}{(h/f + \sin \theta) \sin^2 \theta} \left(\frac{\rho^*}{\rho^s} \right)^3 \quad (9)$$

$$\frac{E_w^*}{E^s} = \frac{h/f + \sin \theta}{\cos^3 \theta} \left(\frac{\rho^*}{\rho^s} \right)^3 \quad (10)$$

where h , f and θ are geometrical parameters of the hexagon cell.

Analysing the CPCC unit-cell structure along the two in-plane directions, it is clear that the response of the structure to a compressive load under the l and w directions is different. Along the w direction, the load is mainly supported by the circular part

of the unit cell, thus giving a mechanical response similar to the elliptical honeycomb. On the other side, when the cell is loaded along the l direction, the predominant mechanism is the compression of the corrugated plies, thus similar to the hexagonal honeycomb. The geometrical approximations and relative parameters are given in Figure 6.4. Using the equations (9) and (8), the following values can be estimated for the in-plane elastic moduli:

$$E_l^* = 234 \text{ MPa}$$

$$E_w^* = 111.07 \text{ MPa}$$

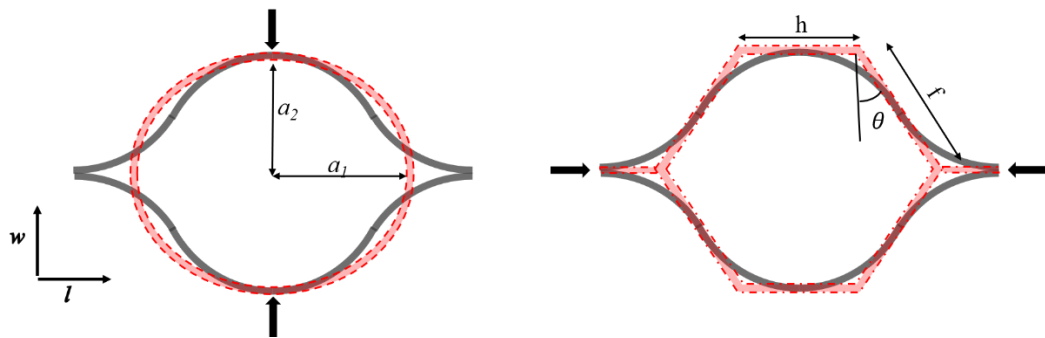


Figure 6.4 - Geometrical approximations of the unit cell under in-plane compressive loads

It is important to highlight that the estimations provided here are based on assumptions of perfect material and ideal boundary conditions. These values will be used to validate the FEM model of the unit-cell with ideal parameters and boundary conditions.

3. Analysis

In this section, some analytical considerations and numerical studies of the CPCC core are illustrated. First, the analytical equation governing the bistability of curved unsymmetric laminates is described. Then, the residual stress and strain fields are numerically calculated using a FEM analysis of the single wall and single unit cell. The influence of the residual stress over the mechanical properties of the unit-cell is evaluated by simulating the mechanical tests and validated through comparison

with the analytical calculations of the elastic moduli provided in the previous section. Successively, the FEM model is expanded to a whole CPCC sample and compression tests, both out-of-plane and in-plane, are simulated.

3.1. Bistability description

Considering a traditional CFRP, the coefficient of thermal expansions of the resin ($35\text{-}65\cdot 10^{-6} \text{ K}^{-1}$) is significantly different from that of the fibres ($\sim 0 \text{ K}^{-1}$) [64]. As a consequence, in a laminate with a unsymmetric fiber orientation, the difference of thermal expansion of the laminae will generate residual stresses after the cure that will lead to a not-flat shape. For an unsymmetric composite laminate, the classical lamination theory (CLT) predicts a saddle shape at room temperature after the cure [65], however, the same theory does not apply for thin rectangular laminates, where thermal stresses lead to two cylindrical stable shapes, as demonstrated by Hyer [58] and illustrated in Figure 6.5b and Figure 6.5c. While the saddle shape is characterised by a curvature along both in-plane directions (x and y in figures), the two cylindrical configurations present curvature along only one direction. These configurations are both stable at room temperature, and laminates can suddenly pass between the two if a sufficient external moment is applied, leading to the so-called snap-through phenomenon.

The most used analytical model to correctly predict these stable shapes of bistable composite laminates is the Rayleigh-Ritz energy method [60,66,67]. Ryu et al. [68] presented the explicit model to estimate the cured curvature and strain fields of a unsymmetric cross-ply laminate in $[0, 90]$ configuration, cured over a curved mould. Lee et al. [69] expanded this model to evaluate the laminate residual moments, and thus the snap-through load, applying the classical laminate theory. Given the similarity of the single cell wall of the CPCC core to the case studied in these two works, these analytical models are briefly described in this section.

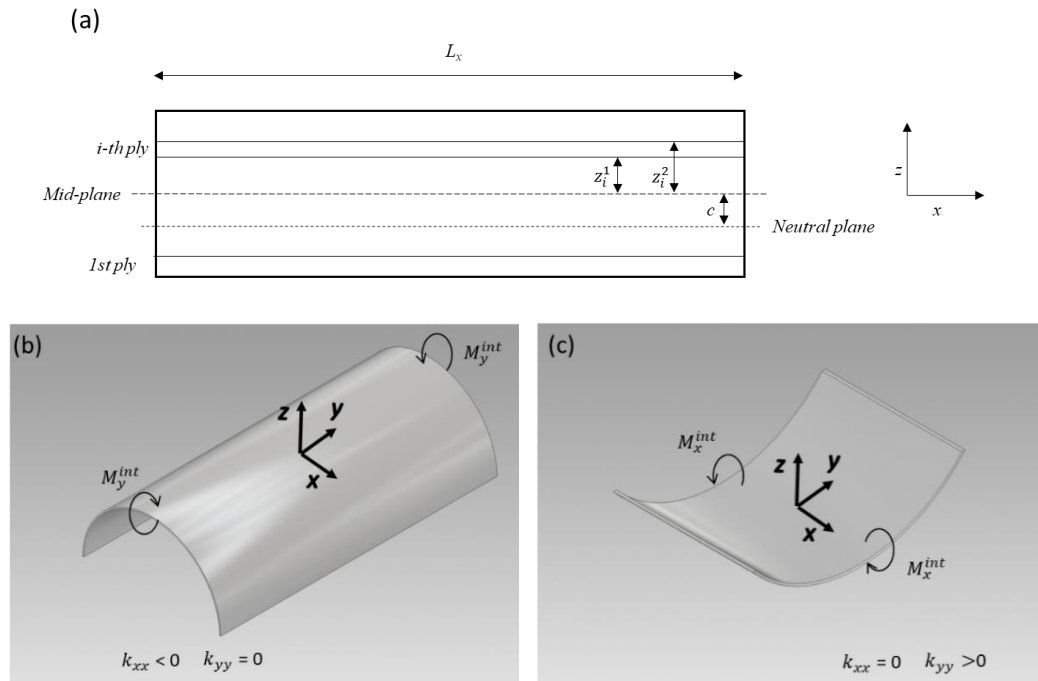


Figure 6.5 - Geometry of the composite laminate and axes orientations: a) cross section of flat configuration; b) first stable configuration with curvature along the y -direction; c) second stable configuration with curvature along the x -direction

The explicit model proposed by Ryu et al. [68] to evaluate the Green-Lagrangian strain field and strain energy function is based on the following three assumptions:

- The existence of a linear constitutive equation between the Green-Lagrangian strain and the second P-K stress (infinitesimal strain)
- Neglection of the edge effects (constant curvature)
- Kirchhoff-Love thin plate assumption (small thickness-to-side ratio)

As mentioned above, the shape of the stable configuration may be of two kinds: saddle, that is when both sides of the laminate are curved at the same time, or cylindrical, when only one of the two sides is curved. In this work we focus only on the second case, cylindrical shape, that is the predominant shape when the laminate is thin and presents a side sufficiently longer than the other one. Indeed, when thin composites present a rectangular plane shape, the strain energy of the laminate in the cylindrical configuration is lower than the one in the saddle shape, and thus it is the stable one. In a cylindrical shape, only one of the two curvatures,

either k_{yy} or k_{xx} , is equal to zero in each configuration, as illustrated in Figure 5b and Figure 5c, respectively.

The Rayleigh-Ritz energy method is based on the minimization of the total potential energy Π^T giving a moment equilibrium condition, and thus equalling the first variation $\delta\Pi^T$ to zero. The model describes the equilibrium of the laminate as governed by an internal moment. Considering an external moment M^{ext} acting on the bistable composite, the difference between the external and internal moments gives the moment equilibrium constraint:

$$\delta\Pi^T = \delta\Pi + \delta \left\{ \Lambda \left(\int_{-\frac{L}{2}}^{\frac{L}{2}} [(M)]^{ext} - M^{int} dl \right) \right\} = 0 \quad (11)$$

where Λ is the Lagrange multiplier. The aim of this work is to take advantage of this internal moment to create a stress that works along the same direction and opposite sign of the external load, improving the mechanical response of the structure. In order to do this, an optimisation of the fiber orientation through the core is needed by means of numerical studies of the residual thermal stresses.

3.2. Finite element analysis

3D implicit FEM models of the composite core were developed using Ansys[®] /LS-Dyna[®] software. Each ply was modelled using fully integrated 0.211 mm thickness shell elements (type 16), which uses a local element coordinate system, defined as in the Belytschko-Tsay element [70], that rotates with the material. The properties listed in Table 6.1 were used to define the orthotropic material using a Chang matrix failure criterion [71] (MAT_54_ENHANCED_COMPOSITE_DAMAGE). Tie-break contacts (AUTOMATIC_SURFACE_TO_SURFACE_TIEBREAK) were applied at plies interface in order to simulate interlaminar contacts, whose properties are listed in Table 6.2.

Table 6.1 - Material properties (subscripts 11 refer to fiber direction, 22 to in-plane direction perpendicular to the fibers and 33 through the thickness): RO density; E modulus of elasticity; PR Poisson's ratio; G shear modulus; XC and XT longitudinal compressive and tension strengths; YC and YT transverse compressive and tension strength; SC shear strength.

Material properties	RO	E ₁₁	E ₂₂	E ₃₃	PR ₂₁	PR ₃₁	PR ₃₂	G ₁₂
	[Kg mm ⁻³]	[GPa]	[GPa]	[GPa]				
Values	1.23·10 ⁻⁶	130	10.3	10.3	0.0535	0.0535	0.449	4.37
Material properties	G ₂₃	G ₃₁	XC	XT	YC	YT	SC	
	[GPa]	[GPa]	[GPa]	[GPa]	[GPa]	[GPa]	[GPa]	
Values	3.43	3.43	1.5	2.58	0.236	0.082	0.09	

Table 6.2 - Tie-break contact properties: FS and FD static and dynamic coefficients of friction; NFLS normal failure stress; SFLS shear failure stress.

Contact properties	FS	FD	NFLS	SFLS
			[GPa]	[GPa]
Values	0.4	0.3	0.082	0.09

The numerical study started with the analysis of a simple curved double layer of CFRP material, that is half of the CPCC unit cell (Figure 6.6). The structure was modelled as two layers of shell elements. Periodic conditions were applied to the two sides of the model in order to simulate the presence of the adjacent cells.

A coupled thermal-structural FEM analysis was performed on the model simulating the cooling cycle, lowering the temperature from 130 °C to 5 °C in 1 sec in order to generate thermal stresses. The model is expected to fail for buckling when loaded under out-of-plane compression. In such a kind of failure, a side of the structure will be subjected mainly to tensile stress, while the opposite side will be under compression. Based on this, the model is expected to have different mechanical responses in function of the order of the fiber orientations of the two shell element layers due to the anisotropy of the material. Two fiber configurations were

considered: [0,90] and [90,0], where the 0 degree is the orientation along the wall curvature and the 90 along the vertical direction. In the nomenclature, the first orientation from the left is referred to the external shell layer (the red face in Figure 6.6).

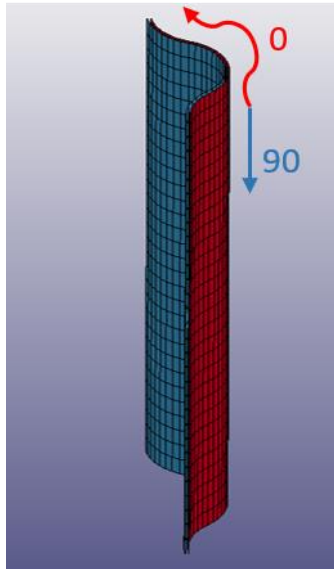


Figure 6.6 - FEM model of the unit cell wall with fiber orientation [0 (red), 90 (blue)]

As it is possible to see from Figure 6.7, that shows the vertical component of stress distribution after the structural-thermal analysis, there is a difference in the stress distribution between the [0,90] (Figure 7a) and [90,0] (Figure 6.7.b) configurations, as expected, but in both cases the stress is positive (tension) in all the elements. This tension stress will act against the compression stress of the external load.

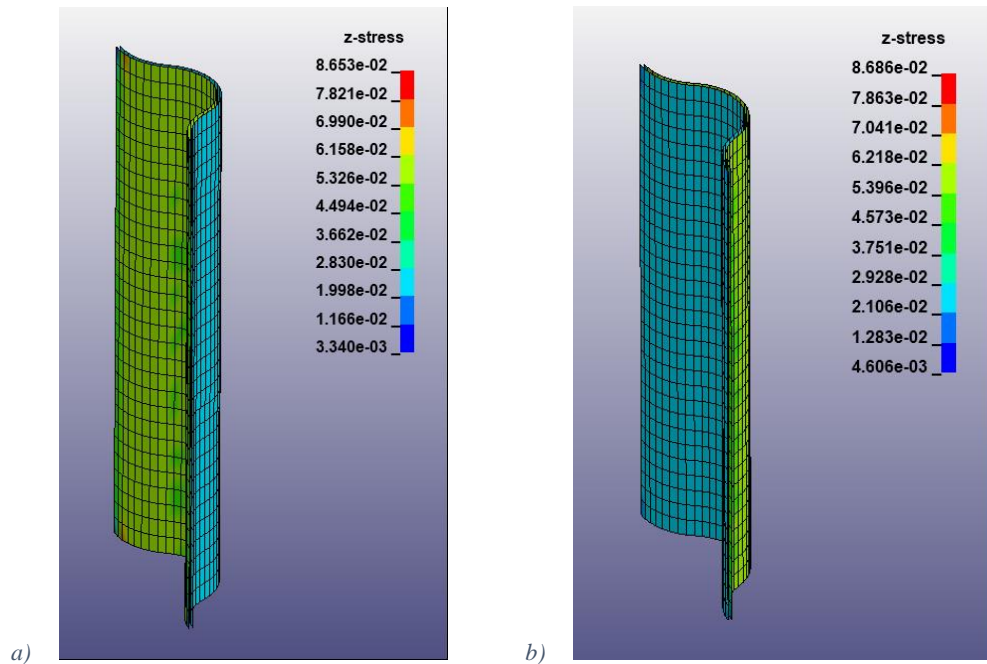


Figure 6.7 - Thermal stress [GPa] t -direction component for a) [0,90] and b) [90,0] configurations

The stress status and deformed shape of each element after the structural-thermal analysis were imported in a new FEM model to perform structural tests. In order to study the influence of the residual stresses on the mechanical properties of the part, an out-of-plane compression test was simulated.

The displacement of the bottom nodes was constrained in all the degrees of freedom (DOF), while the top ones were constrained only in the in-plane DOF and a vertically prescribed motion of 0.5 mm/min was applied to compress the structure. The boundary conditions are illustrated in Figure 6.8, where blue nodes are constrained in all DOF, red are constrained along the in-plane directions and have a prescribed motion along the vertical direction and the yellow nodes represents the period boundaries. A mesh convergence study has been performed at this stage, in order to determine the number of elements required along the direction of load to obtain results independent from the mesh size, basing the analysis on the failure load values. An optimal number of 30 shell elements (side dimension 0.75 mm) along the direction of load was selected, which lead to a total of 1920 elements and 2046 nodes.

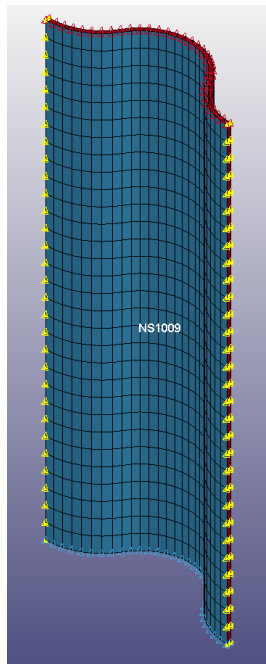


Figure 6.8 - Cell wall model boundary conditions. Blue nodes (bottom): all DOF constrained; red nodes (top): in-plane DOF constrained and out-of-plane prescribed motion; yellow nodes (sides) periodic conditions at all DOF.

The simulation was also performed on the same models without applying any kind of prestress, in order to simulate the material manufactured following traditional slow cooling down process. Indeed, without the fast cooling down process, the material has the time to adapt to the thermal deformations, relaxing the residual stresses. For all the 4 combinations ([0,90] and [90,0], with and without prestresses) the failure occurred for buckling of the cell wall. In Figure 6.9.a, the load displacement curves for the [0,90] configuration with and without residual stresses are compared. The mechanical responses of the two models are different: the unstressed structure presents one failure at 0.87 kN, after which the load decreases, while the prestressed one shows a second increment of load after the first failure due to the bistability of the structure, which occurred at a value 15% lower than the unstressed. The numerical results show that at the time of the second failure, a sudden displacement of the structure occurs in the same location of the buckling failure, suggesting the presence of the snap-through phenomenon between the two stable configurations. The phenomenology of the event, illustrated in Figure 6.9.b, suggests that after the begin of the buckling failure (a), the external force works

against the residual stresses (b) that are in opposite direction to the stresses generated by the buckling. This creates a new increment of the load carried by the structure, until the compressive stresses overtake the residual stresses (c), generating the sudden displacement (d and e) due to the bistability. It can be argued that the residual stresses contribute in two ways for the [0,90] configuration: they reduced the ultimate load by 15% but created a second load peak and a snap-through event, that improves the absorbed energy (+ 10%).

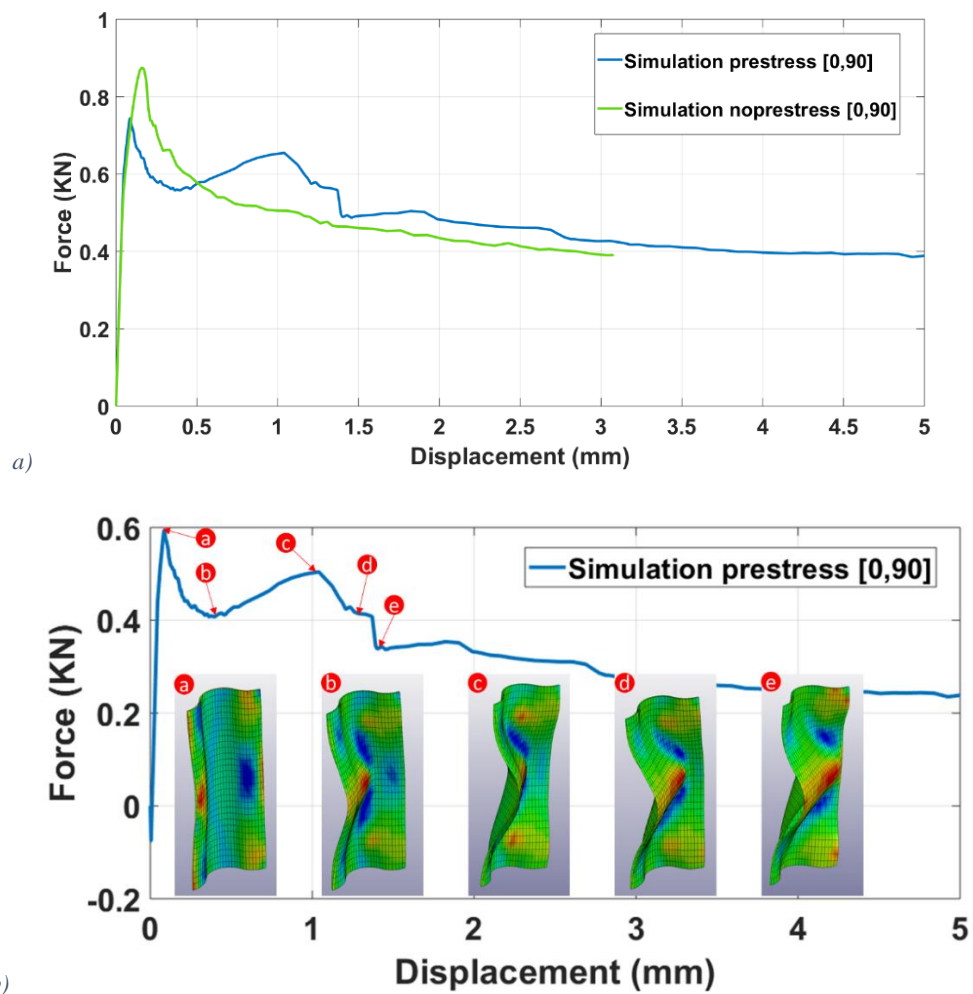


Figure 6.9 - a) Force-displacement curves from FEM analysis on prestressed and not prestressed unit cell wall model in [0,90]; b) details from FEM analysis results on pre-stressed [0,90] model

On the other side, the ultimate load for the [90,0] configuration is increased by approximately 19% due to the presence of the residual stresses, as it is possible to see from Figure 6.10. In this case, the shape of the two curves is very similar, but with a difference in terms of carried load. Given that the snap-trough depends on

the fiber orientations, in this configuration the phenomena is not visible probably because the residual stress is overtaken by the external stress before the buckling failure happens. This means that the residual stress contributes only on the ultimate load, working against the compressive stress, but without any snap-through phenomena.

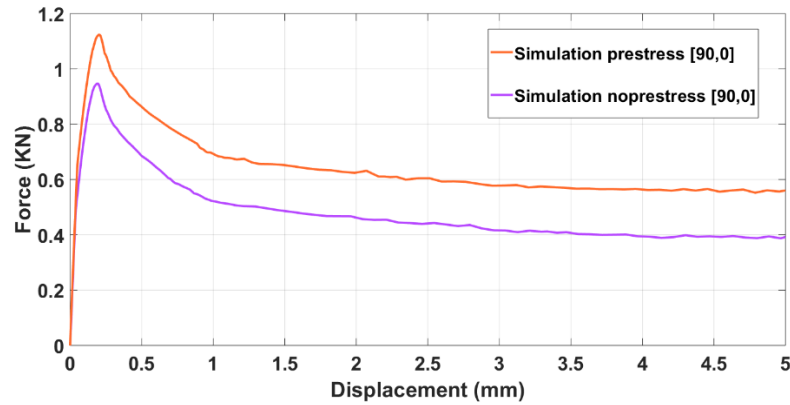


Figure 6.10 - Force-displacement curves from FEM analysis on prestressed and not prestressed unit cell wall model in [90,0]

The clear difference in behaviour between the [0,90] and [90,0] configurations can be attributed to the asymmetry of the geometry and the different properties of the two fibers orientations. Given that the buckling failure creates compressive and tensile stresses on the two opposite sides, the response of the structure strongly depends on the mechanical properties of the two layers under these two kinds of load, which are very different between 0 and 90 degrees layers. Therefore, if the layer on the internal side, where the tensile component of the buckling stress acts, is the 90 degree one ([0,90] configuration), the mechanical response is different from the [90,0] configuration, where the internal layer is the 0 degree one. This difference leads to two different buckling failures: towards the centre of curvature for the [90,0] and towards the external side of the curvature for the [0,90]. The direction of buckling for the [90,0] is the same direction of the snap-through, which therefore cannot happen. This explains the similarity of the two curves in Figure 6.10 and the absence of sudden displacement episodes.

After the analysis of the residual thermal stress distribution and compressive behaviour of the single wall, the analysis was extended to the unit-cell. The unit-

cell of the circular honeycomb structure is composed of two cell walls attached to each other. For the FEM model, in order to take into consideration the mechanical properties of the contact between two adjacent cells, the unit-cell has been considered as two half-cells, as shown in Figure 6.11, leading to a total of 3840 shell elements and 4092 nodes. From an analytical point of view, for the evaluation of the elastic properties, this unit-cell is the same as the one showed in the previous section (Figure 6.3), and thus the results in terms of elastic moduli can be compared. In order to have symmetry, and thus symmetric residual stresses, two configurations are possible: $[0,90]_s$ (Figure 6.11.a) and $[90,0]_s$ (Figure 6.11.b). The same boundary conditions and properties of the single cell wall model were used.

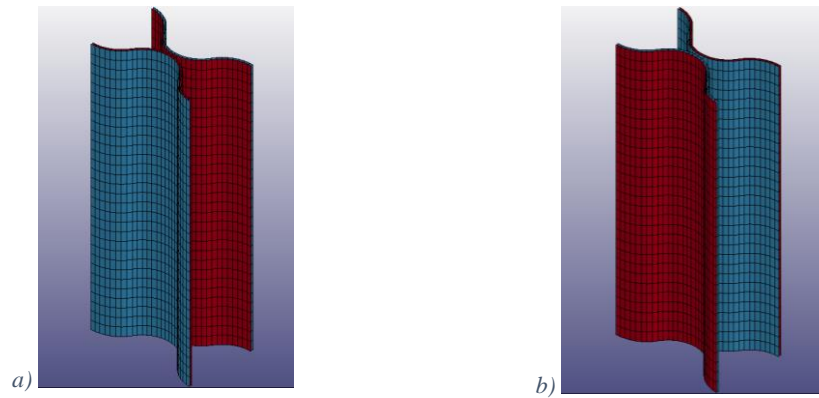


Figure 6.11 - FEM model of the unit cell in a) $[0,90]_s$ and b) $[90,0]_s$ configurations. In red the 0 and in blue the 90 fiber orientations

As for the cell wall FEM models, the unit cells were first modelled under thermal cycle and then the residual stresses imported in the structural analysis in order to simulate a compression test.

When in the unit-cell configuration, the behaviour of the $[0,90]$ wall changes, as it is possible to see in Figure 6.12.a where the load displacement curves are plotted. When the $[0,90]$ wall is attached to a symmetric wall to form the $[0,90]_s$ unit cell, the compressive ultimate load of the prestressed structure is higher than the unstressed one by 17.3%. In this case, no snap-through phenomena are shown by the numerical results. However, it is possible to say that when the thermal stresses are applied to the $[0,90]_s$ structure, they improve the ultimate load, but no snap-

through events are shown, leading to a load displacement curve with a similar shape of non-prestressed one.

Totally different is the mechanical behaviour of the [90,0] wall when modelled in the symmetric structure [90,0]_s. As it is possible to see from the plot in Figure 6.12.b, there is a very large increment in terms of ultimate load carried by the unit-cell when compared to the non-prestressed one (+74.6%) and a snap-through event in correspondence with a 1 mm displacement.

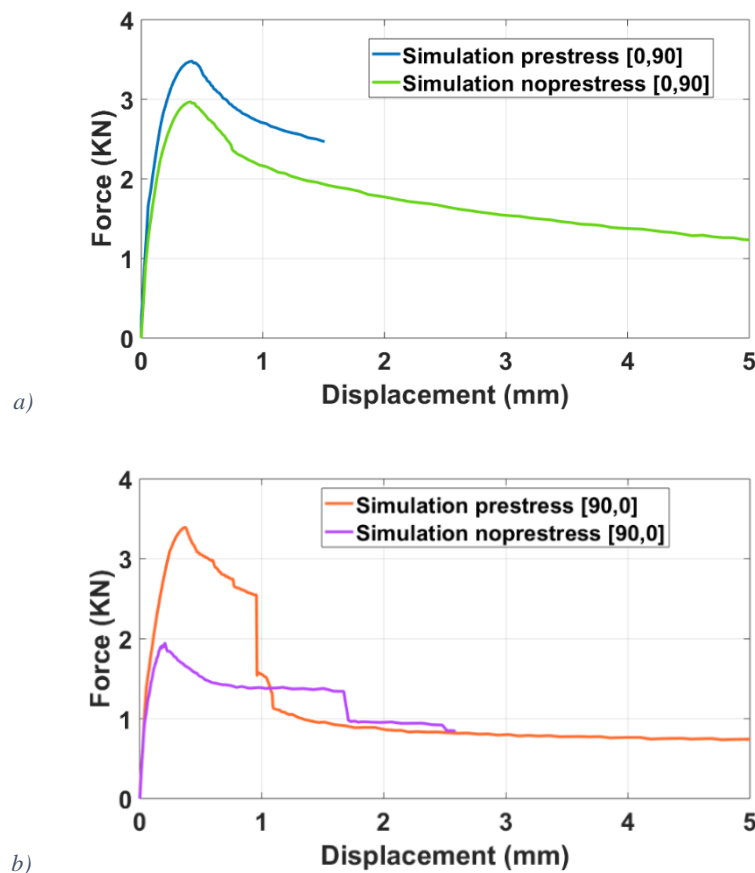


Figure 6.12 - Force-displacement curves from FEM analysis on prestressed and non-prestressed unit cell model in a) [0,90]_s and b) [90,0]_s configurations

Comparing the results of the single cell walls and the unit cells, it is possible to see how the stress strain curves of the [90,0]_s is similar to the [0,90], showing a substantial difference between the prestressed and unstressed curves, while [0,90]_s showed a response similar to the [90,0] configuration. This can be explained by analysing the position of the 90 layers in the two configurations. In this layer the

reinforcement is orientated along the vertical direction, therefore is the layer that carries most of the load. As it is possible to see in Figure 6.13, in the $[0,90]_s$ configuration the 90 layers are divided by the 0 ones, and thus respond as separated structures. On the other hand, in a $[90,0]_s$ the 90 layers are connected in the centre of the cell, and therefore fail as one layer, optimising their mechanical respond. The buckling failure in the $[0,90]_s$ can happen in both directions (bistability), depending on local instabilities such as material defects.

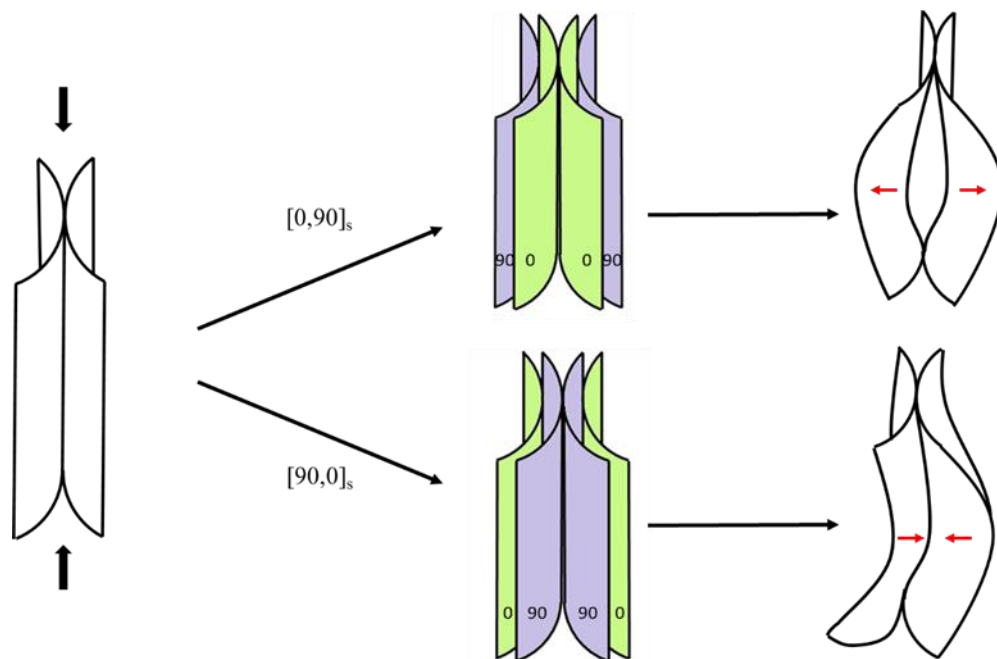


Figure 6.13 - Bistable buckling failures of unit cells

Unlike the cell wall cases, both symmetric unit-cell configurations showed improvements in terms of ultimate load. Particularly interesting is the case of $[90,0]_s$ where, in addition to an increment of 74.6% of the maximum load, larger values of absorbed energy (area below the curve) have been shown from results, and it is possible to see an actual bistability of the structure.

From the unit-cell FEM analysis results, it is possible to conclude that the residual stresses generated from a fast cooling cycle lead to improvements in terms of out-of-plane mechanical properties of the core and can generate additional energy absorption phenomena. In order to obtain the symmetric unit-cells, an alternate fiber orientation that creates a symmetric lamination at the joining points of the circular

honeycomb structure is needed, as described in section 4. Using the alternate fiber orientation, the core will include both $[0,90]_s$ and $[90,0]_s$ configurations.

In order to compare the numerical results with experimental tests, the unit-cell FEM model was repeated in the space to obtain the CPCC sample FEM model, which for the compression out of plane test have dimensions of 50x50mm leading to a total of 57600 elements and 58317 nodes. As for the unit-cell, the residual thermal stress distribution was evaluated and results for the t direction component of stress are showed in Figure 6.14.

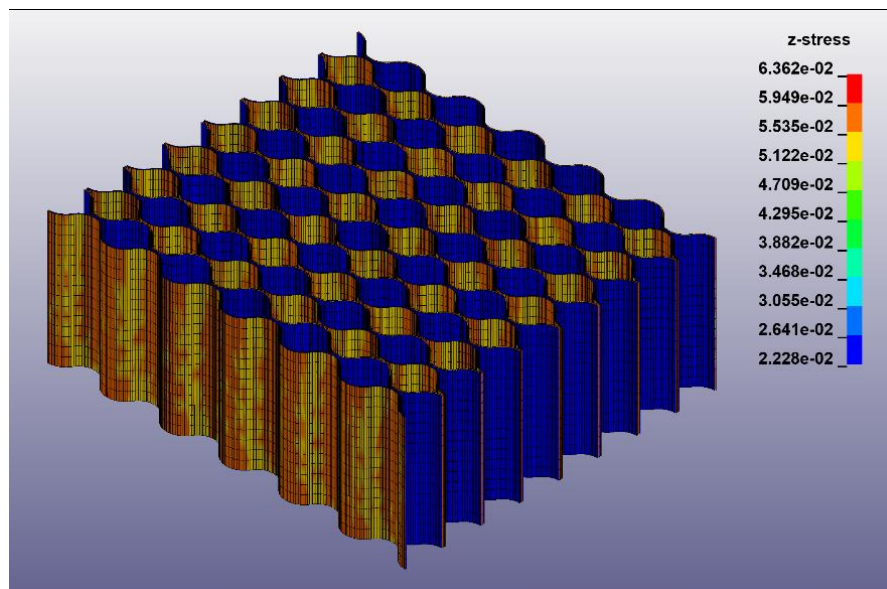


Figure 6.14 - Thermal stress [GPa] t -direction component

The compression out-of-plane test was simulated modelling two steel plates at the top and bottom of the sample. Given that deformations in the steel were negligible and not of interest, simple elastic material (MAT_001_ELASTIC) was used, with an elastic modulus of 200 GPa and Poisson's ratio of 0.3. The bottom plate was constrained in all the DOF, whereas a prescribed vertical displacement was applied at the top plate. An automatic contact (AUTOMATIC_SINGLE_SURFACE) has been used between the steel plates and the core, with friction coefficients of 0.3 (static) and 0.2 (dynamic). Given that half of the fibers are loaded axially, it is expected that the results are strongly influenced by the defects in the structure, i.e. misalignment of the fibers. In order to take this aspect into consideration, the

simulated test was performed for different percentages of defected nodes in the model, simulated as random dislocations (in the range of ± 0.05 mm, that is half of the shell thickness) of the nodes' coordinates. The defected nodes were also considered during the thermal simulation step. Figure 6.15 shows the resulting stress-strain curves for 0%, 10% and 20% of modified nodes. The results confirm the strong dependence of the out-of-plane mechanical properties of the FEM model from the presence of defects.

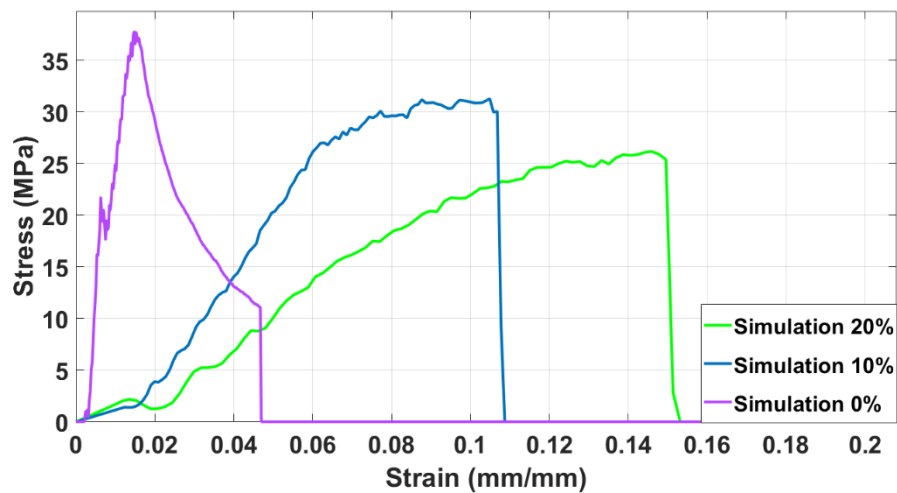


Figure 6.15 - FEM analysis stress-strain curves of compression-out-of-plane simulated tests at various percentages of modified nodes

In-plane compressive tests along the l and w directions were also simulated with the same parameters and boundary conditions. Results will be illustrated and discussed in section 6.2. In order to validate the numerical model, core samples were manufactured using the fiber orientation analysed through the numerical model (alternating $[0,90]_s$ and $[90,0]_s$) and experimentally tested.

4. Materials and Methods

The structure of the CPCC is based on a 2D *close-packing* pattern of circular cells, that is the geometrical arrangements that allows the largest number of cells per unit area, with walls fabricated using CFRP prepreg layers. The fibre orientations were chosen in order to optimise the mechanical properties along the thickness of the

core (90°) and the length of the layer (0°) (out-of-plane and in-plane directions, respectively) and to activate the thermal prestresses due to the asymmetry of the thermal properties. Unlike aluminium, CFRP prepreg layers can be co-cured at the joining points between the strips, generating the cells without the need of external adhesives, thus avoiding the generation of discontinuities in the material structure.

The material used is the UD HS200 ER450 epoxy resin pre-preg with HS Carbon T700 24k fibres produced by CIT Composite Materials. The stripes were prepared by layering two plies of prepreg in a $[0, 90]$ configuration. The different coefficient of thermal expansions of resin and fibres, coupled with the laminate asymmetry, generates residual thermal stresses when the material is exposed to a strong thermal shock, as previously described. During the manufacturing of the laminates, the air trapped between the two layers of each laminate strip was eliminated with a 15 minutes vacuum process using an ultrasonic consolidation technique, which improves the removal of interlaminar air and, thus, the mechanical properties of the final part [72].

In order to reproduce the circular cell honeycomb structure, a fixture, illustrated in Figure 6.16, was designed and manufactured, consisting of a double rail system, two bases and up to 30 pins per row with a diameter of 5 mm.

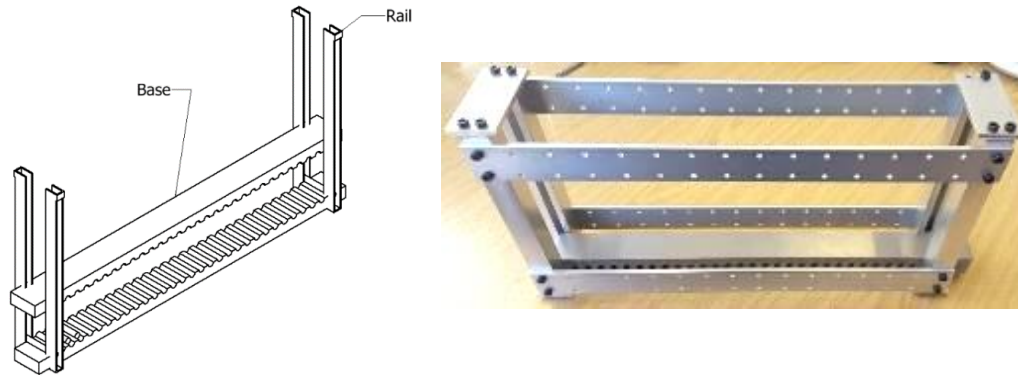


Figure 6.16 - CPCC manufacturing fixture

A release agent was applied three times on all the surfaces of the fixture in order to guarantee an easy removal of the pins after the cure and avoid damaging the material. The lay-up process starts from a line of pins placed on the lower base (respectively in blue and grey in Figure 6.17.a); after this, a first $[0, 90]$ CFRP layer is positioned, following the curves of the pins (in purple in Figure 6.17.b); another row of pins is then placed on the upper side of the CFRP layer in the concavities between the pins of first row (Figure 6.17.c); at this point, another CFRP layer can be placed in the same manner of the first one, but with opposite orientation $[90, 0]$, and attached to the first layer in the spaces between the pins, forming the circular cells (Figure 6.17.d); the process continues in with the described steps until the desired dimension is obtained and the upper base is positioned. The lateral rails were added in order to limit the horizontal movement of the pins and bases and control the horizontal (l) dimension.

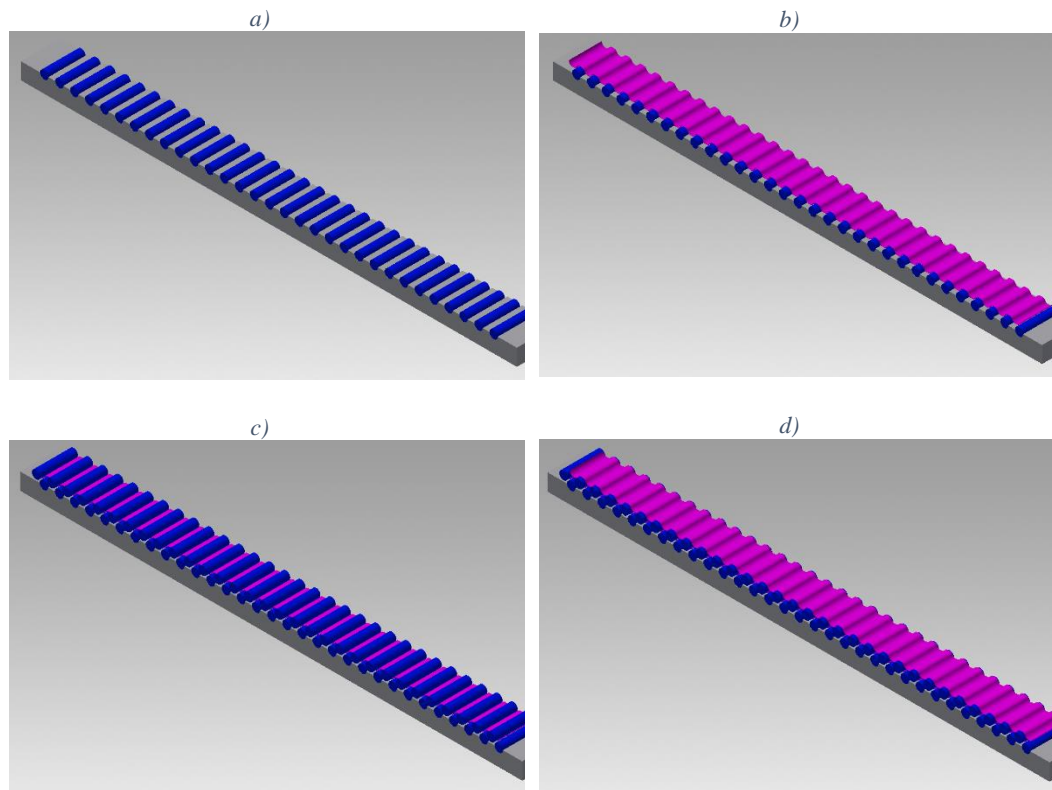


Figure 6.17 - CPCC lay-up steps: a) the first row of pins (blue) is placed in the base (grey) grooves; b) the first CFRP layer (purple) is placed on top of the pins; c) another row of pins is placed on the CFRP layer following the pattern of spaces left from pins of the first row; d) a second CFRP layer is positioned on the second row of pins

During the cure cycle, pressure was applied between upper and lower supports in order to consolidate the material while the joints are squeezed between the layers. Figure 6.18 illustrates a finished lay-up process, with CFRP layers and pins compressed between the two bases. A cure cycle of 2.5 hours at 130 °C was applied, followed by a water-cooling cycle from 130 °C to 5 °C in around 10 seconds to insure generation of thermal stresses. A fast cooling is necessary to not allow time for the polymer matrix crystalline structure to adapt and relax the residual stresses. The pins were removed after the cooling cycle, leaving circular empty spaces (cells) in the laminate.

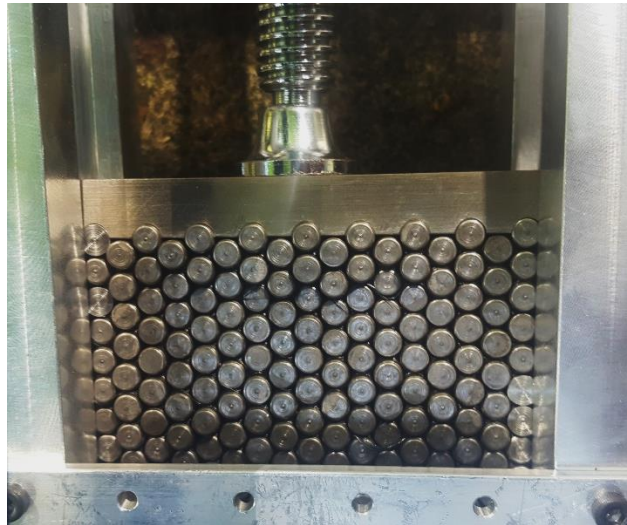


Figure 6.18 - Manufacturing of CPCC samples

As mentioned above, the $[0, 90]$ strips were stacked in an alternate way, so that the side of a strip will face the side with the same fiber orientation in the next strip, creating symmetry at the cells' interfaces. A schematic representation of the fibre orientation in the core is shown in Figure 6.19.a. Following this procedure, the in-plane components of the thermal prestresses in a strip will be oriented in the opposite direction to the ones in the adjacent strip, improving the mechanical response of the core, as previously proved with the FEM analysis. The final product, showed in Figure 6.19.b, has a cellular dimension of 5 mm and a density of 0.225 g/cm^3 ; this value is in accordance with the analytical predicted value of 0.228 g/cm^3 .

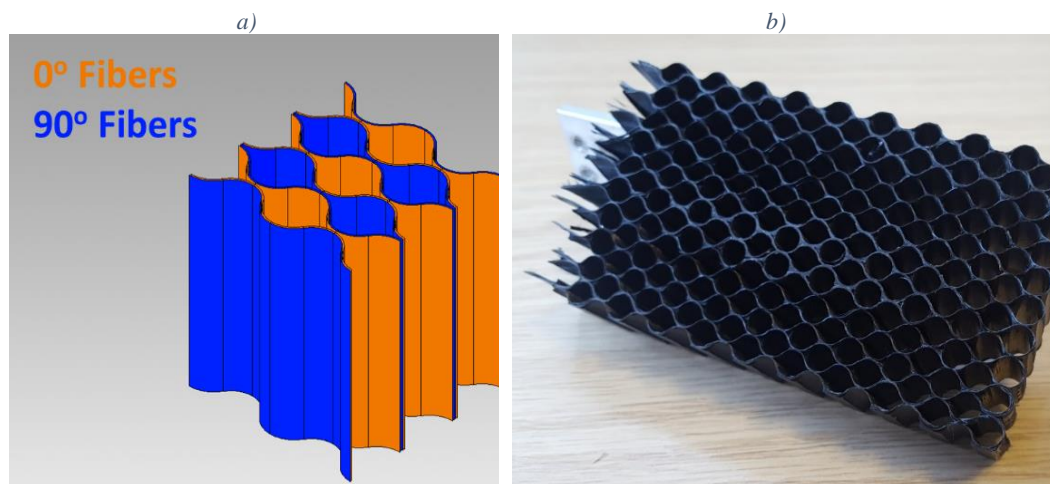


Figure 6.19 - CPCC a) fibre orientation and b) final product

5. Experimental investigation

As shown by Gibson et al. [1], the contribution of the core in the mechanical behaviour of a sandwich structure mainly depends on its compressive and shear properties. Based on this, an experimental campaign consisting of four mechanical tests (compression out-of-plane, compression in-plane along l and w directions and beam flexure) was carried out in order to determine the compressive and shear properties of the CPCC core.

Core samples were tested under flatwise out-of-plane compression load, following the ASTM C 365-03 [73] standard. The samples were tested without any support (bare compression test, see Figure 6.20.a) and with a cross-head displacement rate of 0.75 mm/min. Following the same standard, flatwise in-plane compression tests (Figure 6.20.b) were performed in the two principal planar directions: l , along the long edge of the strips, and w , perpendicular to it. A cross-head displacement rate of 0.5 mm/min was used.

Shear properties of the core were evaluated through a beam flexure test, following the standard ASTM C 393-16 [74]. The test consists of applying a bending moment to a beam of sandwich structure along the out-of-plane direction. In order to perform the test, sandwich samples were manufactured using CPCC core with 1 mm aluminium skins bonded with 3Mtm adhesive film AF 555 (see Figure 6.20.c). Support and loading bars consisting of 25 mm diameter steel cylinders were used, with a displacement rate of 0.2 mm/min, as suggested by the standard.

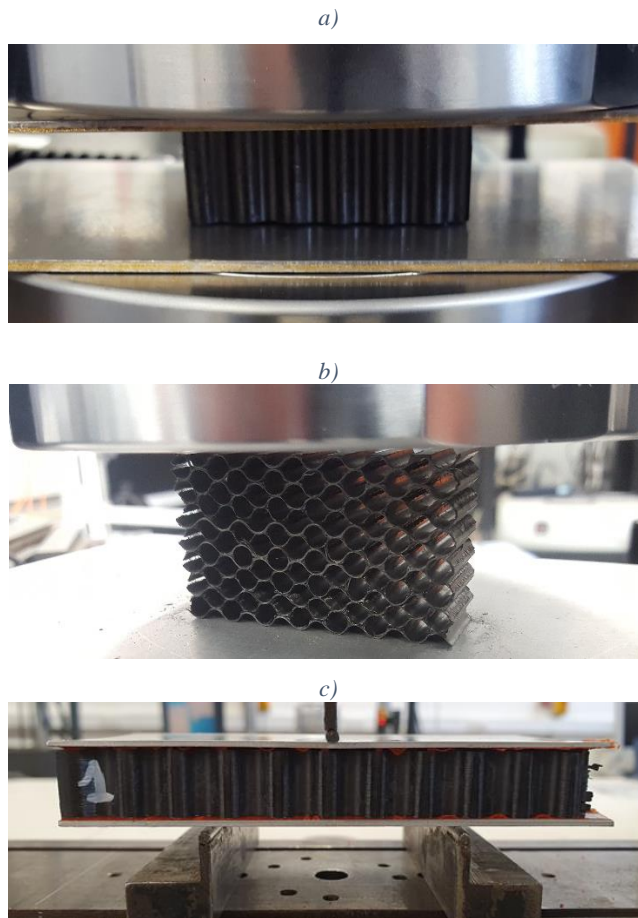


Figure 6.20 - CPCC mechanical tests: a) compression out-of-plane; b) compression in-plane (w direction); c) beam flexure

In order to have a comparison of the mechanical properties with core materials currently in use in advanced engineering applications, the results were compared with those obtained from tests on aluminium honeycomb core. The material used to manufacture the aluminium samples is the HexWeb[®] CR-PAA Honeycomb provided by Hexcel[®]. The core consists of expanded aluminium strips with a thickness of 0.076 mm, bonded together by adhesive layers, and has a density of 0.130 g/cm³. Cell-size, wall thickness and density of the two cores are compared in Table 6.3.

Table 6.3 - Cores specifications

	Cell-size	Wall thickness	Density ρ^*	Relative Density ρ^*/ρ^s
<i>CPCC</i>	5 mm	0.422 mm	0.225 g/cm ³	0.144
<i>Aluminium honeycomb</i>	4.762 mm	0.076 mm	0.130 g/cm ³	0.099

6. Results and discussions

6.1. Experimental results

The stress-strain curves resulting from out of plane, l and w in-plane compression and beam flexure tests on CPCC samples (labelled CPCC) are plotted and compared with samples with same dimensions made of traditional aluminium honeycomb (labelled H). The relative properties of the cores are also calculated and compared in terms of percentage variations.

Figure 6.21 shows the stress-strain curves for the compression out-of-plane test. As can be seen from the curves, the CPCC samples support higher stresses during the test. It is also clear that the area under the CPCC curves is larger than the one under the H curves, as it will be proved by the calculation of the energy absorbed under compression further in this section.

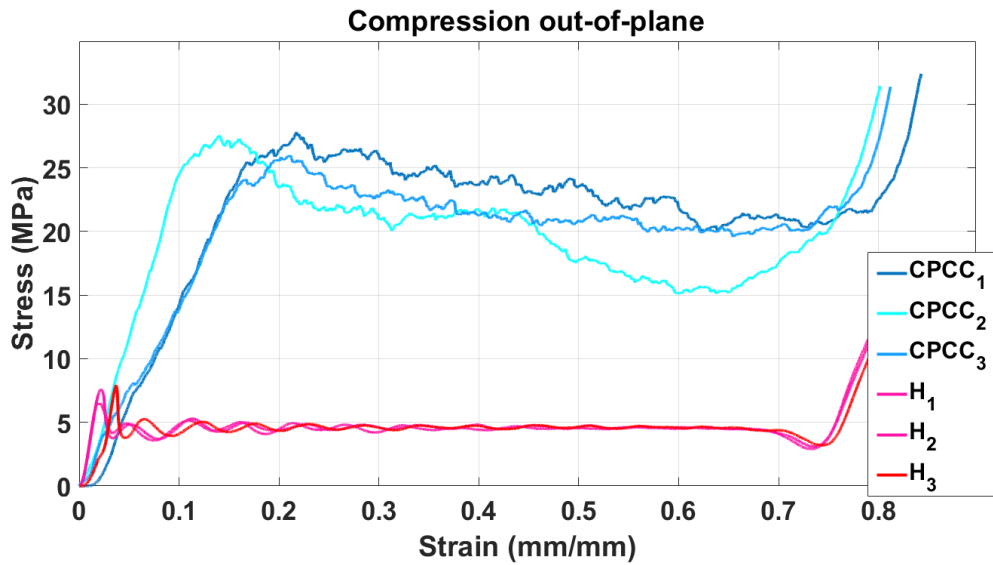


Figure 6.21 - Compression out-of-plane stress-strain curves of CPCC and honeycomb samples

Figure 6.22 illustrates a magnification of the elastic part of the stress-strain curves of the CPCC samples. The three samples show at first a higher modulus, but the slope changes for samples 1 and 3 at different values of stress, as highlighted in the image. This change in slope of the linear elastic part has been observed in honeycomb cores by Wilbert et al. [75] and explained as the start point of the elastic buckling of the thin cell walls, which strongly depends on the defects in the structure, explaining the difference between the curves. At the end of the tests, all the samples presented positive peaks at similar values of strain, which is typically due to the densification of the core.

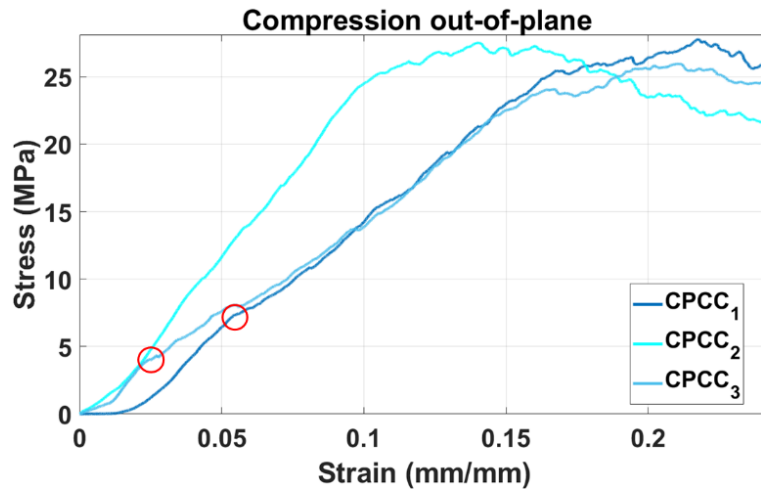


Figure 6.22 - Compression out-of-plane stress-strain curves of CPCC samples: elastic part detail

Local brittle failures were observed during the test, which lead to the macroscopic pseudoplastic crush of the core, that corresponds to the plateau of the stress-strain curves in Figure 6.21. As it is possible to note from the comparison with the honeycomb curves, the brittle nature of the CFRP material leads to more oscillations during the compression, but at higher values of stress.

The compression in-plane stress-strain curves are plotted in Figure 6.23.a for the l direction and Figure 6.23.b for the w direction. CPCC samples supported higher values of loads along the in-plane directions in comparison with honeycomb. Also, it is possible to notice that the CPCC curves showed more oscillations after the linear elastic part. As for the compression out-of-plane, these oscillations may be correlated to the opening of cracks and delamination of the CFRP material that creates numerous local small failures during the crush of the core.

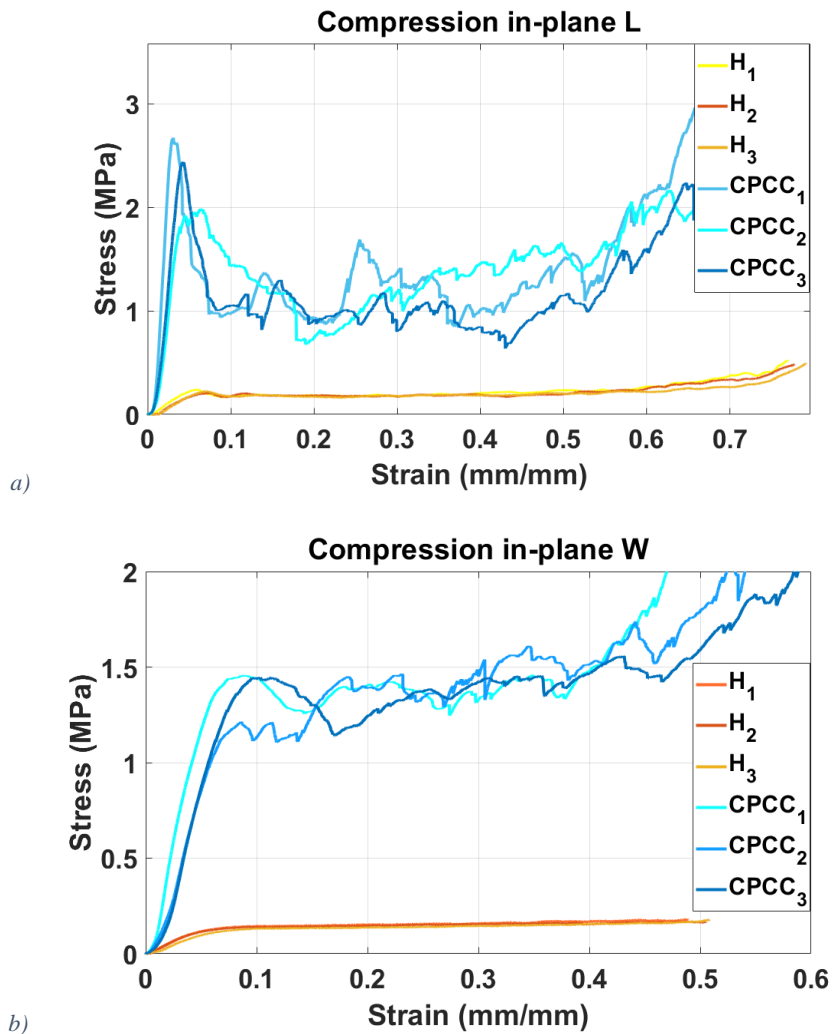


Figure 6.23 - Compression in-plane stress-strain curves along a) L and b) W directions

In Figure 6.24, the in-plane crush failures of the cores are illustrated for the CPCC (a and b) and aluminium honeycomb (c and d). The failure of the two kinds of core is very similar for the in-plane compression along the l direction (a and c in figure), as predicted in the analytical evaluation of the elastic modulus in section 2: the failure happens for bending of the single walls. The failure along this direction is therefore strongly influenced by the material and thickness of the single cell walls: the CFRP will show higher mechanical properties (modulus and strength) with local brittle failures of the cell walls (large oscillations in the plastic part of the curve).

On the other side, the failure for compression along the w direction (b and d in figure) is instead very different between the two cores. For the CPCC, the stress is

distributed in an “arch” shape, reflecting the circular shape of the unit-cell along the direction perpendicular to the load, whereas the aluminium honeycomb presents a “X” shape, and the cells fold in the middle of the sample. This diversity is mainly due to the different cell geometry and material properties. Indeed, given the “arch” deformed shape, the stress will be carried by the fibers distributed along the circular walls for the CPCC, providing high mechanical properties.

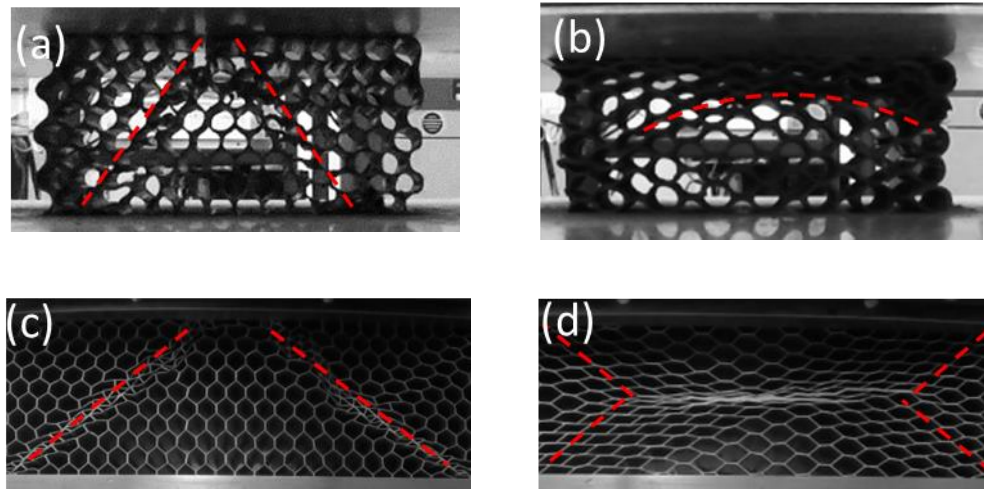


Figure 6.24 - In-plane compressive failure of CPCC (a) (l-direction) and (b) (w-direction) and aluminium honeycomb (c) (l-direction) and (d) (w-direction)

Figure 6.25 shows the flexural stress-strain curves of the CPCC and aluminium honeycomb samples calculated from the beam flexure tests. The curves are very similar for the two materials and the difference in terms of carried stress is less clear than in the previous tests, but an improvement in terms of modulus and failure stress is still notable. The failure happened at the upper interface between core and skin for all the samples, as shown in Figure 6.26. This kind of failure is acceptable by the standard and can be used as value of comparison between the two cores since the same kind and dimensions of both the adhesive layers and skins were used. Therefore, a larger value of ultimate stress in this test would mean a better interface strength between the core and the adhesive layer. The adhesive used to manufacture the sandwich samples is an epoxy resin-based material generally used in high performance applications of sandwich structures with honeycomb cores. The higher bonding resistance of the samples with CPCC core can be attributed to two reasons:

the chemical compatibility between core and adhesive materials, since they are both based on an epoxy resin matrix, and the higher contact surface given by the larger thickness of the CPCC walls. These two factors led to a stronger sandwich structure capable of carrying higher values of flexural load.

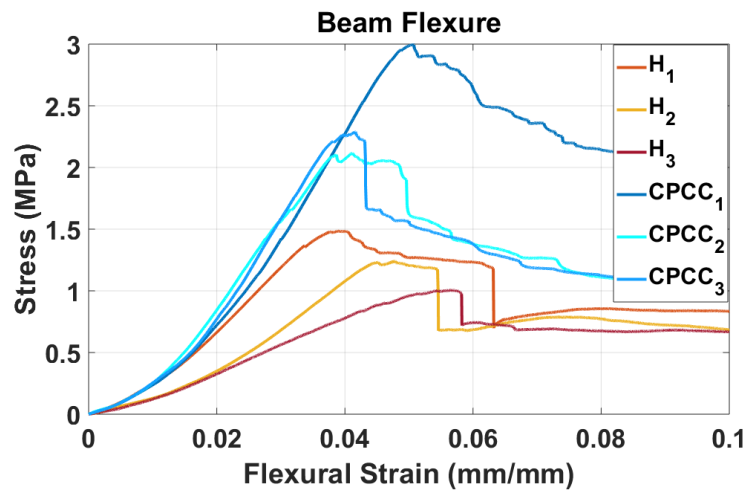


Figure 6.25 - Beam flexure stress-flexural strain curves



Figure 6.26 - Detail of failure between the core and upper skin during the beam flexure test

For the compressive tests, modulus and ultimate strength were calculated as follow:

$$E = \frac{S \cdot t}{A}$$

$$\sigma = \frac{F_{max}}{A}$$

where E is the compressive modulus (MPa), S is the slope of the initial linear portion of load-displacement curve (N/mm), t is the core thickness along the loading direction (mm), A is the cross sectional area (mm²), σ is the ultimate compressive strength (MPa) and F_{max} is the maximum compressive force (N).

In order to take into consideration, the difference in density between the two cores, the energy absorbed per unit mass of the material, called Specific Energy Absorption (SEA), was calculated using the following equation:

$$SEA = \frac{e}{m} = \frac{\int_0^{s_f} F ds}{m}$$

Where m is the sample mass (g), s_f is the final length before material compaction and e is the energy absorbed during the test (J), calculated by integrating under the load (F)-displacement (s) curve [76].

The core shear modulus and ultimate strength were calculated as follow:

$$G = \frac{S \cdot t}{A}$$

$$\tau = \frac{F_{max}}{(d + t)b}$$

here G is the core shear modulus (MPa), τ is the shear ultimate strength (MPa), F_{max} the maximum force prior to failure (N), d and t are respectively the sandwich and core thicknesses (mm) and b is the sandwich width (mm).

Table 6.4 and Table 6.5 summarise the results of the mechanical tests performed on the two cores.

Table 6.4 - Mechanical tests results mean values, standard deviation in brackets: compression out-of-plane and compression in-plane L

	Compression out-of-plane			Compression in-plane l	
	E [MPa]	σ [MPa]	SEA [J/g]	E [MPa]	σ [MPa]
CPCC	235.9 (22.6)	27.1 (.98)	70.04 (5.96)	81.15 (31.1)	2.365 (.349)
Aluminium honeycomb	382.0 (122.8)	8.40 (1.56)	28.48 (.23)	5.54 (.79)	0.222 (.015)

Table 6.5 - Mechanical tests results mean values, standard deviation in brackets: compression in-plane *w* and beam flexure

	<i>Compression in-plane w</i>		<i>Beam flexure</i>	
	<i>E</i> [MPa]	σ [MPa]	<i>G</i> [MPa]	τ [MPa]
<i>CPCC</i>	26.23 (4.68)	1.45 (.006)	66.18 (5.16)	2.47 (.47)
<i>Aluminium honeycomb</i>	2.36 (.24)	0.146 (.005)	30.28 (8.23)	1.24 (0.24)

In order to take into account the difference between the densities of the two cores, specific properties were calculated dividing the values by the density of the material. The resulting properties are the specific modulus and specific strength, also known as specific stiffness and strength-to-weight ratio. Specific properties, listed in Table 6.6 and Table 6.7, allow a reliable comparison between the mechanical properties of the two cores. The comparison is expressed as percentage variation of the CPCC results respect to the aluminium honeycomb ones and summarised in Table 6.8.

Table 6.6 - Specific Mechanical tests results mean values: compression out-of-plane and compression in-plane *L*

	<i>Compression out-of-plane</i>			<i>Compression in-plane l</i>	
	$\frac{E}{\rho}$ [Pa m ³ /g]	$\frac{\sigma}{\rho}$ [Pa m ³ /g]	<i>SEA</i> [J/g]	$\frac{E}{\rho}$ [Pa m ³ /g]	$\frac{\sigma}{\rho}$ [Pa m ³ /g]
<i>CPCC</i>	1048.4	120.4	70.04	360.7	10.51
<i>Aluminium honeycomb</i>	2938.5	64.61	28.48	42.61	1.71

Table 6.7 – Specific mechanical tests results mean values: compression in-plane *W* and beam flexure

	<i>Compression in-plane w</i>		<i>Beam flexure</i>	
	$\frac{E}{\rho}$ [Pa m ³ /g]	$\frac{\sigma}{\rho}$ [Pa m ³ /g]	$\frac{G}{\rho}$ [Pa m ³ /g]	$\frac{\tau}{\rho}$ [Pa m ³ /g]
<i>CPCC</i>	116.6	6.44	294.1	10.98
<i>Aluminium honeycomb</i>	18.15	1.12	232.9	9.54

Table 6.8 - Specific mechanical properties percentage variation between aluminium honeycomb and CPCC

	<i>Compression out-of-plane</i>			<i>Compression in-plane L</i>		<i>Compression in-plane W</i>		<i>Beam flexure</i>	
	$\frac{E}{\rho}$	$\frac{\sigma}{\rho}$	<i>SEA</i>	$\frac{E}{\rho}$	$\frac{\sigma}{\rho}$	$\frac{E}{\rho}$	$\frac{\sigma}{\rho}$	$\frac{G}{\rho}$	$\frac{\tau}{\rho}$
<i>Variations [%]</i>	-64.3	86.4	145.9	746.3	515.5	542.2	473.8	26.3	15.1

As shown by the percentage variations, there is a clear improvement in almost all the measured specific mechanical properties, with a minimum advantage of +15.1% in shear ultimate strength and a maximum of 746.3% increase in in-plane compressive modulus along *L* direction. Particularly interesting is also the increment in SEA (+ 145.9%), that is an important parameter that describes the energy absorbed by the core during the crushing. Furthermore, the higher value of shear ultimate strength leads to a better compatibility of the CPCC core to the adhesive material, increasing the mechanical properties of the sandwich structure.

The only mechanical decrement has been found in the out-of-plane compressive modulus (~60%). This result was unexpected, because the CFRP compressive modulus in [0, 90] configuration should be theoretically equal or higher than the aluminium one when loaded in compression along one of the fibres directions. This mechanical decrement in compressive modulus may be caused by manufacturing defects: strips misalignment, variations of fibres orientation, low pressure applied

during the cure, not-flat specimens' edges, operator errors, etc. These defects can be reduced or eliminated with an automatic manufacturing process. The influence of the defects on the compressive modulus of the core will be numerically proved. Xiong et al. [31] provided the Ashby's modified chart for out-of-plane compressive strength vs. density for materials with low density (under 2000 kg/m^3). This chart is shown in Figure 6.27 where the results from this work have been added in the yellow circle named CPCC. As it can be seen from the chart, the compressive strength to density ratio of CPCC core falls in a new region for these typologies of cores. The only materials with comparable values of compressive strength, such as carbon fiber honeycombs and natural materials, present considerable higher densities. This comparative result highlights the importance and novelty of this work, obtaining values of compressive strength to density ratio not available in literature.

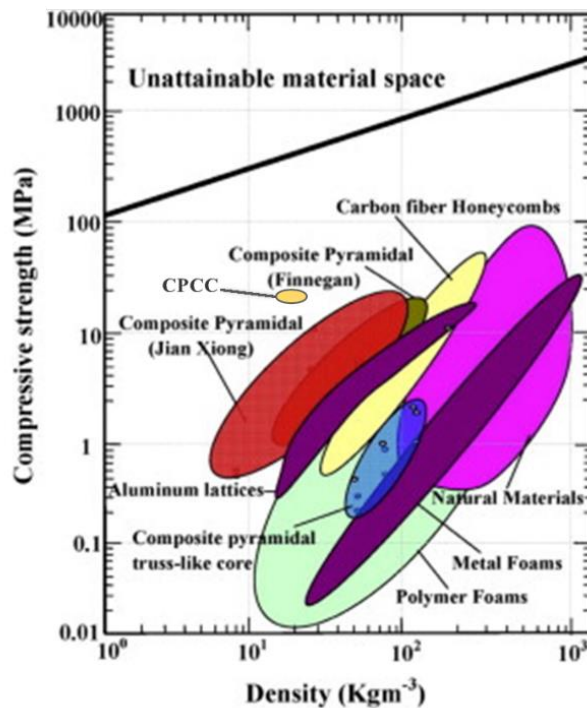


Figure 6.27 - Modified Ashby's chart for compressive strength vs. density for low density materials. Original figure from [31]

6.2. Numerical results

In order to validate the unit-cell numerical model, the Young's moduli of the cell loaded under out-of-plane and in-plane compression have been calculated and compared to the ones analytically obtained. As it is possible to see in Table 6.9, the FEM and analytical values match with small variations (under $\pm 10\%$). In addition, the failure of the samples during the experimental tests along the in-plane directions validates the analytical approximation to hexagonal and elliptical geometries when loaded along the l and w directions, respectively.

Table 6.9 - Unit-cell elastic moduli: analytical and FEM evaluations

	E_t^*	E_l^*	E_w^*
<i>Analytical</i>	10.53 GPa	234 MPa	111 MPa
<i>FEM</i>	11.03 GPa	256 MPa	117 MPa

The results of out-of-plane compression of the experimental and FEM analysis tests of the core samples are compared in Figure 6.28. A displacement was applied to the defected nodes in the range of ± 0.05 mm using the Matlab random function in order to simulate the material defects. The stress strain curves resulting from FEM analysis present sudden drop to zero at the points where the solver is not able to find solution convergence, thus interrupting the calculations, however the FEM curve that matches the experimental data is the one obtained from the 20% modified nodes model. Given that the modulus is decreasing with the percentage of modified nodes, it is possible to confirm that, as previously hypothesized, the low values of E_t are due to the manufacturing defects, and thus can be improved by means of automated manufacturing processes.

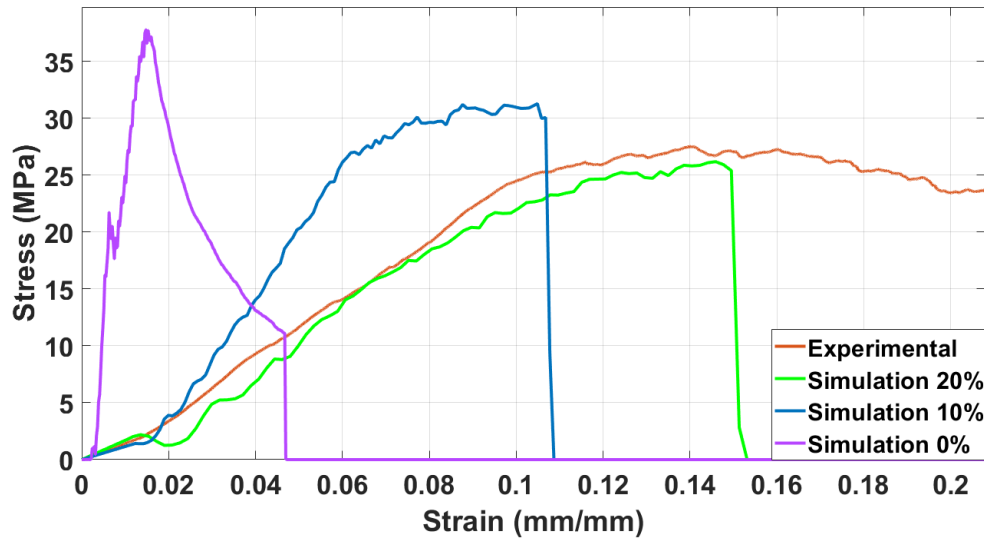


Figure 6.28 - Compression out-of-plane stress-strain curves, comparison between numerical and experimental results

In-plane compressive tests were simulated using the same FEM parameters and with 20% of damaged nodes. Experimental and numerical analyses results for the in-plane compression tests along w and l directions are compared in Figure 6.29.a and Figure 6.29.b, respectively.

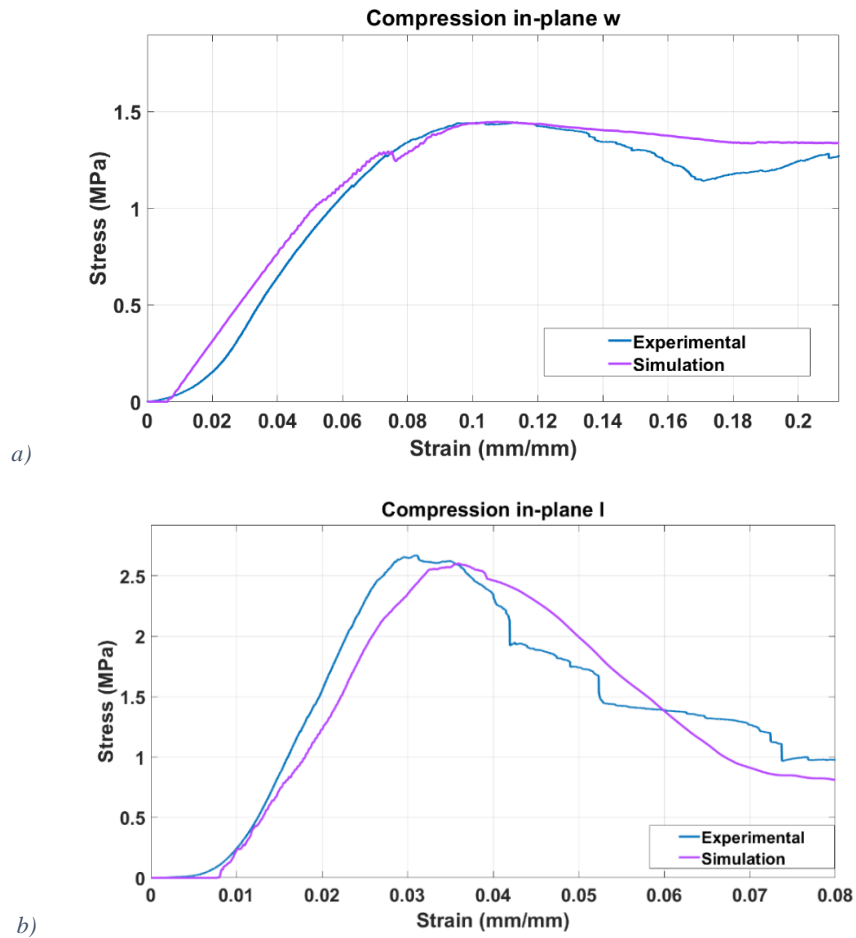


Figure 6.29 - Compression in-plane stress-strain curves in a) w and b) l directions, comparison between numerical and experimental results

The numerical results fit well the experimental curves with a variation in mechanical properties below 10%, proving the validity of the FEM model in the prediction of the mechanical properties of the core.

7. Conclusions

In this work a CFRP core with bistable circular cell structure, named CPCC, is proposed, manufactured and tested. The structure of the core is a circular honeycomb made with CFRP strips and has a cellular size of 5 mm. Thermal induced pre-stresses were applied to the material during the manufacturing in order to increase the energy absorption capability of the core exploiting the bistable behaviour of the asymmetric laminates. The CPCC was designed with the aim of

taking advantage of carbon fibre reinforcement along the out-of-plane and in-plane directions, in order to give high mechanical properties where more needed.

FEM analyses of the cell wall, unit cell and core sample were performed to predict the residual stress distribution generated during the manufacturing of the core. The FEM models were used to study the influence of the fiber configurations on the residual stress and on the crushing behaviour of the unit cell, and to predict the mechanical properties of the core.

CPCC samples were mechanically tested under out-of-plane compression, in-plane compression along two directions and beam flexure and compared with an aluminium honeycomb core. In order to have a consistent comparison with the aluminium core and given the importance of the structural weight in sectors such as aerospace and automotive, specific properties were calculated to take into account the material density. Specific results showed large increments in almost all the characterised mechanical properties in comparison with the aluminium core, with a minimum increment of +15% in specific shear ultimate strength. The highest increments were found to be in in-plane specific compressive properties along both L and W directions, with a maximum of +764% in elastic modulus in L direction.

Numerical results from FEM analysis showed good match with experimental results, thus validating the model. The validated FEM model of the core allows for reduction in future experimental tests and for an optimisation of the core design parameters.

The developed high-performance sandwich core has been proved to provide large improvements in terms of mechanical properties in comparison with the cores currently in use in engineering sectors maintaining a low value of density, and therefore can be employed in high-demanding structural applications.

References

- [1] Gibson LJ, Ashby MF. Cellular solids: structure and properties. Cambridge university press; 1999.
- [2] Akil Hazizan M, Cantwell WJ. The low velocity impact response of an aluminium honeycomb sandwich structure. *Compos Part B Eng.* 2003;34:679–687.
- [3] Akay M, Hanna R. A comparison of honeycomb-core and foam-core carbon-fibre/epoxy sandwich panels. *Composites.* 1990;21:325–331.
- [4] Tavares SS, Caillet-Bois N, Michaud V, et al. Vacuum-bag processing of sandwich structures: Role of honeycomb pressure level on skin-core adhesion and skin quality. *Compos Sci Technol.* 2010;70:797–803.
- [5] Wang Z, Qin Q, Zhang J, et al. Low-velocity impact response of geometrically asymmetric slender sandwich beams with metal foam core. *Compos Struct.* 2013;98:1–14.
- [6] Kulkarni N, Mahfuz H, Jeelani S, et al. Fatigue crack growth and life prediction of foam core sandwich composites under flexural loading. *Compos Struct.* 2003;59:499–505.
- [7] Harte AM, Fleck NA, Ashby MF. The fatigue strength of sandwich beams with an aluminium alloy foam core. *Int J Fatigue.* 2001;23:499–507.
- [8] Harte A-M, Fleck NA, Ashby MF. Sandwich Panel Design Using Aluminum Alloy Foam. *Adv Eng Mater* [Internet]. 2000;2:219–222. Available from: [http://dx.doi.org/10.1002/\(SICI\)1527-2648\(200004\)2:4%3C219::AID-ADEM219%3E3.0.CO%5Cn2-#](http://dx.doi.org/10.1002/(SICI)1527-2648(200004)2:4%3C219::AID-ADEM219%3E3.0.CO%5Cn2-#).
- [9] Zhang G, Ma L, Wang B, et al. Mechanical behaviour of CFRP sandwich structures with tetrahedral lattice truss cores. *Compos Part B Eng.* 2012;43:471–476.
- [10] Finnegan K, Kooistra G, Wadley HNG, et al. The compressive response of carbon fiber composite pyramidal truss sandwich cores. *Zeitschrift fuer Met Res Adv Tech.* 2007;98:1264–1272.
- [11] Côté F, Fleck NA, Deshpande VS. Fatigue performance of sandwich beams with a pyramidal core. *Int J Fatigue.* 2007;29:1402–1412.
- [12] Queheillalt DT, Wadley HNG. Titanium alloy lattice truss structures. *Mater Des.* 2009;30:1966–1975.
- [13] Bitzer T. Honeycomb Technology: materials, design, manufacturing, applications and testing [Internet]. Springer-Science+Business Media, B. V.; 1997. Available from: <http://link.springer.com/10.1007/978-94-011-5856-5>.

- [14] Xiong J, Ma L, Wu L, et al. Fabrication and crushing behavior of low density carbon fiber composite pyramidal truss structures. *Compos Struct.* 2010;92:2695–2702.
- [15] Ashby MF, Bréchet YJM. Designing hybrid materials. *Acta Mater.* 2003;51:5801–5821.
- [16] Russell B, Deshpande V, Wadley H. Quasistatic deformation and failure modes of composite square honeycombs. *J Mech Mater Struct [Internet]*. 2008;3:1315–1340. Available from: <http://msp.org/jomms/2008/3-7/p07.xhtml>.
- [17] Petrone G, Rao S, Rosa S De, et al. Vibration characteristics of fiber reinforced honeycomb panels : experimental study. *Proc ISMA 2012 Conf. Leuven, Belgium*; 2012. p. 1911–1920.
- [18] Petrone G, Rao S, De Rosa S, et al. Initial experimental investigations on natural fibre reinforced honeycomb core panels. *Compos Part B Eng.* 2013;55:400–406.
- [19] Petrone G, Rao S, De Rosa S, et al. Behaviour of fibre-reinforced honeycomb core under low velocity impact loading. *Compos Struct.* 2013;100:356–362.
- [20] Jin F, Chen H, Zhao L, et al. Failure mechanisms of sandwich composites with orthotropic integrated woven corrugated cores: Experiments. *Compos Struct.* 2013;98:53–58.
- [21] Fan H, Zhao L, Chen H, et al. Ductile deformation mechanisms and designing instructions for integrated woven textile sandwich composites. *Compos Sci Technol.* 2012;72:1338–1343.
- [22] Fan H, Zhou Q, Yang W, et al. An experiment study on the failure mechanisms of woven textile sandwich panels under quasi-static loading. *Compos Part B Eng.* 2010;41:686–692.
- [23] Fan H, Yang W, Zhou Q. Experimental research of compressive responses of multi-layered woven textile sandwich panels under quasi-static loading. *Compos Part B Eng.* 2011;42:1151–1156.
- [24] Brandt J, Drechsler K, Arendts FJ. Mechanical performance of composites based on various three-dimensional woven-fibre preforms. *Compos Sci Technol.* 1996;56:381–386.
- [25] Fan HL, Meng FH, Yang W. Sandwich panels with Kagome lattice cores reinforced by carbon fibers. *Compos Struct.* 2007;81:533–539.
- [26] Fan HL, Meng FH, Yang W. Mechanical behaviors and bending effects of carbon fiber reinforced lattice materials. *Arch Appl Mech.* 2006;75:635–647.
- [27] Russell BP, Liu T, Fleck NA, et al. The soft impact of composite sandwich beams with a square-honeycomb core. *Int J Impact Eng.* 2012;48:65–81.

- [28] Russell BP, Liu T, Fleck NA, et al. Quasi-Static Three-Point Bending of Carbon Fiber Sandwich Beams With Square Honeycomb Cores. *J Appl Mech* [Internet]. 2011;78:031008. Available from: <http://appliedmechanics.asmedigitalcollection.asme.org/article.aspx?articleid=1418319>.
- [29] Xiong J, Vaziri A, Ghosh R, et al. Compression behavior and energy absorption of carbon fiber reinforced composite sandwich panels made of three-dimensional honeycomb grid cores. *Extrem Mech Lett*. 2016;7:114–120.
- [30] Xiong J, Ma L, Pan S, et al. Shear and bending performance of carbon fiber composite sandwich panels with pyramidal truss cores. *Acta Mater*. 2012;60:1455–1466.
- [31] Xiong J, Ma L, Wu L, et al. Mechanical behavior and failure of composite pyramidal truss core sandwich columns. *Compos Part B Eng*. 2011;42:938–945.
- [32] Fan H, Yang L, Sun F, et al. Compression and bending performances of carbon fiber reinforced lattice-core sandwich composites. *Compos Part A Appl Sci Manuf*. 2013;52:118–125.
- [33] Fan H, Yang W, Wang B, et al. Design and manufacturing of a composite lattice structure reinforced by continuous carbon fibers. *Tsinghua Sci Technol*. 2006;11:515–522.
- [34] Alia R, Al-Ali O, Kumar S, et al. The energy-absorbing characteristics of carbon fiber-reinforced epoxy honeycomb structures. *J Compos Mater* [Internet]. 2019 [cited 2021 Mar 29];53:1145–1157. Available from: <http://journals.sagepub.com/doi/10.1177/0021998318796161>.
- [35] Hsiao HM, Lee SM, Buyny RA. Core crush problem in manufacturing of composite sandwich structures: Mechanisms and solutions. *AIAA J*. 2006;44:901–907.
- [36] Oruganti RK, Ghosh AK. FEM analysis of transverse creep in honeycomb structures. *Acta Mater*. 2008;56:726–735.
- [37] Swanson S. Introduction to design and analysis with advanced composite materials. 1997.
- [38] Gibson RF. Principles of Composite Material Mechanics. 1994; Available from: <http://www.loc.gov/catdir/toc/ecip0714/2007013616.html>.
- [39] Davies GAO, Olsson R. Impact on composite structures. *Aeronaut. J*. 2004.
- [40] Tissington B, Pollard G, Ward IM. A study of the impact behaviour of ultra-high-modulus polyethylene fibre composites. *Compos Sci Technol*. 1992;
- [41] Yuan Q, Wu D, Gotama J, et al. Wood fiber reinforced polyethylene and polypropylene composites with high modulus and impact strength. *J*

Thermoplast Compos Mater. 2008;21:195–208.

- [42] Ko FK, Hartman D. Impact behavior of 2-d and 3-d glass/epoxy composites. 31st Int SAMPE Symp Exhib 1986 Mater Sci Futur. 1986.
- [43] Liu D. Delamination resistance in stitched and unstitched composite plates subjected to impact loading. *J Reinf Plast Compos*. 1990;9:59–69.
- [44] Lopresto V, Melito V, Leone C, et al. Effect of stitches on the impact behaviour of graphite/epoxy composites. *Compos Sci Technol*. 2006;66:206–214.
- [45] Bunsell AR, Harris B. Hybrid carbon and glass fibre composites. *Composites*. 1974;
- [46] Naik NK, Ramasimha R, Arya H, et al. Impact response and damage tolerance characteristics of glass–carbon/epoxy hybrid composite plates. *Compos Part B Eng*. 2001;32:565–574.
- [47] Marom G, Drukker E, Weinberg A, et al. Impact behaviour of carbon/Kevlar hybrid composites. *Composites*. 1986;
- [48] Bradley PD, Harris SJ. Strategic reinforcement of hybrid carbon fibre-reinforced polymer composites. *J Mater Sci*. 1977;
- [49] Pinto F, Rizzo F, Meo M. Impact resistant smart hybrid laminates. *Proc SPIE - Int Soc Opt Eng*. 2017;
- [50] Scarselli G, Nicassio F, Pinto F, et al. A novel bistable energy harvesting concept. *Smart Mater Struct*. 2016;25.
- [51] Nawy EG. *Prestressed concrete : A fundamental approach*. 2nd ed. Upper Saddle River N.J.: Prentice Hall; 1996. p. 789.
- [52] Winkelmann C, Kim SS, La Saponara V. Design and development of hybrid composite bistable structures for energy absorption under quasi-static tensile loading. *Compos Struct* [Internet]. 2010;93:171–178. Available from: <http://dx.doi.org/10.1016/j.compstruct.2010.06.002>.
- [53] Whitman Z, La Saponara V. Bistable structures for energy absorption, I: Metallic structures. *J Mech Mater Struct*. 2007;2:347–358.
- [54] Whitman Z, Saponara V La. Bistable Structures for Energy Absorption II. Composite Structures under Tension. *J Mech Mater Struct*. 2007;
- [55] Keadze E, Guest SD, Pellegrino S. Bistable prestressed shell structures. *Int J Solids Struct*. 2004;41:2801–2820.
- [56] Schultz MR, Hulse MJ, Keller PN, et al. Neutrally stable behavior in fiber-reinforced composite tape springs. *Compos Part A Appl Sci Manuf*. 2008;39:1012–1017.
- [57] Diaconu CG, Weaver PM, Mattioni F. Concepts for morphing airfoil sections

- using bi-stable laminated composite structures. *Thin-Walled Struct.* 2008;46:689–701.
- [58] Hyer MW. Some observations on the curved shapes of thin unsymmetric laminates. *J Compos Mater.* 1981;15:175–194.
- [59] M.Jones R. *Mechanics of Composite Materials.* Mech. Compos. Mater. 1983.
- [60] Dano ML, Hyer MW. Thermally-induced deformation behavior of unsymmetric laminates. *Int J Solids Struct* [Internet]. 1998 [cited 2020 May 13];35:2101–2120. Available from: [http://dx.doi.org/10.1016/S0020-7683\(97\)00167-4](http://dx.doi.org/10.1016/S0020-7683(97)00167-4).
- [61] Daynes S, Diaconu CG, Potter KD, et al. Bistable prestressed symmetric laminates. *J Compos Mater.* 2010;44:1119–1137.
- [62] Yang X, Asce AM, Wei J, et al. Shape Effect on the Performance of Carbon Fiber Reinforced Polymer Wraps. *ascelibrary.org* [Internet]. 2004 [cited 2020 Jul 28];8:444–451. Available from: [https://ascelibrary.org/doi/abs/10.1061/\(ASCE\)1090-0268\(2004\)8:5\(444\)?casa_token=4-Mc2YC8i3UAAAAA:N80-Uh-cSrZ9amlCFpHOFFTZ7pAMosfomJ2_U_lasMZulezIRm85EKDDBxi9yt9Axd3ry8Xwy_s](https://ascelibrary.org/doi/abs/10.1061/(ASCE)1090-0268(2004)8:5(444)?casa_token=4-Mc2YC8i3UAAAAA:N80-Uh-cSrZ9amlCFpHOFFTZ7pAMosfomJ2_U_lasMZulezIRm85EKDDBxi9yt9Axd3ry8Xwy_s).
- [63] Chung J, Waas AM. Inplane elastic properties of circular cell and elliptical cell honeycombs. *Acta Mech.* 2000;144:29–42.
- [64] Ishikawa T, Koyama K, Kobayashi S. Thermal Expansion Coefficients of Unidirectional Composites. *J Compos Mater.* 1978;12:153–168.
- [65] Emam SA, Inman DJ. A Review on Bistable Composite Laminates for Morphing and Energy Harvesting. *Appl Mech Rev.* 2015;67:1–15.
- [66] Dang J, Tang Y. Calculation of the room-temperature shapes of unsymmetric laminates. *Proc Int Symp Compos Mater Struct.* 1986. p. 201–206.
- [67] Jun WJ, Hong CS. Effect of residual shear strain on the cured shape of unsymmetric cross-ply thin laminates. *Compos Sci Technol.* 1990;38:55–67.
- [68] Ryu J, Kong JP, Kim SW, et al. Curvature tailoring of unsymmetric laminates with an initial curvature. *J Compos Mater.* 2013;47:3163–3174.
- [69] Lee JG, Ryu J, Kim SW, et al. Effect of initial tool-plate curvature on snap-through load of unsymmetric laminated cross-ply bistable composites. *Compos Struct* [Internet]. 2015;122:82–91. Available from: <http://dx.doi.org/10.1016/j.compstruct.2014.11.037>.
- [70] Hallquist JO. *LS-DYNA @ THEORY MANUAL* [Internet]. 2006 [cited 2021 Jan 15]. Available from: www.lstc.com.
- [71] Chang F-K, Chang K-Y. Post-Failure Analysis of Bolted Composite Joints

in Tension or Shear-Out Mode Failure. *J Compos Mater* [Internet]. 1987 [cited 2021 Jan 26];21:809–833. Available from: <http://journals.sagepub.com/doi/10.1177/002199838702100903>.

- [72] Flora F, Rizzo F, Pinto F, et al. Ultrasonic consolidation (UC) debulking of thermosetting prepreg for autoclave curing of composite laminates. *Mater Today Proc.* 2021;34:106–112.
- [73] ASTM International. ASTM Standard C365/C365M, 2003, “Standard Test Method for Flatwise Compressive Properties of Sandwich Cores.” *Current* [Internet]. 2003;i:2–4. Available from: www.astm.org.
- [74] ASTM Standard. ASTM C393-16 Standard Test Method for Core Shear Properties of Sandwich Constructions by Beam Flexure. *ASTM Int.* 2016;i:1–7.
- [75] Wilbert A, Jang WY, Kyriakides S, et al. Buckling and progressive crushing of laterally loaded honeycomb. *Int J Solids Struct* [Internet]. 2011;48:803–816. Available from: <http://dx.doi.org/10.1016/j.ijsolstr.2010.11.014>.
- [76] Stamenovic M, Putic S, Zrilic M, et al. Specific Energy Absorption Capacity of Glass-Polyester Composite Tubes Under Static Compressive Loading. *Metalurgija.* 2011;50:197–200.

7. Paper 5: Experimental and numerical analysis of an impact resistant sandwich structure with thermal pre-stressed carbon-fibre reinforced lattice core

The previous chapters illustrated several methodologies aimed to decreasing manufacturing defects and improving mechanical properties and failure resistance of CFRP parts.

Chapter 3 and 4 described a method for reduction of voids content in prepreg laminates. This technique, based on ultrasonic waves, proved to be a valid method to increase some mechanical properties from one side, and decrease manufacturing time from the other. In chapter 6, the author illustrated the design and manufacturing of a novel CFRP core for sandwich structures with residual thermal stresses. This structure showed high mechanical performances and unique strength to density ratio.


In this chapter, these concepts have been collected into the final design of a high-performance sandwich structure. This structure is based on the pre-stressed carbon fibre reinforced lattice core illustrated in chapter 6 and used to design an all-composite sandwich. The sandwich takes advantage of the enhanced mechanical properties of the core and the compatibility with CFRP skins, being made of the same prepreg material. Indeed, the structure does not require an adhesive layer or any kind of third interface between the core and the skins. Moreover, the skins were subjected to the UC debulking illustrated in chapter 3 and 4, during the lay-up and the attachment to the core. Therefore, this sandwich structure is designed to have a reduced possibility to show a premature debonding failure.

The residual thermal stresses, introduced in the core by means of drastic change in temperature during the manufacturing of the same, are known to generate a residual internal moment. This concept has been used in the design phase of the core in such

a way that the residual moment opposes to the predicted failure, thus enhancing the mechanical and energy dissipation properties of the structure during LVI events. In this work, the residual thermal stresses have been proved to improve the impact properties of the structure and reduce the damaged area by experimental and numerical analysis in comparison with a not-prestressed reference. As for the chapter 5, the experimental campaign has been also carried in comparison with aluminium honeycomb sandwich samples, demonstrating the notable improvements provided by the use of the CPCC core, even when specific properties are taken into account. This work has shown the potentiality of the CPCC core to be used to fabricate sandwich structures with unique LVI impact resistance, reducing considerably the damage extension and limiting it around the impact point.

The Statement of Authorship Form and the paper can be found next.

This declaration concerns the article entitled:	
Experimental and numerical analysis of an impact resistant sandwich structure with thermal pre-stressed carbon-fibre reinforced lattice core	
Publication status (tick one)	
Draft manuscript	
Submitted	✓
In review	
Accepted	
Published	
Publication details (reference)	
Flora, F., Pinto, F., & Meo, M. (2022). Experimental and numerical analysis of an impact resistant sandwich structure with thermal pre-stressed carbon-fibre reinforced lattice core. Submitted at <i>Journal of Impact Engineering</i>	
Copyright status (tick the appropriate statement)	
I hold the copyright for this material	✓
Copyright is retained by the publisher, but I have been given permission to replicate the material here	
Candidate's contribution to the paper (detailed, and also given as a percentage)	
The candidate contributed to/ considerably contributed to/predominantly executed the...	

Formulation of ideas:	100%	I provided most of the idea, the hypothesis, the methodology and the experimental tests.	
Design of methodology:	100%	I manufactured all the samples used in the experimental campaign and designed all the experimental tests carried out in the work. I realised the FEM of the sandwich structure and conducted all the numerical analysis.	
Experimental work:	100%	I carried out all the experimental tests, collected all the data, and analysed all the outputs.	
Presentation of data in journal format:	90%	I designed the manuscript structure, wrote all the drafts and realised all. My supervisors provided feedback on the draft and help for the paper review and submission.	
Statement from Candidate			
This paper reports on original research I conducted during the period of my Higher Degree by Research candidature.			
Signed		Date	29/01/2022

Experimental and numerical analysis of an impact resistant sandwich structure with thermal pre-stressed carbon-fibre reinforced lattice core

Francesco Flora¹, Fulvio Pinto¹, Michele Meo^{1*}

¹ *Department of Mechanical Engineering, University of Bath, Bath, Ba2 7AY, UK*

* Corresponding author: m.meo@bath.ac.uk

Keywords: *Sandwich; honeycomb; core; low velocity impact; CFRP; pre-stress.*

Abstract

The interest of aerospace and automotive engineering sectors in the improvement of energy absorption properties of composite materials has stimulated researchers in the design of new typologies of cores and sandwich structures and in the study of their behaviour under impact events. In this work, a sandwich structure based on pre-stressed bistable carbon fibre composite core is studied under low-velocity impact events. The core, named Circular Prestressed Carbon Core (CPCC), takes advantage of the asymmetric fibres orientation and the bistability concept to enhance energy dissipation and reduce the damage extension during impact events. The core is co-cured to the CFRP skins, taking advantage of Ultrasonic Consolidation to remove air and improve the adhesion. The impact campaign was conducted both experimentally and numerically to analyse the mechanical properties of the core and to study the contribution of the residual stresses. Experimental results were compared with an aerospace grade aluminium honeycomb core and a not-prestressed version of the core. Results proved the unique impact characteristics of the core, showing, especially at higher levels of impact energy, an improvement of the maximum force of 171% and 23% in comparison with aluminium honeycomb and not-prestressed CPCC samples, respectively. Furthermore, the specific properties of the CPCC have been demonstrated to be considerably higher than the aluminium sandwich, with peak force values up to +75% and striker penetrating displacement reduced up to -71%, despite the higher density of the first. The NDE of tested samples demonstrated that residual thermal stresses have positively contributed to reduce the energy absorbed in generating damage, with a reduction of the projected damaged area by ~20% and an improvement the residual thickness of the core by ~10%, a showing a damaged area strongly limited around the impact point and also widely outperforming the aluminium honeycomb counterpart. Based on these results it is possible to conclude that the CPCC structure constitutes a novel solution for the manufacturing of high performance sandwich parts particularly prone to impact events.

1. Introduction

Nowadays, composite laminates are widely used for both primary and secondary structures in several engineering sectors: automotive, aerospace, marine, energy, and others [1–4], thanks to the numerous advantages of this kind of materials, such as unique specific mechanical properties, tailorability and corrosion resistance. For the automotive and aerospace sectors, aluminium and other traditional materials have been largely substituted by Carbon fibre reinforced polymers (CFRPs) to improve the mechanical properties whilst reducing the weight of the structures. In these fields, CFRPs laminates are often attached to both sides of a lightweight core in order to increase the bending stiffness of the part in what is commonly called a composite sandwich structure [5].

One of the main advantages in introducing the core into a monolithic laminate to form a sandwich structure is the improvement of the energy absorption and shock resistance properties in comparison with monolithic designs [6]. Indeed, one of the principal concerns in the use of CFRP laminates is their low resistance to out-of-plane Low-Velocity Impacts (LVIs), which may cause delamination and damage, thus compromising the integrity of the component. This typology of impact events is of particular interest in the aforementioned engineering sectors, because it arises from common events such as runway debris, tool drops, hail and others [7]. In this context, the interest in the improvement of energy absorption properties has stimulated researchers in the design of new typologies of cores and sandwich structures and in the study of their behaviour under impact events. Most of the early research studies involving sandwich structures with honeycomb core [8–10] highlighted how the damage in LVI events is most limited to the top skin, the core, and their bonding areas, which for lattice-type cores represents a particular weak region due to the small contact area of the material. In order to improve the mechanical response of core-skin interface, Brandt et al. [11] and, successively, Fan et al. [12–15] studied the mechanical performances of integrated woven lattice cores, while Potluri et al. [16] developed a novel stitch-bonding technique to mechanically reinforce the bonding interface between a close-cellular core and

glass fabric reinforced resin. These kinds of sandwich structure present an extremely high debonding resistance, thanks to the reinforced core-skin interface, but the complicated manufacturing process strongly limits their application.

Sandwich cores can vary in both materials and geometries, and the most commons are honeycomb structures (made of aluminium, Nomex or Kevlar), foams and corrugated cores. The need of new typologies of cores with enhanced mechanical properties and low density has driven many recent works about fibre reinforced lattice cores. Russel et al. [17–19] manufactured and characterised a structure made of CFRP strips connected through mechanical and adhesive joints to form a square honeycomb lattice. Results from an experimental campaign showed that this core is characterised by an excellent compressive-strength-to-density ratio and impact properties, demonstrating that the introduction of fibre reinforcements can lead to properties not obtainable with traditional core materials. Fan et al. [20,21] proposed two typologies of Kagome lattice cores reinforced by carbon fibres, interlacing the lattice structure with fibres aligned along the struts, and interlocking the grid structure with fibres along the thickness. These studies proved that, even if the structures' mechanical properties were strongly degraded by manufacturing imperfections (i.e., waviness of the struts, non-circular cross-sections and cantilever ribs) their stiffness and strength were still considerably higher than those of traditional cores with the same density. Xiong et al. [22–24] studied egg and pyramidal honeycomb grids cores reinforced with carbon fibres, analysing their failure modes both analytically and experimentally. The results in terms of compression properties and energy absorption capacity showed large improvements in comparison with honeycomb cores characterised by the same density. Based on the works in literature it appears clear that reinforcing cores with fibres is a promising approach to potentially overcome the mechanical properties of traditional cores such as foams and aluminium honeycomb, however it comes at the cost of more complex and expensive manufacturing procedures.

In this context, the authors of this work presented in a previous article [25], the design of a new CFRP lattice core structure, named Circular Prestressed Carbon

Core (CPCC), which takes advantage of an asymmetrical fibre orientation to generate residual thermal stresses to further improve the energy absorption properties of the part. Indeed, when asymmetrical laminates are subjected to a sudden change in temperature, the large difference of thermal expansion (around one hundred times larger) between the matrix and the fibres will result in a distribution of residual stress through the thickness in the cured part [26]. Under certain loading and boundary conditions, these stresses cause the laminate to snap-through two stable shapes, a phenomenon commonly called bistability. The bistability was originally recognised as manufacturing defect to be avoided, but in the 1981 Hyer [27] was the first to understand the potentialities of those structures for advanced applications. These researches however have been mainly oriented towards the shape-changing feature of bistability [28–30], with only few works focusing on their energy absorption characteristics [31,32]. In order to fill this gap, the previous work [25] focused on the design and manufacturing of the novel CFRP core and on the analysis of the influence of residual thermal stresses on the mechanical properties and failure mechanisms during quasi-static tests was performed.

This work constitutes the natural progression of [25], being focused on the manufacturing and characterisation of a complete carbon reinforced sandwich structure made with a CPCC core and CFRP skins both from a numerical and experimental perspective, with a particular attention to the contribution of the residual stresses to the impact resistance in LVI conditions. The sandwich structure was manufactured in a two-step procedure (core cure and skins co-cure), thus removing the traditional skin to core assembly step, taking advantage of the same resin matrix of both core and skins to create a strong interface without the use of external mechanical or adhesive joints. The samples were experimentally characterised under LVI tests with medium and high energy levels, in order to analyse two different failure mechanisms: skin-to-core delamination and core failure. The same tests were performed on traditional honeycomb sandwich structures, in order to have a comparison with a structure commonly in use in the aerospace sector. To evaluate the influence of the residual thermal stresses on the

energy absorption properties and failure mechanisms, the experimental campaign was also conducted in comparison with sandwich samples with CPCC cores manufactured without the temperature cycle necessary for the generation of the residual thermal stresses. To have a deeper understanding of the failure phenomena and extension of internal damage, Phased Array Ultrasonic Testing (PAUT) method and Computed Tomography (CT) scan have been employed to characterise the internal damage after the impact events. Given the complexity and the numerous variables that have to be encountered for a structure like the CFRP lattice core (fibre orientation, residual stress distribution, lattice core cell size, manufacturing imperfections and defects to name some), the development of a digital twin of the structure is an indispensable tool for the future designs. Based on this, the finite element model (FEM) of the core developed in [25] was used to realise the CPCC sandwich structure numerical model and validated against the LVI experimental results. The numerical model has been used in this work to study the evolution of the stress distribution during the impact test in both prestressed and not-prestressed cores, in order to understand the contribution of the residual stresses in the energy dissipation and damage generation of the CPCC core.

2. Materials and samples manufacturing

Materials

The CPCC sandwich panels were fabricated using a unidirectional carbon-fibre reinforced prepreg UD-HS200 produced by CIT Composite Materials, based on ER450 epoxy resin system with HS Carbon T700 24k fibres. According to the material datasheet, the prepreg has nominal fibre areal weight of 200 g/m^2 and a nominal cured ply thickness of 0.211 mm.

For the comparison with traditional sandwich structures used in aircraft applications, HexWeb[®] CR-PAA aluminium Honeycomb was employed to manufacture the cores. The 5052-grade aluminium expanded honeycomb has a hexagonal cell/size with nominal dimension 4.762 mm, foil thickness 0.076 mm

and a density 0.130 g/cm^3 . This kind of core is a top-quality core designed for aerospace applications with an enhanced bonding properties [33].

The design of the CPCC core is illustrated in details in [25], therefore the manufacturing procedure is here just summarised. The core consists of a 2D close-packing lattice core with a 5 mm diameter circular cell, which was manufactured by firstly cutting the prepreg materials into strips and laminating them in a [0,90] configuration. The debulking step during the lamination of the strips was performed using ultrasonic consolidation (UC) technique [34], which was applied for 15 minutes in order to ensure an optimal level of air bubbles removal. The strips were then used to manufacture the core by means of the frame illustrated in Figure 7.1, whose scope is to keep in place the prepreg strips and the metal pins, which are used to create the circular empty cells. After the application of the release agent to the frame and pins, the prepreg strips were laid with alternated orientation ([0,90], [90,0], [0,90], [90,0], etc.) to optimise the response of the prestressed CFRP walls [25]. Afterwards, the material was put in an oven with constant pressure applied on the two sides of the frame, applying a cure cycle of 2.5 hours at $130 \text{ }^\circ\text{C}$ followed by a rapid water-cooling cycle to $5 \text{ }^\circ\text{C}$ in approximately 10 seconds.



Figure 7.1 - CPCC core manufacturing frame

Thanks to the different thermal expansion coefficients of carbon fibres and epoxy resin, and thus of the 0 and 90 orientations, each CFRP layers is subjected to thermal stresses that are “frozen” into the polymeric structure by the rapid cooling cycle,

which impedes the relapse of the matrix crystalline structure, resulting in the internal distribution of residual stresses. After the cure, the pins were easily removed from the core, leaving the 2D circular pattern in the structure, as shown in Figure 7.2. Core samples without residual thermal stress were also fabricated, providing a controlled cooling down rate of 5 °C/min, thus preventing the formation of residual stresses. For the experimental campaign, a batch of 30 60x60x18.5 mm sandwich samples were manufactured, following the guidelines of the ISO standard [35,36].

Due to the different coefficient of thermal expansions of resin ($35-65 \cdot 10^{-6} \text{ K}^{-1}$) and fibres ($\sim 0 \text{ K}^{-1}$) [37], when the UD layer of CFRP is exposed to a thermal variation, it shows a large expansion or contraction in the direction perpendicular to the fibres, while it will remain almost unchanged in the fibre direction. When the asymmetric laminate (not symmetric material properties about the middle surface through the thickness), of which the CPCC core is made of, is exposed to the sudden post-cure cooling cycle, the asymmetric thermal properties create a distribution of stresses along the two faces of the laminate, producing two curved stable configurations. This phenomenon is defined bistability. The transition between the two stable configurations is called *snap-through* phenomenon and requires a force (bending moment) to be activated.

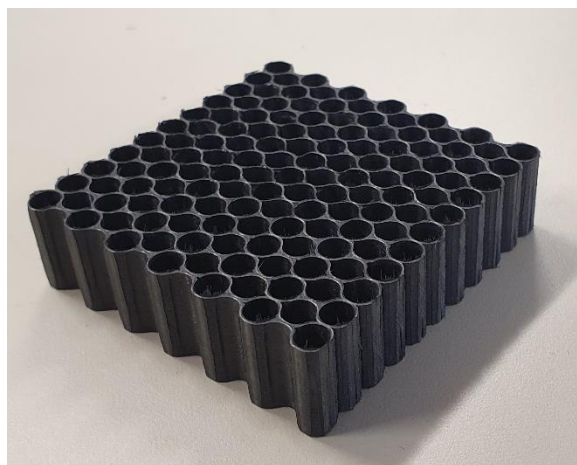


Figure 7.2 - CPCC core manufactured sample

The previous work [25] has studied the contribution of such moments in the increment of the resistance of the structure to vertical loads. The CPCC structure was manufactured in such a way that the face of a cell wall is always supported by a face with symmetric fibres direction on the other side, resulting in an opposite curving and stresses (Figure 7.3).

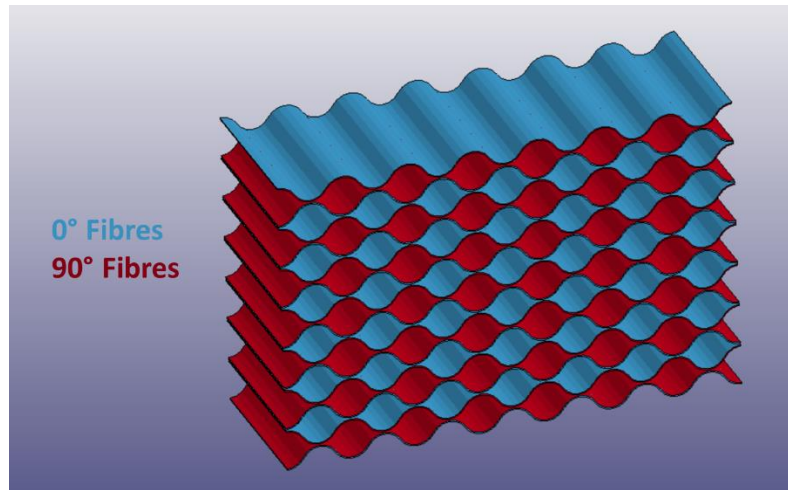


Figure 7.3 - CPCC opposite fiber configuration

Therefore, when the structure is subjected to an external vertical load, the bistability is expected to contribute in two ways: from one side, as demonstrated in [25], the opposite stresses will increase the compressive out-of-plane strength of the cell; from the other, the failure of the core, and thus of the connections between the unit-cell walls, will release the constrained stresses, thus absorbing energy from the impact. These concepts are schematically illustrated in Figure 7.4.

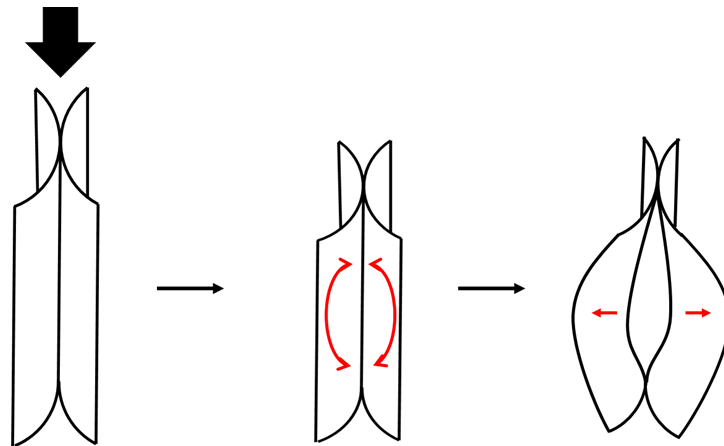


Figure 7.4 - Schematic representation of unit-cell walls failure and residual thermal stresses contribution ($[0,90]_s$)

CPCC sandwich panels fabrication

A 16 mm thickness CPCC core was used to fabricate sandwich samples, using the same prepreg material for the manufacturing of the skins. Eight layers were laid on top of an aluminium plate for each skin, following a $[0, 90, 0, 90]_s$ stacking sequence, and successively attached to the two sides of the core. Unlike traditional skins-to-core bonding, the two components of the sandwich structure under study do not require additional resin layers thanks to the fact that are made of the same polymeric matrix, and thus are perfectly compatible. Therefore, this manufacturing procedure uses the excess resin of the prepreg system to create a strong joint between the two components. To ensure an efficient removal of air bubbles from the liquid resin, and thus improve the interlaminar and core-to-skins delamination resistance, UC debulking technique was applied on each side of the uncured sandwich structure for 15 minutes.

After the debulking, sandwich samples were cured in autoclave with a cure cycle of 2.5 hours at 130 °C and 20 psi, followed by a controlled cooling down cycle with a rate of 5 °C/min. The same procedure was applied for the manufacturing of both prestressed and not-prestressed samples. Figure 7.5 illustrates a sample before cure with aluminium plates on each side (a) and after the cure (b).

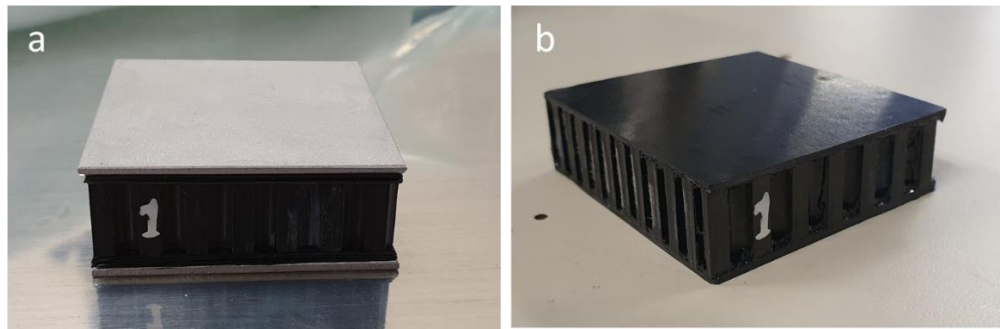


Figure 7.5 - CPCC Sandwich sample before (a) and after (b) skins cure

Honeycomb sandwich panels fabrication

To compare the experimental results with a structure commonly used in structural aerospace applications, aluminium honeycomb sandwich samples were also produced. The honeycomb core was cut into the desired shape, while the CFRP skins were produced using the same material and orientation of the CPCC samples. Finally, honeycomb core and CFRP skins were bonded together with the adhesive film to fabricate the final sandwich samples. A 3M™ Scotch-Weld™ structural adhesive film AF 555 was used for the attachment of the aluminium core to CFRP skins.

3. Experimental setup

Impact tests

Experimental characterisation of the sandwich structure response under LVI were performed following the BS EN ISO 6603-1:2000 [35] and BS EN ISO 6603-2:2000 [36] standards. The tests were conducted by using the impactor rig illustrated in Figure 7.6, which consists of a sample holder (1) and an impacting striker (2) connected to an accelerometer, and an impacting head with weights (3). The voltage vs time plot was recorded during the test by the accelerometer, which can be successively converted into force vs time and force vs displacement plots, as for standard guidelines. The impactor head, of known weight (9.353 kg) and dropping distance from the samples top surface, was used to generate impacts with energies of 20 and 45 J. These values of impact energies were selected thanks to a preliminary FE analysis of the CPCC samples and are expected to induce top skin-to-core interlaminar failure at 20J and total skin failure and core crush at 45J for the composite core sandwich samples.

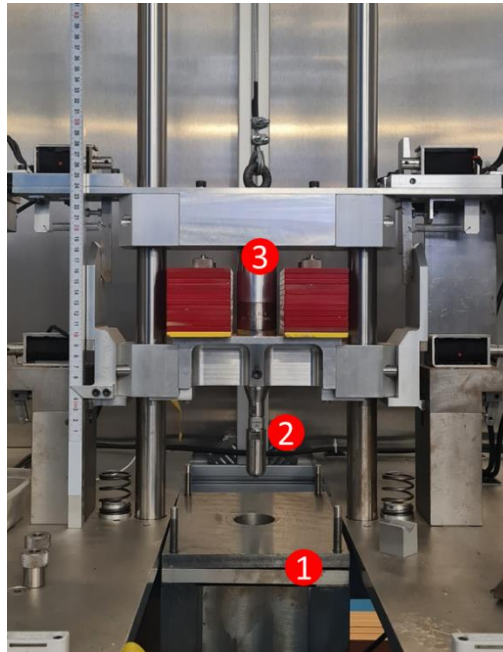


Figure 7.6 - Impactor testing machine: sample holder (1), impactor striker (2) and impactor head (3)

NDE analysis

Given the complexity of failure mechanisms that characterise fibre reinforced materials, especially when damaged by impact events, non-destructive evaluation (NDE) techniques can provide precious information in terms of mechanical properties and structure integrity of the part being inspected, with reducing risks and costs [37]. In this work, a 128 channel 5 MHz phased array transducer was employed to conduct Phased Array Ultrasonic Testing (PAUT) method, in order to characterise the internal damage of skins and skins-to-core interface after the impact events. PAUT methodologies employ a pulser-receiver array of piezoelectric elements to steer an ultrasonic plane wave through the material and capture any anomaly of the reflected wave due to internal discontinuities [39,40]. By combining the acquired signal from all the piezo elements, a planar view of the sample can be evaluated, with a colour-scale indicating the gated wave amplitude at each control point (Amplitude C-Scan), or the time location of the gated peaks, mapped to their x-y position (Time Of Flight C-Scan).

In addition, Computed Tomography (CT) scan was performed using Nikon XT H 225 ST CT scanner with a Tungsten target and Perkin Elmer 1620 16-bit (2000 by 2000 pixel detector) and a 225kV microfocus source with a minimum 3 μ m spot size. The scan was carried on representative samples to have a detailed 3D image of the impacted core. CT techniques rely on the difference in absorption of the penetrating x-ray energy in the inspected part, where thickness, density and shape variation can be visualised as a contrast change of the image created by means of an unabsorbed radiation propagating through the material, generating a detailed 3D image of the sample outer and inner parts [41,42].

4. Numerical model

In a previous paper, the authors [25] provided and validated against experimental quasi-static tests a FEM of the CPCC core, analysing the contribution of the residual thermal stresses and of the structural defects. In the present work, this FEM model has been expended by adding the numerical model of top and bottom skins, creating a digital twin of the sandwich structure. In order to reduce the computational cost of the simulations, only the unclamped part of sandwich impact sample was simulated via LS-DYNA software, applying appropriate boundary conditions, as it will be described further in this section. The model was first used to perform a preliminary analysis of the impact events in order to evaluate the energy levels required to induce failure in the top skin-core interface (without complete penetration of the top skin) and to generate core crush failure. Eight layers of eight-node brick solid elements with constant stress formulation with one integration point (ELEFORM=1) and 0.211 mm of thickness were used to model each skin. The core was modelled with two layers of shell elements (type 16), which use a local element coordinate system that rotates with the element (as in the Belytschko-Tsay element [43]). Tie-break contact was used for the simulation of the joint between the layers, which allows the failure, and thus the delamination, for normal and shear stresses, and switches general contact with friction after the failure. As for the materials, Mat Composite Failure Option Model (MAT 059) was used for solid elements, which applies a three-dimensional stress-based criterion to model the progressive failure damage, while Mat Enhanced Composite Damage (MAT 054) was applied on shell elements to simulate the core, which uses the Chang matrix failure criterion [43]. Contact and materials properties are summarised in Table 7.1.

The impactor striker tip was simulated as a 10 mm radius hemispherical part using eight-node brick solid elements (ELEFORM=1) and isotropic elastic material (MAT 001). The material was simulated as simple elastic because the impact energy is not expected to generate plastic deformation in steel material. The impactor striker was divided in two parts: the tip was simulated using standard steel density,

while the back part was simulated with higher density calculated in function of the impact energy required. Table 7.1 lists the material properties used for the impactor striker, where ρ_{steel} and ρ_{mass} indicate the density used for the tip and back parts, respectively.

Table 7.1 - Material properties used in the model for MAT 054, MAT 059 and MAT 001 (subscripts 11 refer to fibre direction, 22 to in-plane direction perpendicular to the fibres and 33 through the thickness); ρ density; E modulus of elasticity; ν Poisson's ratio; G shear modulus; X_c and X_T longitudinal compressive and tension strengths; Y_c and Y_T transverse compressive and tension strength; Z_c and Z_T (only for solid elements) normal compressive and tension strength; SC shear strength; subscriptions steel and mass refer to bottom and top part of the striker; F_s and F_D contact static and dynamic coefficients of friction; $NFLS$ contact normal failure stress; $SFLS$ contact shear failure stress.

<i>Material properties</i>	ρ	E_{11}	E_{22}	E_{33}	ν_{21}	ν_{31}	ν_{32}	G_{12}	G_{23}
(MAT 54 and MAT 59)	[Kg mm ⁻³]	[GPa]	[GPa]	[GPa]				[GPa]	[GPa]
<i>Values</i>	1.23·10 ⁻⁶	130	10.3	10.3	0.0535	0.0535	0.449	4.37	3.43
<i>Material properties</i>	G_{31}	X_c	X_T	Y_c	Y_T	Z_c	Z_T	SC	
(MAT 54 and MAT 59)	[GPa]	[GPa]	[GPa]	[GPa]	[GPa]	[GPa]	[GPa]	[GPa]	
<i>Values</i>	3.43	1.5	2.58	0.236	0.082	0.236	0.082	0.09	
<i>Material properties</i>	ρ_{steel}	ρ_{mass}	E	ν					
(MAT 001)	[Kg mm ⁻³]	[Kg mm ⁻³]	[GPa]						
<i>Values</i>	8·10 ⁻⁶	9.17·10 ⁻³	200	0.3					
<i>Tie-Brake contact properties</i>	F_s	F_s	$NFLS$	$SFLS$					
			[GPa]	[GPa]					
<i>Values</i>	0.4	0.3	0.082	0.09					

In order to simulate the contribution of the residual thermal stresses into the model, a thermal analysis was first performed on the core simulating the cool down cycle, using the same procedure illustrated in [25]. The output, in terms of residual stresses, was exported for each element and then imported in the sandwich model for the structural simulations. Figure 7.7 illustrates the Von Mises stress status in GPa of the sandwich model prior to impact simulation; given that the skins were added after the cooling down cycle of the core, they result in zero stress status. Boundary conditions of constrains along the z-direction were applied on the external nodes of the model to best reproduce the real experimental conditions.

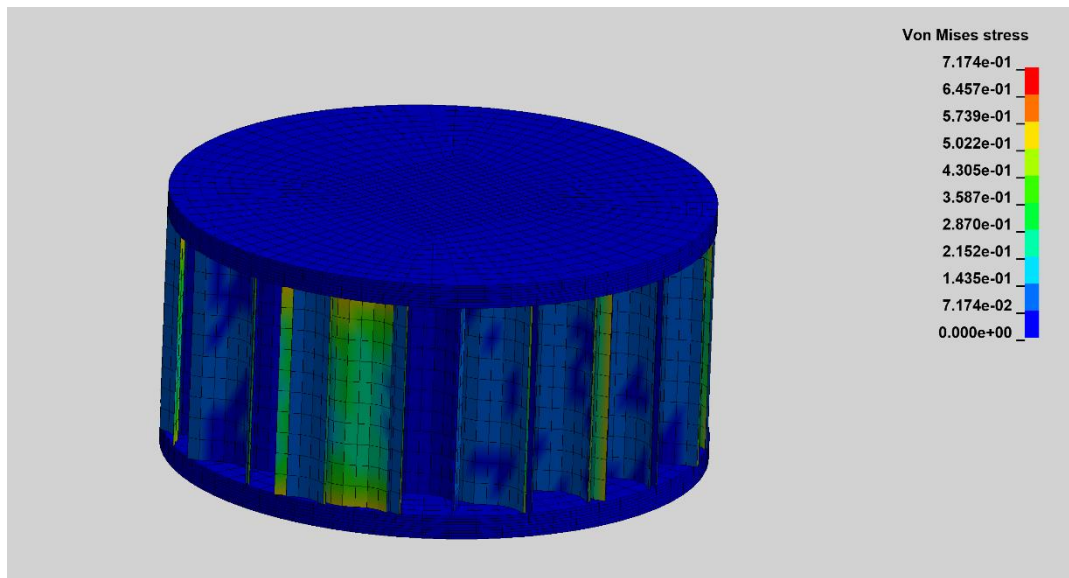


Figure 7.7 -Residual thermal Von Mises stress contour plot of the CPCC sandwich FE model

5. Results and discussion

LVI tests results

LVI experimental impact tests were performed on CPCC (CP samples), CPCC without prestress cycle (C samples) and aluminium honeycomb (H samples) sandwich structures at 20J and 45J.

Following the standards [35,36], the accelerometer output signal recorded during the tests was converted from time vs voltage into force vs time and force vs

displacement plots. Figure 7.8 and Figure 7.9 illustrate the Force-Time and Force-Displacement curves obtained from the 20J and 45J impact tests, respectively, with a comparison between for CP, C and H samples.

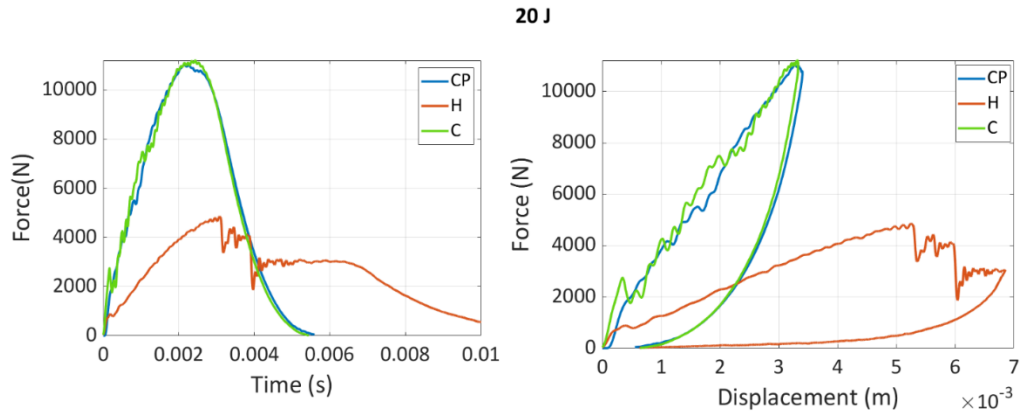


Figure 7.8 - Time vs force and displacement vs force curves obtained from 20J impact tests on CP, C and H representative sandwich samples

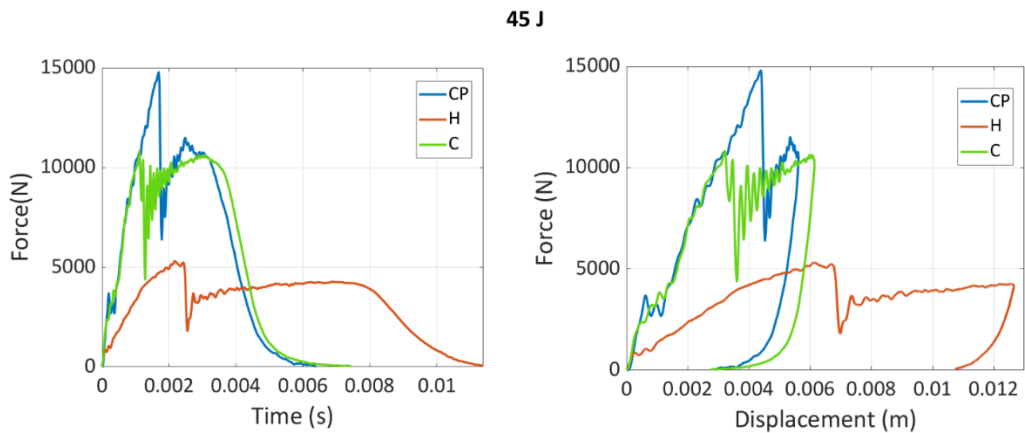


Figure 7.9 - Time vs force and displacement vs force curves obtained from 45J impact tests on CP, C and H representative sandwich samples

Figure 7.8 indicates a clearly different impact response between the carbon fibre reinforced cores and the aluminium honeycomb during the 20J impact event, with the former being able to sustain higher levels of force (more than +120% in average) showing a mainly elastic behaviour, with small plastic deformations. On the other side, the aluminium honeycomb samples show drastic failure for less than half of the force, followed by several failure events represented by the curve oscillations. This contrast is also confirmed by the clear difference in terms of time of impact

and maximum displacement between the two typologies of core (around -60% and -50% in CP and C samples, respectively). As expected, for the 20J impact there is not a significant difference in terms of resulting curves between the CP and C samples since this energy level was selected to generate failures mainly at the skin-to-core interface. Therefore, the small extension of core failure may be not enough to highlight the effect of the residual stresses.

The divergence between the CPCC and aluminium honeycomb cores is even larger for the 45J impact test, with the latter being totally destroyed by the impact event. Indeed, the top skin of the H samples was completely perforated by the striker and the cores crushed for the whole length under the impact point, as showed in Figure 7.10, while the extension of the damage was localised in the contact area for both the CP and C configurations.

At 45J the difference between the C and CP configurations is strongly evident, with Figure 7.9 showing a clear variation in the values of force at failure, with the prestressed samples reaching the higher values of maximum force (+23%). From the force versus displacement curve, it is possible to note that the striker reached lower values of maximum displacement (-12%) when impacting CP samples, suggesting a stiffer response. Furthermore, the oscillations of force values protract for longer in terms of both time and displacement for C samples, indicating the possible presence of larger damaged areas inside the sample, as the NDE results will confirm.

Figure 7.10 illustrates the post impact top view of six samples representative of CP, C and H categories tested at 20J (left) and 45J (right). As it is possible to see, the striker generated a small indent on the top surface of CP and C samples at 20J (a and c), while the extension of damage was substantially larger in H samples (e), with a considerable crush of the aluminium core and consequent large deformation of the top skin. At 45J, the CP samples (b) showed the smaller magnitude of damage and depth of indent, which was larger in the C samples (d). However, both typologies of CFRP core showed a structural integrity of the impacted sample, with damage apparently limited to a small area around the contact point. On the other

side, H samples (f and g) showed a complete perforation of the top skin, a significant crush of the aluminium honeycomb core and large delamination areas of the core-to-skin interface for both top and bottom skins, with damage propagated in the whole sample.

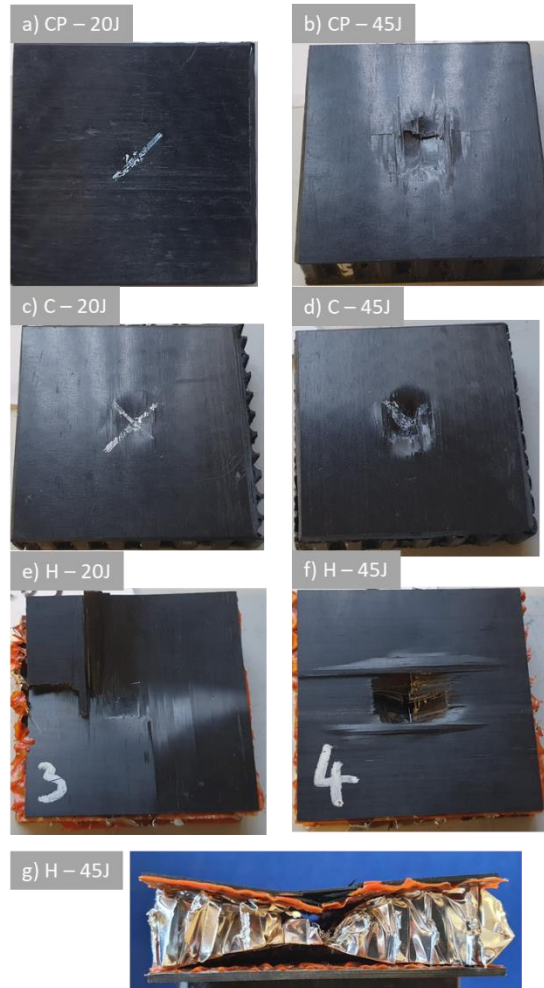


Figure 7.10 - Representative 20J (left) and 45J (right) CP (a and b), C (c and d), H (e and f) tested samples and a detail of the side view (g) of 45J H tested sample

Table 7.2 – 20J LVI experimental results mean values, standard deviation in brackets, and percentage variations

20J impact results	<i>Time of contact</i> [ms · 10 ⁻³]	<i>Peak force</i> [kN]	<i>Max displacement</i> [mm · 10 ⁻³]	<i>Absorbed energy</i> [J]
<i>C</i>	5.60 (0.21)	10.5 (0.47)	3.45 (0.11)	14.1 (0.58)
<i>H</i>	14.2 (0.72)	4.99 (0.13)	6.83 (0.14)	17.2 (0.23)
<i>CP</i>	5.63 (0.06)	11.1 (0.27)	3.48 (0.08)	12.6 (0.32)
<i>Variation from C</i>	+0.54%	+5.71%	+0.87%	-10.64%
<i>Variation from H</i>	-60.35%	+122.44%	-49.05%	-26.74%

Table 7.3 - 45J LVI experimental results mean values, standard deviation in brackets, and percentage variations

45J impact results	<i>Time of contact</i> [ms · 10 ⁻³]	<i>Peak force</i> [kN]	<i>Max displacement</i> [mm · 10 ⁻³]	<i>Absorbed energy</i> [J]
<i>C</i>	7.27 (0.19)	11.2 (0.36)	6.37 (0.09)	40.5 (0.56)
<i>H</i>	13.7 (0.89)	5.09 (0.22)	12.9 (0.33)	41.7 (1.43)
<i>CP</i>	6.68 (0.27)	13.8 (0.41)	5.62 (0.10)	38.9 (0.89)
<i>Variation from C</i>	-8.12%	+23.21%	-11.77%	-3.95%
<i>Variation from H</i>	-51.24%	+171.12%	-53.52%	-6.71%

Table 7.2 summarises the experimental results obtained from the 20J LVI tests. The only notable difference between the two CPCC samples is a slight increment in peak force (+5.4%) and a reduction in absorbed energy (-11.9%) of the prestressed core in comparison with the C samples, suggesting a stiffer response with less

damage, as it will be explained further in this section. On the other side, the results from H samples are strongly different from the CPCC samples, with the last showing a significantly lower time of contact (-60%), maximum displacement (around -50%) and higher peak force (+120%). The results suggest a substantial failure of the H samples, with a considerable crush of the core, as suggested by the larger value of absorbed energy.

The previous conclusions can be observed in an extended way in the 45J LVI results reported in Table 7.3. The percentage variations of the mean values between the CP and H samples are considerably high, reflecting the difference in failure and damage generated during the impact illustrated in Figure 7.10.

On the other side, the average peak force of CP samples reaches a value that is 23.21% higher than the one obtained from C samples. Furthermore, a decrement in time of contact (8.12%) and maximum displacement (11.8%) can be observed in comparison with the not prestressed counterpart, implying a general greater resistance of the part to impact events.

In order to take the different value of density of the CFRP and of aluminium sandwich structures into consideration, and evaluate the specific advantage in the CPCC sandwich, specific impact properties were evaluated and reported in Table 7.4. As it is possible to appreciate in the percentage variations, despite the higher value of density, the advantages of CP samples against aluminium honeycomb sandwiches are still large, such as the higher reacting force (up to +75%) and reduced penetrating displacement (up to -71%).

Table 7.4 - LVI experimental specific results mean values and percentage variations. Specific properties (divided by the density) are denoted by *

Specific impact properties		Density	Time of contact*	Peak force*	Max displacement*	Absorbed energy*
		[g/cm ³]	[ms · 10 ⁻³] · [g/cm ³] ⁻¹	[kN] · [g/cm ³] ⁻¹	[mm · 10 ⁻³] · [g/cm ³] ⁻¹	[J] · [g/cm ³] ⁻¹
20J	H	0.33	43.29	15.21	20.82	52.44
	CP	0.51	11.08	21.85	6.85	24.80
	Variation	54.88%	-74.40%	43.63%	-67.10%	-52.70%
45J	H	0.33	41.77	15.52	39.33	127.13
	CP	0.51	13.15	27.17	11.06	76.57
	Variation	54.88%	-68.52%	75.05%	-71.87%	-39.77%

In order to understand these results, it is important to analyse how the impacting object transmits energy to the part during an impact event [45–47]. During a LVI, part of the energy is given back to the object after the part reaches the maximum displacement, and is represented by the elastic energy term ($E_{elastic}$). The energy absorbed by the part is defined as the difference between the impacting energy (E_{impact}) and the elastic energy [48]. The energy can be absorbed by a component during the LVI event in three main ways: generating damage as interlinear cracks or fibre rupture, by vibration damping [48] or absorbed by dissipation mechanisms (inelastic and non-linear behaviours, heat, sound, etc.). The mechanism of energy dissipation during the impact event can be summarised by the following formula:

$$E_{impact} = E_{elastic} + E_{damage} + E_{damping} + E_{dissipation}$$

Given that the same material constitutes the CP and C samples, which only differs by the presence or absence of the residual thermal stresses, $E_{damping}$ term will be the same for both configurations. Therefore, since CP and C samples showed comparable values of total absorbed energy (11% and 4% lower in CP samples for 20J and 45J, respectively), a lower extension of damage in the tested samples, and thus a lower level of E_{damage} , would suggest an increment in the energetic

contribution related to dissipation phenomena ($E_{dissipation}$). In other words, the additional contribution given by the residual stresses to the energy dissipation mechanisms would lead to a decrement in the energy available for damage generation. The dissipation of the energy activated by the thermal prestress and bistability of the composite laminate of which the CPCC core is constituted has been described for static load events in the previous work [25]. This concept can be expanded to dynamic events, by analysing the extension of damage in the parts through the analysis of NDE results and the analysis of the stress distribution during the simulated impact test in the following sections.

NDE results

As previously illustrated in Figure 7.10, aluminium honeycomb samples presented damage easily visible to the naked eye and therefore did not require any kind of NDE tests. On the contrary. PAUT experimental results on four representative CPCC sandwich samples (CP and C for 20J and 45J) are shown in Figure 7.11 and Figure 7.12, in terms of Amplitude and TOF C-Scan, showing for all samples a complex failure mechanism given by the carbon structure. Results indicated that the presence of the prestress within the CPCC cores allows for an optimisation of the energy dissipation mechanisms, resulting in the reduction of the internal damaged area in comparison with the results obtained from the configuration with no prestress. This effect seems to be more relevant with an increasing value of the impact energy, going from a 7% decrease for the 20 J impacts (175 vs 189 mm²) to a large 20% decrease for the 45J impacts (334 vs 414 mm²).

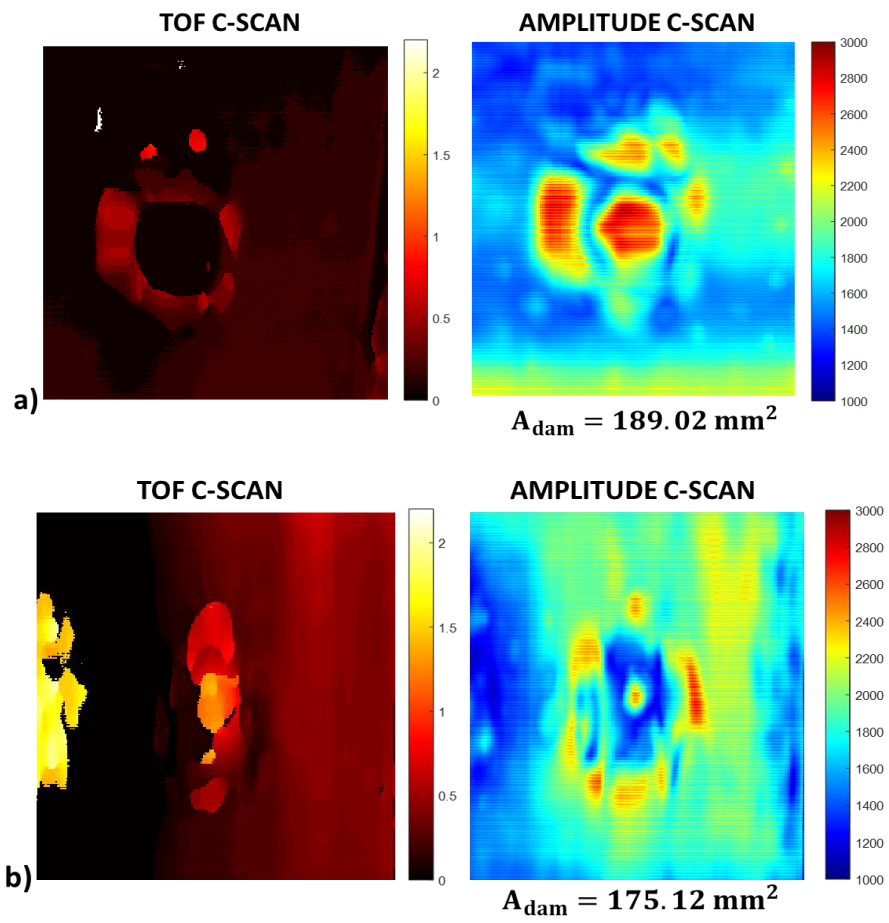


Figure 7.11 - TOF C-scan and Amplitude C-Scan imaging - 20 J a) C sample; b) CP sample

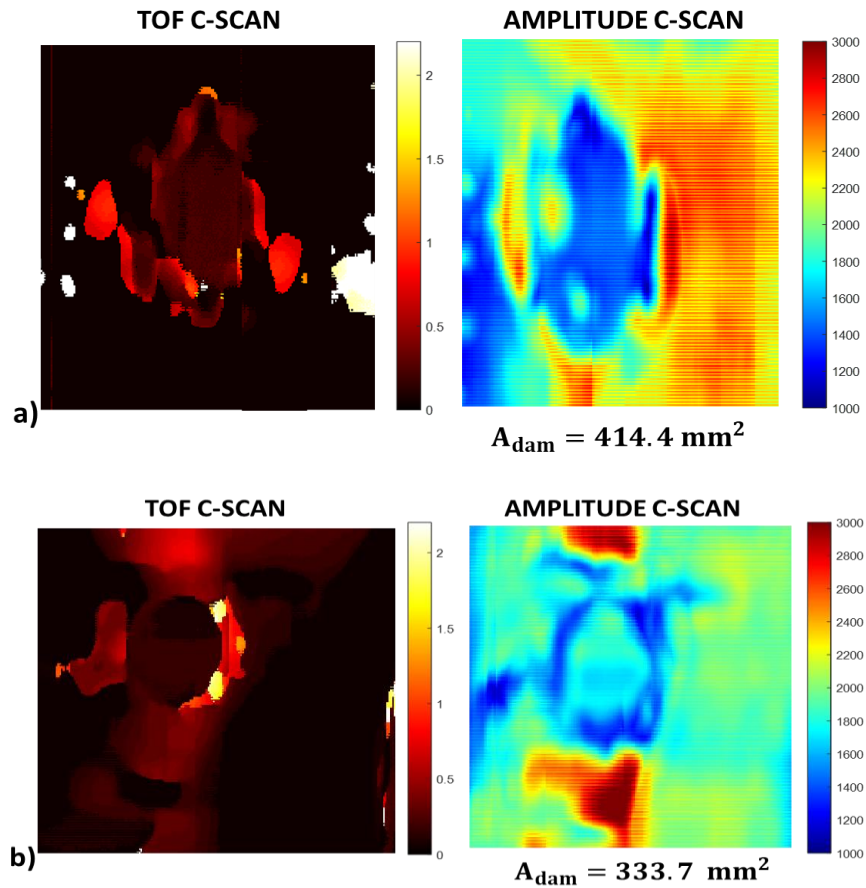


Figure 7.12 - TOF C-scan and Amplitude C-Scan imaging - 45 J a) C sample; b) CP sample

CT-scan of four representative samples were also performed to investigate the extension of damage along the thickness and to analyse the typology of damage induced in the core, whose quarter sections are illustrated in Figure 7.13. From the scan, it was possible to evaluate and compare the residual thickness of the core, showing an increase of around 10% for both the 20 and 45J impacts in the passage between the C and CP samples, confirming the positive effect given by the prestress.

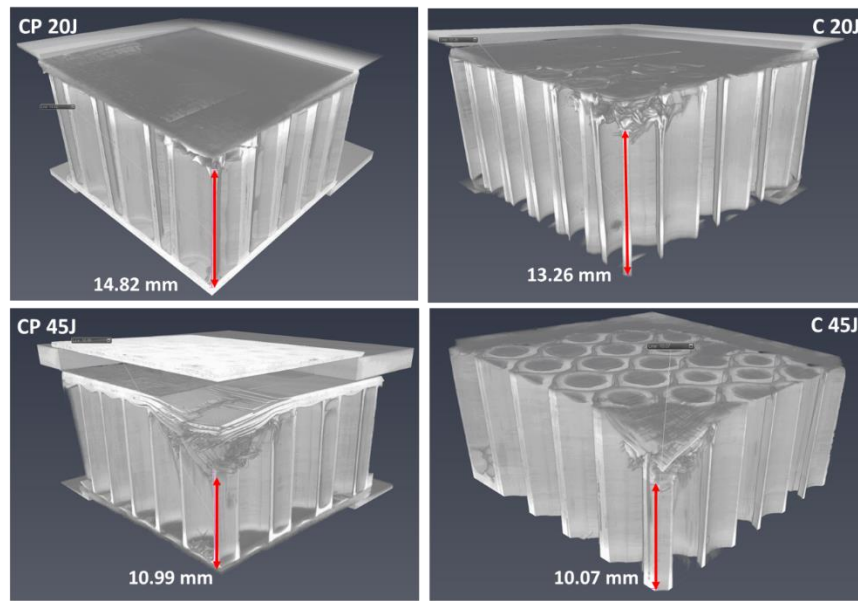


Figure 7.13 – CT scan quarter sections from representative CP (left) and C (right) samples impacted at 20J (top) and 45J (bottom)

Table 7.5 – Damage area and residual thickness values resulting from NDE analysis of CP and C samples with percentage variation

NDE results		Damage area [mm ²]	Residual thickness [mm]
20 J	CP	175.1	14.82
	C	189.0	13.26
	Variation	-7.35 %	+11.76 %
45 J	CP	333.7	10.99
	C	414.4	10.07
	% variation	-19.47 %	+9.14 %

Table 7.5 summarises the results of the NDE analyses and the percentage variations between the two composite cores. The PAUT and CT scan analysis of the samples confirmed that the extension of the damaged area along all the three directions was considerably lower for the CP configuration in comparison to the C samples. These results proved the positive contribution of the residual thermal stresses and bistability to the energy dissipation mechanisms of the structure when subjected to

LVI events, reducing the amount of energy available for the generation of internal damage.

Numerical model validation and discussions

The FE model of the unclamped part of the CP sandwich samples was used to simulate the residual thermal stresses, and then the mechanical response to 20 and 45J LVI impacts. The numerical model of C sample was also simulated and used at the end of this paragraph to compare the stress distribution in the two cores during the impact event and analyse how the residual stress contributes to the energy dissipation mechanisms. Results of the numerical test in terms of time versus force and displacement versus force were extrapolated for the CP sample and compared with experimental data in Figure 7.14.

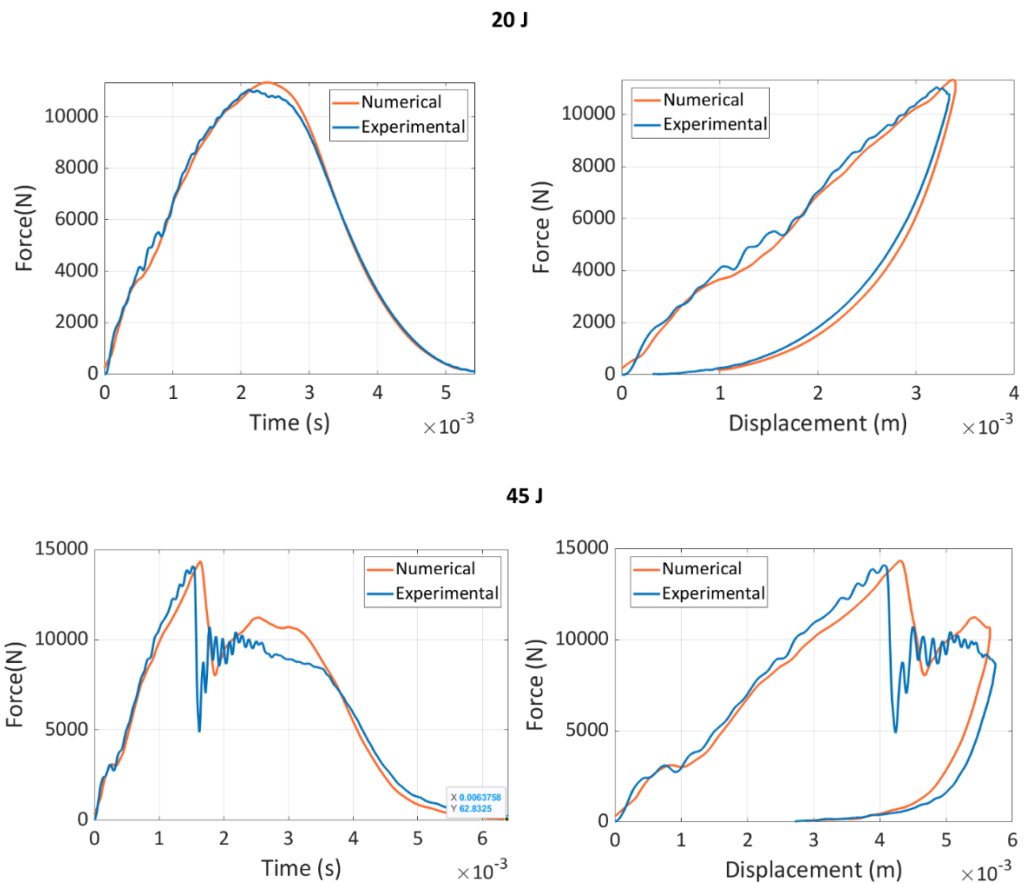


Figure 7.14 - Comparison between numerical (orange) and experimental (blue) results for 20J (top) and 45J (bottom) LVI tests

Table 7.6 – Average experimental results and numerical results for 20J and 45J impact tests

	<i>Time of contact</i> [ms · 10 ⁻³]	<i>Peak force</i> [kN]	<i>Max displacement</i> [mm · 10 ⁻³]	<i>Absorbed energy</i> [J]
<i>Experimental (20J)</i>	5.63	11.1	3.48	12.6
<i>Numerical (20J)</i>	5.46	11.3	3.40	13.1
<i>Experimental (45J)</i>	6.68	13.8	5.62	38.9
<i>Numerical (45J)</i>	6.12	14.3	5.55	41.1

Analysing the curves in Figure 7.14, it is possible to observe that the FE analysis accurately predicts the mechanical behaviour of the CP subjected to impact events, showing a maximum error of just 9.1% in the time of contact for 45J LVI test (see Table 7.6).

The validity of the model is further confirmed by comparing the geometry of the impacted core and its residual core length along the thickness direction in Figure 7.15. The figure shows a very similar damage extension between the real samples (analysed via CT Scan) and the numerical model, with an error in terms of residual thickness of less than 2%.

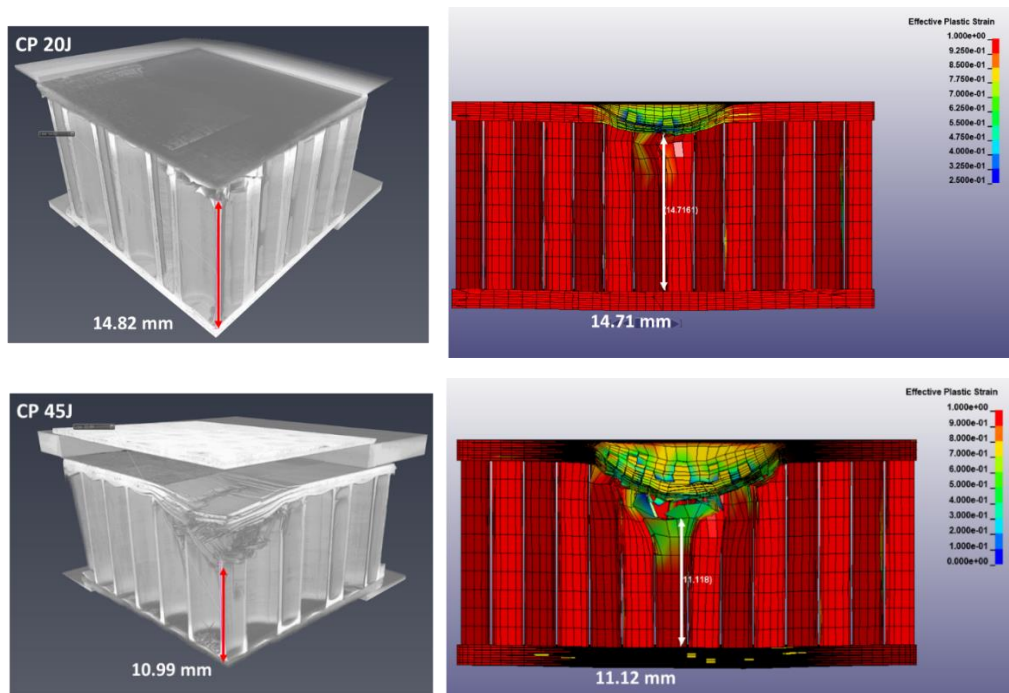


Figure 7.15 – Comparison of impacted structure and residual core thickness between CT scan (left) and FE model (right) of 20J (top) and 45 (bottom) impacted CPCC samples

The validated numerical model is a fundamental tool to understand the contribution of the residual stress distribution in the mechanical response of the core during the impact event. With this aim, the following images illustrate the Von Mises stress distribution during the 45J impact along the central section of the core for both 0° and 90° oriented plies, with a comparison between the CP and C samples. The frames are collected in three points in time during the simulation: prior the start of the contact with the impact striker (T0, Figure 7.16), at the beginning of the impact event (T1, Figure 7.17) and the crush failure of the core (T2, Figure 7.18).

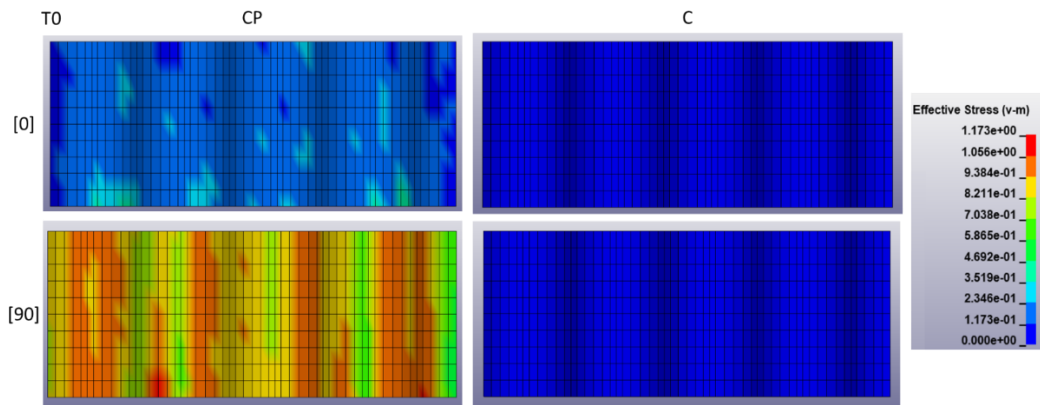


Figure 7.16 – Von Mises stress distribution in GPa in CP (left) and C (right) core along central section for [0] (top) and [90] (bottom) orientation before impact event (T0)

As illustrated in Figure 7.16, the residual stresses mainly involve the 90° orientated ply of the CP core, this is because the 90° fibres are straight and shorter than the 0° ones, which follow the curvature of the core cells. As expected, the C sample does not show any residual stress in both orientations.

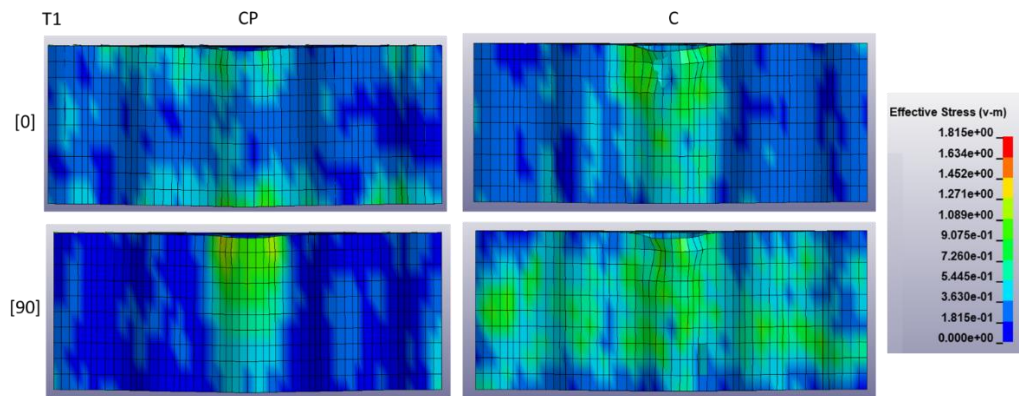


Figure 7.17 - Von Mises stress distribution in GPa in CP (left) and C (right) core along central section for [0] (top) and [90] (bottom) orientation during the impact event (T1)

After the striker hits the sample (Figure 7.17), the load in the C sample is almost equally distributed through both 0° and 90 plies°, allowing larger deformations due to the greater weakness of the 0° ply along the vertical direction. On the opposite side, the residual stress (and strain) of the CP sample redirects the load to be mainly carried by the 90° ply, absorbing more energy and reducing plastic deformations. Finally, at the beginning of the crush of the core (Figure 7.18), the C sample shows

large deformations and failure of elements, while the CP one has absorbed more energy thanks to the residual stresses and therefore shows smaller damage.

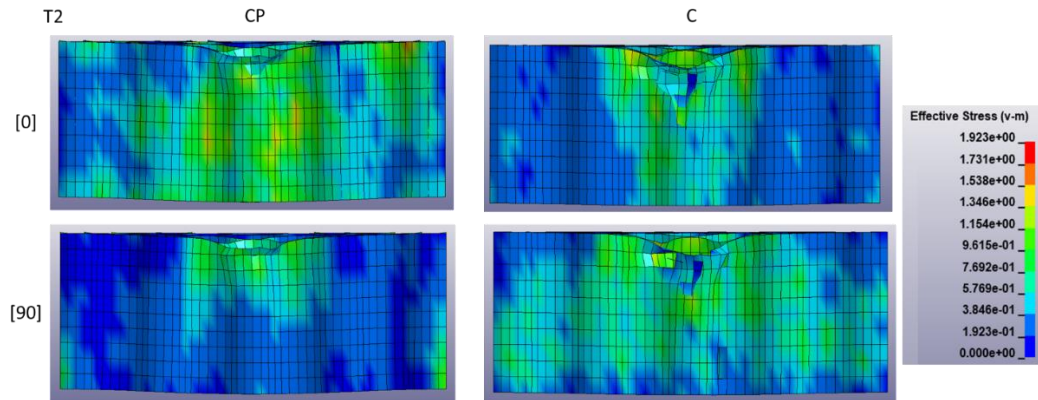


Figure 7.18 - Von Mises stress distribution in GPa in CP (left) and C (right) core along central section for [0] (top) and [90] (bottom) orientation during impact event at the crush failure of the core (T2)

As it is possible to conclude from the FEM analysis, the residual stresses and strains generate a residual internal momentum with direction opposite to the natural bending that initiates the crush of the core. This residual moment is a peculiarity of asymmetrical unidirectional reinforced polymers subjected to a rigid temperature change in curing phase, and can be analytically predicted [25]. In other words, the plies are preloaded in a way that is opposite to the failure one, leading to improvements in terms of out-of-plane mechanical properties of the core, as confirmed by both experimental and numerical results.

6. Conclusions

This work aimed at analysing the impact response of an all-composite sandwich structure based on the CPCC core and studied the contribution of the induced residual thermal stresses to its energy dissipation mechanisms. The residual thermal stresses were introduced in the core by means of drastic change in temperature during the manufacturing process in order to generate a residual internal moment given by the unsymmetric CFRP layup. This concept has been used in the design phase of the core in such a way that the residual moment opposes the predicted failure, thus enhancing the mechanical and energy dissipation properties of the structure during LVI events.

In order to characterise the impact properties and the positive contribution of the residual thermal stresses, experimental LVI impact tests and NDE analyses have been conducted in comparison with an aluminium honeycomb core and with all-carbon samples without residual stresses, for two levels of energy. The results prove that the CFRP sandwich samples are significantly more resistant to impact events than the aluminium honeycomb ones, maintaining structural integrity with limited damaged areas even at higher levels of impacting energy. On the other side, sandwich samples with aluminium honeycomb were strongly damaged by the impact event, with the impactor striker penetrating for more than a third of samples thickness at 20J and more than half for 45J. In comparison, the maximum displacements in CPCC samples were around 50% lower, applying a reacting force with peak values up to 170% higher than the aluminium samples. Similar discussion can be applied to the specific impact results, where sandwich properties were calculated taking into account the difference in density of the two structures. Despite the higher density of the CPCC sandwich, the properties are considerably better than the aluminium ones, with a value of peak force up to 75% higher, and maximum penetrating displacement reduced up to -71%. These differences can be clearly observed in tested samples images, where aluminium honeycomb samples appear totally crushed by the impacts, while the CPCC ones maintained their integrity.

Experimental tests confirmed the improvements provided by the residual thermal stresses in the core, in particular improving the impact properties (+23% of peak force and -12% of maximum displacement) and reducing the energy available for damage generation (-7% at 20J and -20% at 45J of delaminated area). The numerical model of the CPCC sandwich structure has been used in this work to study the evolution of the stress distribution during the impact test in both prestressed and not-prestressed cores, in order to understand the contribution of the residual stresses in the energy dissipation and damage generation of the CPCC core. The numerical results obtained from the simulated tests show how the residual stress (and strain) redirects the impact stresses to be mainly carried by the ply with

reinforcement along the loading direction, improving the mechanical response, the energy absorption and, thus, reducing the plastic deformations of the structure.

In conclusion, this work has shown the possibilities of the CPCC core to be used for the production of sandwich structures with unique LVI impact resistance, reducing considerably the damage extension and limiting it around the impact point. The introduction of thermal residual stresses, as confirmed by the experimental results and the numerical analysis, has been demonstrated to enhance impact resistance, acting on the failure mode of the core walls and reducing the energy available to generate damage.

References

- [1] Mahajan G V, Aher VS. Composite material: A review over current development and automotive application. *Int J Sci Res Publ* 2012;2:1–5.
- [2] Mouritz AP, Gellert E, Burchill P, Challis K. Review of advanced composite structures for naval ships and submarines. *Compos Struct* 2001;53:21–42.
- [3] Mishnaevsky L, Branner K, Petersen HN, Beauson J, McGugan M, Sørensen BF. Materials for wind turbine blades: an overview. *Materials (Basel)* 2017;10:1285.
- [4] Ramakrishna S, Mayer J, Wintermantel E, Leong KW. Biomedical applications of polymer-composite materials: a review. *Compos Sci Technol* 2001;61:1189–224.
- [5] Allen HG. Analysis and design of structural sandwich panels: the commonwealth and international library: structures and solid body mechanics division. Elsevier; 2013.
- [6] Xiong J, Du Y, Mousanezhad D, Eydani Asl M, Norato J, Vaziri A. Sandwich Structures with Prismatic and Foam Cores: A Review. *Adv Eng Mater* 2019;21:1800036. <https://doi.org/10.1002/adem.201800036>.
- [7] Hosur M V., Abdullah M, Jeelani S. Manufacturing and low-velocity impact characterization of foam filled 3-D integrated core sandwich composites with hybrid face sheets. *Compos Struct* 2005;69:167–81. <https://doi.org/10.1016/j.compstruct.2004.06.008>.
- [8] Kim CG, Jun EJ. Impact Resistance of Composite Laminated Sandwich Plates. *J Compos Mater* 1992;26:2247–61. <https://doi.org/10.1177/002199839202601504>.
- [9] Charles J-P, Guedra-Degeorges D. Impact damage tolerance of helicopter sandwich structures. *Adv Mater Process* 1991;23:51–61.
- [10] Herup EJ, Palazotto AN. Low-velocity impact damage initiation in graphite/epoxy/Nomex honeycomb-sandwich plates. *Compos Sci Technol* 1998;57:1581–98. [https://doi.org/10.1016/S0266-3538\(97\)00089-4](https://doi.org/10.1016/S0266-3538(97)00089-4).
- [11] Brandt J, Drechsler K, Arendts FJ. Mechanical performance of composites based on various three-dimensional woven-fibre preforms. *Compos Sci Technol* 1996;56:381–6. [https://doi.org/10.1016/0266-3538\(95\)00135-2](https://doi.org/10.1016/0266-3538(95)00135-2).
- [12] Jin F, Chen H, Zhao L, Fan H, Cai C, Kuang N. Failure mechanisms of sandwich composites with orthotropic integrated woven corrugated cores: Experiments. *Compos Struct* 2013;98:53–8. <https://doi.org/10.1016/j.compstruct.2012.09.056>.
- [13] Fan H, Zhao L, Chen H, Kuang N, Yang C, Huang S, et al. Ductile deformation mechanisms and designing instructions for integrated woven textile sandwich composites. *Compos Sci Technol* 2012;72:1338–43. <https://doi.org/10.1016/j.compscitech.2012.04.017>.

- [14] Fan H, Zhou Q, Yang W, Jingjing Z. An experiment study on the failure mechanisms of woven textile sandwich panels under quasi-static loading. *Compos Part B Eng* 2010;41:686–92. <https://doi.org/10.1016/j.compositesb.2010.07.004>.
- [15] Fan H, Yang W, Zhou Q. Experimental research of compressive responses of multi-layered woven textile sandwich panels under quasi-static loading. *Compos Part B Eng* 2011;42:1151–6. <https://doi.org/10.1016/j.compositesb.2011.03.008>.
- [16] Potluri P, Kusak E, Reddy TY. Novel stitch-bonded sandwich composite structures. *Compos Struct* 2003;59:251–9. [https://doi.org/10.1016/S0263-8223\(02\)00087-9](https://doi.org/10.1016/S0263-8223(02)00087-9).
- [17] Russell B, Deshpande V, Wadley H. Quasistatic deformation and failure modes of composite square honeycombs. *J Mech Mater Struct* 2008;3:1315–40. <https://doi.org/10.2140/jomms.2008.3.1315>.
- [18] Russell BP, Liu T, Fleck NA, Deshpande VS. Quasi-Static Three-Point Bending of Carbon Fiber Sandwich Beams With Square Honeycomb Cores. *J Appl Mech* 2011;78:031008. <https://doi.org/10.1115/1.4003221>.
- [19] Russell BP, Liu T, Fleck NA, Deshpande VS. The soft impact of composite sandwich beams with a square-honeycomb core. *Int J Impact Eng* 2012;48:65–81. <https://doi.org/10.1016/j.ijimpeng.2011.04.007>.
- [20] Fan HL, Meng FH, Yang W. Mechanical behaviors and bending effects of carbon fiber reinforced lattice materials. *Arch Appl Mech* 2006;75:635–47. <https://doi.org/10.1007/s00419-006-0032-x>.
- [21] Fan HL, Meng FH, Yang W. Sandwich panels with Kagome lattice cores reinforced by carbon fibers. *Compos Struct* 2007;81:533–9. <https://doi.org/10.1016/j.compstruct.2006.09.011>.
- [22] Xiong J, Ma L, Wu L, Liu J, Vaziri A. Mechanical behavior and failure of composite pyramidal truss core sandwich columns. *Compos Part B Eng* 2011;42:938–45. <https://doi.org/10.1016/j.compositesb.2010.12.021>.
- [23] Xiong J, Ma L, Pan S, Wu L, Papadopoulos J, Vaziri A. Shear and bending performance of carbon fiber composite sandwich panels with pyramidal truss cores. *Acta Mater* 2012;60:1455–66. <https://doi.org/10.1016/j.actamat.2011.11.028>.
- [24] Xiong J, Vaziri A, Ghosh R, Hu H, Ma L, Wu L. Compression behavior and energy absorption of carbon fiber reinforced composite sandwich panels made of three-dimensional honeycomb grid cores. *Extrem Mech Lett* 2016;7:114–20. <https://doi.org/10.1016/j.eml.2016.02.012>.
- [25] Flora F, Pinto F, Meo M. Manufacturing and characterisation of a new thermal pre-stressed carbon fibre-reinforced lattice core for sandwich panels. *J Compos Mater* n.d. <https://doi.org/10.1177/00219983211021659>.
- [26] Kim SW, Koh JS, Lee JG, Ryu J, Cho M, Cho KJ. Flytrap-inspired robot

using structurally integrated actuation based on bistability and a developable surface. *Bioinspiration and Biomimetics* 2014;9:36004–18. <https://doi.org/10.1088/1748-3182/9/3/036004>.

- [27] Hyer MW. Some Observations on the Cured Shape of Thin Unsymmetric Laminates. *J Compos Mater* 1981;15:175–94. <https://doi.org/10.1177/002199838101500207>.
- [28] Thill CL, Etches J, Bond I, Potter K, Weaver P. Morphing skins. *Aeronaut J* 2008;112:117–39.
- [29] Daynes S, Weaver PM. Review of shape-morphing automobile structures: concepts and outlook. *Proc Inst Mech Eng Part D J Automob Eng* 2013;227:1603–22.
- [30] Troldborg N, Sørensen JN, Mikkelsen R, Sørensen NN. A simple atmospheric boundary layer model applied to large eddy simulations of wind turbine wakes. *Wind Energy* 2014;17:657–69.
- [31] Winkelmann C, Kim SS, La Saponara V. Design and development of hybrid composite bistable structures for energy absorption under quasi-static tensile loading. *Compos Struct* 2010;93:171–8. <https://doi.org/10.1016/j.compstruct.2010.06.002>.
- [32] Abarotin CA, Myers OJ, Pataky GJ. Low Velocity Impact of Bistable Laminated CFRP Composites. *J Dyn Behav Mater* 2019;5:432–43. <https://doi.org/10.1007/s40870-019-00209-8>.
- [33] Hexcel. HexWeb ® CR-PAA TM - Product data n.d.
- [34] Flora F, Rizzo F, Pinto F, Meo M. Ultrasonic consolidation (UC) debulking of thermosetting prepreg for autoclave curing of composite laminates. *Mater Today Proc* 2021;34:106–12. <https://doi.org/10.1016/j.matpr.2020.01.376>.
- [35] ISO EN. 6603–1: 2000, “Determination of puncture impact behaviour of rigid plastics – Part 1: non-instrumented impact testing.” ISO Norm 2000.
- [36] ISO E. 6603-2: 2000, “Determination of puncture impact behaviour of rigid plastics – Part 2: instrumented impact testing.” ISO Norm 2000.
- [37] Ishikawa T, Koyama K, Kobayashi S. Thermal Expansion Coefficients of Unidirectional Composites. *J Compos Mater* 1978;12:153–68. <https://doi.org/10.1177/002199837801200204>.
- [38] Boccaccio M, Rachiglia P, Malfense Fierro GP, Pio Pucillo G, Meo M. Deep-Subwavelength-Optimized Holey-Structured Metamaterial Lens for Nonlinear Air-Coupled Ultrasonic Imaging. *Sensors* 2021;21:1170.
- [39] Cochran S. Ultrasonics Part 12. Fundamentals of ultrasonic phased arrays. *Insight-Non-Destructive Test Cond Monit* 2006;48:212–7.
- [40] Taheri H. Utilization of Non-destructive Testing (NDT) Methods for Composite Materials Inspection (Phased Array Ultrasonic) 2014.
- [41] Heimbs S. Foldcore sandwich structures and their impact behaviour: an

overview. *Dyn Fail Compos Sandw Struct* 2013;491–544.

- [42] Wang J, Waas AM, Wang H. Experimental and numerical study on the low-velocity impact behavior of foam-core sandwich panels. *Compos Struct* 2013;96:298–311.
- [43] Hallquist JO. *LS-DYNA ® THEORY MANUAL*. 2006.
- [44] Chang F-K, Chang K-Y. Post-Failure Analysis of Bolted Composite Joints in Tension or Shear-Out Mode Failure. *J Compos Mater* 1987;21:809–33. <https://doi.org/10.1177/002199838702100903>.
- [45] Hallquist JO. *LS-DYNA keyword user's manual*. Livermore Softw Technol Corp 2007;970:299–800.
- [46] Thota NM, Epaarachchi JA, Lau KT. Evaluation of the blunt thoracic trauma due to baseball impacts—review of the Blunt Criterion 2014.
- [47] Smith L, Nevins D, Dat NT, Fua P. Measuring the accuracy of softball impact simulations. *Sport Eng* 2016;19:265–72.
- [48] Rizzo F, Cuomo S, Pinto F, Pucillo G, Meo M. Thermoplastic polyurethane composites for railway applications: Experimental and numerical study of hybrid laminates with improved impact resistance. *J Thermoplast Compos Mater* 2019. <https://doi.org/10.1177/0892705719856049>.
- [49] Jones DIG. *Handbook of viscoelastic vibration damping*. John Wiley & Sons; 2001.

8. Conclusions

The aim of this thesis was to study solutions for the design, manufacturing and development of novel advanced composite sandwich structures for high performance engineering applications, by acting on the known weak points of such materials: core mechanical properties and interlaminar strength of laminated skins and of core to skins interface.

The research and development of novel mechanically improved sandwich structures require solutions to overcome their limitations, exploring new manufacturing techniques for core, skins and their bonding. In this context, the reduction of manufacturing defects plays a fundamental role in the reduction of composite laminates premature failure. This can be done by acting in two ways: improving the manufacturing techniques in order to reduce the quantity of generated defects and developing damage localisation techniques able to reject defected parts during the production phase. Moreover, core mechanical properties and adhesion properties to the skins can be improved by acting on the design and constituent material of the same.

In this thesis, the approach to obtain this aim was based on the following points:

- The development of a novel manufacturing technique for composite laminates that use ultrasound consolidation procedure to obtain improvements in terms of interlaminar properties and defects reduction;
- The use of an innovative undamaged baseline approach in a novel NDE technique to detect defected parts during automatic composite manufacturing processes;
- The design of a new CFRP lattice core structure, named Circular Prestressed Carbon Core (CPCC), which takes advantage of an asymmetrical fibre orientation to generate residual thermal stresses to further improve the mechanical properties of the part;

- The design, manufacturing and impact characterisation of a novel high-performance 3D fibre reinforced sandwich structure based on the CPCC core, with a particular attention to the contribution of the residual stresses to the impact resistance in LVI conditions.

The reliability of the first approach, the use of Ultrasonic Consolidation debulking on laminated CFRP prepreg layers, was studied in this thesis both experimentally and analytically. First, the technique was used to manufacture several samples and its effect on the mechanical properties of the part studied through mechanical tests. Then, the phenomena of ultrasonic waves propagating through the prepreg systems and its effect on the voids transportation, coupled with vacuum pressure, were analytically studied. The experimental studies on this technique proved its effectiveness in considerably reduce the manufacturing time, reduce the voids content up to 96% and improving the mechanical properties, such as ILSS and flexural modulus, of the final parts.

The second approach to improve the manufacturing procedure consists in the development of a *real-time* NDE technique for defects recognition during automatic composite manufacturing. This NDE hardware has been installed directly on the automated machine and take advantage of the manufacturing heat source to generate thermography images of the part. Collecting data from the numerous parts produced, the system is able to learn information about the heat field, building an undamaged baseline, and recognise eventual anomalies due to possible defects such as voids, wrinkling or unwanted inclusions. The experimental work has proved the effectiveness of the method in detect several typologies of damage, with particular focus on the improvement provided by the manufacturing data-base undamaged baseline. This approach provides a method to reduce the number defected parts produced with the modern composite manufacturing procedures, such as automatic fibre placement, automatic tape placement or automatic induction welding, thus reducing the possibility of premature failures of parts such as sandwich skins.

The successive work presented in this thesis focused on the design of a novel CFRP lattice core, whose design is based on three concepts:

- The use of CFRP material to obtain high mechanical properties along the loaded directions, maintaining a low density;
- The use of a circular cell *close-packing* 2D structure design;
- The application of residual thermal stresses in order to enhance the compressive and energy absorption properties.

The core was experimentally and numerically characterised under several typologies of load, and results compared with a traditional aluminium honeycomb core in order to have a comparison with a structure commonly used in aerospace applications. The results showed large improvements when compared with the traditional core, especially for the in-plane properties. Of particular interest is the unique strength-to-density ratio obtained from the experimental tests, which places the core in a unique position in the range of known materials.

The final approach was aimed to the realisation of a novel sandwich structure using the CPCC core and CFRP skins and applying UC technique during the manufacturing of the skins, core and the bonding of them. The sandwich structure was experimentally and numerically studied under low-velocity impact loadings and the results compared with the same structure realised without core thermal residual stresses. Furthermore, a comparative campaign was conducted with sandwich panels made with aerospace grade aluminium honeycomb core in order to evaluate the competitiveness of the CPCC core in the field. The results validated the hypothesis of the contribution of residual thermal-stresses in improving the mechanical response and reducing damage extension of the part, which demonstrated to be able to carry large impacting loads limiting the damage extension to a small area and maintaining the structural integrity.

The works and results illustrated in this thesis provide several contributions to the design, manufacturing and development of advanced CFRP composites and sandwich structures, accomplishing the aim of the thesis.

8.1. Future Works

The works presented here can be continued in several manners. The UC technique can be further studied by applying it on more complex structures (larger dimensions, curvature, complex shapes) and experimentally study the influence of variables such as frequency of the wave, number of ultrasonic transducers, room temperature, and others.

The potentialities of the *real-time* NDE system may be expanded by combining it with artificial intelligence algorithms such as machine learning and deep learning, therefore providing the ability of improving the baseline with data collected during every manufactured part. In addition, the method can be experimentally proved on industrial machines such robotic lamination arms.

Finally, the CPCC core and sandwich structures can see several future paths. From the design side, the core can be further numerically and experimentally studied by varying design variables such as unit cell dimension, temperature ramp in residual stress formation and fibre orientation. The manufacturing procedure of the core needs to be improved in order to be suitable and attractive for industrial production. On this, a thermoplastic matrix version of the material can help from one side in making the core adaptable to the known thermoplastic honeycomb fabrication procedures, and on the other side making it compatible with the interests of engineering sectors of developing more recyclable and eco-friendly materials. On the characterisation of the sandwich structure, it can be of strong interest to experimentally study the after-impact mechanical properties, such as compression and flexural. Indeed, the results obtained during the work presented in chapter 7 suggest a strong structural integrity of the impacted samples that needs further analysis and characterisation.

8.2. PhD Activities

During the PhD programme at University of Bath, a number of scientific papers has been published in international peer-reviewed journals and a number of conference

proceedings of research works presented into international. Only part of these works was used in this thesis work.

Peer-reviewed Journals (published order):

1. Flora, F., Rizzo, F., Pinto, F., & Meo, M. (2021). Ultrasonic consolidation (UC) debulking of thermosetting prepreg for autoclave curing of composite laminates. *Materials Today: Proceedings*, 34, 106-112.
2. Flora, F., Boccaccio, M., Fierro, G. P. M., & Meo, M. (2021). Real-time thermography system for composite welding: Undamaged baseline approach. *Composites Part B: Engineering*, 215, 108740.
3. Fierro, G. P. M., Flora, F., Boccaccio, M., & Meo, M. (2021). Real-time automated composite scanning using forced cooling infrared thermography. *Infrared Physics & Technology*, 118, 103860.
4. Flora, F., Pinto, F., & Meo, M. (2021). Manufacturing and characterisation of a new thermal pre-stressed carbon fibre-reinforced lattice core for sandwich panels. Accepted for publication at *Journal of Composite Materials*
5. Russo A., Meo M., Zarrelli M., Flora F., Riccio A. (2021). An Experimental Assessment on the Influence of Carbon Nanotubes Matrix Charging on the Fatigue Behaviour of Composite Laminates. Accepted for publication at *Macromolecular Symposia – POLCOM 2021*
6. Flora, F., Rizzo, F., Pinto, F., & Meo, M. (2022). Development of an analytical model for optimisation of the ultrasonic consolidation of composite prepreg. Submitted (under review) at *Composites Part B*.

7. Flora, F., Pinto, F., & Meo, M. (2022). Experimental and numerical analysis of an impact resistant sandwich structure with thermal pre-stressed carbon-fibre reinforced lattice core. Submitted at *Journal of Impact Engineering*

Conference Papers (published order):

1. Fierro, G. P. M., Flora, F., & Meo, M. (2019, November). Thermal wave imaging for defect determination during automated fibre placement. In *12th International Workshop on Structural Health Monitoring: Enabling Intelligent Life-Cycle Health Management for Industry Internet of Things (IIOT), IWSHM 2019* (pp. 2294-2301). DEStech Publications Inc..
2. Flora, F., Boccaccio, M., Fierro, G. P. M., & Meo, M. (2020, April). Non-destructive thermography-based system for damage localisation and characterisation during induction welding of thermoplastic composites. In *Thermosense: Thermal Infrared Applications XLII* (Vol. 11409, p. 114090I). International Society for Optics and Photonics.

The research work I conducted during PhD period has been funded by the EXTREME project of the European Union's Horizon 2020 research and innovation programme under grant agreement No. 636549.

References

- [1] The Importance of Sandwich Structures and the Development of Kordsa's First Composite Sandwich Panel [Internet]. [cited 2020 Jul 8]. Available from: <https://www.reinforcer.com/en/category/detail/The-Importance-of-Sandwich-Structures-and-the-Development-of-Kordsas-First-Composite-Sandwich-Panel/86/451/0>.
- [2] Xu LR, Rosakis AJ. Impact failure characteristics in sandwich structures. Part I: Basic failure mode selection. *Int J Solids Struct*. 2002;39:4215–4235.
- [3] Hsiao HM, Lee SM, Buyny RA. Core crush problem in manufacturing of composite sandwich structures: Mechanisms and solutions. *AIAA J*. 2006;44:901–907.
- [4] Zhu S, Chai GB. Damage and failure mode maps of composite sandwich panel subjected to quasi-static indentation and low velocity impact. *Compos Struct* [Internet]. 2013;101:204–214. Available from: <http://dx.doi.org/10.1016/j.compstruct.2013.02.010>.
- [5] M.Jones R. *Mechanics of Composite Materials*. Mech. Compos. Mater. 1983.
- [6] Soutis C. *Aerospace engineering requirements in building with composites*. Polym Compos Aerosp Ind. Elsevier; 2020. p. 3–22.
- [7] Jones RM. *Mechanics of Composite Materials - 2nd Ed*. Taylor Fr. Gr. 1999.
- [8] Breuer UP. *Manufacturing Technology. Commer Aircr Compos Technol*. Springer; 2016. p. 73–132.
- [9] Elkington M, Bloom D, Ward C, et al. Hand layup : understanding the manual process Hand layup : understanding the manual process. *Adv Manuf Polym Compos Sci* [Internet]. 2015;1:138–151. Available from: <http://dx.doi.org/10.1080/20550340.2015.1114801>.

- [10] Fierro GPM, Flora F, Meo M. Thermal wave imaging for defect determination during automated fibre placement. *Struct Heal Monit* 2019 Enabling Intell Life-Cycle Heal Manag Ind Internet Things - Proc 12th Int Work Struct Heal Monit. DEStech Publications Inc.; 2019. p. 2294–2301.
- [11] Wilson AC, Us MA, Zhang H, et al. COMPOSITE TAPE LAYING APPARATUS AND METHOD. 2016;2.
- [12] G.G. Liversidge J.F. Bishop, D.A. Czekai KCC. FIBER PLACEMENT MACHINE. 1980;96:62–66.
- [13] Venkatesan C, Velu R, Vaheed N, et al. Effect of process parameters on polyamide-6 carbon fibre prepreg laminated by IR-assisted automated fibre placement. *Int J Adv Manuf Technol*. 2020;108:1275–1284.
- [14] Solvay. Technical Data Sheet CYCOM ® 977-2 and 977-2A PREPREG. 2020; Available from: <https://www.solvay.com/en/product/cycom-977-2>.
- [15] ASC Process Systems. ASC Process Systems Manufactured the World’s Largest Autoclave System [Internet]. 2021. Available from: <http://www.aschome.com/index.php/it/products/control-systems/2-uncategorised/327-world-s-largest-composites-autoclave>.
- [16] Breuer U. Commercial aircraft composite technology [Internet]. 2016 [cited 2020 Sep 15]. Available from: <https://link.springer.com/content/pdf/10.1007/978-3-319-31918-6.pdf>.
- [17] Qureshi Z, Swait T, Scaife R, et al. In situ consolidation of thermoplastic prepreg tape using automated tape placement technology: Potential and possibilities. *Compos Part B Eng*. 2014;66:255–267.
- [18] Kuenzi EW. Structural sandwich design criteria. 1959;
- [19] Noor AK, Burton WS, Bert CW. Computational Models for Sandwich Panels and Shells. *Appl Mech Rev* [Internet]. 1996;49:155. Available from: <http://appliedmechanicsreviews.asmedigitalcollection.asme.org/article.aspx?articleid=1395680>.

- [20] Fairbairn W. An account of the construction of the Britannia and Conway tubular bridges, with a complete history of their progress [Internet]. 1849 [cited 2020 Jul 14]. Available from: [https://books.google.it/books?hl=en&lr=&id=TriXdVPqOwYC&oi=fnd&pg=PA71&dq=Fairbairn+W+\(1849\),+An+Account+of+the+Construction+of+the+Britannia+and+Conway+Tubular+Bridges,+John+Weale,+London&ots=wOvUquPEqM&sig=tqXSfoguN4l220NtTriNpWjzTcw](https://books.google.it/books?hl=en&lr=&id=TriXdVPqOwYC&oi=fnd&pg=PA71&dq=Fairbairn+W+(1849),+An+Account+of+the+Construction+of+the+Britannia+and+Conway+Tubular+Bridges,+John+Weale,+London&ots=wOvUquPEqM&sig=tqXSfoguN4l220NtTriNpWjzTcw).
- [21] Zenkert D. THE HANDBOOK OF SANDWICH CONSTRUCTION [Internet]. 1997 [cited 2020 Jul 13]. Available from: <https://www.diva-portal.org/smash/get/diva2:1366187/FULLTEXT01.pdf>.
- [22] Feichtinger KA. Test Methods and Performance of Structural Core Materials -1. Static Properties. *J Reinf Plast Compos*. 1989;8:334–357.
- [23] Symposium on Structural Sandwich Constructions [Internet]. ASTM International; 1957. Available from: <https://books.google.co.uk/books?id=ThmbamnVF7kC>.
- [24] Lewis WC, others. Cellular cellulose acetate core material in shear. *FATIGUE Sandw Constr Aircr*. 1946;
- [25] Boller KH. Buckling Loads of Flat Sandwich Panels in Compression: The Buckling of Flat Sandwich Panels with Either All Edges Simply Supported Or All Edges Clamped (cores of Paper Honeycomb and Facings of Glass Cloth Laminate). Forest Products Laboratory; 1948.
- [26] Reissner E. On the theory of bending of elastic plates. *J Math Phys*. 1944;23:184–191.
- [27] Reissner E. The effect of transverse shear deformation on the bending of elastic plates. *J appl Mech*. 1945;A69--A77.
- [28] Reissner E. On bending of elastic plates. *Q Appl Math*. 1947;5:55–68.
- [29] Engineers DF-T of the AS of C, 1957 undefined. Thick rectangular plates on an elastic foundation. *cedb.asce.org* [Internet]. [cited 2020 Jul 15];

Available from:
<https://cedb.asce.org/CEDBsearch/record.jsp?dockkey=0294337>.

- [30] Salerno VL, Goldberg MA. Effect of shear deformations on the bending of rectangular plates. *J Appl Mech Trans ASME*. 1960;27:54–58.
- [31] Koeller R, Mech FE-P 4th UNCA, 1962 undefined. Shear deformation in rectangular plates.
- [32] Speare PRS, Kemp KO. A simplified reissner theory for plate bending. *Int J Solids Struct*. 1977;13:1073–1079.
- [33] Libove C, Batdorf S. A general small-deflection theory for flat sandwich plates. 1948 [cited 2020 Jul 15]; Available from: <https://apps.dtic.mil/sti/citations/ADA298666>.
- [34] Mech. RM-J appl., 1951 undefined. Influence of rotatory inertia and shear on flexural motions of isotropic, elastic plates. *ci.nii.ac.jp* [Internet]. [cited 2020 Jul 15]; Available from: <https://ci.nii.ac.jp/naid/10007241429/>.
- [35] Allen HG. *Analysis and design of structural sandwich panels*. Oxford Pergamon Press. 1969;
- [36] Hall DJ, Robson BL. A review of the design and materials evaluation programme for the GRP/foam sandwich composite hull of the RAN minehunter. *Composites*. 1984;15:266–276.
- [37] Gdoutos E, Daniel IM. Failure modes of composite sandwich beams. *Theor Appl Mech*. 2008;35:105–118.
- [38] Daniel IM, Gdoutos EE, Wang K, et al. Failure modes of composite sandwich beams. *Int J damage Mech*. 2002;11:309–334.
- [39] Gdoutos EE. *FAILURE MECHANISMS OF COMPOSITE SANDWICH*. 2014;
- [40] Gdoutos EE, Daniel IM, Wang K-A. Compression facing wrinkling of composite sandwich structures. *Mech Mater*. 2003;35:511–522.

- [41] Abot JL, Daniel IM, Gdoutos EE. Contact law for composite sandwich beams. *J Sandw Struct Mater.* 2002;4:157–173.
- [42] Abot JL, Daniel IM, Gdoutos EE. Failure mechanisms of composite sandwich beams under impact loading. *Proc 14th Eur Conf Fract Cracow.* 2002. p. 13–19.
- [43] Gdoutos EE, Daniel IM, Wang KA. Indentation failure in composite sandwich structures. *Exp Mech.* 2002;42:426–431.
- [44] Daniel IM, Gdoutos EE, Abot JL, et al. Effect of loading conditions on deformation and failure of composite sandwich structures. *Am Soc Mech Eng Appl Mech Div AMD.* 2001;248:1–17.
- [45] Gdoutos EE, Daniel IM, Wang KA. INDENTATION FAILURE OF SANDWICH PANELS. *6th Natl Congr Mech.* 2001. p. 320.
- [46] Daniel IM, Gdoutos EE, Abot JL, et al. Core failure modes in composite sandwich beams. *Am Soc Mech Eng Appl Mech Div AMD.* 2001;249:293–303.
- [47] Daniel IM, Abot JL, Wang KA. Testing and analysis of composite sandwich beams. *Proc ICCM.* 1999.
- [48] Daniel IM, Abot JL. Fabrication, testing and analysis of composite sandwich beams. *Compos Sci Technol.* 2000;60:2455–2463.
- [49] Dan Zenkert. *The Handbook of Sandwich Construction.* 1995;442. Available from: <https://www.diva-portal.org/smash/get/diva2:1366187/FULLTEXT01.pdf>.
- [50] Hoff NJ, Mautner SE. The buckling of sandwich-type panels. *J Aeronaut Sci.* 1945;12:285–297.
- [51] Plantema FJ. *Sandwich Construction,* Wiley, New York, 1966.
- [52] Mansourinik M, Taheri-Behrooz F. The effect of interface debonding on flexural behaviour of composite sandwich beams. *J Sandw Struct & Mater [Internet].* 2020;22:1132–1156. Available from:

<https://doi.org/10.1177/1099636218781981>.

- [53] Vadakke V, Carlsson LA. Experimental investigation of compression failure of sandwich specimens with face/core debond. *Compos part b Eng*. 2004;35:583–590.
- [54] Yan B, Wang X, Pan S, et al. Stability and Failure of the Edge-Closed Honeycomb Sandwich Panels with Face/Core Debonding. *Appl. Sci.* . 2020.
- [55] Soden PD. Indentation of composite sandwich beams. *J Strain Anal Eng Des*. 1996;31:353–360.
- [56] Shuaeib FM, Soden PD. Indentation failure of composite sandwich beams. *Compos Sci Technol*. 1997;57:1249–1259.
- [57] Olsson R, McManus HL. Improved theory for contact indentation of sandwich panels. *AIAA J*. 1996;34:1238–1244.
- [58] Petras A, Sutcliffe MPF. Indentation failure analysis of sandwich beams. *Compos Struct*. 2000;50:311–318.
- [59] Y. F, M. B. Localized Load Effects in High-Order Bending of Sandwich Panels with Flexible Core. *J Eng Mech [Internet]*. 1996;122:1069–1076. Available from: [https://doi.org/10.1061/\(ASCE\)0733-9399\(1996\)122:11\(1069\)](https://doi.org/10.1061/(ASCE)0733-9399(1996)122:11(1069)).
- [60] Reddy JN. A simple higher-order theory for laminated composite plates. 1984;
- [61] Jeong H. Effects of Voids on the Mechanical Strength and Ultrasonic Attenuation of Laminated Composites. *J Compos Mater [Internet]*. 1997;31:276–292. Available from: <https://doi.org/10.1177/002199839703100303>.
- [62] Lionetto F, Anna RD, Montagna F, et al. Modeling of continuous ultrasonic impregnation and consolidation of thermoplastic matrix composites. *Compos PART A [Internet]*. 2016;82:119–129. Available from: <http://dx.doi.org/10.1016/j.compositesa.2015.12.004>.

- [63] Chu Q, Li Y, Xiao J, et al. Processing and characterization of the thermoplastic composites manufactured by ultrasonic vibration – assisted automated fiber placement. 2018;
- [64] Rizzolo RH, Walczyk DF. Ultrasonic consolidation of thermoplastic composite prepreg for automated fiber placement. 2016;
- [65] Farhang L. Void evolution during processing of out-of-autoclave prepreg laminates. 2014;222.
- [66] Arafath ARA, Fernlund G, Poursartip A. Gas transport in preregs: model and permeability experiments. Proc 17th Int Conf Compos Mater [Internet]. 2009;1–9. Available from: <http://www.iccm-central.org/Proceedings/ICCM17proceedings/Themes/Manufacturing/RESIDUAL STRESS & PROCE/C4.9 Fernlund.pdf>.
- [67] Xiong J, Ma L, Wu L, et al. Mechanical behavior and failure of composite pyramidal truss core sandwich columns. Compos Part B Eng. 2011;42:938–945.